Customizable Drug-Loaded Implants Produced via Fused Deposition Modeling

Inaugural-Dissertation

zur Erlangung des Doktorgrades der Mathematisch-Naturwissenschaftlichen Fakultät der
Heinrich-Heine-Universität Düsseldorf

vorgelegt von

Hanna Ponsar
aus Bergheim

Düsseldorf, Mai 2022

aus dem Institut für Pharmazeutische Technologie und Biopharmazie
der Heinrich-Heine-Universität Düsseldorf

Gedruckt mit der Genehmigung der
Mathematisch-Naturwissenschaftlichen Fakultät der
Heinrich-Heine-Universität Düsseldorf

Berichterstatter:

1. Prof. Dr. Jörg Breitkreutz
2. Prof. Dr. Dr. h.c. Peter Kleinebudde

Tag der mündlichen Prüfung: 04.08.2022

„Just keep swimming.“

- Dory, Finding Nemo.

Publications

Parts of this thesis have already been published in peer-reviewed journals or conferences.

Original Publications

I. El Aita, I., Ponsar, H., Quodbach J., 2018. *A Critical Review on 3D-printed Dosage Forms.* Curr Pharm Des. 24(42): p. 4957-4978.

DOI: 10.2174/1381612825666181206124206

Ilias El Aita was invited by the journal Current Pharmaceutical Design to contribute a review on 3D-printing of pharmaceutics. The design of the review article and keyword selection was developed by Ilias El Aita and Hanna Ponsar and optimized based on the advice of Julian Quodbach. The systematic literature research was conducted by Ilias El Aita and Hanna Ponsar using pre-selected keywords. The manuscript was written by Ilias El Aita and Hanna Ponsar and revised by Julian Quodbach.

Evaluation of the authorship I: "*A Critical Review on 3D-printed Dosage Forms*". Parts of contribution in %.

Author	Idea	Study design	Evaluation	Manuscript
Ilias El Aita	30	35	60	40
Hanna Ponsar	30	35	40	40
Julian Quodbach	40	30	-	20

II. Ponsar H., Wiedey R., Quodbach J., 2020. *Hot-Melt Extrusion Process Fluctuations and their Impact on Critical Quality Attributes of Filaments and 3D-printed Dosage Forms*. Pharmaceutics. 12(6): 511.

DOI: 10.3390/pharmaceutics12060511

Hanna Ponsar was responsible for the idea and the study design for the manuscript. Julian Quodbach provided help for the conceptualization of the idea and the development of the study design. The experimental work, formal analysis and data evaluation were performed by Hanna Ponsar. Raphael Wiedey contributed to a part of the statistical analysis (bootstrap analysis). The manuscript was written by Hanna Ponsar and revised by Julian Quodbach.

Evaluation of the authorship II. "*Hot-Melt Extrusion Process Fluctuations and their Impact on Critical Quality Attributes of Filaments and 3D-printed Dosage Forms.*" Parts of contribution in %.

Author	Idea	Study design	Experimental	Evaluation	Manuscript
Hanna Ponsar	80	80	100	85	80
Raphael Wiedey	0	0	0	5	5
Julian Quodbach	20	20	0	10	15

Oral Presentation

Ponsar H. and Quodbach J., *Process Optimization of Filament Production for 3D-Printing via Hot-Melt Extrusion*. 13th Annual Meeting of the Pharmaceutical Solid State Research Cluster (PSSRC), Duesseldorf (Germany) 2019.

Poster presentation

Ponsar H. and Quodbach J., *Development of Non-biodegradable Filaments for 3D-printed Implant Inserts.* 3rd European Conference on Pharmaceutics, Bologna (Italy) 2019.

Ponsar H. and Quodbach J., *Hot-Melt Extrusion Process Analysis and Optimization of Filament Production for Pharmaceutical 3D-Printing*. 12th World Meeting on Pharmaceutics, Biopharmaceutics and Pharmaceutical Technology (PBP), Vienna (Austria) 2020. *Comment: Abstract submitted and accepted. The conference was cancelled due to the Covid-19 pandemic and therefore poster has not been presented.*

Table of Contents

Abbreviations and non-SI units

α	significance level
3PBT	three-point bend test
A	surface area
ACN	acetonitrile
API	active pharmaceutical ingredient
CAD	computer-aided design
CBS	conveyor belt speed [mm/s]
CE	conveying element
CI	confidence interval
CoV	coefficient of variation
CQAs	critical quality attributes
CRS	chemical reference standard
DaB	distance at break
DDS	drug delivery system
DIN	Deutsches Institut für Normung
DS	degree of substitution
DSC	differential scanning calorimetry
EC	ethyl cellulose
EDQM	European Directorate for the Quality of Medicines and Healthcare
FDA	Food and Drug Administration
FDM^{TM}	fused deposition modeling
FFF	fused filament fabrication
HME	hot-melt extrusion
HEPES	4-(2-hydroxyethyl)-1-piperazineethanesulfonic acid
Hertz	Hz
HPLC	high performance liquid chromatography
HPMC	hydroxypropyl methylcellulose
i.art.	intraarticular
ICH	International Council for Harmonisation of Technical Requirements for Pharmaceuticals for Human Use
IQR	interquartile range
ISO	International Organization for Standardization
KB	kneading blocks
KE	kneading elements
LC-MS	liquid chromatography-mass spectroscopy

LFR	liquid feed rate
LOD	limit of detection
LOQ	limit of quantitation
LPCE	long pitch conveying elements
MMU	multi material unit
MW	molecular weight
m/z	mass to charge ratio
n	number of samples
N	Newton
PBS	phosphate-buffered saline
PFR	powder feed rate
pH	negative decadic logarithm of the hydrogen ion activity
Ph. Eur.	European Pharmacopoeia
PLA	polylactic acid
PLGA	poly(lactic-co-glycolic acid)
QbD	quality by design
R^2	coefficient of determination
rH	relative humidity
RMSEP	root mean squared error of prediction
RT	room temperature
s	standard deviation
SA	stearic acid
SFL	specific feed load
SLA	stereolithography
SLS	selective laser sintering
SPS	sodium pyrosulfite
STL	stereolithographic file format
TA	triamcinolone acetonide
TEC	triethyl citrate
T_g	glass transition temperature
T_m	melting temperature
t_R	retention time [min]
TRIS	trometamol
USP	United States Pharmacopoeia
UV	ultraviolet
YM	Young’s modulus

1. Introduction

1.1 3D-Printing Technologies in Pharmaceutics

In recent years, 3D-printing, also known as additive manufacturing or rapid prototyping, has become an emerging topic within the pharmaceutical area due to its high potential for individualized therapy. The quantity of published pharmaceutical literature using the keywords “3D-printing” and “Pharmaceutics” between the years 2000 and 2020 extracted from Pubmed is depicted in Figure 1. The research has grown extensively during and after 2015 when the Food and Drug Administration (FDA) approved the first 3D-printed medicinal product Spritam® (Aprecia Pharmaceutical, LLC). This step was indicative of new pathways in pharmaceutical manufacturing [1].

Researchers are investigating several 3D-printing techniques related to their feasibility for pharmaceutical application.

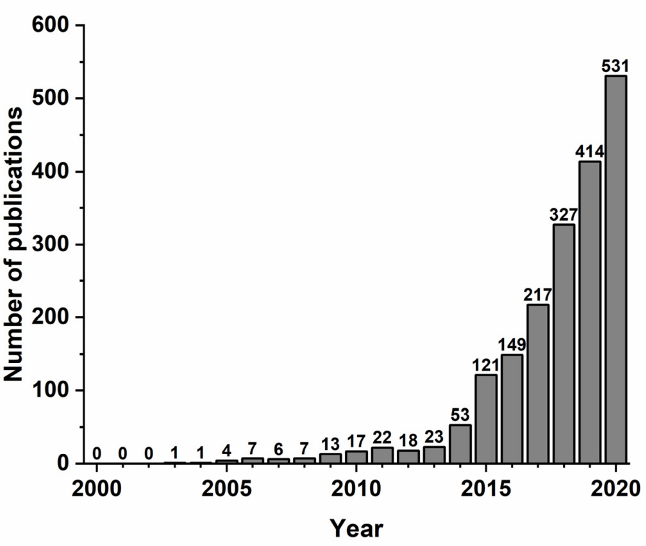

Figure 1. Number of publications about 3D-printing of pharmaceutics between 2000 and 2020. Data was extracted from Pubmed using the search terms “3D-printing” and “Pharmaceutics”.

In general, 3D-printing is a layer-wise production of 3D-objects from digital design [2]. By changing the digital model, the same starting material can be used to create an unlimited variety of sophisticated geometries. Thereby, e.g., hollow networks are printable as exemplarily depicted in Figure 2, not realizable with any other commonly used pharmaceutical manufacturing technique. All printing technologies have the following basic manufacturing steps in common:

1. Design: Creation of the targeted 3D-object using computer-aided design (CAD) software based on predefined shape requirements.
2. Conversion of the digital model into a machine-readable format (e.g., *.stl*-file), describing the object surface in triangles.

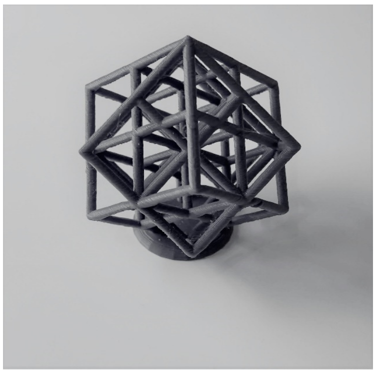

Figure 2. 3D-printed object using commercial PLA-filament showing the opportunities of creating sophisticated geometries. The CAD file was downloaded and modified from a template provided by thingiverse.com [3].

3. Slicing and G-code generation: Processing of the *.stl*-file to separate the object in distinct horizontal, printable layers of a predefined height and conversion into a G-code, which is a programming language for numerical computer control, containing commands for the printer to operate (e.g., printing speed, print-head route).
4. Printing: Starting material is processed into the predesigned 3D-object, starting from the bottom.

For some 3D-printing methods, post-processing is required, e.g., sintering, drying or removal of supportive structures.

The most important 3D-printing technologies can be mainly categorized into laser-, powder-based inkjet- and extrusion-based printing systems (Figure 3). The corresponding term is related to the principle of layer formation.

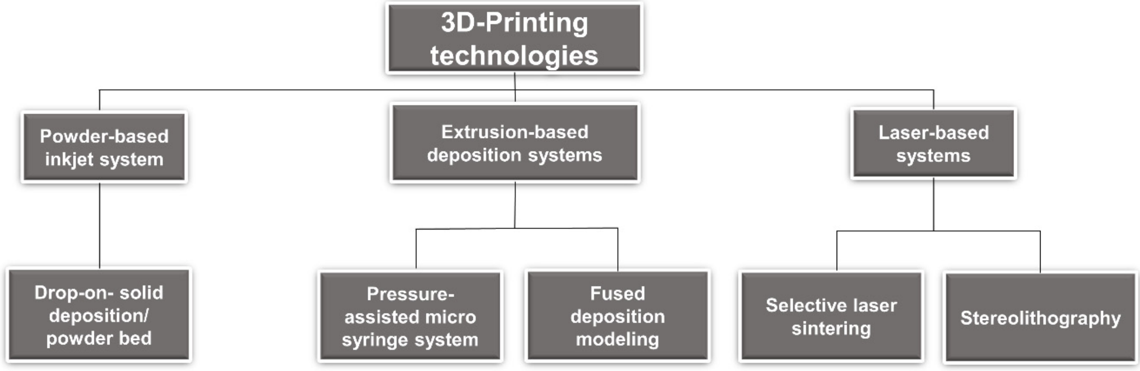

Figure 3. Overview of the most important 3D-printing technologies for pharmaceutical applications.

Laser-based systems can be divided into selective laser sintering (SLS) and stereolithography (SLA). 3D-printing via SLS is performed by sintering powder particles using a laser beam as schematically depicted in Figure 4a. This technique is widely used for metals. A high resolution of objects is enabled by a small laser spot size [4, 5]. In combination with active pharmaceutical ingredients (APIs) the high energy input might induce degradation and is therefore of minor relevance compared to other technologies to produce medicinal 3D-printed products, but nevertheless researched [6, 7].

SLA 3D-printing methodology offers the highest object resolution amongst all methods. As starting materials resins are utilized, photo polymerising on a build plate applying a laser beam comparable to SLS (Figure 4b) [4, 8]. The building plate is integrated within the resin bath. After solidifying the first layer, the build plate moves down corresponding to the set layer height. The next layer is built likewise. A rotating mirror allows to accurately move the laser spot, and consequently a precise layer formation in x- and y-direction [9]. The most relevant drawback is the lack of resins with sufficient pharmaceutical quality with low toxicity [1, 10].

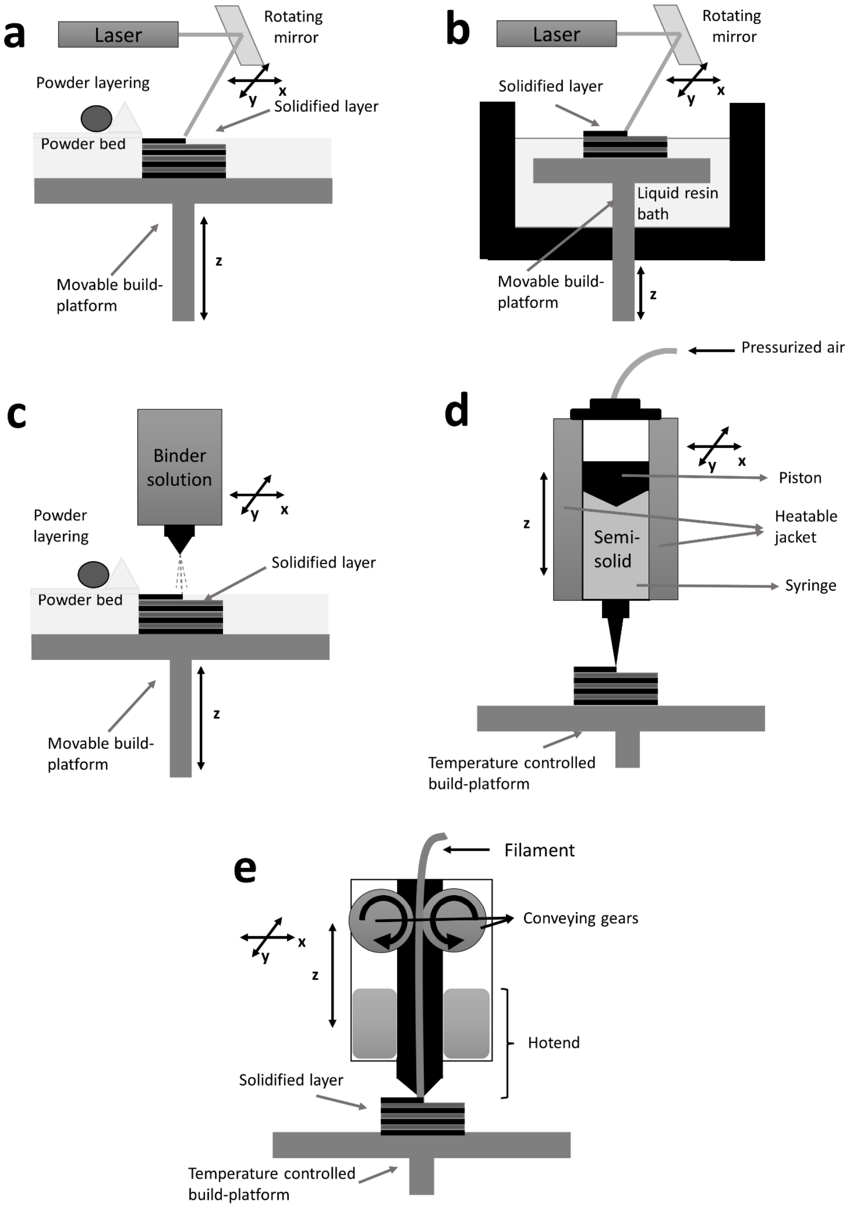

Figure 4. Schematic depiction of different pharmaceutical relevant 3D-printing processes: (a) SLS, (b) SLA, (c) binder deposition (drop-on-solid), (d) pressure-assisted micro syringe system and (e) FDM^{TM} (modified and adjusted from [1]).

The binder deposition (drop-on-solid) method belongs to the powder-based inkjet methods. This technology is used for Spritam®, where a binder solution is printed onto a powder bed (Figure 4c) [11]. The solidification mechanism of each layer is enabled analogue to wet granulation via adhesive bonding by a binder or solution of particles and subsequent recrystallisation [12]. After the finalization of one layer, the next powder layer is spread, e.g., via a scraper. The resolution of the object is mainly dependent on the particle size of the powder [13]. The drug substance is either incorporated into the powder or the binder solution. Due to the low thermal stress, it is feasible to process thermo-sensitive APIs. Unbound powder serves as support to allow sophisticated free-standing prints. The obtained 3D-object is usually highly porous and enables a rapid disintegration [11, 14]. As it is a comparable process to wet granulation, a wide range of processable raw materials is available [10]. The main drawbacks are a high friability and low mechanical resilience of products and the required post-processing steps of additional drying, removal and recycling of residual powder.

Worldwide, extrusion-based 3D-printing methods are the most commonly used techniques and are extensively explored amongst pharmaceutical researchers [15]. Forcing substances through a nozzle of the print-head depicts the basic principle. Layer creation can be consequently done onto different surfaces or substrates [16].

One technique of this category is the pressure-assisted micro syringe system, most established in the field of tissue engineering (bioprinting), but also frequently investigated for medicinal product manufacturing [17]. Viscous semi-solids serve as starting materials and require challenging formulation development related to viscosity and potential segregation [13]. The mass is filled into a syringe equipped with a piston to extrude the material via pressurized air with predefined speed through a nozzle with variable size as schematically depicted in Figure 4d [18]. The extruded strands are deposited on a platform to obtain the desired object. As the printing formulation is based on solvents, post-processing via additional drying is required. An advantage of this technique is that the printing process can be performed at room temperature (RT). Consequently, thermo-sensitive APIs can be processed in combination with volatile solvents. In addition, flexible objects can be realized. A common problem is nozzle clogging. To avoid this, organic solvents like methanol, acetone and dimethyl sulfoxide are commonly used, limiting the application for certain patient groups [18-22]. Residual solvents in printed dosage forms must therefore comply with International Council for Harmonisation (ICH) guidelines [23]. Further drawbacks are potential object deformation upon drying and a comparatively low print resolution [1].

The second extrusion-based and most explored 3D-printing technique for pharmaceutical products is the so-called fused deposition modeling (FDM™), trademark by Stratasys, Inc., or fused filament fabrication (FFF). Prefabricated thermoplastic, polymeric filaments serve as feedstock material. For the printing process, the solid filament is conveyed via counter-rotating gears inside the print-head and molten within the heated part, named hotend (Figure 4e). Subsequently, the molten mass is pushed by unmolten conveyed filament sections through the nozzle and deposited in distinct layers on a temperature-controlled build plate. The desired 3D-object is realized by movements in x-, y- and z-directions of the building plate and/or the print-head. The printing temperature is a decisive parameter to ensure a suitable melt viscosity of the polymer to generate a constant flow and deposition while avoiding degradation of the material [24]. The temperature of the build-platform is usually considerably lower to guarantee sufficient solidification. However, the temperature difference between the molten material and the platform should not be too high to realize a proper adherence between the single layers. The printing resolution depends on the selected speed, layer height and nozzle diameter [24]. Besides the removal of potential support structures, if overhangs are needed, a post-processing step is not required. APIs can be incorporated by either impregnation of drug-free filaments into drug-loaded solutions [25, 26] or by hot-melt extrusion (HME) of drug-loaded polymer mixtures [27, 28]. The main drawback is the applied thermal stress, during FDM^{TM}, increasing the risk of potential thermal degradation.

The FDM^{TM} technology was selected during the present work to develop customizable 3D-printed implants for several reasons. First, it offers printing with low-cost equipment and the possibility to individualize dosage forms adapted to patient needs and application sites in versatile ways [10, 29]. It presents, compared to other printing technologies, a promising approach for compounding dosage forms in hospitals and pharmacies, where industrially manufactured filaments serve as feedstock material. Once a suitable filament composition is found, sophisticated objects with high dose flexibility and impact on dissolution profiles can be realized [25, 29, 30]. Compared to the other presented technologies no powder handling (e.g., in case of high potent APIs), radiation or solvents are necessary during printing. This is often crucial in terms of occupational safety. The risk of segregation and resulting inhomogeneous drug distribution within the drug delivery system (DDS) is unlikely, due to the applied solid starting material, simplifying on-demand manufacturing.

In addition, printing and combining different materials are feasible using multiple print-heads or automatic filament-changers. Thereby, incompatible APIs can be jointly processed in one DDS [31]. Also, multidrug, or multi-formulations dosage forms can be realized [32-34], which might increase the individualization degree, therapeutic efficacy or enables different release characteristics. Further, the drug release can be easily modified by changing the geometry or infill-density originating from the same start formulation [29, 35, 36], which makes this technology particularly suitable for the investigations in the framework of this work.

1.2 Hot-melt Extrusion Coupled with Fused Deposition Modeling

As previously described, FDM^{TM} requires filaments, consisting of thermoplastic solid-state polymers as starting material. A production of pharma-grade drug-loaded filaments is needed, since only drug-free commercial (non-pharmaceutical quality) ones are currently available, not suitable for medicinal products.

The most favoured manufacturing technique for pharma-grade filaments is HME [37]. HME is a well-established pharmaceutical process, ensuring a solvent-free production and simplified scalability [38]. During HME a polymeric powder blend is fed into a heated extruder barrel and molten. Depending on the applied extrusion process single- or twin-screw set-ups knead the mixture and convey it. The molten mass is then extruded through a die with a defined diameter to create a filament. As the production of high-quality filaments is challenging within the pharmaceutical area, many researchers focused on formulation development and filament fabrication to access the coupling of HME with FDM^{TM}-printing in recent years [24, 27, 28, 38-42]. Although many thermoplastic polymers are suitable for HME, most of them are not appropriate for filaments, as they do not exhibit the thermal and mechanical properties, required for a robust and reliable FDM^{TM} process. The mechanical resilience of pharma-grade filaments is decisive, as they undergo continuous stress (tensile and compressive forces) in transversal and longitudinal direction within the print-head [27, 40, 43, 44].

Drug-loadings of filaments can be achieved in two ways: either by impregnation of drug-free filaments with organic drug solutions or HME extrusion of API-polymer blends. The benefit of the impregnation method is the reduced degradation risk, as no thermal stress occurs. Due to the limited drug-load capacity < 2 % [25, 26, 45, 46] and the need for organic solvents accompanied with an additional drying step, this approach is unfavoured in an industrial environment [45, 47]. In contrast, the direct processing of API and polymer or polymer blends combined with further excipients (e.g., plasticizer, pore former) via HME offers high flexibility related to drug-loads. Drug concentrations up to 60 % were realized in the filaments [48]. The avoidance of an additional manufacturing and post-processing and the possibility of continuous production are superior process characteristics within the pharmaceutical industry. A drawback is the thermal stress during both processes - HME and FDM^{TM}-, increasing the risk of API degradation at the required extrusion temperature for polymers.

In early studies, the development and production of drug-loaded filaments was mainly performed in small-scale extrusion processes, using single-screw extruders [29, 49-52], conical twin-screw extruders [30, 36, 41, 53, 54] or ram extruders [55, 56]. The process batch size varied between 5 to 50 g. This might be sufficient for a first polymer screening and formulation development but is not representative for an industrial-scale process. Neither a change of screw configuration nor a continuous manufacturing process is enabled. These might be given for single-screw extruders, but they do not meet pharmaceutical standards compared to twin-screw extrusion processes. Latter are preferred due to comparably improved melting and feeding properties, degassing capabilities, as well as dispersive and distributive mixing under controlled conditions [57]. A few scientists applied co-rotating 11-mm twin-screw extruders, better indicating a continuous process [28, 58-60]. However, only few researchers focused on larger batch sizes using 16 mm 40D co-rotating twin-screw extruders considering the impact of process parameters on critical quality attributes (CQAs) [27, 42]. One of the most important quality attributes potentially influenced by HME process parameters is the filament diameter and its homogeneity to ensure a reproducible 3D-object printing. It must therefore be monitored strictly. A target diameter is achieved by stretching the filament behind the die, e.g., on conveyor belts. However, a continuous process with automatic filament collection and precise diameter monitoring was rarely applied. In the past, diameters were often measured manually via callipers and undesired parts were discarded [32, 40, 61, 62], which is not applicable and adequate in terms of proper quality control.

Further studies increasing the knowledge of coupling HME with FDM^{TM} towards continuous filament production based on quality by design (QbD) within the pharmaceutical industry area is a huge demand.

1.3 Parenteral Depot Systems

According to the European Pharmacopoeia (Ph. Eur.) monograph 0520, “parenteral preparations are sterile preparations intended for administration by injection, infusion or implantation into the human or animal body” [63]. They have been developed for the medication of various diseases and are administered via implantation in the respective organ or tissue or by different routes including intravenous (i.v.), subcutaneous (s.c.), intramuscular (i.m.), epidural, intraarticular (i.art.), intravitreal application [64, 65]. Over the past decades, extended-release parenteral applications are in focus for efficient therapy, as systems release the API from a reservoir (also called depot) constantly over an extended period within the therapeutic range. They are of interest in case of issues during oral administration, like e.g., first-pass inactivation, low oral bioavailability, and the need for prolonged drug release and/ or a targeted drug delivery to a specific application site [66]. In comparison to immediate release parenteral dosage forms, depot DDS enable a homogeneous drug distribution at the relevant compartment avoiding fluctuations. The administered drug amount can be reduced, as it is directly introduced to the target site not affected by the first-pass metabolism. Simultaneously, systemic side effects can be minimized, especially important in terms of high-potent APIs. Combined with a reduced frequency of administration the patient adherence is increased [66, 67]. Latter is beneficial, especially for patient groups who are unable, physically or mentally, to adhere to the medication regimens. The drug release can either take place on a systemic level or directly at the target site for a local treatment.

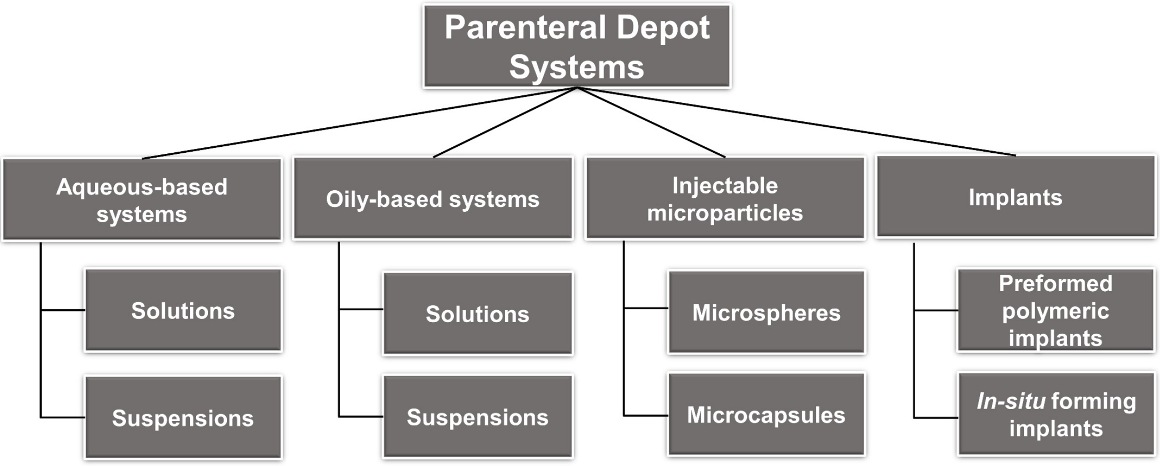

Figure 5. Overview of galenical options to enable parenteral depot systems.

Different pharmaceutical strategies are applied to enable the desired depot effect (Figure 5). The choice of the respective approach depends on several aspects, such as API characteristics, stability, targeted duration, application site and indication.

Aqueous or oily depot injectables are beneficial related to simple and cost-effective manufacturing. In case of solutions, the extension of drug release is mainly dependent on the used vehicles (aqueous vs. oily), the application site and the viscosity. They are often used in combination with molecularly modified APIs via application of low soluble salts or pro-drug formation (e.g., esterification, complexation) [65]. The drug release from oily solutions is mainly controllable by the partition coefficient between the depot and tissue fluid, the interfacial area and diffusivity [65, 68]. The clinical relevance of these approaches is minor, as options for tailoring the drug release are limited [65].

The depot effect from injectable nano- and microcrystal-suspensions can be further prolonged as the API release is mainly affected by the dissolution kinetics in the surrounded body fluid and the surface area of particles [69]. Especially aqueous crystal suspensions with poorly soluble APIs are marketed for several indications to prolong the drug release via s.c., i.m., i.art. or intravitreal injection (e.g., Agofollin Depot®, Zyprexa®, Kenalog®, Depo Medrol/Lidocain®). The depot effect can be mainly controlled by the lipophilicity of the drug, the particle size and API concentration [69]. The main challenge of these systems is the maintenance of physical stability (e.g., Ostwald ripening, sedimentation) and quality during sterilization and storage [65]. The limited options to influence the drug release are a major drawback.

Formation of microparticles from solid or liquid drug substances is another strategy for parenteral depot systems. In case of microspheres, APIs are embedded (suspended or dissolved) in a polymer matrix, whereas in microcapsules the drug substances are surrounded by a polymeric shell [70]. Microparticles are, e.g., realized via interfacial polymerisation, coacervation, solvent evaporation or spray drying and applied by s.c. or i.m. injections [71]. Biodegradable polymers, e.g., alginates, collagen or poly(lactic-co-glycolic acid) (PLGA) have been used [65]. Obtained microparticles offer protection from degradation, improved compatibility and less toxicity within the tissues while prolonging the drug release between days and months [65]. Marketed PLGA-based microparticles are, e.g., Arestin ®, Nutropin Depot®, Trelstar® LA or Zilretta®. The API release is controlled by diffusion from the matrix or through the capsule wall, and possibly also by simultaneous polymer swelling and the erosion rate of the biodegradable polymers [65]. The drug release kinetics can be modified by e.g., the microparticle size, surface porosity, polymer molecular weight and added excipients [72]. Main limitations are the elaborated and expensive, not easily scalable manufacturing processes and constraints related to high drug-loads [65, 72].

Implants are the fourth group of parenteral depot systems. According to the Ph. Eur., implants are "solid sterile preparations of suitable size and shape for parenteral implantation. They provide drug delivery over an extended period. […]" [63]. *In-situ* forming depot formulations are also often summarized as implants. They consist of a biodegradable polymeric injectable liquid or semi-solid and undergo a spontaneous solidification or gelation upon injection, mainly through different precipitation via phase separation/solvent extraction, pH-shift or cross-linking [73]. The resulting dissolution kinetic is driven by diffusion and polymer erosion. The drug release can be controlled depending on the used polymer and solvents [74]. Marketed *in-situ* formed implants based on the so-called Atrigel® system are Atridox®, Preseris® or Eligard®. The advantages of these systems are a relatively simple manufacturing technique, localized API application and the ability to prolong drug delivery with less invasive application. A major challenge is the use of organic solvents and the frequently observed burst effect [74].

The classical solid drug-loaded implants are polymeric, mainly cylindrical, rods. They consist either of non-biodegradable or biodegradable materials. In the first case, removal at the end of the therapy is required. Depending on their size or application site they are surgically implanted or subcutaneously injected. The surgical implantation and possibly explantation depict the major drawbacks. However, frequent injections can be avoided, accompanied by repeated doctor visits.

Currently, manufacturing techniques of drug-loaded implants are HME, injection moulding, compression, or solvent casting. The dissolution kinetics of polymeric implants is diffusion-controlled and in case of the biodegradable polymers additionally dependent on polymer erosion. The drug release control is restricted to the polymers and one formulation. This is the case for all polymeric long-acting parenteral DDS. An advantage compared to the other presented depot approaches is an easy implant removal in case of adverse reactions to terminate the therapy if required [75].

Marketed implantable devices are primarily used for systemic application for contraception (e.g., Implanon®, Nexplanon®) and cancer treatment (e.g., Leuprone Hexal®, Suprefact®, Zoledan®). Besides a systemic therapy via s.c. application, solid implants can be introduced in the peripheral system to allow a targeted local treatment or replace body parts for repair, support, or therapy purposes. Simultaneously, the systemic drug level can be reduced to avoid severe side effects in healthy tissues. This offers major benefits compared to oral or injectable depot systems, especially in the fields of cancer, dental, orthopaedic, post-operative local antibiotic, cardiovascular and rheumatic therapy [76, 77]. Approved medicinal products for these intents are limited. For instance, Gliadel® wafers (compressed-moulded platelets containing carmustine) provide local therapy in the brain cavity after tumour resection. CiproScrew® is a biodegradable implant used for fracture fixation, while simultaneously preventing post-surgical infections associated with mechanical fixations.

Long-acting implantable devices gained a lot of attention among researchers for certain clinical applications to overcome limitations of current depot-systems and improve therapy efficiency as well as patient compliance [77-79]. An important limitation is that currently a shape adaption independent from dose or drug release alteration adapted to individual anatomical structures is not possible in the presented cases and applied manufacturing techniques. Another challenge is the on-demand capability of such systems, to provide higher flexibility and targeted therapy in clinical routine operation [76]. Advances in novel technologies and further research therefore may result in the opportunity to create more complex implantable devices, improving the dose, drug release control and targeting adapted to individual patient conditions and diseases, with minimal drawbacks.

1.4 Opportunities and Challenges of 3D-Printing to Produce Customized Drug-loaded Implants

Individualized medicines have gained a lot of attention over the past years in the medical and pharmaceutical field. For specific diseases or treatments adapted to populations and patient-specific conditions like gender, age, body mass, multimorbidity or genetic heterogeneity adapted therapies are desirable [80-83]. Dose and drug release personalisation as a response to assayed biomarkers, or predefined pharmacodynamics or -kinetics is therefore of rising interest [84, 85]. Thereby, the therapeutic efficacy can be potentially increased, whereas side effects can be reduced, resulting in increased therapeutic safety. Moving away from the “one-size-fits-all” approach, patients should be treated with the right medicinal product using the right dose at the right time [86].

Due to the already reported advantages of drug-eluting implants, they represent an effective option in this matter. APIs of particular interest are antibiotic, anti-inflammatory, immunosuppressive drugs, anti-cancer drugs or APIs for tissue and cellular regeneration/proliferation [78, 87-91]. Traditional methods to produce implantable devices are well established in terms of process understanding, quality attributes and regulatory pathways. However, they show limited individualization and flexibility degrees. Commonly applied implants like contraceptives (Nexplanon® [92] or Jadelle® [93]) are rod-shaped, which do not offer the possibility to adjust the drug release using the same formulation or enabling a shape adaption. The biggest challenges of those implants are how to control drug release within the therapeutic window, how to individualize such drug dosage forms also related to dose and shape and how to target the application site of interest, by adapting to anatomical structures. To face these challenges, new manufacturing technologies and research are urgently needed to realize patient centricity.

3D-printing technologies provide effective solutions in this context. Wu et al. demonstrated already in 1996 the opportunity of 3D-printed implants to allow a controllable long-term parenteral drug therapy [94]. It shows competitive advantages for complex customized medicinal products to potentially improve therapeutic efficacy. Using additive manufacturing techniques, especially FDM^{TM}, nearly every complex shape and geometry can be realized via CAD models as depicted in Figure 2. This is especially promising in terms of drug-loaded implants administered to application sites with high anatomical variability. Thereby, a fast individual adjustment of the shape to body cavities is possible to support structures and make local therapy more efficient due to high API exposure. Anatomical data for the production of shape adapted implants can be obtained from medical image technologies, like computed tomography or magnetic resonance tomography [95]. Resulting image data are processed using Data Imaging and Communications in Medicine (DICOM) software. Areas of interest can be segmented and converted into *.stl*-files, enabling customized adaptions in hospitals [96]. This was already done for prostheses in the dental and orthopaedic fields for anatomic reconstruction without containing actives [97, 98].

In addition, the size or the geometry/inner structure can be adapted to customize the dose [30] and/ or the drug release, e.g., via different infill densities [35]. This can be easily performed via the 3D-printing slicer software using the same bulk formulation. Drug combinations in one DDS adapted to patient conditions can be realized, where the different APIs are divided into sections achieving different release profiles [19].

3D-printing has already been evolved in literature for different implant applications to evaluate the performance and applicability towards an improvement and customization of therapy [99]. The design, material choice, drug-loadings have to be carefully aligned to the respective disease, localization and individual human conditions to achieve an effective therapy, with appropriate release performance and treatment period [99]. Some opportunities for drug release modification of implants via 3D-printing have been already demonstrated. Stewart et al. [100], e.g., developed different implants with reservoir types and Allen et al. [101] devices with varying channel diameters, whereby the drug release could be varied between a few days and months using the identical bulk feedstock material.

Besides drug release modification of implants, API combinations were investigated in the context of post-surgical infections. This is a common problem after surgeries or surgical insertion of implants, accompanied by a long-term oral antibiotic therapy. Studies using 3D-printed implants combined with an additional antibiotic API have been shown to be an effective approach to reduce bacterial growth [102-105]. Weisman et al. incorporated gentamycin and methotrexate into different implantable geometries (catheters, discs and beads) to prevent bacterial growth while decreasing osteosarcoma cell growth [104]. Water et al. developed antibiotic eluting feedstock material for FDM^{TM} with Nitrofurantoin, containing additionally hydroxyapatite to facilitate simultaneous bone growth [103]. This eliminates the need for oral antibiotic therapy after surgeries or surgical insertion of an implant, which is associated with many side effects.

The shown flexibility of freedom of design, drug release control and free choice of API combinations demonstrated the potential of 3D-printing for the on-demand manufacturing of highly sophisticated, customizable parenteral DDS. As individual adaptions can be done in real-time and the equipment for 3D-printing is simple and low-cost, a production at the point of care appears possible [1]. Further research in this area is therefore inevitable to evolve the capability of this technique.

In contrast to the various opportunities of 3D-printing of medicinal devices and medicinal products, the approach is accompanied with some challenges, open questions and limitations, which are already known. The limitations of different technologies were already reported in detail in section 1.1. The manufacturing efficiency of 3D-printing technologies is not comparable in throughput to industrial well-established processes. An option might be the parallel working of multiple printers to allow larger-scale production. 3D-printing might be most suitable for the on-demand manufacturing of small batches of patient-specific DDS, especially for solid parenteral dosage forms [106].

Notably, in terms of personalized medicine, regulatory challenges and limitations remain a key topic for 3D-printed medicinal products [107]. Compliance with Good Manufacturing Practices is required for pharmaceutical manufacturing under federal regulation CFR21 part 211. Current printing equipment is not compliant in this regard. Open questions are related to cleaning procedures for the avoidance of cross-contamination and process control via process analytical tools. Efforts from printer provider might solve these issues. Fortunately, this is not required in hospital and pharmacy settings, but a certain standard will have to be met. For this, it has to be clarified if products can be considered as pharmacy preparations according to EU directive 2001/83/EC Article 3 (magistral or officinal formulas) or extemporaneous preparations defined in the Ordinance on the Operation of Pharmacies [108, 109]. The regulatory effort might be reduced. However, the responsibilities in case of adverse incidents are a key factor to be clarified (e.g., manufacturer of the starting feedstock material, the printing operator, or the owner of the pharmacy).

Further, the quality assessment of 3D-printed medicinal products is different, due to the novelty and uniqueness of these processes [106]. Current requirements by the United States Pharmacopoeia (USP) and the Ph. Eur. might be not applicable, requiring new quality attributes (e.g., printing defects such as shrinkage or layer separation), test methods and standardizations for the feedstock material and dosage forms. In conclusion, a deeper understanding of the process and CQAs to transfer to a community or hospital pharmacy setting and additional control methods are required to guarantee the quality, efficacy and safety of 3D-printed products.

Another remaining key challenge of solid parenteral preparations in this context is the warranty of sterility. In terms of real-time production, effective methods must be established at the point of care. Heat-sterilisation is, e.g., not applicable to FDM^{TM}-printing technologies and thermosensitive APIs, most suitable for pharmacies and hospitals. Aseptic manufacturing or sterilized starting materials and subsequent transfer to the local manufacturing site might be an option. However, clean-room concepts need to be established to maintain sterility during printing of dosage forms.

1.5 Triamcinolone Acetonide for Individualized Parenteral Drug Treatment

Triamcinolone acetonide (TA) was used as model API in the present work. The chemical structure is shown in Figure 6. TA is a synthetic glucocorticoid with predominantly anti-inflammatory activity by repression of inflammatory transcription and subsequently induced gene activation pathways [110]. It is commonly used for skin, rheumatic, respiratory, ophthalmic and allergic diseases [111, 112]. It is a lipophilic derivate of triamcinolone with poor water solubility and therefore with low oral bioavailability, belonging to the biopharmaceutical classification system class IV [113]. Treatments are consequently limited to topical or parenteral applications. Crystal suspensions are marketed for sublesional, i.m., intrafocal and i.art. administration [114]. The local application via i.art. injection is indicated for inflammatory joint-diseases, exudative arthritis, activated arthrosis, hydrops artulorum intermittens and acute forms of perioarthropathia humeroscapularis [114]. As consequence of systemic side effects, the injection frequency of glucocorticoids is restricted to three-times per year and intermissions of six weeks are recommended [115], impeding pain complaint management. Further, the residence time of TA within the synovial cavity is limited to three to four days [116, 117] as a trans-synovial efflux causes a frequent complete fluid replacement within 24 h [118]. Consequently, pain relief associated with glucocorticoid injections decreases following treatment, restricting the clinical benefits only up to

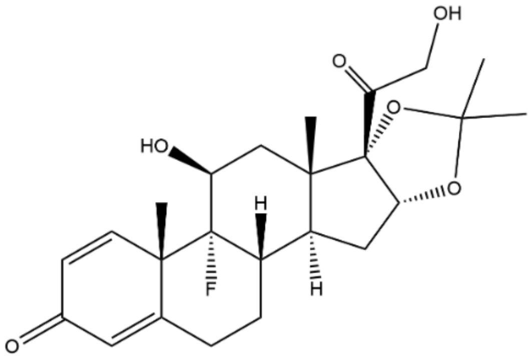

Figure 6. Chemical structure of TA.

four weeks [119, 120]. The accompanied rapid systemic absorption can result in an increase of cardiovascular and metabolic side effects [121] and reduced therapy efficacy and patient compliance.

To overcome the limitations of the i.art. application and adverse reactions, a prolonged residence time within the joint cavity and controlled drug release by applying shape-adapted implantable devices might therefore be beneficial to achieve constant local TA levels while reducing systemic absorption. Recently, Zilretta® (research code FX600), a PLGA-based microsphere formulation, was approved by the FDA as extended-release TA injection preparation [122]. In clinical phase 2 and 3 trials, it was shown that Zilretta® shows measurable TA concentrations within the synovial fluid up to 12 weeks and diminished plasma peak levels compared to TA crystal suspensions [65, 116, 123]. Therapy efficiency related to pain, stiffness and physical functions could be improved clinically significant because of a prolonged residence time and increased synovial fluid TA concentrations [116, 124, 125]. However, the modification of drug release kinetics and the personalization degree of microspheres is limited.

Studies show that there is a need to improve the i.art. application of TA via new approaches and DDS developments [126]. 3D-printing provides a great potential to create tailor-made TA eluting implantable preparations in this context as both, dose and drug release, can be adapted and controlled to individual conditions. Additionally, the opportunity to print complex TA-loaded structures matched accurately to the joint cavity or an artificial knee prosthesis is a move forward to improve the efficacy and safety of osteoarthritis treatments.

2. Aims and Outline

The existing various parenteral dosage forms, some of which require a high level of manufacturing effort, are not suitable for enabling individualized depot dosage forms produced on-demand in hospitals. For TA a need has been identified to improve therapeutic efficiency and patient compliance of the i.art. application. This might be achieved by the prolongation of articular residence time and control of drug release while enabling simultaneously a shape adaption.

The aim of this work was therefore the development of TA-loaded printable filaments via HME and subsequently novel customizable implants using the FDM^{TM} 3D-printing technology. All phases of drug product development shall be addressed. A generally applicable implant concept shall be designed, enabling a high individualisation degree regarding dose and drug release adaption independent of the shape and vice versa. Adapted to the defined target product profile of a customizable implant, the first part of the thesis focuses on a systematic development of drug-free and TA-loaded filament formulations via twins-screw HME. Based on mechanical properties and the targeted sustained release behaviour over several months, plasticizers and the pore former hypromellose (HPMC) in different concentrations shall be evaluated.

Once suitable formulations for the intended use are found, a rational HME process analysis and optimization using the QbD-approach shall be aimed at, identifying optimal process parameters for filament production. As important filament CQA, the diameter consistency and its impact on mechanical properties and content uniformity of printed DDS will be investigated.

In addition, developed filaments shall be subjected to a stability analysis taking packaging and different storage conditions into account. Thereby, critical factors on filament quality and shelf-life shall be elaborated.

For the examination of newly developed 3D-printed implants, *in vitro* long-term dissolution studies for the assessment of TA release are obligatory. Therefore, an appropriate dissolution method set-up and protocol including analytical development shall be developed. The main aspects to consider are TA stability in the aqueous dissolution medium in long-term studies and the opportunity to investigate simultaneously multiple implant designs at a reduced volume.

The final goal of the work was the investigation of the potential of different network designs via 3D-printing to modify the drug release over the targeted period. The individualization and prediction degree of the release behaviour of 3D-printed implants shall be investigated. Thereby, the analysis effort shall be reduced and transferability towards production in hospitals or pharmacies achieved.

3. Results and Discussion

3.1 Development of a Customized Implant System and Formulation Development of 3D-printable Filaments for Implants

3.1.1 Introduction and Objectives

The first and fundamental aim of the present work was the development of a generally applicable customizable modular implant design, allowing independent individualization of dose, drug release, and shape, adaptable to anatomical structures. This is necessary in advance to identify the required filament types and formulation attributes for the intended use. The literature related to 3D-printed implants, especially using FDM^{TM}, is limited. Shape adaptions via 3D-printing were extensively explored in the orthopaedic and dental field but without incorporation of an API [97, 98, 127]. Few research groups evaluated metal implants produced via SLS, offering a highly resilient structure against load, with a hollow reservoir consisting of channels to enable drug elution [101]. Other researchers soaked different printed implantable shapes with anti-cancer drug suspensions [128]. These concepts offer somehow the opportunity to modify the drug release and dose to a limited degree of freedom, while a shape adaption without influencing the drug-eluting surface is not possible. To the best of my knowledge, the literature related to drug-loaded FDM^{TM}-printed implants covers neither shape adaptions, nor a combination of shape, drug release and dose tailoring. In addition, a concept applicable to various treatments was not described. This was taken as motivation to provide such a concept towards the direction of customizable parenteral therapy using TA as a clinically relevant model drug.

Based on the developed target design of the modular drug-loaded implant and predefined requirements the second aim was the formulation development of printable filaments via HME. Filament production was performed on a twin-screw hot-melt extruder to achieve an industrially applicable process. Suitable excipients combinations for the intended use must be selected and manufacturing processes for filaments had to be developed following a rational route.

The formulation development should be performed based on the systematic approach presented by Korte [109], slightly modified to achieve the aimed objectives. Figure 7 shows the modified flowchart of Korte for the development of a printable filament, considering flowchart symbols of Deutsches Institut für Normung (DIN) 66001 [109, 129] (changes to Korte`s flowchart are marked in light blue). A detailed explanation of the flowchart as introduction is given in the following.

After predefining the general filament requirements based on the target profile of the printed medicinal product the formulation development starts with the selection of an API-polymer-combination. The thermal drug stability at the processing temperature of used polymers and targeted drug release behaviour must be considered as selection criteria. Different ratios of polymer and API should be tested during an initial screening using ram extrusion with a small batch size between 5-10 g [109, 130]. Thereby, a rough estimation of the API polymer compatibility and a suitable process temperature to avoid degradation can be determined with reduced material consumption.

The selected drug load of the filament is decisive for the printed DDS size correlating with the target dose. Although 3D-printing allows for flexible dose adjustment by size adaption [30], still a determination of a minimum and maximum suitable size and subsequently drug-load of filaments for the intended application is necessary. Additionally, the drug-load might have an impact on mechanical and solid-state properties of filaments and consequently printing performance [109].

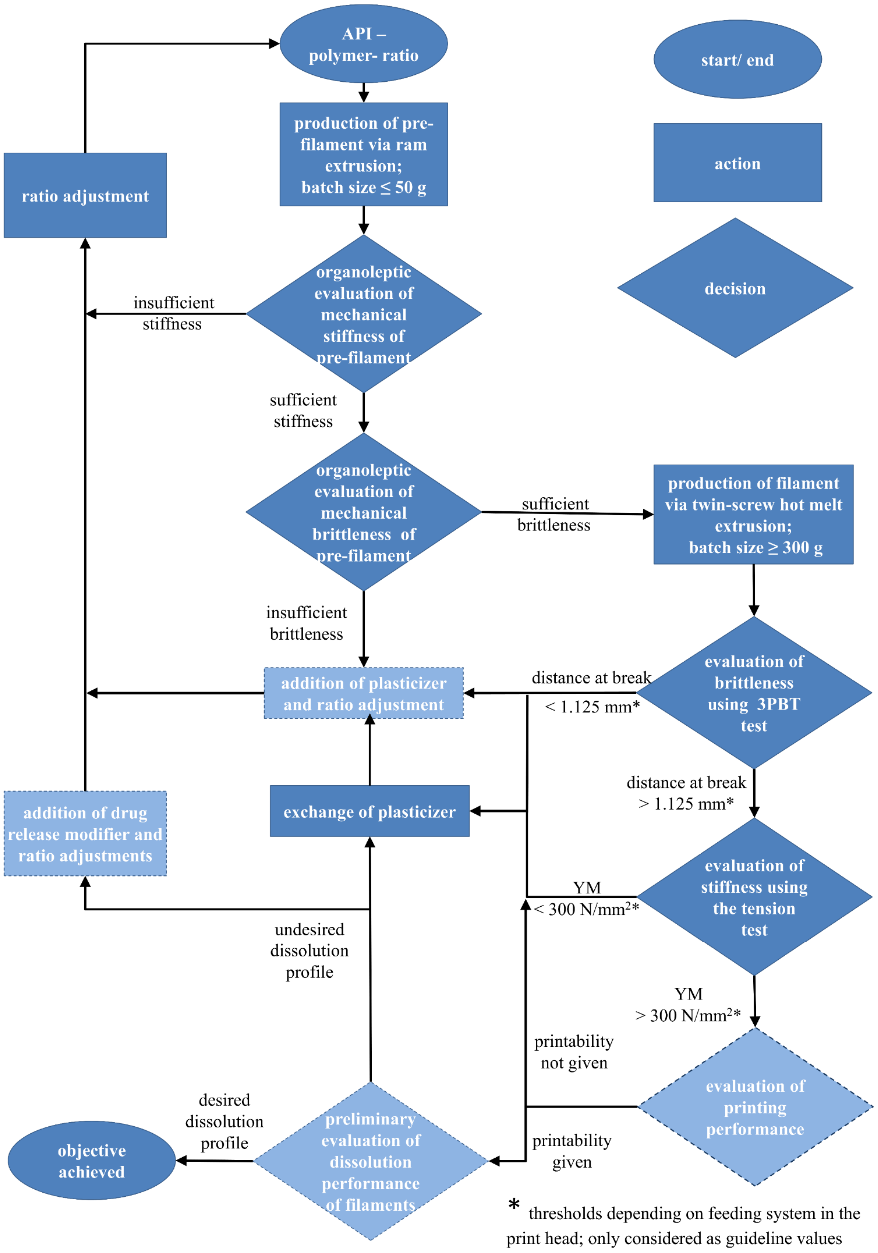

* thresholds depending on feeding system in the print head; only considered as guideline values

Figure 7. Flowchart for formulation development of printable filaments for the intended use adapted and modified from Korte [109]. Changes to Korte's flowchart are marked in light blue.

Pre-filaments produced via ram-extrusion should then undergo an organoleptic evaluation of the mechanical properties, as main factor to ensure printability [27, 28]. Filaments with decreased stiffness or increased brittleness might fail in printability, thoroughly discussed in section 3.1.4.2.2. Only a rough assessment of pre-filaments is possible, as the achieved quality via ram-extrusion is limited due to the diameter and surface irregularities. In addition, the mixing capacity of the ram extruder is not sufficient. Therefore, data obtained from mechanical testing and other analysis would not be representative. If the mechanical stiffness in longitudinal direction appears organoleptically too low, ratio adjustments are required. An increase of the solid fraction via higher suspended API and/or excipient concentration, serving as structure-giving component, might be useful [109]. If the stiffness is sufficient, the brittleness in transversal direction should be evaluated subsequently. In case the filament brittleness is too high, a plasticizer must be added. Different ratios should be tested to improve and tune the resilience of filaments in axial direction until apparent good filament formulations are found. Once a promising formulation is discovered, the transfer to twin-screw HME must be demonstrated and initial process parameters shall be evaluated to yield evaluable and printable filaments. Subsequently, the mechanical properties distance at break (DaB) and Young`s modulus (YM) of produced drug-loaded filaments are determined in a three-point-bend test (3PBT) and a tensile test based on the testing regime developed by Korte and Quodbach [27].

Sufficient resilience for printability is given according to [27], if the DaB exceeds 1.125 mm and 300 N/mm^2 for the YM. In this work, these thresholds are going to be used only as guideline values and for comparison purposes of different formulations, as they depend on the used filament feeding system inside the print-head. Hence, thresholds are not generally applicable and can vary. A verification via an additional printability test was therefore included (section 5.5.8). If none of the filaments with different plasticizer or plasticizer ratios are printable an exchange of polymers might be helpful.

An evaluation of the practical handling, related to storage, winding and unwinding from spools should also be considered as selection criterium. Especially in terms of industrial production, further extensions of the flow chart might be necessary and other thresholds must be examined. In case printable filaments could be produced successfully, preliminary dissolution studies of filaments are mandatory. It has to be kept in mind that the drug release from the polymer matrix is additionally influenced by various factors, like additional excipients (e.g., plasticizer, pore former), the solubility of the API in the dissolution medium, API-polymer interaction and the subsequently printed structure [109]. However, the general applicability of the formulation for the intended use can be tested and further drug release modulators might be added. If the drug release behaviour is promising the aimed objective is achieved. If not, two options for modification exist. If the drug release is dependent on the plasticizer type (hydrophilic or lipophilic) and its amount, ratios can be adjusted. The second option is the addition of drug release modifiers (pore former or pore blocker).

In this case ratios must be re-adjusted until the desired dissolution performance is achieved. In terms of long-term drug release, a short investigation period should be tested and predictive approaches are beneficial to estimate the long-term performance. With each change of the plasticizer or other additives, the impact on mechanical properties and consequently printability needs to be reassessed.

The described development concept by Korte was adapted and modified for the intended use. Key excipient selection criterium for the drug-loaded formulation for implants was a prolonged TA release ideally over several weeks up to months. Therefore, a model base polymer had to be selected, enabling a very low release rate. Different compositions, plasticizers and ratios should be evaluated to yield suitable filament formulations to produce customizable TA-loaded implants via 3D-printing. After a promising base composition was found, the drug release behaviour of the base filament formulation shall be modified by the incorporation of a pore former in different ratios.
As part of the study, the mechanical and solid-state properties of the filament formulations were investigated. The filament diameters shall be additionally assessed as further quality attribute. The filament surface and component distribution were evaluated using confocal Raman microscopy.

3.1.2 Modular Implant Design for Individualization of Shape, Dose and Drug Release Using 3D-Printing

The starting point of the project was the development and realisation of a customizable implant design. The i.art. application of the TA-loaded implant should increase the residence time in different kinds of joints up to multiple months. In this context, a release period of up to three months was targeted.
Although a specific API and a target application site were selected, the provided concept shall be generally applicable. The evaluated approach must be transferable to various parenteral treatments and targets, where a shape adaption to the individual anatomical variety appears reasonable. Simultaneously, the dose and drug release should be individualizable considering different patient needs and diseases. Thereby, a synergistic effect of an anatomical defect replacement or adaption and local drug therapy can be offered. This was considered beneficial to reduce treatment duration and medical outcome in orthopaedic surgeries [131]. Consequently, the novel design shall provide a universal approach to adapt the shape to the target application site, independently from dose and drug release adjustments. This was aimed at, as every change in shape and size would affect the dose as well as drug release, limiting individualization [30]. By using the opportunities offered by 3D-printing, implants with the freedom to adapt to a variety of anatomical structures shall be created.
The idea was to develop a customizable modular implant-inlay design only feasible using dual 3D-printing. The implant consists of a drug-free shell (module I), wherein a drug-loaded inlay (module II) is embedded as exemplarily depicted in Figure 8. The inlay can be systematically tailored in

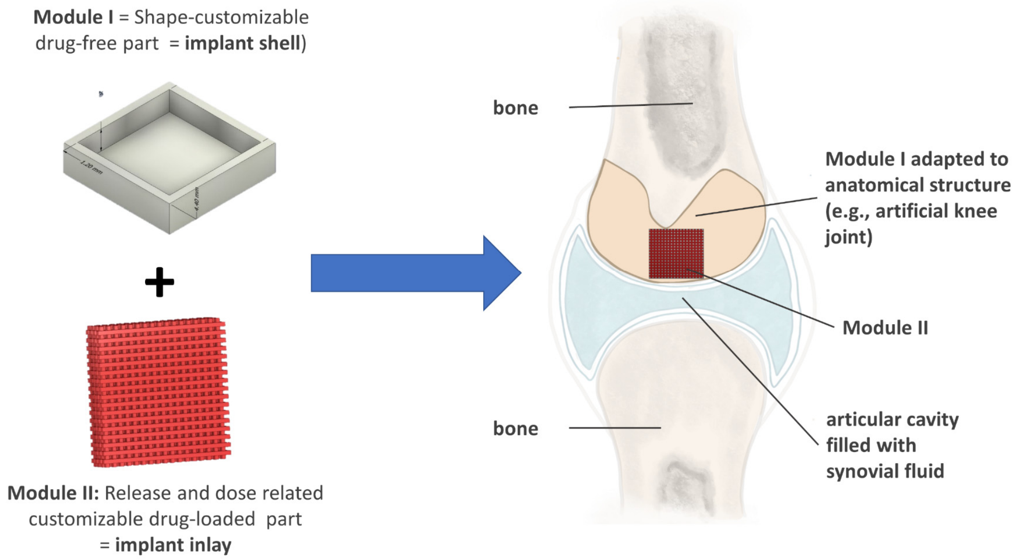

Figure 8. Designed modular implant concept and exemplary application within the articular cavity adapted to anatomical structures.

terms of drug release and dose, whereas the outer drug-free part can be adapted independently to other anatomical structures, e.g., joint, bone or brain cavities. Module I is designed to allow unidirectional drug release with only one side facing the medium. The remaining sides are covered by the drug-free sheath. This offers the advantage that the implant is not limited in thickness depending on the size of the anatomical part to be replaced. The biggest benefit, however, is that the treatment can be focused locally, increasing possibly treatment efficiency while reducing systemic and local side effects at the surrounding tissue. Module II consists, e.g., of a mesh and can be modified for dose and/or drug release adaption independently from module I. The potential variations of the drug-loaded inlay to influence the drug release is discussed in detail in section 3.4.2. With the presented design a concept was created, which offers a high potential to realize a flexible customizable implant.

3.1.3 Excipient Selection for Filament Development

The choice of materials is a fundamental part of designing solid drug dosage forms with predefined specifications. Regarding formulation development of printable filaments for FDM^{TM}-printing different aspects must be considered. So far, there are no benchmarks for material properties to ensure their suitability for FDM^{TM}-printing of drug dosage forms. The physicochemical properties of the material already have a huge impact on the drug release behaviour. Solid-state characteristics are important to consider in terms of the thermally guided manufacturing processes. The suitability of the material for HME and subsequent 3D-printing is restricted to the thermoplastic rheological melt behaviour of the polymer, as well as the thermal stability of all constituents as previously reported. Additionally, the number of regulatory approved polymer excipients is limited [132]. Related to pharmaceutical implants the used components must be biocompatible and in cases where anatomical structures are replaced resistant against movement stress. Therefore, the availability of proper pharmaceutical grade excipients for FDM^{TM}-printing of implants for i.art. administration is limited. In literature, many polymers for different applications were evaluated for their suitability for FDM^{TM}-printing coupled with HME [13]. But for pharmaceutical 3D-printed implants this issue was hardly addressed and only few researchers covered the topic so far [39, 133].

For the designed implant concept as described in section 3.1.2, a drug-free filament is required to enable a shape-adapted unidirectional drug release and a TA-loaded filament formulation for long-term drug release over approximately three months. As Kempin et al. demonstrated, the release properties of drug-loaded implants were highly affected by the material used [39].

For both filament types, a low substituted (N-type; 48.0-49.5 % ethoxy group per anhydroglucose unit) ethyl cellulose (EC) was chosen as main base, recommended for HME applications [57]. It is a natural biocompatible, non-biodegradable pharma-grade polymer, which has been used as a coating agent, tablet binder or filler in many different dosage forms in the past [134, 135]. In chemical terms, it is a polysaccharide of 1.4- β-linked D-glucose units derived semi-synthetically from cellulose (Figure 9). Depending on the degree of substitution (DS), the hydroxyl groups are partially substituted with ethyl groups. EC is inert, practically insoluble in water and a non-swellable thermoplastic polymer [136]. Due to these characteristics, EC is suitable for non-biodegradable, implantable DDS with a strong diffusion-controlled sustained release profile and was therefore selected as model polymer [39, 137, 138]. Additionally, it is suitable as shell-matrix to allow the targeted unidirectional drug release. Since HME is used for the manufacturing of filaments, extrudability and thermal stability are important to consider. In pharmaceutical research, HME of matrices using EC was extensively explored, demonstrating its feasibility and advantageous thermal viscoelastic behaviour [139-143]. In addition, it was already used in filament preparations for 3D-printed oral dosage forms [28, 144, 145], drug-free barriers [40] and implants [39] showing a good FDM^{TM-} printing performance.

Although TA release was expected to be too slow using EC in form of a high dense FDM^{TM}-printed product, first different additives for mainly mechanical optimization should be evaluated before modifying the drug release via pore formers. Two different plasticizers were included in different concentrations to investigate their influence on the glass transition temperature (T_g) of polymers

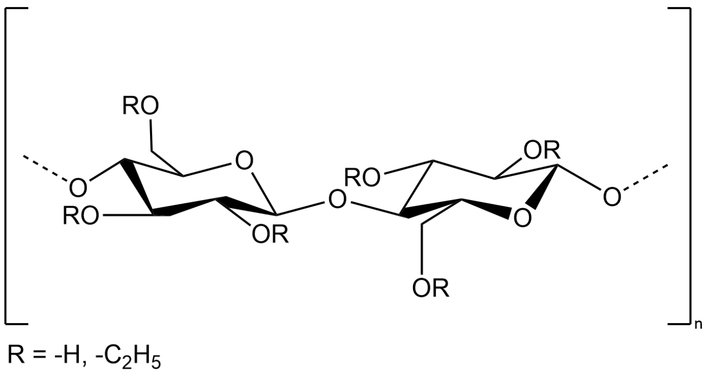

Figure 9. General chemical structure of EC.

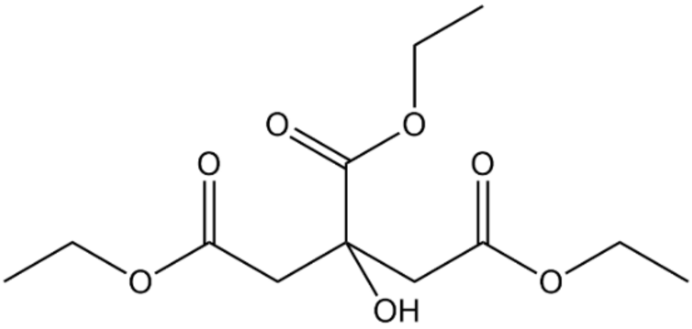

Figure 10. Chemical structure of TEC.

and the mechanical properties of filaments. The processability, but also the practical handling, like winding on spools in continuous industrial manufacturing, as well as transport should be addressed to find suitable compositions. The combination of triethyl citrate (TEC) as liquid plasticizer and EC has already been reported in the literature [146]. The main advantage is that for formulation development the introduced amount can be easily adapted within one experiment during twin-screw HME. This may reduce time and material efforts. A drawback is the higher tendency for evaporation during high-temperature processes [134]. Thereby the manufacturing might be influenced, resulting in higher process fluctuations or the relative API content is changed. Therefore, stearic acid (SA) was included additionally as solid plasticizer, suitable for HME in combination with EC [57, 147]. TEC is a commonly used plasticizer in pharmaceutical formulations, especially for coatings. According to the Ph. Eur.it is a physiologic harmless clear, viscous liquid and soluble in water [148]. It is an ester of citric acid as depicted in Figure 10.

SA is a fatty acid, consisting of stearic (C_{18}) and palmitic (C_{16}) acid according to the Ph. Eur. monograph [150] (Figure 11). It has lipophilic properties and is practically insoluble in water. SA is a common pharmaceutical excipient, e.g., as lubricant in roller compaction or tabletting [149]. It was also used as plasticizer to produce printable filaments [35].

After a base formulation was found, HPMC was selected as pore former in a second step to modify systematically the drug release. It is a mixed ether of cellulose with methyl and hydroxypropyl functions, soluble in water. To control the drug release, it is the most widely used hydrophilic additive for oral DDS [150]. It shows a high swellability depending on the DS, influencing significantly drug release kinetics [151]. Also depending on the DS and the chain length, polymer dissolution occurs, increasing the released API amount due to pore formation. With decreasing viscosity grades the rate of polymer dissolution and consequently drug-eluting rate increases [143].

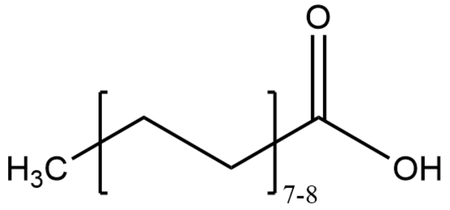

Figure 11. Chemical structure of SA ($C_{16/18}$) according to the definition of the Ph. Eur.

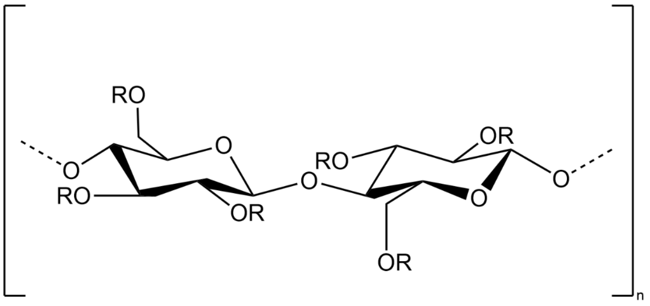

R = -H, $-CH_3$, $-CH_2CHOH-CH_3$

Figure 12. General chemical structure of HPMC.

This was shown for hot-melt extruded and 3D-printed implants [58, 152-154]. Therefore, HPMC with the substitution type 2910 according to the USP with low viscosity of 50 mPa · s (2 % aqueous solution at 20 °C) was chosen to enhance the drug release from high-density 3D-printed EC-based implants [155]. It was already a successful approach in diverse studies to accelerate the drug release from extruded EC-containing matrices, coatings, or 3D-printed tablets [143, 145, 154, 156].

All different investigated filament compositions evaluated in this work can be found in Table 1. In all formulations, fumed silica was added to the powder mixture in 0.4 % (w/w) to ensure proper powder feed inside the barrel during HME.

Table 1. Investigated filament compositions [% (w/w)].

Substance	**TA**	**EC**	**SA**	**TEC**	**HPMC**	**Fumed silica**
Function / Formulation	**API**	**Thermoplastic polymer**	**Plasticizer**		**Pore former**	**Glidant**
F1	-	94.6	5	-	-	0.4
F2	-	89.6	10	-	-	0.4
F3	5	89.6	5	-	-	0.4
F4	5	84.6	10		-	0.4
F5	-	94.62	-	5	-	0.38
F6	-	89.64	-	10	-	0.36
F7	5	89.62	-	5	-	0.38
F8	4.74	84.64	-	10	-	0.36
F9	10	79.64	-	10	-	0.36
F10	10	74.64	-	10	5	0.36
F11	10	64.64	-	10	15	0.36
F12	10	54.64	-	10	25	0.36
F13	-	74.64	-	10	15	0.36

3.1.4 Evaluation of Different Base Filament Formulations

3.1.4.1 Production of Different Formulations via Hot-Melt Extrusion

To find suitable base formulations for the printing of drug-free and drug-loaded implant parts, nine different filament compositions (F1-F9, Table 1) were screened. This was done according to the rational approach presented in section 3.1.1. Filaments containing EC as sustained matrix-forming polymer were investigated with different drug-loads, types and concentrations of plasticizer.

As presented in the flowchart (Figure 7, section 3.1.1), initial trials were performed with a capillary rheometer (Rosand RH 2000, Malvern, UK) used as ram extruder to identify suitable ratios of polymer, plasticizer and API at small batch sizes (20-30 g). Filaments manufactured by ram extrusion made from pure EC showed strong brittleness. Hence, different ratios of the two selected plasticizers SA (solid) and TEC (liquid) were pre-evaluated. Based on an organoleptic evaluation 5-10 % concentration appeared sufficient to improve the mechanical resilience in both cases. Due to the occurrence of melt fracture and insufficient homogeneity, these studies gave only preliminary evidence for suitable ratios. Subsequently, identified options were produced using a 16 mm 40D twin-screw extruder (batch size > 300 g) to obtain filaments with smooth quality for a reliable analysis related to the solid-state properties, mechanical resilience and printability of all formulations (F1-F9).

An exemplary extrusion set-up used during formulation development is depicted in Figure 13. The exact procedure is described in section 5.3.2.1. For the tested formulations containing TEC, the liquid plasticizer was pumped continuously with a liquid feed rate (LFR) adapted to the powder feed rate (PFR) into the barrel. Behind the die (1.75 mm), extruded filaments were stretched by a conveyor belt and cooled at ambient conditions to obtain the target diameter of 1.75 mm proposed by the printer manufacturer. The diameter was constantly measured and monitored using a laser-based measurement module prior collecting the filament as rolled-up strands. For the formulations, different extrusion settings were applied as listed in Table 2. The PFR was in all cases 5 g/min to

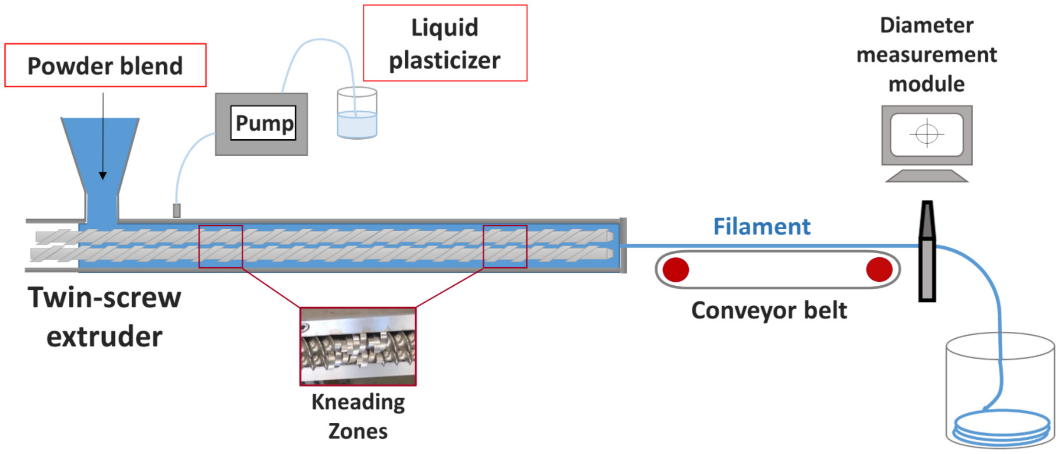

Figure 13. Schematic HME set-up of filament production.

enable proper handling and sufficient cooling time. As die temperature 170 °C was selected based on the solid-state properties (section 3.1.4.2.1., Figure 15B) and extrusion process data was recorded to ensure proper melt flow.

Table 2. HME barrel temperatures, screw speed and conveyor belt speed (CBS) applied for the different filaments during formulation development.

Formulation	Barrel temperature from zone T1 (gear) to T10 (die) [°C]										Screw speed [rpm]	CBS [mm/s]
	T1	T2	T3	T4	T5	T6	T7	T8	T9	T10		
F1	-	30	100	160	160	160	160	160	170	170	35	52.9
F2	-	30	100	160	160	160	160	160	170	170	35	48.6
F3, F4	-	30	100	160	160	160	160	160	170	170	30	49.6
F5	-	30	100	160	160	160	160	160	170	170	35	40.4
F6	-	30	100	160	160	160	160	160	170	170	35	41.5
F7	-	30	100	160	160	160	160	160	170	170	35	43.3
F8	-	30	100	160	160	160	160	160	170	170	35	46.8
F9	-	30	100	170	170	170	170	170	170	170	35	54.9

The screw configuration I, equipped with two kneading blocks (KBs) as depicted in Figure 81 (section 5.3.2.1) was applied. The screw speed varied between 30 and 35 rpm, depending on the recorded process parameter (material pressure, power consumption) of the respective formulation. Depending on the formulation diameter fluctuations and filament windings occurred caused by the shear stress at the die. Therefore, the conveyor belt speed (CBS) was adapted individually to obtain homogenous, straight filaments with the targeted diameter. An exemplary picture of drug-loaded and drug-free filaments (F5-F8), containing TEC as plasticizer, is depicted in Figure 14. Filaments with SA looked similar. Pre-selected filament compositions were all extrudable via twin-screw HME. Homogenous filaments without irregularities were obtained and used for further characterization. The drug-free formulations (F1, F2, F5, F6) were transparent as TEC was miscible with EC and SA soluble in the polymer. Filaments loaded with TA (F3, F4, F7, F8, F9) appeared opaque, which indicated that TA is at least partially insoluble in the EC-matrix.

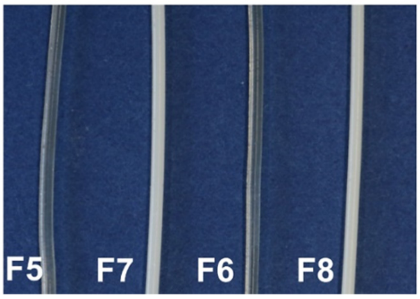

Figure 14. Exemplary image of filaments (F5-F8) containing TEC as plasticizer, produced via twin-screw HME.

3.1.4.2 Characterization of Filaments

3.1.4.2.1 Solid State Properties

Since during both processes, the HME and FDM^{TM}-printing, formulations undergo thermal stress, the stability at process temperature is important to consider preventing degradation of API and excipients. Therefore, it is necessary to evaluate their solid-state properties. The thermal analysis gives additional valuable insights into the suitability and compatibility of components and the plasticizing capabilities of the different plasticizers used [157, 158]. Differential scanning calorimetry (DSC) measurements were conducted as described in section 5.5.10.

Pure substances were heated twice, with a defined cooling step in between. This procedure mimics the material history during processing, as the powder mixtures are subjected to two heating steps within HME and subsequent 3D-printing. For evaluation of the pure nature of the powder material, if no degradation in the first heating cycle occurred, the data of the second heating step was used for evaluation to reduce effects of processing and storage of material. For TA, the first heating cycle was analysed to assess the melting temperature, since during cooling no recrystallization occurred, but a glass transition. In contrast, extrudates were just heated once, as they were already molten during extrusion.

In Figure 15, the obtained DSC thermograms of excipients and selected filament formulations (F4, F6) are depicted, indicating that no thermal decomposition below 190 °C was visible. Pure SA was heated only to 120 °C, however thermal stability until 300 °C was described in [109].

Besides the thermal stability, the information of solid-state properties of raw materials and extrudates were assessed. For TA and SA melting peaks were observed due to their crystalline character (melting temperature (T_m) for TA: 284/296 °C; for SA: 61 °C Figure 15A, B). TA shows pseudo-polymorphism, which is indicated by the two melting peaks at 284 °C and 296 °C in accordance with the literature [159]. The mainly occurring modification I (296 °C) is a hydrate of modification II (284 °C) [160]. Thus, melting during extrusion within the temperature window is not possible.

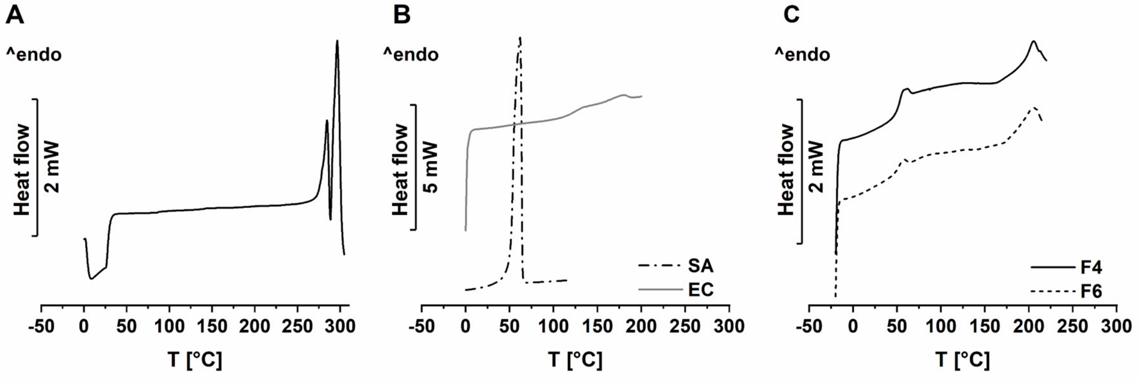

Figure 15. DSC thermograms of TA (A), EC and SA (B) and extrudates of F4 and F6 (C). Scaled differently to improve visibility.

The polymer EC showed a glass transition around 131 °C, indicating a strong glass former. Although EC is not described as semi-crystalline, at around 180 °C an endothermic peak was noted (Figure 15B). Lai et al. proposed as cause melting of microcrystals composited of unsubstituted sections within the cellulose backbone based on quasi-isothermal modulated temperature DSC results and hot stage microscopy combined with simultaneous transmitted light intensity measurements [161].

DSC thermograms of filament formulations F4 (TA 5 % and SA 10 %) and F6 (TA 5 % and TEC 10 %) were exemplary selected and depicted in Figure 15C. Formulation F4 and F6 showed a T_g of 47 °C and 40 °C, respectively in agreement with literature data for EC and TEC combinations [162]. The reduced glass transition compared to pure EC revealed the plasticizing effect of SA and TEC, confirming their suitability to decrease the melt viscosity and potentially improve mechanical properties of EC-based filaments for further processing. The effect can be explained with the free volume theory [147, 163, 164]. Small molecules are introduced between the polymer chains, thereby the free volume increases, resulting in increased molecular mobility. This is manifested amongst others in a decrease of T_g. SA seemed to be completely dissolved within the polymer as no melting peak was recorded. TEC appeared miscible with EC and showed a slightly higher plasticizing potency compared to SA. Above 190 °C thermal degradation of EC was observed, known from the literature, limiting the extrusion temperature window [140]. Due to the low concentration of API in the extrudates and simultaneous occurring degradation of EC above 190 °C, an evaluation of API solubility within the polymer is not possible. A thermal decomposition at extrusion temperature can be excluded, as TA is stable until 296 °C (Figure 15).

3.1.4.2.2 Diameter

One of the most important CQAs of filaments for 3D-printing is the diameter. The technically acceptable diameter depends on the dimensions of the print-head and the feeding system of the printer, it varies between 1.75 and 3 mm [26, 55, 165]. For the FDM^{TM}-printer used in the present work the targeted diameter for self-produced drug-loaded and drug-free filaments was 1.75 mm. Besides the mean diameter also diameter homogeneity along the whole filament length is decisive to ensure printability, dose accuracy and print resolution of printed dosage forms (detailed examination in section 3.2.3). In commercially available printer software, the mean diameter can be set, but an adaptive speed control for diameter variations is not offered. Therefore, fluctuations, depending on the extent, might lead to dose inaccuracies of printed dosage forms [166]. A loss of printability due to clogging if the diameter is too high or breakage in case of filaments with smaller diameter sections during conveying inside the print-head might also be problematic. This plays additionally a decisive role for sufficient and consistent characterization of filaments. The determination of mechanical resilience, as well as dissolution rate, might be highly affected by the diameter. If the variances are high, these properties cannot be reliably guaranteed.

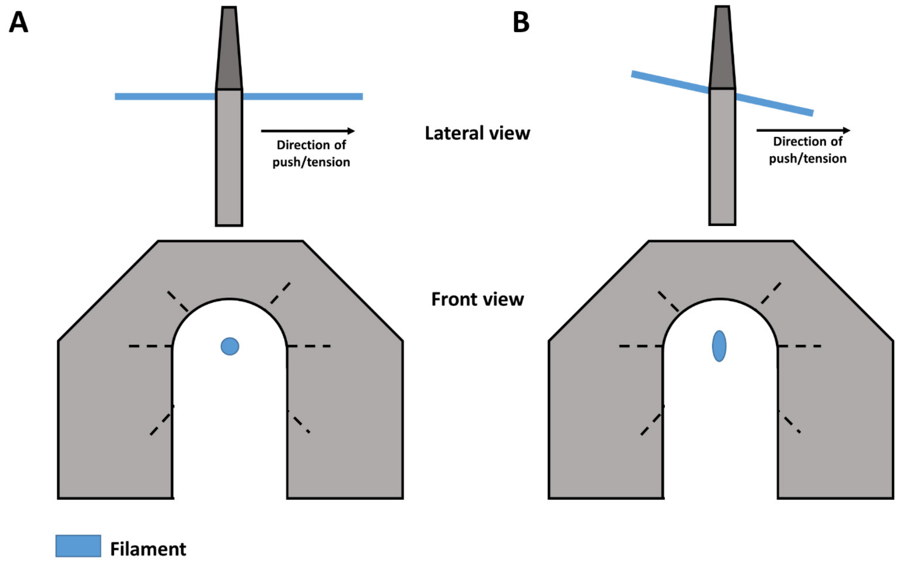

Figure 16. Diameter measurement module with detection of filament in optimal straight position (A) and biasing lopsided position (B). Dashed lines represent three laser beams (adopted and modified from Korte [109]).

Produced filaments were stretched behind the extruder outlet (die diameter: 1.75 mm) using the conveyor belt. The target diameter was set by the adaption of the CBS, which was varied for the respective formulation to ensure a homogenous filament transport and to counterbalance die swell and material transport fluctuations. The applied CBS for each formulation can be found in Table 2. The filament diameter was recorded and monitored inline using a laser-based measurement module as described in section 5.5.6 and schematically depicted in Figure 16A. The diameter measurement module determines the diameter with three lasers from different directions with a sampling rate of 1 Hz. The resulting projections are detected by detectors, captioning the product diameter. As result the mean, minimum and maximum recorded diameter is calculated. However, the determined diameter might be biased if the filament passes the laser unit in a lopsided position (Figure 16B), measuring a false oval cross-section. For instance, this could happen due to filament movements by rolling up the filaments in a bucket (see Figure 13) or if the filament adhesion on the conveyor belt is not sufficient to pass the unit horizontally. To reduce potential measurement errors, the minimum recorded diameter was used for data evaluation, assuming the filament cross-sections were round-shaped.

In Figure 17, the inline recorded diameter data for produced filaments (F1-F9) is depicted as box plots. For the evaluation of diameter variations, the interquartile range (IQR, box width) was selected, as it can be calculated without the assumption of the present distribution function of the test set and it is a robust statistical measure towards outliers. Calculations were based on 293 (F5) to 1220 (F4) measurement values since sampling times differed. However, data were considered comparable, as a value of 293 represents already a high sample size.

On average, a diameter of 1.633 ± 0.076 mm of filaments was achieved, which is considerably lower than the targeted diameter of 1.75 mm. The reduction was caused by increased CBS to counterbalance filament windings behind the die during extrusion experiments depending on the

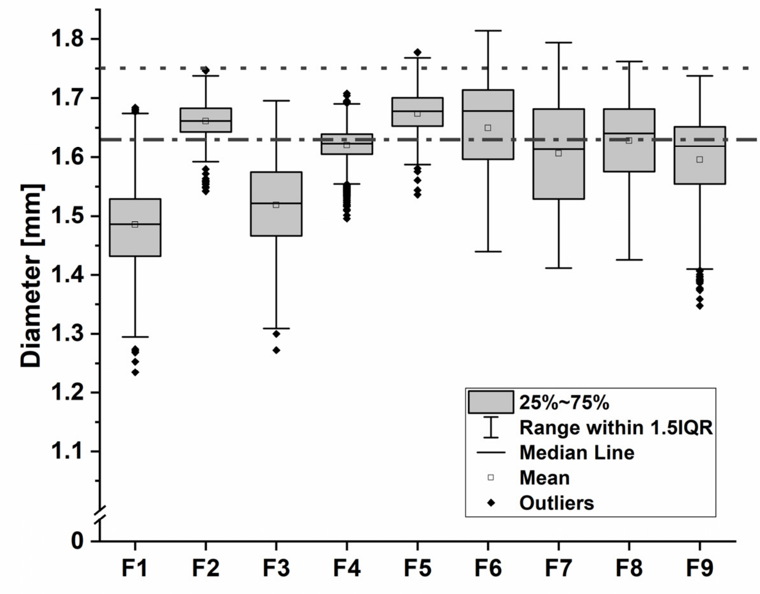

Figure 17. Inline recorded filament diameter of formulations F1-F9 (n = 293-1220), depicted as box plot. The dotted line indicates the die diameter and the dashed line the mean diameter value of all formulations.

formulations as shown in Figure 18. Thereby, a compromise between a straight filament without irregularities and a slightly reduced diameter must be accepted. The windings result from a rapid material pressure increase caused by a temporarily raised material throughput, which will be explained in section 3.2.3.3. The resulting flow instabilities lead to volume distortions which are reflected in a wavy filament [167]. Additionally, due to the short dwell time within the die, the elastic behaviour superimposes viscous effects, leading to extrudate fluctuations [168]. The extent depends on the material (e.g., molecular weight (MW), melt viscosity, operating conditions (temperature, flow rate, barrel filling degree) and geometry of the die-channel [167, 169, 170]. This was most pronounced with formulations, containing 5 % SA (F1 and F3), reflected in the lowest achieved diameter. Due to the lower plasticizer concentrations, the melt viscosity was potentially increased compared to formulations with 10 % SA (F2 and F4).

Diameter variations were observed, reflected in the diameter IQR (Figure 17). This was caused by an inhomogeneous melt-transport along the barrel, as result of material accumulation in front of the KBs [109]. The material amount passing the die varied and consequently the diameter. The extent might be dependent on the melt rheology of different formulations. The conditions of material transport fluctuations are extensively discussed in chapter 3.2. The coefficient of variation (CoV)

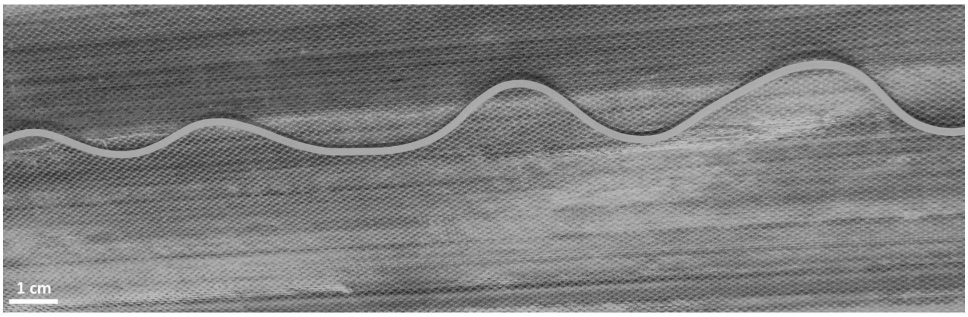

Figure 18. Filament windings behind the extruder-outlet due to material fluctuations and increased shear stress at the die.

and IQR of diameter were different for the manufactured filaments. As different previously described phenomena might have interfered, it is difficult to obtain conclusive correlations between formulations and diameter data. Another factor affecting diameter consistency was proper adhesion of the filament on the conveyor belt, which must be sufficient to enable a reproducible and representative diameter adaption. This was especially problematic in case of SA-containing filaments. However, the lower mean diameter as well as CoV between 1.99 and 5.39 % were considered acceptable for a first characterization of filaments.

Based on the problems identified, a systematic analysis and optimization of both the extrusion set-up (diameter measurement and adaption, die) and the process settings (PFR, screw speed, temperature) were indispensable for the final filament compositions to achieve reproducible and homogenous filament diameter (refer to section 3.2).

3.1.4.2.3 Mechanical Properties and Printability

The mechanical resilience was identified as key characteristic for a proper conveyance inside the print-head to ensure printability during FDM^{TM} [27, 28, 171]. It is mainly dependent on the used composition, including API, polymers and plasticizer, as well as their ratios. Therefore, and for comparison, different extruded filaments were analysed regarding their mechanical properties (stiffness and brittleness) to find an optimal composition for subsequent printing of implants. In Figure 19 (top), an exemplary print-head assembly of an FDM^{TM}-printer is depicted. The filament is conveyed via counter-rotating gears/ belts through the heated part, the so-called hotend. The polymeric material is molten and extruded through the nozzle. A constant conveyance is mandatory, enabling an accurate dosing and print job. During printing, the not molten extrudate part serves as

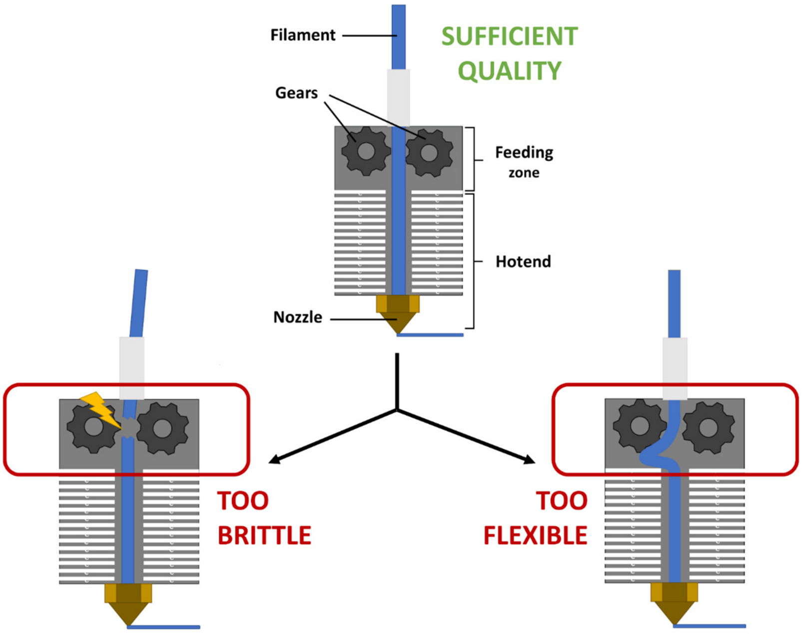

Figure 19. Schematic depiction of an FDM^{TM} -print-head with sufficient (top), too brittle (bottom left) and too flexible (bottom right) filament properties leading to feeding failure.

a piston to force the molten part through the die. Hence, it must show sufficient stiffness in longitudinal direction. If it is too flexible, it will deform and uniform continuous conveying cannot be ensured (Figure 19, bottom right) [28]. The same is valid for filament break, which can occur for brittle materials caused by the transversally applied punctual stress of the gears (Figure 19, bottom left) [28]. This is especially problematic for many pharma-grade polymers, often in combination with high drug loads, resulting in brittle extrudates [24]. To circumvent stress on brittle materials and consequently breakage, researchers used so-called Bowden printers, where a large distance (several cm) between the feeding gears and the hotend is present connected via Teflon tubes. The self-produced filaments are then placed manually in the tube and promoted by commercial filaments fixed between the gears [39, 44, 56]. This approach is not applicable to continuous processes since the distance and consequently, the feedable filament length is limited. This is also the case for highly flexible filaments, where this approach leads to nozzle clogging. Consequently, proper formulation development is unavoidable if no specialized printers for pharma-grade materials with insufficient mechanical resilience are going to be developed.

Mechanical strength, apart from printability, is also particularly decisive in terms of industrial manageability during continuous processing, storage and transport. Filaments must therefore show good resistance and winding properties on spools without deformation or breakage.

To compare different formulation compositions related to their suitability for FDM^{TM}-printing the testing regime and data evaluation were adopted from Korte and Quodbach [27], performing a combination of a tensile test and 3PBT. Thereby both stress directions inside the print-head were examined. This was considered beneficial compared to test regimes where only one characteristic was measured [28, 172]. Hence, the filament stiffness, expressed as YM was determined in a tensile test and the brittleness as DaB in a 3PBT (section 5.5.7). Accordingly, testing conditions were taken from Korte and Quodbach [27] and Zhang et al. [28]. Exemplary measurement curves are depicted in the analytical method part (Figure 83, section 5.5.7). The YM was calculated as slope between 0.05 and 0.25 % of obtained stress-strain curves in the linear elastic range according to DIN-EN-ISO 527-1 [173]. Formulations showed mainly plastic deformation along with higher strains, indicated by a deviation from the linear area. Below 0.25 % strain, all filaments showed linear behaviour, justifying the YM calculation. The YM is proportional to the filament stiffness. The DaB was directly obtained from force-elongation curves, as distance where the maximum force was measured (Figure 83, section 5.5.7). The lower the distance, the more brittle is the filament.

The results of mechanical properties for all produced filament formulations are shown in Figure 20. Most of the formulations had small confidence intervals (CI), showing the suitability of the test method and uniformity of tested filaments. Filaments showed suitable stiffness expressed in a high YM and were flexible enough in transversal direction expressed in a sufficient DaB for conveyance inside the print-head, as they exceeded strongly both printer-specific thresholds (DaB = 1.125 mm/

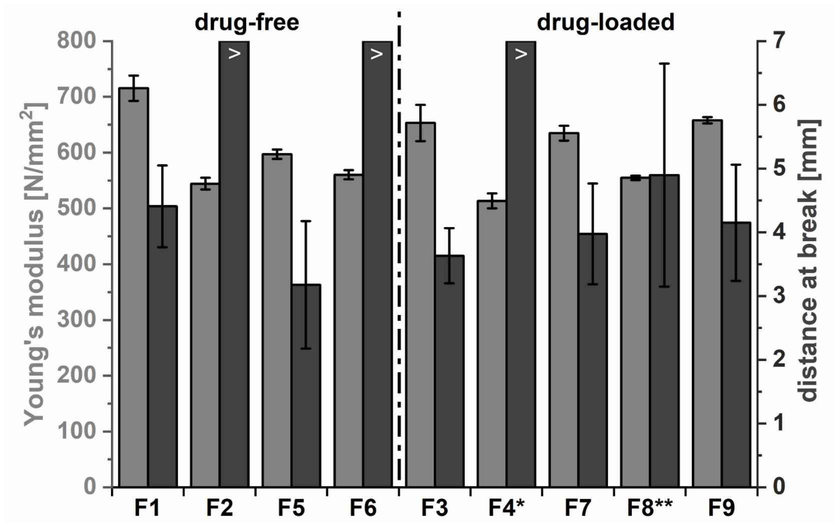

	F1	F2	F5	F6	F3	F4*	F7	F8**	F9
TA	-	-	-	-	5	5	5	4.7	10
SA	5	10	-	-	5	10	-	-	-
TEC	-	-	5	10	-	-	5	10	10

Figure 20. YM determined in a tensile test and DaB determined in a 3PBT (n = 6, mean ± CI; α = 0.05) for the investigated EC-based formulations containing different ratios of TA and plasticizer. Columns marked with ">" did not break under the applied conditions (travel depth 5 mm).
*** 2/6 samples did break and were excluded for calculation.**
**** 2/6 samples did not break and were excluded for calculation.**

YM = 300 N/mm^2) specified in literature for printability [109]. As a different printer was used in the present work, the results were verified with additional performed printer feeding experiments, as described in section 5.5.8.

For the DaB higher variations were measured, indicated by high CI. Hence, only tendencies could be evaluated. The reason for higher variations is the 3PBT itself, which is in general valid for brittle materials, whereas tested filaments were flexible in transversal direction. In addition, filament diameter fluctuations up to 5.4 % (Figure 17) potentially influenced the measurement, since thinner sections broke faster compared to thicker sections. This was especially visible for formulations F4 and F8, where some sections broke and others not. For an initial evaluation, obtained values were considered acceptable.

With increasing plasticizer concentrations, the YM decreased while the DaB increased as expected. Related to the drug-free formulations TEC showed in 5 % concentration a higher impact on the YM compared to SA (F1 = 715.4 ± 22.7 N/mm^2 vs. F5 = 597.3 ± 8.4 N/mm^2). Consequently, for TEC a moderately higher plasticizing efficiency was assumed. For plasticizer concentrations of 10 % comparable YM values for both, SA and TEC, were obtained (F2 = 544.4 ± 10.6 N/mm^2 vs. F6 = 560.3 ± 8.3 N/mm^2). In contrast, 5 % SA (F1) showed a slightly higher effect on the DaB compared to TEC (F5) with DaBs of 4.408 ± 0.642 mm and 3.175 ± 0.978 mm, respectively. But this was not statistically relevant ($p = 0.108$; $\alpha = 0.05$). For F2 and F6 with 10 % plasticizer no breakage could be observed under the applied testing conditions, showing a high resilience of compositions against transversally applied stress. The observed trends were also true for drug-loaded formulations (F3, F4, F7 and F8).

When comparing drug-loaded with drug-free formulations, an influence of TA-load was visible (Figure 20), especially between TA-loads of 0 and 10 % (F6 and F9). An increased drug load led to an increased YM. Between 0 and 5 % TA-load the effect was of minor relevance.

An analogue effect for the DaB is known from the literature, where higher drug-loads (suspended) were compared [109]. The DaB decreases with increasing API content. A similar tendency could be observed for the investigated formulations (e.g., F6, F8 and F9), as TA is mainly suspended inside the EC-matrix, this leads to predetermined breaking points, lowering the DaB.

The DaB cannot be influenced independently from the YM. Consequently, to optimize formulations related to the mechanical strength by the addition of plasticizer, a compromise between sufficient stiffness and simultaneously less brittleness must be found. In total sufficient stiffness and brittleness were obtained for the tested formulation options, even with the targeted drug load of 10 %. Plasticizer concentrations of 10 % were preferred since it was planned to add further excipients for drug release modification. These might potentially have an impact on brittleness as well. Drug-free filaments with 10 % SA (F2) showed a loss of transparency over storage. This was likely caused by time-dependent recrystallisation potentially due to an exceed of solubility within the polymer. Thereby, the mechanical properties and printability over storage could be negatively affected. The brittleness might be increased due to the precipitated SA and the loss of dissolved plasticizer. Formulations with SA as plasticizer were therefore rejected. The plasticizer TEC in a concentration of 10 % was considered promising to obtain filaments with sufficient mechanical resilience (F6, F8 and F9). Filaments showed haptically also improved practical handling with less tendency for breakage.

As result of the performed studies, suitable base formulations (drug-free and drug-loaded) were successfully identified using the systematic approach adopted from Korte [109]. Although all formulations were printable, the formulation F9 consisting of 10 % TA, EC as sustained-release polymer and 10 % TEC as plasticizer were used for further analyses and optimization due to the above-mentioned reasons. The higher drug load of 10 % was selected to have more flexibility regarding implant size.

3.1.4.2.4 Preliminary Drug Release Studies

An essential part of formulation development is the drug release performance. The final goal is to enable a prolonged TA release over several months. Although this can be highly influenced by the 3D-printed structure and the resulting drug-eluting surface area, preliminary evaluation was performed with filaments only instead of printed geometries.

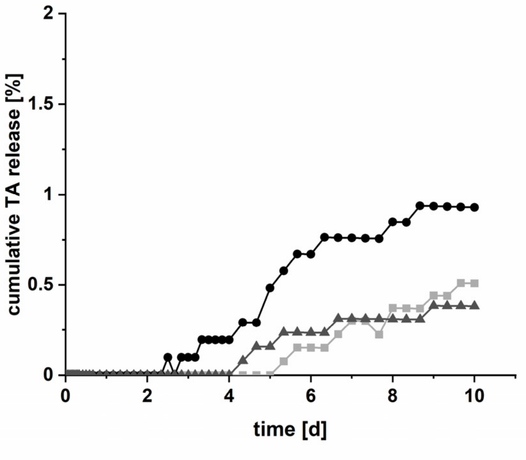

Figure 21. Preliminary cumulative TA release from filament formulation F9 (n = 3, displayed as single curves; 37 ± 0.5 °C, 100 rpm, 1000 mL PBS 0.05 M, pH = 7.4).

To get first valuable insights into the retardation effect of the EC-matrix on TA release, the developed and selected base filament formulation F9 (TA 10 %, TEC 10 %) was subjected to preliminary dissolution studies. It was expected that the drug release will be too slow from the dense 3D-printed product consisting of EC, especially using an API with low aqueous solubility of 21 mg/L [174]. This was consequently supposed to be used as start-point for further modification of the drug release by the addition of pore former as discussed in the following chapter 3.1.5. Preliminary experiments were performed in a USP Apparatus I (rotating basket, described in section 5.5.22.1) to avoid floating and/ or friction of filaments. Studies were conducted over ten days with a rotational speed of 100 rpm and 1000 mL of 0.05 M phosphate-buffered saline (PBS) at pH 7.4 at 37 ± 0.5 °C. Concerning comparability of the analysed filaments with subsequently optimized formulations the drug-releasing surface should be kept similar. Hence, filaments were cut in 2.5 cm sections. Six filament sections were placed in one basket (n = 3), corresponding to a TA dose between 36 and 41 mg.

In Figure 21, the result of TA release from filament formulation F9 (10 % TA) is depicted. Almost no TA was released within ten days (~1 %). EC as sustained-release polymer had a strong retardation effect on the poorly water-soluble API, as expected. EC is a water-insoluble polymer forming a matrix, where diffusion of water into the inner core of the filament to dissolve TA particles is not possible. The dissolved TA amount and total TA concentration were too low to form pores to decrease diffusion path lengths. The measured TA concentration was restricted to drug particles located directly on the filament surface. An apparent lag time is given of two to five days, where no API concentration was measured at all, which is certainly caused by the quantitation limit of the used ultraviolet (UV) method. This could be manageable by the reduction of volume to 500 mL (limit for qualified equipment). No further reliable input was expected, also taking the long measurement time into consideration. It was demonstrated that the TA release must be strongly accelerated by further formulation optimization. Thereby, also the influence on other CQAs must be considered.

3.1.5 Formulation Optimization by Addition of a Pore Former

3.1.5.1 Pretext

Within the first step of the systematic formulation development of printable filaments for printing of customizable implants, suitable base TA-loaded and drug-free compositions were found. Preliminary dissolution studies of filaments revealed that the TA release from the EC matrix must be strongly accelerated to ensure a constant release of the poorly water-soluble API over multiple months. This part of the work aimed therefore at a filament formulation optimization for customizable 3D-printed TA-eluting implants.

An obvious and frequently used approach for matrix systems is the incorporation of pore-forming agents to effectively enhance the dissolution behaviour, also done for implantable DDS [153, 154]. As described in section 3.1.3 a common additive for EC-coatings, matrices and 3D-printed DDS is the water-soluble and swelling polymer HPMC [134, 143, 145, 156]. Hence, the polymer was selected to modify the TA release over at least three months. The effect of HPMC concentration on TA release from the EC filaments should be investigated, next to their impact on several filament properties.

3.1.5.2 Production of Filaments with varying HPMC concentrations

Based on filament formulation F9 (10 % TA, 10 % TEC), three different compositions with 5, 15 and 25 % HPMC (F10, F11 and F12, Table 1 in section 3.1.4.1) were produced via twin-screw HME. The extrusion set-up and diameter measurement were the same as used for the preliminary formulation development (Figure 13, section 3.1.4.1 and 5.3.2.1). All extrudates were produced with a PFR of 5 g/min and a screw speed of 35 rpm.

During manufacturing it was observed that increasing HPMC contents led to an increase in material pressure, already known from literature [143]. Consequently, extensive filament windings behind the die occurred. The extrusion temperature was increased for the respective formulation to overcome windings and lower material fluctuations. The temperature was varied between 170 and 190 °C in accordance with the determined solid-state properties (section 3.1.4.2.1). The applied CBS was adapted as previously reported to achieve a straight filament with a target diameter around 1.75 mm. In Table 3, the applied barrel temperatures and CBS can be found compared to the corresponding HPMC-free formulation F9. Sampling was conducted once process equilibrium was achieved, indicated by a constant material pressure and power consumption.

All formulations were extrudable via twin-screw HME and the incorporation of HPMC in developed formulation was successful. Obtained filaments were opaque. Homogenous filaments with sufficient quality for characterization were obtained.

Table 3. HME barrel temperatures and conveyor belt speed (CBS) applied for the different filament formulations with varying HPMC concentration.

Formulation	HPMC content [%]	Barrel temperature from zone T1 (gear) to T10 (die) [°C]										CBS [mm/s]
		T1	T2	T3	T4	T5	T6	T7	T8	T9	T10	
F9	0	-	30	100	170	170	170	170	170	170	170	55
F10	5	-	30	100	160	160	160	160	160	170	170	51
F11	15	-	30	100	160	160	170	170	180	180	180	53
F12	25	-	30	100	170	180	180	180	190	190	190	57

3.1.5.3 Characterization of Filaments

3.1.5.3.1 Surface Analysis of Filament Formulations

A homogeneous filament constitution is of particular interest to ensure sufficient and reproducible filament quality, especially related to dose accuracy and drug release behaviour. A deep knowledge will help to draw right conclusions during formulation development but also later in quality evaluation of the finished product. The start point for the following analysis was the occurrence of rough filaments surfaces in dependency to the HPMC load. The higher the HPMC load, the higher seemed the observed roughness visible in microscopic and scanning electron microscope images of filaments (Figure 22). To assess this phenomenon and to gain more insights about surface quality and distribution of constituents within filaments, confocal Raman microscopy was applied.

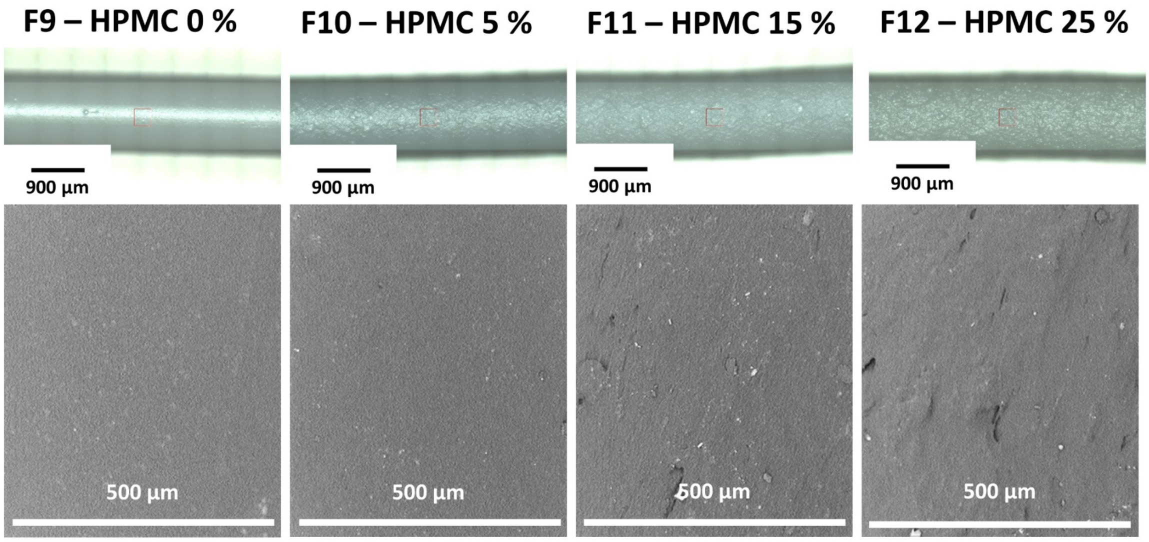

Figure 22. Microscopic images (top, magnification 10x) and SEM texture images (bottom, magnification 530-540x) of surfaces of different filament formulations.

An overview of the results is displayed in Figure 23. Topographic Raman images confirmed that increased HPMC content led to a distinct increase in filament roughness (Figure 23A). This was reflected in the determined surface area of 200 x 200 µm filament sections. For formulation F9 (HPMC 0 %), the surface area was 40494 µm^2 indicating that an almost completely smooth surface was obtained. Whereas for F10 (HPMC 5 %) the surface area was 41116 µm^2, for F11 (HPMC 15 %) 44264 µm^2 and for F12 (HPMC 25 %) 46406 µm^2, respectively. A linear relationship between HPMC load and filament surface area was found with a coefficient of determination of 0.9881. The increase of surface area and thus roughness between F9 and F12 was around 15 %, which could have a distinct influence on characteristics like drug release. It must be emphasized that the measurement was only conducted once in a small area (200 x 200 µm).

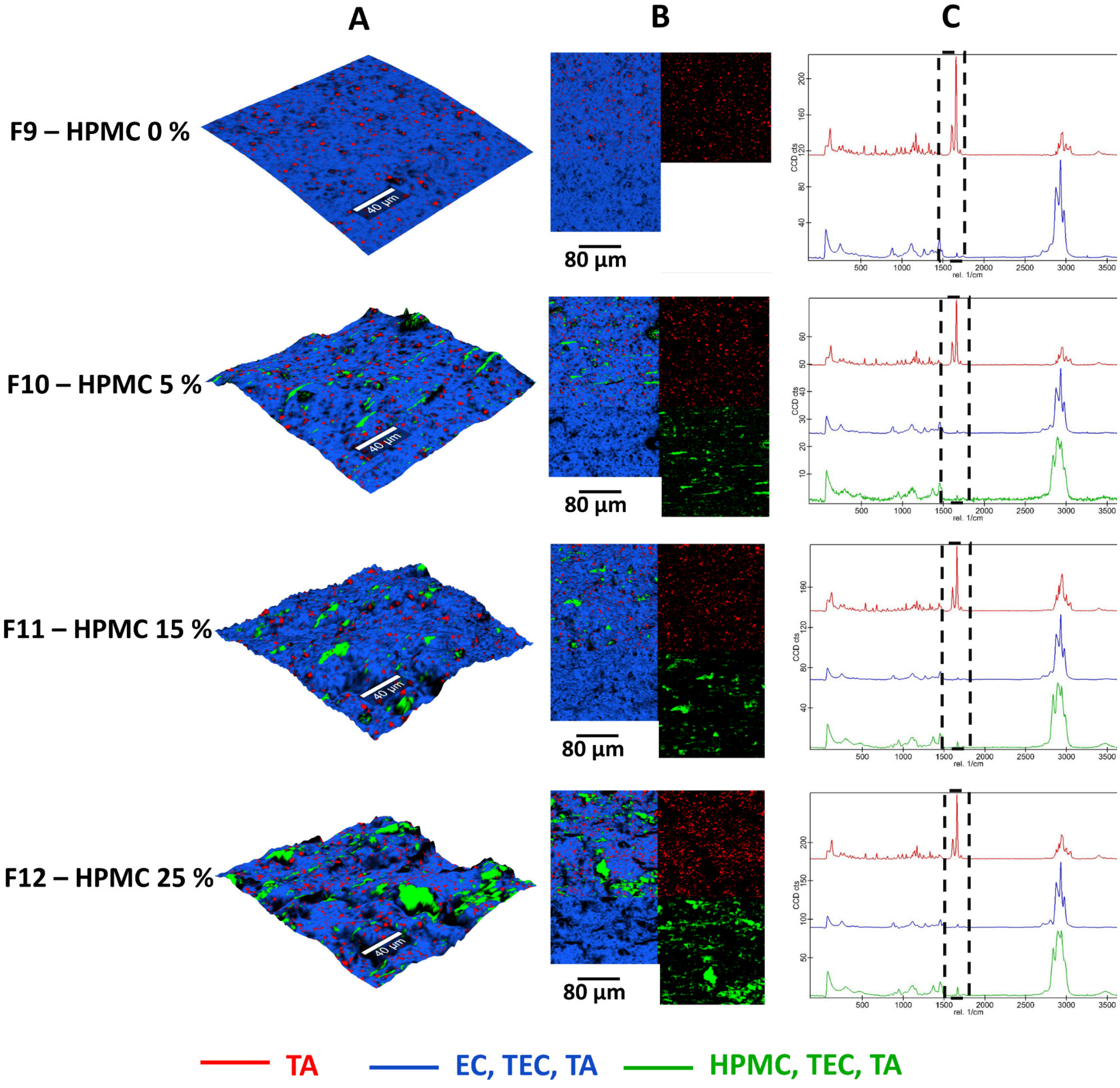

Figure 23. Topographic Raman images (A), spatial distribution plot (B) and averaged Raman spectra (C) of filament surfaces for each formulation (200 x 200 µm; 40000 spectra), false colour representation. Dotted boxes in C mark specific TA-peak at 1600 cm^{-1}.

The topographic Raman images and spatial distribution plots also provided information about the component distribution (Figure 23 A, B) in combination with averaged Raman spectra (Figure 23C). The mainly suspended API (plotted in red) is homogeneously distributed in the EC-containing area (plotted in blue) of the sample. The earlier hypothesized partial insolubility within EC-matrix was confirmed, as in Raman spectra, the characteristic TA peak at 1600 cm^{-1} appeared weakly (dotted boxes in Figure 23C). In the green areas, which consisted of HPMC, TEC and TA, no suspended API particles (red areas) were visible. Consequently, it was assumed that TA is soluble in HPMC. This was further underlined by a peak at 1600 cm^{-1} in the Raman spectra caused by TA, which increased with higher HPMC content (dotted boxes Figure 23C).

In addition, the desired and expected immiscibility of HPMC and EC was observed. The green domains, which contained HPMC were fully separated from EC areas (blue). With increasing content, the green HPMC-containing domains were larger, which indicates that drug release can be accelerated due to the pore-forming effect in contact with the dissolution medium.

Based on the results several effects might be responsible for the previously mentioned filament roughness. The irregular surface is likely induced by the visible phase separation between the two polymers and thus higher interfacial tension, which is already known for film coatings and preparations [175-177]. However, DSC analysis was not able to detect clearly two T_g to verify the result (refer to section 3.1.5.3.2). Further, the roughness might result from the different viscoelastic properties of the two polymers, which depend on polymer chain length, MW and degree and type of substitutions in the main chain [140]. The higher the HPMC concentration, the higher the effect. Additionally, an insufficient softening of HPMC at 180/ 190 °C extrusion temperature (measured T_g: 154 °C, Figure 24A) could reinforce the observed effect [140].

These outcomes could lead to a reduced processability if higher amounts of HPMC are required, which should be considered during formulation development. The increased roughness could have an additional influence on the release behaviour, which needs to be considered during dissolution predictions based on the surface area. The reasons for the roughness with increasing HMPC load could not be conclusively clarified in the work. Most likely it is a result of superimposition of all described effects. But valuable insights about the component distribution were provided using confocal Raman microscopy and it is an important tool to investigate filament quality.

3.1.5.3.2 Solid State Properties

The solid-state properties of EC, HPMC and some produced filaments (F9, F11, F12) were exemplary evaluated. Although a degradation below 200 °C was excluded based on performed DSC runs (section 3.1.4.2.1), potential incompatibilities should be addressed. Analogue to previously performed DSC analysis, powders were subjected to two heating cycles as described in section 5.5.9, eliminating storage history. Additionally, at the beginning powders were heated at 60 °C for

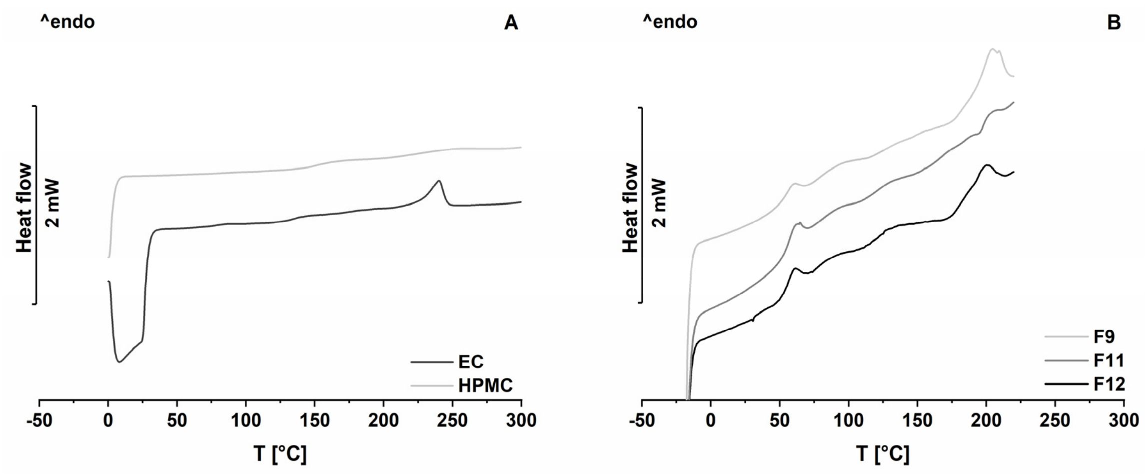

Figure 24. DSC thermograms of pure polymers HPMC and EC (A) and extrudates of F9, F11 and F12 (B).

30 min to remove residual water. Extrudates were heated once since they were already thermally stressed during HME.

In Figure 24A, the results of pure HPMC compared to EC are depicted. The T_g of HPMC was determined at 154 °C. A very broad glass transition was observed, potentially caused by different molecule chain lengths [140, 175]. The thermal analysis of EC until a temperature of 210 °C was extensively discussed in section 3.1.4.2.1. For comparison purposes, the experiment was repeated with improved settings and heated up to 310 °C, as done for HPMC. For EC the thermogram of the first heating was used, due to degradation > 225 °C. The visible exothermic drop between 0-30 °C was caused by uncontrolled cooling from 60 down to 0 °C but is not relevant for evaluation. Again, at 131 °C the T_g was detected in accordance with previously obtained results (refer to Figure 15B). The first endothermic peak at 180 °C observed in previous studies due to microcrystals composited of unsubstituted sections within the EC backbone is hardly visible due to the second endothermic peak at 240 °C. In literature, oxidative degradation is stated, which is usually linked to an exothermic event not visible as a pin-holed pan was used [161]. The observed endothermic event is not well described but was assigned to thermal degradation, proven by Meena et al. via thermogravimetric analysis [140]. No degradation was observed below the maximum extrusion temperature of 190 °C, indicating again the thermal stability under the chosen HME-process conditions.

In Figure 24B, the exemplary thermograms of F9 (without HPMC), F11 (HPMC 15 %) and F12 (HPMC 25 %) are depicted. Formulations F9, F11 and F12 showed a reduced T_g at 40 °C, 53 °C and 50 °C assigned to EC. This showed again the plasticizing effect of TEC for all formulations (refer to section 3.1.4.2.1). As the two polymers were immiscible as visible in the confocal Raman microscopic images (Figure 23, section 3.1.5.3.1), a second T_g was expected for F11 and F12. A glass transition at 121°C and 120 °C for F11 and F12 may be possibly assigned to HPMC. But due to the increased chain mobility above the T_g for the extrudates with thermal history, a baseline drift was observed, complicating a conclusive evaluation. Above 190 °C thermal degradation was observed in line with literature data [140].

3.1.5.3.3 Diameter

The importance of a consistent filament diameter for further analysis and accurate dosing of 3D-printed DDS has already been explained in detail in section 3.1.4.2.2. Therefore, newly produced filaments for optimization purposes were subjected to diameter analysis in comparison to HPMC-free F9. The inline diameter determination during extrusion was performed using the laser-based diameter measurement module as described in sections 3.1.4.2.2 and 5.5.6.

In Figure 25, the results for F9-F12 (HPMC 0 %, HPMC 5 %, HPMC 15 % and HPMC 25 %) are depicted as boxplots. The diameter variations were analysed using the IQR and CoV. To obtain the target diameter, the CBS must be increased with increasing HPMC content as depicted in Table 3. Although the CBS was slightly increased with increasing HPMC load to obtain the target diameter of 1.75 mm (F10 = 51 mm/s; F11 = 53 mm/s and F12 = 57 mm/s) and to circumvent the occurring windings, interestingly higher mean diameters were obtained with increasing HPMC content (Figure 25). Potentially, an increased die swell due to higher relaxation times and consequently elastic recovery with a higher HPMC amount leads to increased filament diameter [167]. Meena et al. [140] stated that HPMC shows a higher melt viscosity at the selected extrusion temperature compared to EC and does not soften properly. This explains potentially also the previously observed increased surface roughness. This could be due to the differences in structure (substituents) and the MW between HPMC and EC [140]. Consequently, stated aspects resulted in increased filament diameter with increasing HPMC content. This is further underlined by the diameter data of the HPMC-free formulation F9, where a CBS of 55 mm/s was utilized, but an even lower mean diameter (1.596 ± 0.072 mm) was obtained.

In terms of diameter consistency HPMC-free filament formulation F9 showed a higher variation compared to HPMC-loaded ones (IQR: F9 = 0.097 mm vs F10 = 0.032 mm; F11 = 0.033 mm and

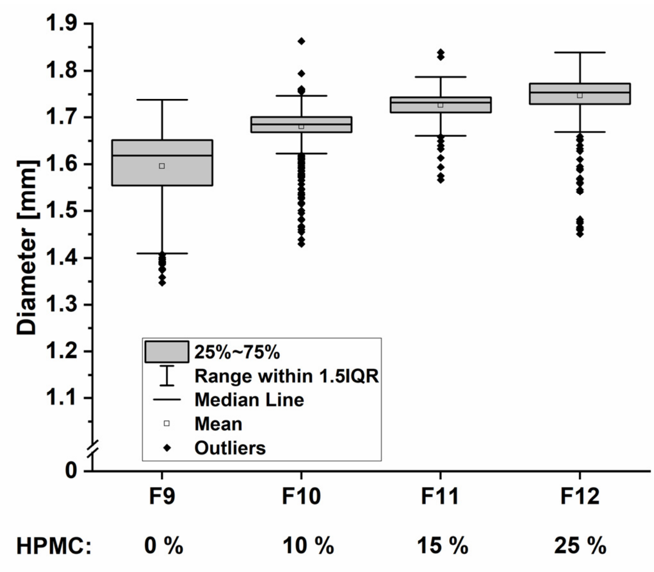

Figure 25. Boxplot of inline recorded filament diameter of formulations F9-F12 (n > 516).

F12 = 0.044 mm). This is likely caused by the explained material fluctuations during the extrusion process. A reason might be that the incorporation of the second polymer resulted in a more stable process due to a potential different melt rheology. Additionally, for filaments with HPMC loads of 15 and 25 % higher extrusion temperatures (F11 = 180 °C and F12 = 190 °C) were applied to circumvent the pronounced windings behind the die (refer to section 3.1.5.2). Thereby, the melt viscosity of EC domains decreased and a more constant melt flow was achieved, reflected in lower diameter variations. The shown outliers marked in the diameter boxplots (Figure 25, right) are caused by punctual drops in filament diameters due to lower material amount passing the die.

The results pointed out again that the process needs to be analysed further to obtain filaments with high diameter consistency, transferable to other formulations. Nevertheless, in all cases HPMC-containing filaments with sufficient diameter quality (CoV between 1.66 and 2.75 %) were obtained to analyse properly their suitability in terms of printability and drug release behaviour to find a promising formulation for 3D-printed TA-loaded implants.

3.1.5.3.4 Mechanical Properties and Printability

The importance of mechanical properties for filament characterization was already described in section 3.1.4.2.3. Since the addition of a second polymer could lead to differences in the resilience and probably in a loss of printability, it was analogously determined as before (section 3.1.4.2.3 and 5.5.7).

The results for produced TA-loaded EC-based formulations with different HPMC concentrations (F10, F11, F12) are shown in Figure 26 and compared to the corresponding HPMC-free formulation (F9). The diagram shows the YM in light grey and the DaB in dark grey for each formulation. The formulation without HPMC showed a higher YM and thus a higher stiffness in longitudinal direction in comparison to HPMC-loaded ones. It can be assumed that the addition of HPMC leads to filaments that are more flexible in transversal direction, possibly again caused by different viscoelastic properties of blends. Comparing the HPMC-loaded extrudates among each other, the influence of the HPMC content on the YM is negligible.

The influence on the DaB and thus brittleness is higher. For HPMC-loaded filaments (F10-12) a conclusive trend was visible. With increasing HPMC concentration, the DaB decreased. As visible in the confocal Raman microscopic images, incoherent phases were obtained. The higher the pore former loading the bigger were the obtained HPMC domains. Due to the discussed differences between EC and HPMC, there might be larger predetermined breaking points, leading to increased DaBs. In comparison, the HPMC-free extrudate (F9) showed surprisingly a DaB, which was in between HPMC-loaded ones, although it was expected to be higher based on the previous observations. This can be explained by the higher flexibility in transversal direction of F9, although it is not reflected in the mean value but indicated by the increased confidence intervals. As already stated, the 3PBT is more suitable for brittle materials, making a conclusively comparison difficult.

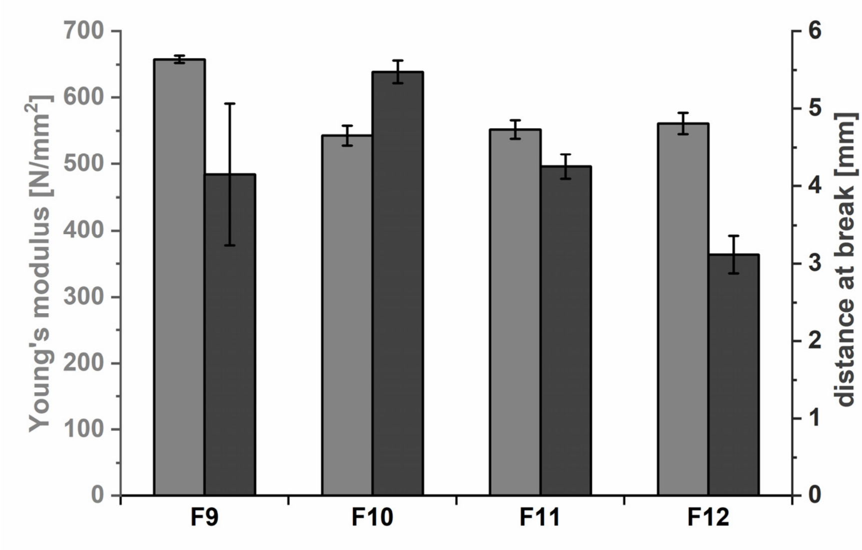

Figure 26. YM determined in a tensile test and DaB determined in a 3PBT (n = 6, mean ± CI; α = 0.05) for TA-loaded EC based filament formulations with different HPMC content (F9 = HPMC 0 %, F10 = HPMC 5 %, F11 = HPMC 15 % and F12 = HPMC 25 %).

In addition, the formulation showed higher diameter variations. Thinner sections therefore tend to break easier compared to thicker sections. The DaB is highly dependent on the diameter. Inconsistencies were therefore potentially reflected in higher mean values as expected and higher variations. The influence of variations on the mechanical properties is discussed in detail in section 3.2.3.4. All HPMC-loaded formulation strongly exceeded the limits established by Korte and Quodbach (YM = 300 N/mm^2; DaB = 1.125 mm) [27]. It can be summarized that all filaments had a desirable stiffness (expressed by a high YM) and had a high resilience against transversally applied stress (less brittleness). Therefore, printability was assumed, which was verified in printability studies with the used printer according to section 5.5.8. All formulations were printable with the specific printer. A constant conveyance of the filaments through the print-head without deformation or breakage was possible and thus dosing. All formulations were subjected to preliminary drug release studies to achieve the final objective for the intended use.

3.1.5.3.5 Preliminary Drug Release Studies

The influence of the pore former concentration on the drug release was investigated in preliminary experiments over seven and 30 days with TA-loaded extrudates. This was done in accordance with the adjusted formulation development flowchart (Figure 7, section 3.1.1) of Korte [109]. First experiments revealed that the TA release from pure EC-filaments F9 (A) was ≤ 1 % after ten days (Figure 21, section 3.1.4.2.4). This was not surprising as EC is a non-erodible and non-swellable polymer, so only the low API amount on the surface of the filament was released.

Since an API release from the articular implant over three months is aimed at, HPMC as pore former was added in different concentrations to find a suitable formulation and modify the drug release. To assess the effect of the pore former concentration on the TA release, preliminary dissolution studies of filaments (F10, F11 and F12) in USP Apparatus I were performed initially over seven

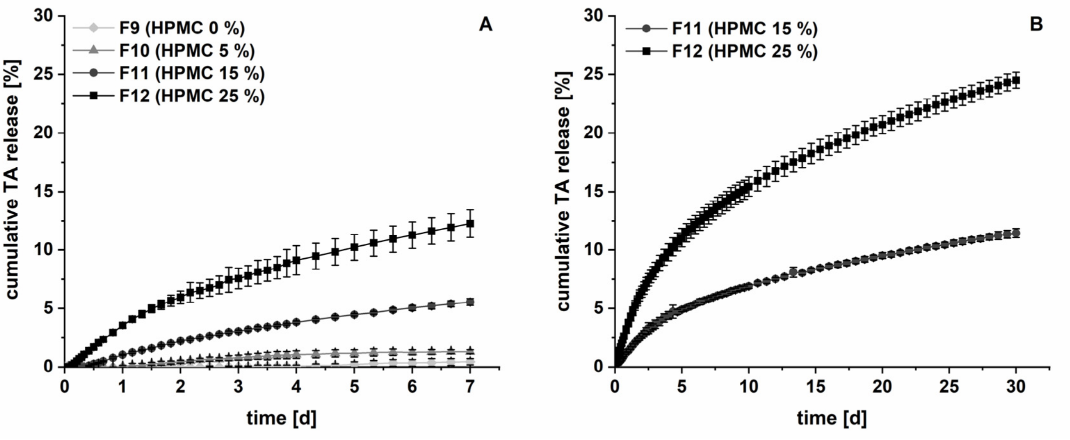

Figure 27. Cumulative TA release from filament formulations F9-F12 (n = 3; mean ± s; 37 ± 0.5 °C, 100 rpm, 1000 mL PBS 0.05 M, pH = 7.4). A = F9-12 over seven days and B = F11 and F12 over 30 days.

days. Filaments were prepared as previously described (section 3.1.4.2.4). Through further findings in the course of the work, it was found that the TA dissolution conditions must be optimized (refer to section 3.3.2). Considering the new insights, the data is still deemed conclusive.

The results are depicted in Figure 27A. The number of data points was reduced due to clarity reasons. The studies showed increasing drug release from the EC-matrix with increasing HPMC concentration, as expected. HPMC is a swellable and water-soluble polymer, so in contact with water, it dissolves and forms pores inside the EC-matrix. Thus, water was introduced inside the matrix to dissolve TA, which diffused through the pores into the medium. The higher the HPMC concentration, larger and more pores were formed as visualized in the confocal Raman microscopic images (Figure 23, section 3.1.5.3.1) and more TA was dissolved. The addition of 5 % pore former (F10) was not sufficient to increase considerably the drug release from the EC-matrix compared to F9. The release from formulations F11 (15 % HPMC) and F12 (25 % HPMC) appeared promising with a drug release of 5 and 10 % after seven days for the intended use.

To gain more insights in the dissolution profiles and potentially determine the underlying release mechanism, filaments with 15 and 25 % HPMC were subjected to *in vitro* dissolution studies over 30 days. The obtained dissolution profiles of both formulations are shown in Figure 27B. A concentration of 15 % HPMC led to a release of 11.42 ± 0.39 % TA in 30 days. Within the first seven days 5.81 % of the TA was released and only 5.61 % were released in the remaining 23 days, hence the drug release rate declined. The filaments consisting of 25 % HPMC released 24.51 ± 0.68 % of TA after 30 days. After seven days approx. 13.0 % of TA was released, whereas the remaining 12 % were released afterwards. First the TA particles on the filaments' surface were released. Over dissolution time, the diffusion path lengths increased and thus the release rate was decreased. This suggests a square-root-of-t kinetic, which was investigated using Korsmeyer's and Peppas' approach. This type of analysis is widely used to distinguish between zero-order and square-root-of-t kinetics in dissolution studies [178]. It must be emphasized that a kinetic analysis at this early dissolution stage, when only a small drug amount is released, provides only first indications to estimate the dissolution performance of newly developed filament formulations.

However, Equation (1) was used to analyse the obtained dissolution kinetics, where $\frac{M_t}{M_\infty}$ represents the released TA amount, which is dependent on time t. The constant k describes the geometry of the analysed dosage form (here cylindric) and n is the diffusional release exponent which is indicative for the present release mechanism [178].

$$\frac{M_t}{M_\infty} = kt^n \tag{1}$$

The application of the common logarithm of Equation (1) led to linearization:

$$log_{10}\frac{M_t}{M_\infty} = log_{10}\,k + n \cdot log_{10}t \tag{2}$$

Figure 28 shows the double logarithmic plot of F11 and F12 according to Equation (2). Values > 5 % were considered to cover the linear range as the release data for the first days was fast compared to the residual drug release and consequently not representative. Diffusional release exponents of n = 0.47 (F11) and n = 0.45 (F12) were obtained as slope from the respective linear fits. According to Ritger and Peppers for cylindrical matrix geometries a diffusional exponent of n = 0.45 indicates a square-root-of-t kinetic and for n = 1 a zero-order kinetics [178, 179]. Consequently, for the investigated formulations the underlying release mechanism appeared as square-root-of-t release mechanism, which was expected from a non-erodible matrix system. It must be considered that the influence of HPMC as swellable polymer may lead to deviating diffusion mechanisms [151].

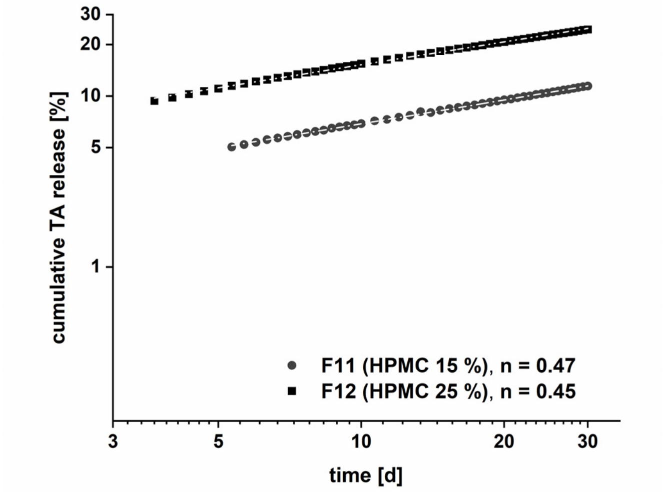

Figure 28. Double logarithmic depiction of TA release from formulation F11 and F12 (> 5 % TA release, n = 3, mean).

3.1.5.3.6 Estimation of TA Dissolution Time based on Higuchi-Model

The underlying dissolution kinetics of TA-loaded filaments with 15 % and 25 % HPMC, were determined based on initial drug release of 10 and 25 %, respectively. For better estimation and comparison purposes of both formulations, it appeared therefore valid to use Higuchi's model to predict roughly the time points of 80 % API release.

The Higuchi's term (Equation (3)) was proven to be valid for drug release description from homogenous porous planar polymer matrix systems [180]. Q represents the released API amount at time point t (M_t) per unit area (A). D is the diffusivity of the drug inside the polymer matrix, ε the porosity of the matrix, τ the tortuosity of the capillary system, C_0 the initial and C_s the saturation concentration within the polymer.

$$Q = \frac{M_t}{A} = \sqrt{\frac{D\varepsilon}{\tau}(2C_0 - \varepsilon C_s)C_s t} \qquad \textbf{(3)}$$

Equation (3) can be simplified as follows, where k combines the diffusional coefficient, the surface area, the porosity and the tortuosity of the porous matrix, as well as the initial and saturation concentration in the polymer [181]:

$$M_t = k\sqrt{t} \qquad \textbf{(4)}$$

In Figure 29, the cumulative drug release was plotted against $t^{0.5}$ according to Equation (4) to estimate the time point, when 80 % of TA is released from the HPMC/EC-matrix.

Values > 5 % drug release for the formulation with 15 % HPMC and above 10 % drug release were used to cover the linear range. Values below were assigned to the initial abnormal transport.

Obtained linear fits (Figure 29) had a coefficient of determination of 0.9992 for HPMC 15 % and 0.9972 for HPMC 25 %. According to the respective linear functions, F11 (HPMC 15 %) will release 80 % of TA within 52 months, whereas 12 months is the calculated time point for F12 containing 25 % HPMC as pore former.

This seemed to be a long period, but it must be considered that printing of different network structures as described in section 3.1.2. and a reduction of the diameter from 1.7 mm down to

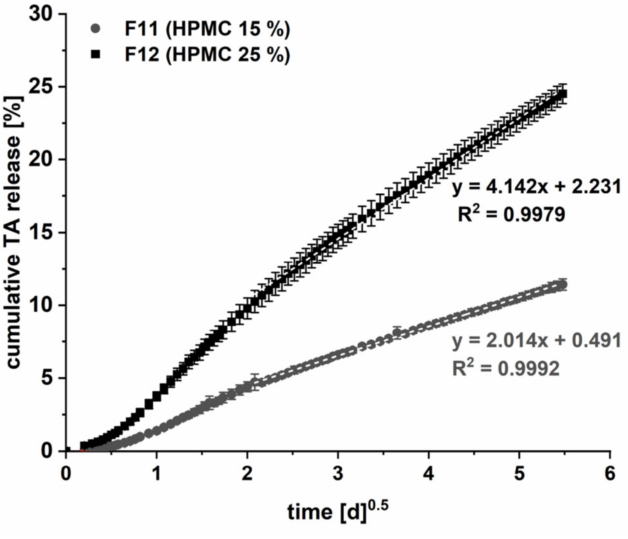

Figure 29. Depiction of cumulative TA release against square root of time from formulation HPMC 15 % and HPMC 25 % (linearization from > 5 %/ 10 % release, n = 3, mean).

approx. 0.4 mm during printing will increase the surface area and, thereby, accelerate the drug release distinctly. In addition, 3D-printing and design of implants can be used to improve the media flow through the matrix, as well as to reduce the diffusion path length to control the released TA amount. Hence, both formulations appeared promising to produce customizable 3D-printed implants, depending also on the solubility of the used API and the targeted residence time. The addition of HPMC ≥ 15 % as pore former was suitable to accelerate the TA release from matrices considerably. Therefore, F11 and F12 will be characterized in subsequent experiments. Based on the time point estimation of 80 % TA release via the Higuchi equation filament formulation F12 will be used for printing of implants and drug release studies since it showed the most promising release behaviour.

3.1.6 Summary

In this chapter, a systematic development approach for TA-loaded 3D-printable filaments for tailored implants was effectively demonstrated. Based on an elaborated implant inlay design, enabling a shape adaption to anatomical structures independent from dose and drug release individualization, suitable excipients were selected. A combination of a drug-free geometric adaptable shell, achieving additionally a unidirectional drug release and a TA-loaded implant inlay was presented for the intended use.

Filaments based on EC as water insoluble pharma-grade thermoplastic polymer, achieving a strong sustained TA release, were produced successfully using a 16 mm 40D co-rotating twin-screw extruder. Two plasticizers in different concentrations were evaluated to find a drug-free and drug-loaded base filament formulation with sufficient processability and suitable mechanical properties for 3D-printing using an adapted approach of Korte [109]. Therefore, filaments were characterized regarding their thermal stability via DSC, diameter uniformity and mechanical properties in a tensile test and 3PBT. All investigated formulations were printable and showed thermal stability proven via DSC. By increasing the plasticizer concentration, the mechanical properties could be optimized in terms of flexibility and brittleness for practical handling. 10 % TEC as liquid plasticizer in combination with EC as polymer with and without TA resulted in the best overall performance and was used for further optimization.

Subsequently, drug-loaded filaments were produced with different HPMC concentrations for potential acceleration of the TA release and characterized afterwards. Related to the mechanical properties the addition of HPMC led to reduced stiffness in longitudinal direction and an increased brittleness, possibly limiting the addable amount. But mechanical properties were sufficient and printability was retained.

Confocal Raman microscopy was found valuable to assist evaluation of surface quality and distribution of the different components along the filaments. With increasing HPMC concentrations rougher filament surfaces were obtained, likely caused by phase separation and differences in the viscoelastic behaviour of EC and HPMC. An apparent homogenous component distribution was achieved, which is discussed further in section 3.2.5.1.

Although the obtained filament diameter homogeneity was acceptable for initial assessment with a CoV < 6 %, it was revealed that a thorough process understanding and optimization is mandatory to improve the continuous manufacturing and quality of filaments and subsequent 3D-printed customizable implants.

The addition of HPMC as water-soluble pore former was effective to model the TA release from hot-melt extruded TA-loaded printable filaments. By screening filaments via *in vitro* dissolution, formulations with 15 and 25 % HPMC (F11 and F12) promising filaments were identified for implants with a residence time of several months, indicating a square-root-of-t kinetic. Based on the Higuchi-model the release period was estimated, simplifying formulation selection. Although the filament formulations with HPMC content < 15 % were not suitable for the specific case, they might be suitable options for other APIs and drug loads. Both drug-loaded formulations (F11 and F12) and drug-free formulation (F6) will be used for further characterization related to process optimization and stability analysis. The drug-free formulation F6 and TA-loaded filament formulation F12 will be used for printing of different implants according to the presented design concept, emphasizing that the unidirectional drug release and the inlay network design will highly influence the released TA amount.

3.2 Systematic Process Development for Printable Filaments via Hot-Melt Extrusion and Filament Analysis

3.2.1 Pretext

The content of this chapter is based on the previously published research article "*Hot-Melt Extrusion Process Fluctuations and their Impact on Critical Quality Attributes of Filaments and 3D-printed Dosage Forms*", Pharmaceutics. 12(6): 511. 2020. (DOI: 10.3390/pharmaceutics12060511). The texts were linguistically adapted and the content has been extended by additional studies and data.

According to MDPI policy all articles published in MDPI journals, copyright is remained by the authors.

3.2.2 Introduction and Objectives

In the previous chapter of the present work, the formulation development of 3D-printable drug-free (F6) and drug-loaded filaments (F11, F12) was shown based on defined requirements for the intended use. During the studies it was demonstrated that the production of highly consistent filaments for 3D-printed medicines is challenging. Optimizations related to process set-up and settings are required to guarantee reproducible filament quality as well as high resolution and dose accuracy of sophisticated printed implants. The following studies were performed to improve the filament production adapted to industrial environment and to gain a deep process understanding to enable increased filament quality in general. Additionally, the developed formulations supposed to be finalized addressing process and product development based on a QbD approach.

The first part of the studies focused initially on HME process set-up adaptions to reduce observed issues, like windings and correct positioning of the filament within the diameter measurement unit. In addition, a winder shall be implemented to ensure a reproducible and representative filament haul-off. The establishment of filament winding on spools was conducted to bridge filament development and industrial continuous manufacturing. The suitability of an exemplary formulation for the winder application should be verified in a feasibility study investigating diameter adaption precision and potential filament deformations.

The filament diameter is a specification of high relevance, which is strongly influenced by HME process parameters and the haul-off set-up [27]. In addition, the diameter consistency is one of the most important CQAs, affecting filament properties and quality of 3D-printed dosage forms, as currently available printer software is not able to counterbalance variations [166].

The hypothesis for the second part of the work was that certain HME process parameters or combinations cause pulsatile melt conveyance along the barrel resulting in diameter fluctuations as discussed in section 3.1.4.2.2. Hence, a rational process analysis was conducted to investigate reasons for the appearance of diameter inhomogeneities. The influence of screw speed, PFR and consequently barrel filling degree was investigated. Subsequently, it was examined how and to what extent potential inaccuracies affect related CQAs of filaments (mechanical properties) and printed dosage forms (uniformity of mass). Thereby, acceptable diameter variations and an optimized continuous twin-screw HME process for filament manufacturing should be identified.

The analysis was conducted by using a representative drug-free filament formulation (F13) consisting of 74.64 % EC and 15 % HPMC, 10 % TEC and 0.36 fumed silica (all w/w) similar to F11.

Afterwards, the gained insights should be used to find optimal extrusion settings for the drug-free and TA-loaded filaments for subsequent printing of customizable implants. The transferability to the drug free formulation F6 (EC with 10 % TEC) and promising 10 % TA-loaded formulations F11 (EC with 10 % TEC and 15 % HPMC) and F12 (EC with 10 % TEC and 25 % HPMC, EC) was investigated. Produced filaments were finally characterised related to their content uniformity and drug distribution along filaments. Printed test geometries were evaluated according to the Ph. Eur. 2.9.6 and 2.9.40.

Filaments will likely be produced in the future by the pharma industry, while the printing of customized dosage forms is planned to be conducted in community pharmacies or hospitals on demand. Therefore, filament stability over storage is important to consider, to assure the quality during shelf-life. Evaporation of the liquid plasticizer, API stability or polymer ageing are commonly described issues affecting CQAs. The developed filament formulations were subjected to stability analysis according to the ICH guideline Q1A (R2) to investigate the influence of storage conditions inclusive primary packaging on CQAs of filaments.

3.2.3 Process Analysis and Optimization

3.2.3.1 Adaptions of the HME Process Line for Filament Production

In section 3.1, issues related to filament transportation due to windings behind the die and reasons for occurrence were extensively discussed. A further problem observed during preliminary trials for process analysis was condensation of liquid inside the barrel inlet of the powder feed unit during long-runs of manufacturing (~ 3000s). Water evaporation was excluded as it was not noticed with formulations containing solid plasticizers.

Although the boiling point of TEC is, according to the certificate of analysis, 294 °C, plasticizer evaporation during extrusion during long process runs appeared reasonable. This was proven by heating TEC in a silicon bath at extrusion temperature, where minor vapour formation was noticed. This could result in problems with homogeneous powder feeding in industrial environment and consequently process fluctuations that might have an impact on mechanical properties and relative API distribution. To circumvent the stated issues general adaptions of the extrusion equipment were made. First, the die diameter was increased from 1.75 to 1.85 mm to reduce the shear stress and thereby resulting filament windings. Additionally, by generating a larger start diameter, the necessary increase of haul-off speed would not result in reduced mean diameter as previously described (section 3.1.4.2.2).

Secondly, the previously used screw configuration I was changed to introduce a degassing port in temperature zone 2 (100 °C, screw configuration II, Figure 30). Potentially generated vapour can escape without condensation in the barrel inlet of the powder feed. Consequently, the KBs were shifted and long pitch conveying elements (LPCE) were placed underneath the degassing port to increase the surface area. The KBs were put closer together to potentially reduce the extent of the material amount difference behind the first KB and in front of the second KB. By these adaptions, TEC condensation during filament extrusion was successfully reduced to maintain a constant homogenous powder feed.

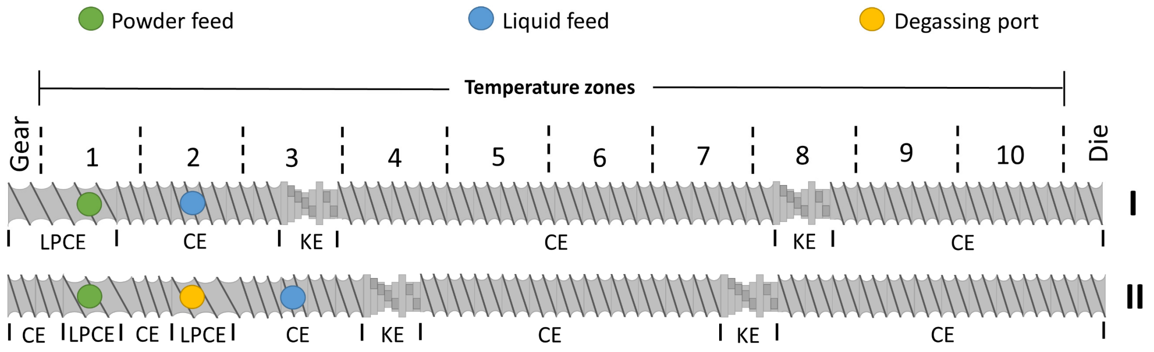

Figure 30. Schematic depiction of adapted HME screw configuration II compared to screw configuration I used during formulation development. Barrel and temperature zones (1-10) are indicated. LPCE = long pitch conveying elements (helix of 3/2 L/D), CE = conveying elements (helix of 1 L/D); KE = kneading elements.

3.2.3.2 Improvement of Continuous Filament Production by Implementation of a Winder

Before starting proper HME analysis related to the impact of process parameters on diameter variation, the first part of this chapter aimed at optimization of the HME process set-up.

To achieve the target filament diameter the filament was commonly stretched and cooled behind the die on conveyor belts as described in section 3.1.4.1 [35, 56, 58, 60, 182]. A prerequisite for reliable and representative diameter adaption is a sufficient adhesion of the filament on the belts. Additionally, a lopsided position of the filament within the laser unit of the measurement module due to movements on the conveyor belt or behind the module induced by the filament collection process (e.g., roll up in a bucket, Figure 31A) distorts the diameter data. To prevent the stated issues and be able to align potential observed diameter fluctuations to certain process parameters or combinations, the previously used extrusion line was expanded by a winder. The implementation of a winder reflects the continuous manufacturing in industry, as a continuous, reproducible filament production and controllable winding on spools for storage is enabled.

In Figure 31, the new extrusion process set-up (B) is depicted compared to the one initially used (A). The implemented winder consists of a haul-off unit, a traverse and a winder unit. The selected haul-off unit uses counter-rotating conveyor belts. A benefit of the fixation between the two belts is that filaments can be conveyed and stretched independently from their adhesion capability on the conveyor belt to obtain a reproducible target diameter. Behind the haul-off unit, the filament is transported over lead roles of the traverse and wound-up on a rotatable spool. The winding process is coupled to the set haul-off and the traverse. The traverse moves in one axis along the spool to drop the filament strands precisely next to each other (Figure 31C). The oscillation speed of the traverse depends on the pre-set haul-off speed, filament and spool diameter. To generate a uniform winding process, the applied tension between the haul-off and traverse can be adjusted.

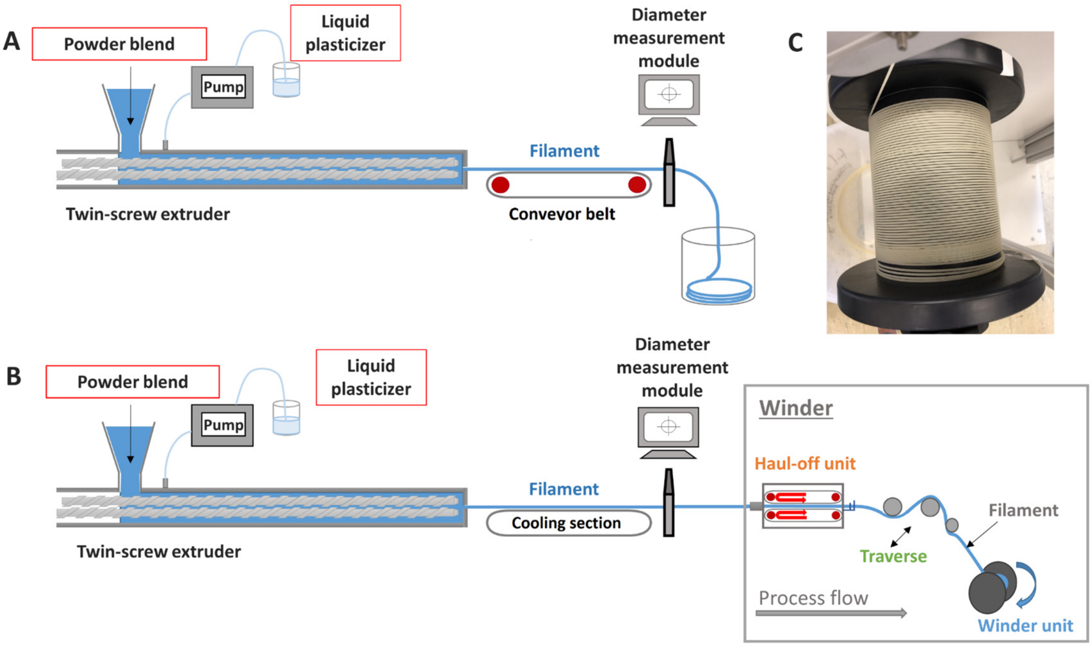

Figure 31. HME set-up for filament production before (A) and after (B) optimization by implementing a winder. Subfigure (C) displays an exemplary winding process of F13 in the winder unit (refer to section 5.3.2.2).

To improve the correct and reproducible positioning of the filament within the diameter measurement module, a self-designed 3D-printed guide rail for filaments was implemented (Figure 32). Subsequently, winder implementation studies were performed to assess the precision of the diameter adaption by the winder and winding capability of the formulation. First, it was tested to what extent a precise diameter adaption via the haul-off unit is feasible. Therefore, filament formulation F13 was produced with 5 g/min and 40 rpm at 190 °C. The exact applied barrel temperatures can be found in Table 27.

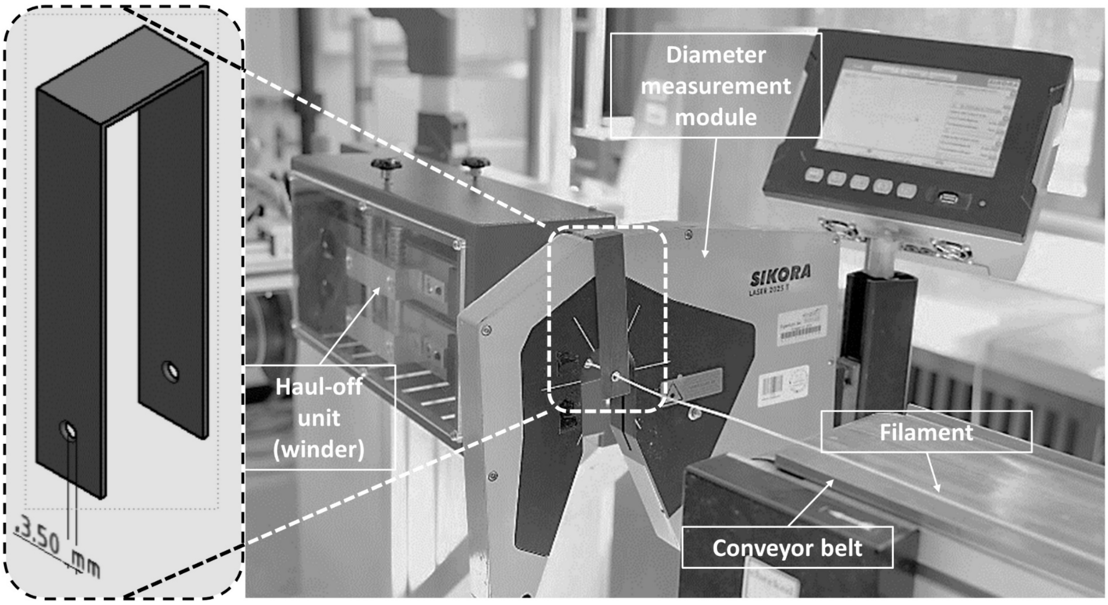

Figure 32. Laser measurement module with highlighted 3D-printed filament guide rail (picture © hhu/ Uli Oberländer). The conveyor belt was used switched off as cooling section for filaments.

Theoretically, the haul-off speed h can be calculated by transforming the mass flow (PFR) (*m/t*) into a volume flow (*V/t*) using the true density of the formulation ($\rho_{F13} = 1.1408 \pm 0.1 \cdot 10^{-3}$ g/cm^3). By transformation of the volume formula of the cylinder by substituting volume flow and the target filament diameter *d,* the haul-off speed was calculated according to Equation (5).

$$h = \frac{V/t}{\pi \cdot (\frac{d}{2})^2} \tag{5}$$

For a filament diameter of 1.75 mm, the theoretical haul-off speed is 1.82 m/min at a PFR of 5 g/min. However, the lowest applicable haul-off speed was 2.0 m/min otherwise windings could not be appropriately counterbalanced. The obtained filament diameter was 1.776 ± 0.031 mm and thus larger than the targeted 1.75 mm, although the haul-off speed was 0.12 m/min faster than calculated due to a die swell of 6 %, comparing theoretical calculated with actual diameters. Therefore, an individual setting for the respective formulation must be explored experimentally. A larger die diameter might be useful to reduce the shear stress at the die and consequently the die swell of extrudates.

To find suitable settings and to evaluate the diameter adaption capability of the winder, the mean diameter of F13 was measured as function of the applied haul-off speed. Six equidistant velocities between 2.0 and 2.5 m/min were applied (minimal steps 0.1 m/min). The results are depicted in Figure 33. A precise diameter adaption via the winder was feasible, enabling, depending on the die swell of formulations, reproducible filament diameter quality. In combination with a PFR of 5 g/min, a haul-off speed of 2.0 m/min is suitable to achieve the target diameter.

In a second step, the winding capability of filaments on spools and a potential elongation or deformation of the filaments due to the applied tension within the winder unit was assessed. For the

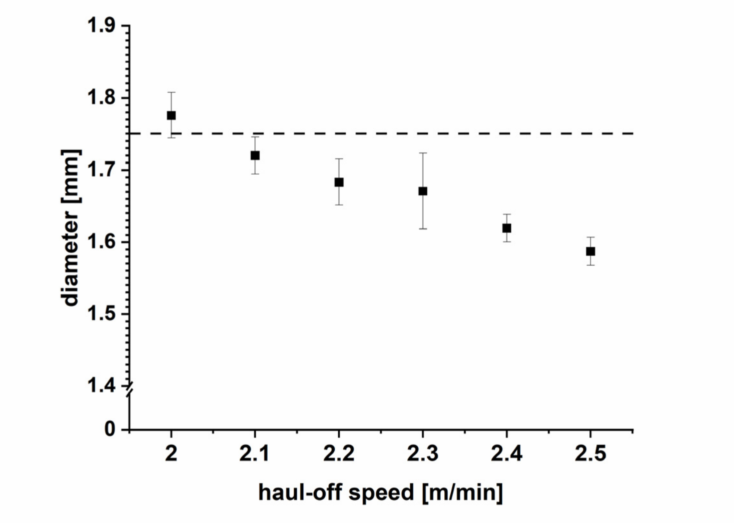

Figure 33. Inline determined filament diameter (mean ± s, n > 238) as function of the applied haul-off speed. The dashed line marks the target value of 1.75 mm.

feasibility study again F13 was extruded using the same process parameters as previously described. Two different PFRs (5 and 10 g/min) were applied since the haul-off speed must be doubled (from 2.0 to 4.1 m/min) to achieve the same diameter of 1.78 mm. Consequently, solidification time was halved keeping the distance between extruder outlet and haul-off unit constant. This might result in filament deformation or elongation during the winding process and was therefore assessed with respect to throughput increase.

The winding capability of F13 was given as intended (see picture in Figure 31C). The formulation was sufficient for being constantly rolled-up without visible deformation or rupturing, which is advantageous for continuous filament production. To measure potential filament deformation during winding, the mean diameter and the ovality were measured offline again after the winding process. The ovality of the filament was defined as difference between minimum and maximum determined diameter. The obtained results are depicted in Figure 34. The inline- and offline determined mean diameter and ovality are plotted as function of extrusion time. Consistent diameters for both settings with 1.781 ± 0.032 mm (5 g/min) and 1.798 ± 0.031 mm (10 g/min) were obtained. Applying a PFR of 5 g/min, no significant difference between inline- and offline-determined diameter was noticed (inline:1.781 ± 0.032 mm; offline 1.783 ± 0.032 mm, $p = 0.455$). In contrast, the ovality showed a significant change before and after the winding process (inline: 0.024 ± 0.003 mm; offline 0.028 ± 0.005 mm; $p << 0.01$). As the filament is not under proper tension during offline feeding, measured changes are likely caused by a lopsided filament positioning within the diameter measurement module (refer to Figure 16). Movements due to uncoiling the filament from the spool might lead to deviating ovalities, which was visible within the first 20 s of the offline measurements. Hence, it was assumed that no considerable deformation occurred. Obtained filaments were almost completely round shaped.

Filaments produced with 10 g/min showed a slightly increased diameter compared to filaments produced with 5 g/min, although a more than doubled haul-off speed was applied (4.1 m/min), likely due to an increased die swell with increasing throughput. After the winding process, filaments showed a significant decrease in mean diameter from 1.798 ± 0.031 mm to 1.774 ± 0.032 mm ($p << 0.01$) as depicted in Figure 34, right. An elongation of the filament was likely due to the applied tension during winding in combination with shortened cooling time. The absolute reduced diameter value is still in the suitable range to be processed via 3D-printing. However, not considering significant diameter differences after the winding process might lead to unnoticed deviation from the targeted 3D-printed dosage form weight and the dosage being out of specification. A difference in ovality due to plastic deformation was hard to interpret since small movements during the offline measurement occurred. Although the values fluctuated, the same ovality values and variations with 0.025 ± 0.005 mm were obtained. Nevertheless, no considerable change in mean filament diameter and ovality was found. If higher throughputs are used, an efficient cooling section, e.g., via fans or other systems are obligatory to ensure reliable diameter measurements and avoid filament deformation or elongation during the winding process.

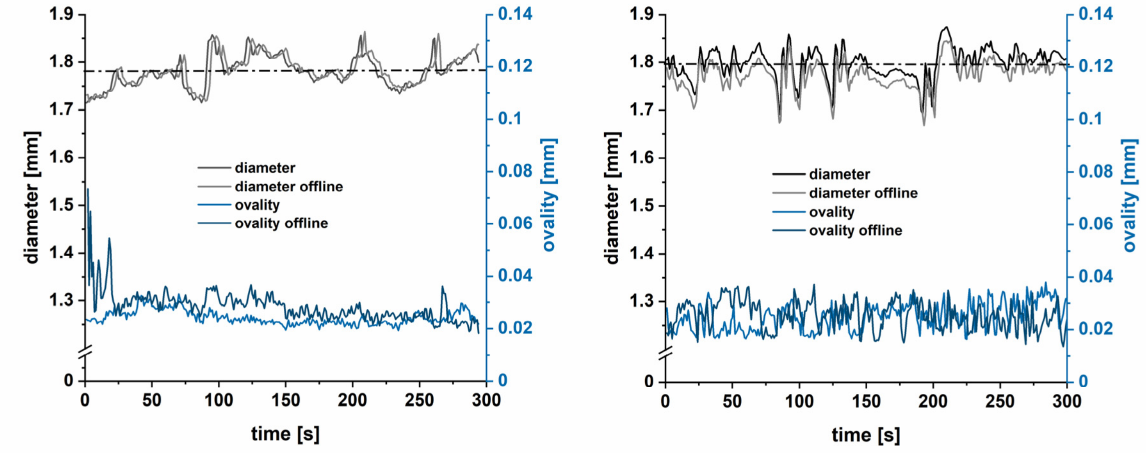

Figure 34. Inline- and offline-determined diameter and ovality ($\Delta Ø_{min/max}$) as a function of time (1 Hz) for a PFR of 5 g/min (left) and 10 g/min (right). The dashed lines indicate the mean inline-determined diameter (figure was adopted from Ponsar et al. [183]).

The set-up adaptions and a winder were successfully implemented to optimize the extrusion line and generate reliable data for process analysis. Previous observed issues were reduced and changes in diameter could now be clearly assigned to pre-set extrusion parameters. The investigated and developed formulation showed good winding capabilities.

3.2.3.3 Process Fluctuations and Their Impact on Critical Quality Attributes of Filaments

Some of the most important CQAs of filaments are the diameter and diameter homogeneity to ensure printability (expressed as mechanical resilience), high printing resolution and dose accuracy as previously mentioned. Diameter variations higher than 2.86 % (1.75 ± 0.05 mm) were defined as not acceptable [184]. In other publications, CoVs between 2 and 19 % were accepted [32, 42, 166, 185].

In the past, the impact of HME process parameters on the mean filament diameter was investigated [27, 42]. However, the impact on diameter variations, the reasons for occurrence and acceptable extent along with CQAs of filaments and 3D-printed dosage forms were not examined. Extrusion experiments during formulation development revealed that recorded material pressure fluctuations at the die were reflected in diameter variations (refer to section 3.1.4.2.2). This was further underlined by preliminary experiments with different applied screw speeds as depicted in Figure 35. This effect was already observed by Korte [109] and explained by pulsatile material conveyance along the extruder barrel. This is most likely caused by material accumulations in front of KBs as a certain melt amount is required, building up enough pressure to push the melt through the KBs and the die. Material transport fluctuations were also observed by Meier et al. for twin-screw granulation processes [186]. As consequence, the material amount passing the die varies and thus the filament diameter. The extent of resulting diameter fluctuations is highly dependent on the viscoelastic behaviour of the used material composition [171]. A linear correlation between material pressure and diameter changes was not found via Pearson correlation.

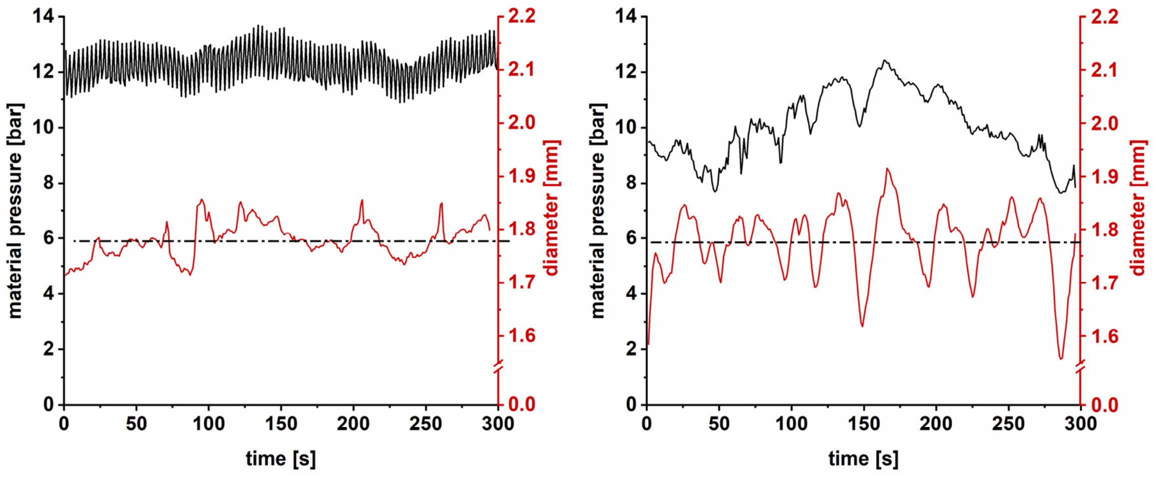

Figure 35. Inline-determined material pressure and diameter as function of time during extrusion of F13. Settings: PFR = 5 g/min; screw speed = 40 rpm (left) and 60 rpm (right). The dashed lines mark the respective mean diameter (adopted from Ponsar et al. [183]).

To exclude inhomogeneous powder feed of the low feed rate of 5 g/min as potential cause, offline accuracy analysis of the loss-in-weight powder feeder was performed. Therefore, the PFR of the powder mixture F13 was determined as function of time (0.5 Hz) over 60 min using an analytical balance as described in section 5.5.4. The normalized absolute mass error was calculated according to Meier et al. to assess deviations from the set PFR for the respective deviation duration [187] (refer to section 5.5.4). Hence, every single mass error deviating from the set value was divided by the mass, which would have been fed by the gravimetric powder feeder in the corresponding time interval.

The results of the PFR as function of time and the corresponding absolute mass errors normalized to the set PFR are depicted in Figure 36. The actual PFR fluctuates randomly around the set value (dashed line, Figure 36A). The dashed boxes mark time intervals when the powder collecting pan on the analytical balance was emptied and values were therefore discarded for calculation of the normalized absolute mass error (Figure 36B). Observed fluctuations were in most cases below 5 s and the normalized mass error was below 0.1, indicating a precise feeding performance at a PFR of 5 g/min. The influence of PFR fluctuations on material fluctuations inside the extruder barrel was consequently classified as minor.

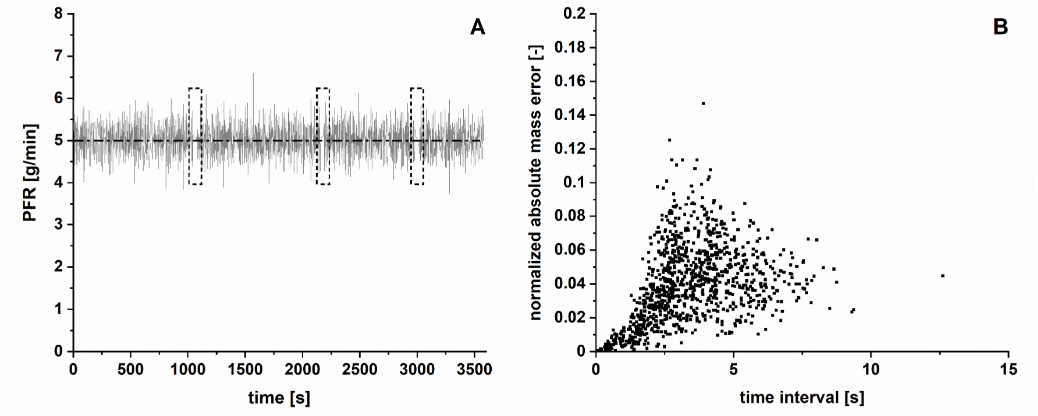

Figure 36. Offline PFR accuracy analysis; A = offline recorded feeding performance of F13; set value: 5 g/min (dashed horizontal line), boxes mark time intervals were the powder collecting pan must be emptied; B = mass error plot derived from feeding performance normalized to the set PFR.

Based on evaluation of process data of preliminary extrusion experiments material transport fluctuations were observed to depend clearly on process parameters, e.g., with increasing screw speed from 40 to 60 rpm higher fluctuations in material pressure were noticed as depicted in Figure 35. A rational process design was applied to investigate the impact of screw speed and PFR on material pressure (as surrogate for material transport fluctuations) and corresponding diameter variations. These parameters were chosen since they affect predominantly the filling degree of the barrel and were assumed to have a distinct influence on material transport fluctuations along the extruder. Accordingly, the PFR was varied on three levels (5, 7.5, 10 g/min) at a screw speed of 40 rpm and the screw speed was varied on five levels (20-60 rpm) at a PFR of 5 g/min (Table 4). The haul-off speed was adapted to the respective PFR to obtain a mean diameter close to 1.75 mm. The experimental settings were changed for each trial and the sampling of filaments was conducted over 300 s after reaching process equilibrium. To quantify potential variations, the IQR of the pressure and diameter data were used for the assessment. Outliers (> 1.5-fold the IQR [188]) were discarded. A bootstrap analysis was performed to assess differences of IQRs statistically as described in section 5.4 since the underlying distribution was not known.

Table 4. Overview of experimental plan for HME process analysis part I (modified from Ponsar et al. [183]).

Trial	Batch Code	PFR [g/min]	LFR [g/min]	Screw speed [1/min]	SFL [-]	Haul-off speed [m/min]
Influence of PFR	B1	5	0.56	40	0.03	2.0
	B2	7.5	0.83	40	0.045	3.0
	B3	10	1.11	40	0.059	4.0
Influence of screw speed	B4	5	0.56	20	0.059	2.0
	B5	5	0.56	30	0.04	2.0
	B1	5	0.56	40	0.03	2.0
	B6	5	0.56	50	0.024	2.0
	B7	5	0.56	60	0.02	2.0

In Figure 37, the results of the influence of different applied PFRs on inline-determined material pressure and diameter are depicted as boxplots. The material pressure increased with higher powder throughput, as a consequence of a rising barrel filling degree (Figure 37A). The IQRs of material pressure were comparable (1.12 bar, 1.16 bar and 1.33 bar). The material amount and resulting pressure was sufficient for a homogenous melt transport through the KBs and the die, reflected in similar diameter IQRs.

The mean diameter was comparable (Table 5, B1-B3) and differences in diameter fluctuations between 5 and 10 g/min were negligible, showing that the PFR had in the pre-selected operation window no impact. However, 5 g/min depicted the minimum possible PFR due to feeding limits of the used weight-loss feeding system and 10 g/min was the maximum applicable PFR with respect to manual handling and solidification time (refer to section 3.2.3.2). At first sight, this outcome appeared unexpected, since the barrel filling degree was distinctly increased and a higher impact was assumed. The reasons will be explained in the further course of this chapter.

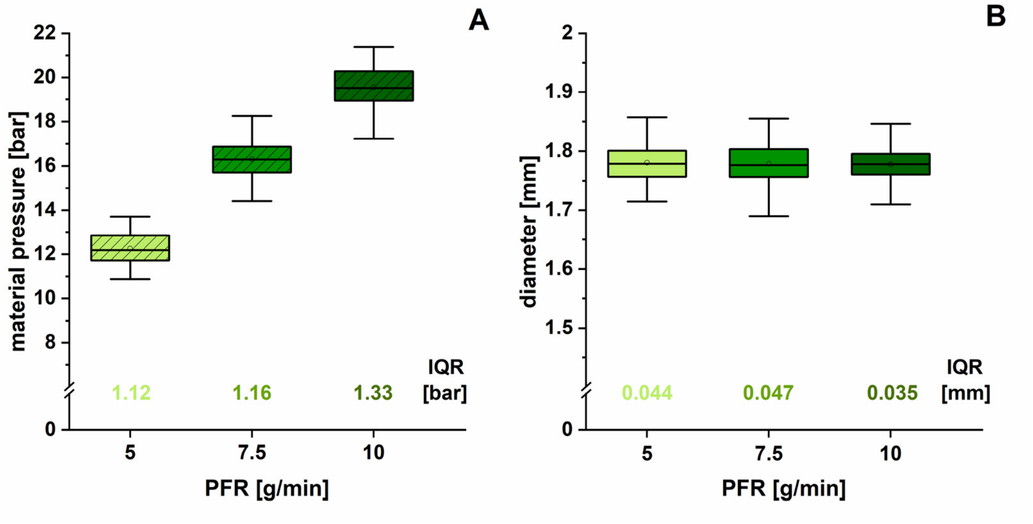

Figure 37. Boxplot of inline measured material pressure at the die (A) and filament diameter (B) (1 Hz, n > 294) for different applied PFRs at a constant screw speed of 40 rpm. The resulting IQRs are indicated (modified from Ponsar et al. [183]).

Table 5. Inline-determined diameter data of produced filaments and commercial PLA (mean, standard deviation (s) and CoV, n = ~ 300). Table modified from Ponsar et al. [183].

Diameter	B1	B2	B3	B4	B5	B6	B7	B8	PLA
Mean [mm]	1.781	1.779	1.778	1.782	1.789	1.776	1.777	1.821	1.756
s [mm]	0.032	0.035	0.033	0.019	0.032	0.054	0.064	0.062	0.004
CoV [%]	1.80	1.98	1.83	1.07	1.76	3.06	3.63	3.38	0.21

In a second step, the influence of screw speed (20-60 rpm) was investigated. In Figure 38A and B, the influence of varying screw speeds on material pressure and diameter variations are shown. As expected, with increasing screw speed the material pressure decreased caused by the reduced barrel filling degree and potential shear-thinning behaviour of thermoplastic polymers. The material pressure variations increased distinctly above 40 rpm. This was potentially caused by a faster removal of material in general at higher screw speeds, but simultaneously material accumulates in front of the KBs until enough is available to build up a certain pressure to push the melt further through the die. This resulted in pulsatile melt conveyance and had a distinct influence on filament diameter homogeneity (Figure 38B). The extent of material fluctuations seemed to depend clearly on the barrel filling degree in combination with the set screw speed, as at lower screw speeds (≤ 40 rpm) the diameter IQRs were lower (0.027 - 0.044 mm). The material amount was sufficient to transport the melt homogeneously, without distinct fluctuations. At 20 rpm, the filaments with the lowest diameter variations were obtained.

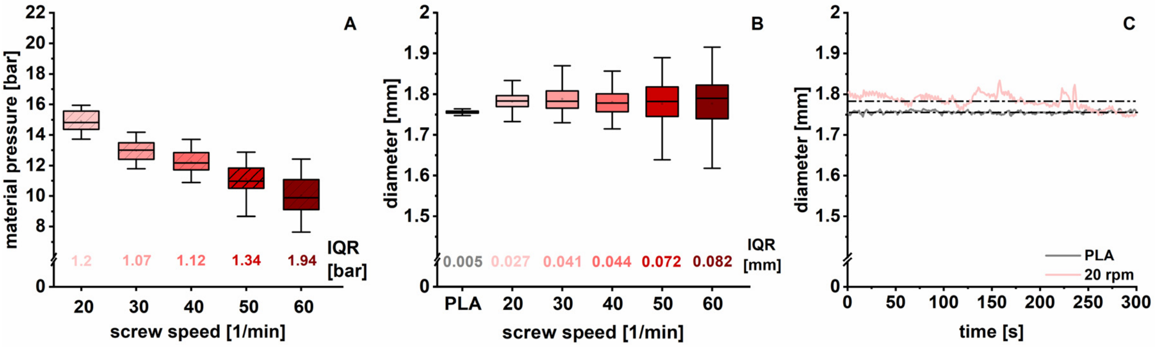

Figure 38. Boxplot of material pressure (A) and filament diameter (B) for different applied screw speeds during extrusion (1 Hz, n > 290) at a PFR of 5 g/min compared to commercial PLA filament diameter. The resulting IQRs are indicated. Inline-determined diameter as function of time for filaments produced at 20 rpm (B4) compared to commercial PLA filament (C); dashed lines mark the respective mean diameter. Figures are modified from Ponsar et al. [183].

For comparison purposes, the diameter and its variation of commercial polylactic acid (PLA) filaments were measured using the winder haul off with a speed of 2.0 m/min (Figure 38B). The commercially available filament (1.756 ± 0.004 mm, CoV = 0.21 %) was much more consistent compared to self-extruded filaments with the lowest variations (1.782 ± 0.019 mm, CoV = 1.07 %). The diameter IQR of the PLA was considerably low with 0.005 mm, whereas the one of in-house extruded filaments was 5-fold higher (IQR = 0.027 mm).

Commercial drug-free filaments, not intended for medicinal use, are usually manufactured with single-screw extruder having always a full barrel and showing low mixing capacity. A homogeneous distribution of an active is not required. A fluctuating material conveyance is therefore not present and filaments with minimal diameter variations are obtained. This is especially visible comparing the diameter as function of time (in Figure 38C). However, for manufacturing of pharmaceutical drug products an extensive, dispersive and distributive mixing under controlled conditions is required to enable product uniformity within specifications. This can be only provided using TSE equipped with KBs [57], especially when liquid components need to be incorporated. Besides the extruder type, the processability is also dependent on the polymer blend properties such as melt rheology and MW [167]. Therefore, the extent of fluctuations depends additionally on the formulation.

Based on obtained results, the barrel filling degree was hypothesized to be decisive for filament diameter consistency. With decreasing screw speed, the barrel filling degree is increased, consequently, a certain threshold must be exceeded to obtain a homogenous melt transport. To verify the hypothesis, the specific feed load (SFL) as dimensionless number for the barrel filling degree for each setting combination was calculated according Kohlgrüber and Wiedemann [189] (Equation (6)).

$$SFL = \frac{\dot{m}}{\rho \cdot n \cdot D^3} \tag{6}$$

$\dot{m}$ = material throughput
ρ = true density of formulation
n = screw speed
D = internal barrel diameter

The higher the SFL the higher the barrel filling degree. Thereby, a comparison with other formulations and equipment was enabled.

In Table 4, the SFLs for the respective PFR/ screw speed combinations are depicted. By plotting the SFL against the respective diameter IQR, a material-dependent threshold of 0.03 was found (Figure 39). At SFLs < 0.03 the material fluctuations are high resulting in increased diameter

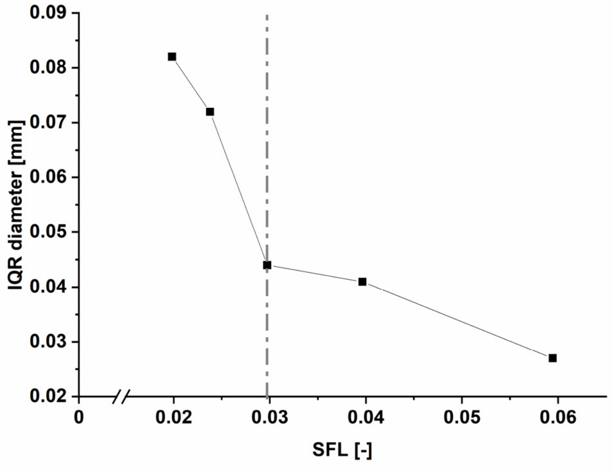

Figure 39. Diameter IQR of filament F13 against the different applied SFL (n > 290). The dashed line marks the material-dependent SFL-threshold. The figure was adopted and adjusted from Ponsar et al. [183].

variations, whereas at SFLs > 0.03 the melt transport is more homogenous. This explains why in the experiment with varying PFR no influence on diameter homogeneity was observed since the resulting SFL was ≥ 0.03 in all cases.

To further prove the SFL as key parameter, it was investigated whether the same diameter quality can be achieved by keeping the SFL constant applying different PFR and screw speed combinations. The SFL was either 0.059 or 0.02. Respective SFLs were investigated on a low throughput level (PFR = 5 g/min; LL) and a high throughput level (PFR = 10 g/min; HL). The pre-set SFLs were achieved by adaption of the screw speed according to Equation (6). The resulting four different setting combinations can be found in Table 6.

Table 6. Overview of the experimental plan of HME process analysis part II. SFL = specific feed load.

Trial	SFL [-]	PFR [g/min]	LFR [g/min]	Screw speed [1/min]	Haul-off speed [m/min]	Batch Code
Influence of SFL	0.059	5	0.56	20	2.0	B4
	0.02	5	0.56	60	2.0	B7
	0.059	10	1.11	40	4.0	B3
	0.02	10	1.11	120	4.0	B8

In Figure 40, the resulting boxplots of the inline-determined material pressure and filament diameter are displayed. At a low SFL, the material pressure was reduced compared to the higher SFL as expected (Figure 40A). At an SFL of 0.02 the material pressure and its variation were comparable as was the filament diameter data (Figure 40B). Although the IQR of the material pressure at an SFL of 0.059 is the same for both combinations, the mean value deviated surprisingly (HL = 19.6 bar vs. LL = 14.9 bar). This was possibly caused by a pressure probe calibration at different temperatures. The observed pressure IQR differences for the two investigated SFLs were not as distinct as previously noted. In contrast the effect on diameter variations was clear ($\mathrm{IQR}_{\mathrm{SFL:0.02}}$ = 0.082 mm (HL and LL) and $\mathrm{IQR}_{\mathrm{SFL:0.059}}$ = 0.35 mm (HL) and 0.027 mm (LL)).

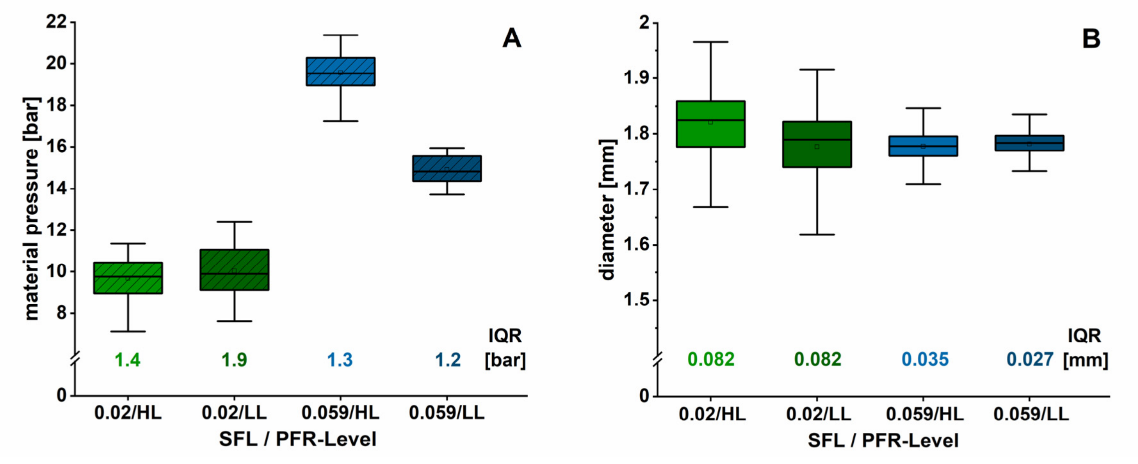

Figure 40. Boxplots of inline-determined material pressure (A) and filament diameter (B) during HME for two different applied SFL on a high (10 g/min, HL) and a low (5 g/min, LL) throughput level, respectively (1 Hz, n > 290). IQRs of pressure and diameter are indicated. The figure was adopted and modified from Ponsar et al. [183].

The limitation of the pressure probe measurements became obvious, resulting in potentially invalid evaluation of absolute pressure values. First, the recorded pressure data depends on the applied screw speed as shown in Figure 35. At 60 rpm the recorded pressure as function of time is obtained as non-fluctuating line, as the data sampling with 1 Hz was always conducted at the same screw position (1 revolution/s). But at 40 rpm an oscillating data signal was obtained, which was not caused by fluctuating melt conveyance, but sampling at different screw positions. Only 2/3 screw revolution per second occurred and thus the start position was reached after every third second, causing fluctuating data.

The second limitation of the pressure monitoring is caused by the device-related low sampling rate of 1 Hz. This is not sufficient to obtain complete and reliable pressure data. The pressure signal to be sampled consists of frequency components that were higher than half of the sampling frequency leading to an artifact. This is known from signal analysis or computer graphics and called Alias effect [190]. Thereby. the output signal is discriminated and causes incorrect amplitudes and apparently lower frequencies [191]. The recorded material pressure minima and maxima are consequently underestimated. However, noted trends as surrogate for material conveyance behaviour are still important information to evaluate corresponding diameter variations as previously shown (Figure 35). But absolute numbers cannot be assessed with high confidence. Improvements are desirable to use the material pressure in combination with melt rheological data as potential process analytical tool during filament fabrication to corresponding diameter fluctuations [167, 170].

Nevertheless, with the obtained diameter data it was shown that the set SFL is decisive for diameter uniformity. It was demonstrated that similar diameter variations were obtained at a given SFL (Figure 40B) independent from the process parameter combination. As previously assumed, at higher SFLs, filaments with reduced diameter fluctuations compared to lower SFLs were obtained due to the more even material transport along the barrel. For SFL = 0.02, the mean diameter at the higher PFR of 10 g/min was slightly increased (1.821 mm ± 0.062 mm) compared to the batch produced with lower throughput (5 g/min; 1.777 ± 0.064 mm). This phenomenon was potentially caused by increased shear stress at the die at the higher PFR in combination with the high screw speed of 120 rpm. A higher die swell and consequently, increased filament diameter was obtained [189].

Based on the obtained data, the SFL was identified as key parameter for diameter consistency. For an SFL of 0.059 (PFR; screw speed = 5 g/min; 20 rpm) the lowest filament diameter IQR was found. These findings are elementary and promising with respect to throughput up-scale in the industrial environment to obtain filaments with consistent quality. Based on the gained knowledge, formulation and process development might be accelerated. The transferability of the results to drug-loaded formulations is described in subchapter 3.2.4.

3.2.3.4 Impact of Filament Diameter Fluctuations on Further Critical Quality Attributes of Filaments and 3D-printed Dosage Forms

To examine the practical relevance of the observed diameter fluctuations and to determine the acceptable extent, the influence on mechanical properties as measure for printability and uniformity of mass of printed dosage forms was analysed. Self-produced filament formulation F13 with different extent of diameter variations (B1, B4-B7, Table 5) were used for this part of the study. With decreasing SFL the diameter IQRs increased due to more inhomogeneous material conveyance (refer to section 3.2.3.3). Filaments with rising diameter IQR were expected to have a distinct impact on further quality attributes of filaments and 3D-printed dosage forms. As the mechanical resilience of filament is declared as main factor for printability the YM and DaB were determined directly after extrusion as previously reported. It was assumed that due to the diameter fluctuations and consequently thicker and thinner sections the mechanical resilience is affected. This causes potential issues during printing.

In Figure 41A, the results are depicted related to the filament diameter IQR. The YM and its deviation as surrogate for stiffness in longitudinal direction were hardly affected. Although a statistically significant increase was noticed between filaments with IQRs of 0.027 and 0.082 mm ($p << 0.01$), the practical relevance and differences were classified as minor (Table 7). Printability should not be negatively influenced. Also, no impact on the mean value of the DaB was observed. In contrast, the CoVs of the measured DaB differed considerably, depending on the diameter variation as shown in Figure 41B. With increasing IQR, the CoV increased considerably from 3 to 20 %. Thin sections tend to break at lower distances compared to thicker sections causing increased CoV with increasing diameter variations. In this specific case, filaments were still printable. But if more brittle formulations are used, as is the case for many pharmaceutical materials with high drug-load, this can lead to an unreliable printing process. In the worst-case, a loss of printability is induced due to frequent filament breakage inside the print-head.

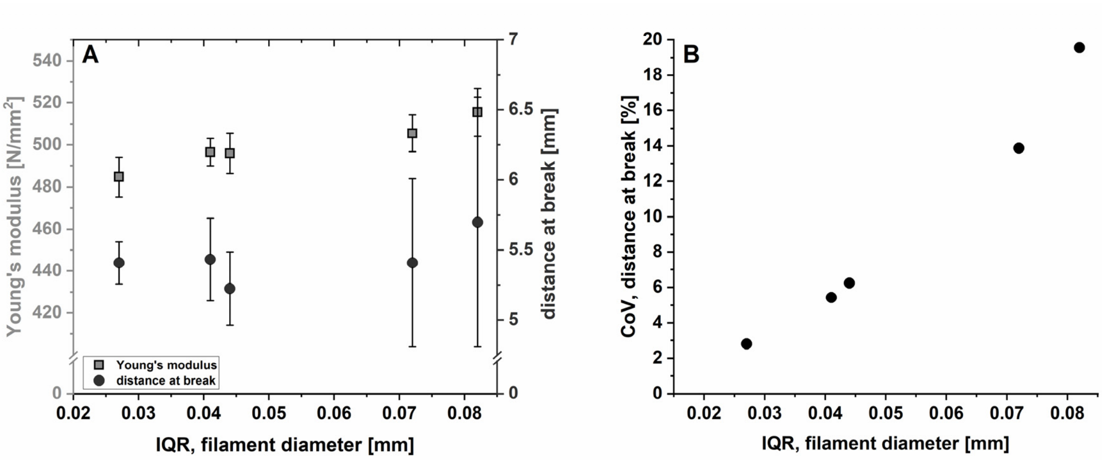

Figure 41. A = Determined YM and DaB of filaments with rising diameter fluctuations (IQR); mean ± CI ($\alpha = 0.05$), n = 6. B = CoV_{DaB} against filament diameter IQR.

Table 7. Overview of the impact of diameter variations (IQRø) on mechanical properties of self-produced filaments and uniformity of mass of printed test objects according to Ph. Eur. 2.9.5 (specification for tablets) (green = passed; red = failed test). (ND = not determined). PLA prints were measured for comparison purposes The table was adopted and modified from Ponsar et al. [183].

Sample	IQRø [mm]	Mechanical properties of filaments		Mass of printed dosage form [mg] (mean ± s, n = 20),	Ph. Eur. 2.9.5	
		YM [N/mm^2] mean ± CI (α = 0.05), n = 6	DaB [mm], mean ± CI, (α = 0.05), n = 6		n > 5 %	n > 10 %
PLA	**0.005**	ND	ND	350 ± 1.5	0	0
B4	**0.027**	484.7 ± 9.4	5.408 ± 0.151	283.8 ± 9.3	1	0
B5	**0.041**	496.5 ± 6.5	5.433 ± 0.295	291.4 ± 9.2	1	0
B1	**0.044**	496.0 ± 9.7	5.225 ± 0.261	306.1 ± 11.5	3	1
B6	**0.072**	505.5 ± 8.7	5.408 ± 0.600	311.9 ± 17.7	7	1
B7	**0.082**	515.5 ± 11.4	5.700 ± 0.892	307.5 ± 21.4	8	3

Finally, the impact of diameter variations on mass uniformity of 3D-printed DDS was investigated. Since FDM^{TM}-printer use a fixed filament diameter, regardless of its variation, for the calculation of the feed rate in the G-Code, it was expected that higher filament diameter IQR will cause reduced mass uniformity of printed objects. To what extent was examined in the following.

Therefore, the uniformity of mass of 20 rectangular test objects (3 x 15 x 7 mm, infill density 85 %, ~ 300 mg, Figure 42) was tested using the same filaments with different diameter IQR (extruded with different SFLs, B1, B4-B7) as well as commercial PLA filament for comparison purposes. The results were evaluated according to the Ph. Eur. monograph 2.9.5 “Uniformity of mass of single dose preparations” [192]. As requirements the thresholds for tablets ≥ 250 mg were chosen, as no specifications for parenteral solid compact dosage forms are listed. Test objects were printed with the settings described in Table 28 (section 5.3.3). For the 3D-printed geometry approx. 13 cm of

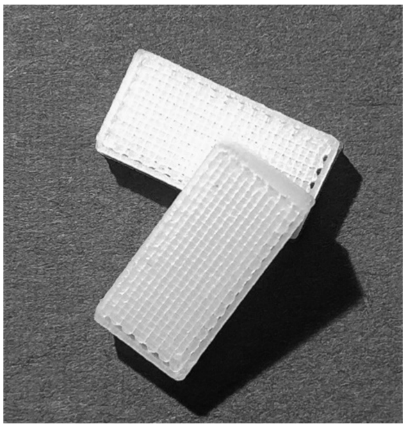

Figure 42. Picture of printed objects (3 x 15 x 7.5 mm, infill density 85 %) using in-house produced filaments F13 for the evaluation of uniformity of mass according to Ph. Eur.2.9.5 (adopted and modified from Ponsar et al. [183].

filament was required, corresponding to 2.6 m in total of filament per batch. Filament sections for printing were taken from the whole filament length to ensure representative results.

In Figure 43A, the results of obtained mean masses of 3D-printed objects for the respective filaments are shown. As visible, the mean mass is not considerably affected by diameter variations. Still, a slight trend towards higher masses with higher diameter IQR ($\text{IQR}_{\varnothing}$) was noted. Filaments produced with higher SFL (B4, $\text{IQR}_{\varnothing}$ = 0.027 mm and B5, $\text{IQR}_{\varnothing}$ = 0.044 mm), were fabricated on different days. The mean mass could therefore be changed by a required reassembly of the print-head in between. A different gap width between conveying gears might have resulted, potentially leading to different feeding properties and deviating mean masses.

In Figure 43B, the CoV_{mass} as function of diameter IQR is depicted. Although the CoV_{mass} of filaments B4 and B5 with the lowest $\text{IQR}_{\varnothing}$ is biased by the lower mean mass due to the mentioned print-head reassembly, a clear trend is visible. A diameter IQR above 0.044 mm led to a sharp increased CoV_{mass} of 6 and 7 %, which is not acceptable to ensure content uniformity of 3D-printed dosage forms. Filaments B1, B4 and B5 ($\text{IQR}_{\varnothing} \leq 0.044$ mm; $\text{CoV}_{\varnothing} < 2$ %) resulted in mass variations of printed test geometries < 4 %.

According to Ph. Eur. 2.9.5 for tablets ≥ 250 mg only two individual masses may deviate by more than 5 % and none by more than 10 % from the mean value. The evaluation revealed that only the test objects produced from filaments with an $\text{IQR}_{\varnothing} \leq 0.041$ mm (B4 and B5) passed the test (Table 7). Whereas the others - produced from filaments with higher $\text{IQR}_{\varnothing}$ (≥ 0.044 mm) - did not comply with the requirements of the Ph. Eur. In case of filament B7 produced with an SFL of 0.02 ($\text{IQR}_{\varnothing}$ = 0.082 mm), eight 3D-printed objects deviated more than 5 % and three by more than 10 %. Although the filaments produced with an SFL of 0.04 and 0.059 showed significant differences in the diameter variations ($\text{IQR}_{\varnothing}$ = 0.041 mm vs. 0.027 mm; $\text{CoV}_{\varnothing}$ = 1.76 vs. 1.07 %) the CoV_{mass} of the respective printed objects were similar. This is potentially caused by the selected printing settings or selected filament sections. Optimizations might lead to further improvements and enable

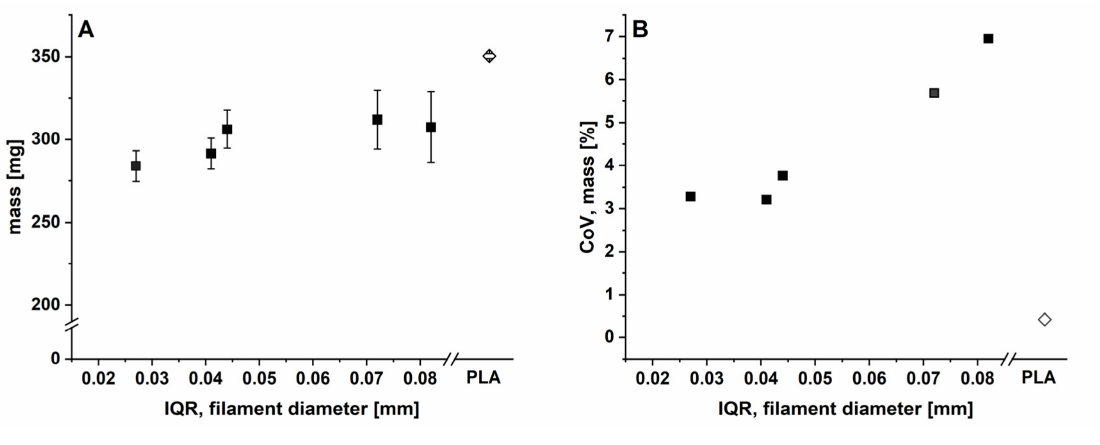

Figure 43. A = mass of printed test geometries (n = 20, mean ± s) of in-house produced filaments with different diameter variations (IQR); B = Resulting CoV_{mass} as function of filament diameter IQR.

visibility of potential differences at even lower $\mathrm{IQRs}_{\text{Ø}}$. In comparison, the CoV_{mass} of printed test objects produced with commercial PLA filaments with highly consistent diameter ($\mathrm{IQR}_{\text{Ø}}$ = 0.005 mm) was considerably lower with 0.5 %. This showed the high precision of the used printer, enabling the production of even higher quality dosage forms if filament diameter consistency and print settings are further improved.

Based on these results it can be concluded that at least for this formulation and set-up, an SFL > 0.04 is required during twin-screw HME for filament fabrication. Thereby, filaments with sufficient diameter homogeneity with an $\mathrm{IQR}_{\text{Ø}} \leq 0.041$ mm and $\mathrm{CoV}_{\text{Ø}} < 1.76$ % are obtained with consistent mechanical resilience leading to 3D-printed DDS compliant with the requirements of the Ph.Eur regarding uniformity of mass. Larger variations can affect their quality distinctly and should be avoided. Specifications for produced filaments must be set accordingly. The presented study discovered that a well-described filament with respect to diameter is of high importance to draw right conclusion and to guarantee the quality of filaments and 3D-printed dosage forms. Offline measurements via callipers are consequently not sufficient to describe variations correctly, as often presented in publications [32, 40, 48].

3.2.4 Transfer of Optimized Continuous Filament Production to Different Formulations

In the previous subchapters, an optimized extrusion set-up and process settings were established for the continuous production of filaments with sufficient quality using an exemplary drug-free formulation (F13). The transferability of these findings to filament formulations F6 (drug-free) and F11 and F12 (TA-loaded, HPMC 15 % and HPMC 25 %) shall be investigated. Therefore, indicated formulations with batch sizes > 400 g were manufactured at 190 °C according to the developed process (PFR = 5 g/min; screw speed = 20 rpm; SFL = 0.057-0.059; haul-off speed: 2.0-2.1 m/min). Beforehand, as consequence of the intended reduction of the barrel temperature in the liquid feed section from 120 °C to 80 °C (Temperature zone 3) to prevent early TEC evaporation, the screw configuration was again adjusted as shown in Figure 44. The KBs have been shifted to keep

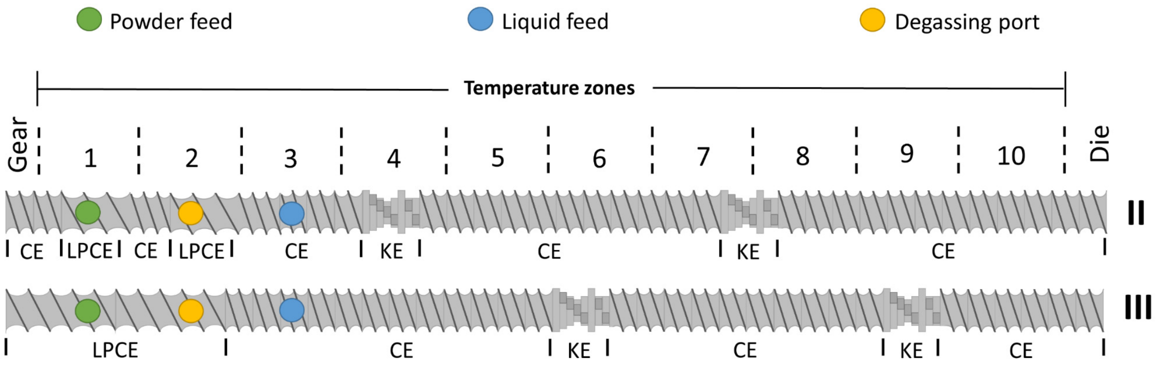

Figure 44. Schematic depiction of adapted HME screw configuration III compared to screw configuration II used during process optimization. Barrel and temperature zones (1-10) are indicated. LPCE = long pitch conveying elements (helix of 3/2 L/D), CE = conveying elements (helix of 1 L/D); KE = kneading elements.

extrusion temperatures as applied before. The exact temperature and haul-off speed settings during extrusion can be found in Table 27 (refer to section 5.3.2.2).

In Figure 45A, the inline-determined diameter for the respective filament is displayed as boxplot. The achieved mean values were 1.736 ± 0.027 mm for the drug-free formulation (F6) and the TA-loaded formulations 1.771 ± 0.029 mm (F11, HPMC 15 %) and 1.739 ± 0.023 mm (F12, HPMC 25 %). The diameter of F11 was slightly larger due to the slower haul-off speed of 2.0 m/min compared to the other two formulations, where 2.1 m/min was used. Since the diameter in the slicer software will be adjusted individually prior 3D-printing of implants, this does not affect the printed object quality.

As indicated, the $\mathrm{IQRs}_{\varnothing}$ were low and comparable to the results obtained during process analysis in section 3.2.3.3. Applying an SFL > 0.04 during extrusion, high diameter consistencies for drug-free and drug-loaded formulations were successfully achieved. Small diameter variations occurred as exemplarily depicted in Figure 45B for F12 due to the already discussed reasons in section 3.2.3.3. The slightly changed screw configuration did not affect the expected diameter quality but plasticizer evaporation could be improved. Obtained diameter data were below the specified values ($\mathrm{IQR}_{\varnothing} \leq 0.041$ mm) and transferability was demonstrated for EC-based formulations, independent from excipient ratios. High-quality filaments were produced for subsequent printing of customizable implants according to the design concept shown in section 3.1.2.

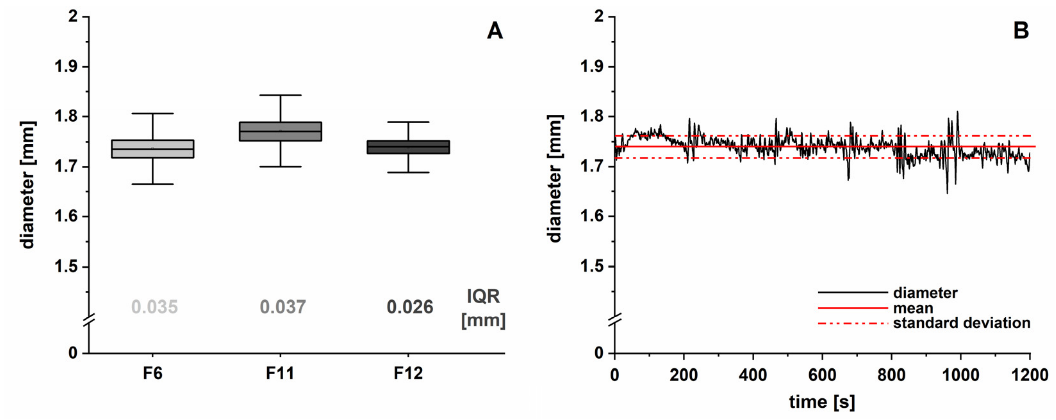

Figure 45. Inline-determined filament diameter. A = Boxplots and indicated IQR for F6, F11, F12 (n > 1218; B = Exemplary diameter data as function of extrusion time for F12 with indicated mean diameter and standard deviation.

A throughput of 5 g/min or 300 g per hour corresponds to a filament length of approx. 120 m/h. Assuming a dosage form weight of 300 mg corresponding to 30 mg TA, the amount is suitable for the printing of ~ 920 DDS. This can be easily upscaled by longer process runs, but also using a doubled PFR of 10 g/min by keeping the SFL constant as shown in section 3.2.3.3. Thereby, the production time and cost of goods can be further decreased.

The studies and obtained results are an important step towards the industrial continuous production of drug-loaded filaments using the QbD-approach.

3.2.5 Triamcinolone Acetonide Content Distribution

3.2.5.1 Drug Distribution along the Filament

Next to filament diameter homogeneity, the drug distribution along the filament is decisive to ensure content uniformity throughout 3D-printed customizable implants. As F11 and F12 with a TA load of 10 % were chosen as appropriate formulations for printing of the drug-loaded part of the implants, drug analysis was performed for both. Filaments were produced as described in the prior subchapter 3.2.4. The whole sampled filament length was approx. 310 m for F12 and 615 m for F11 after reaching process equilibrium. Obtained filaments were split into three sections corresponding to beginning, middle and end of the extrusion process. Two samples per section were analysed. Filament sections were further used for stability analysis as described in section 3.2.6. TA content of filament samples (~ 200 mg) was determined via UV-spectroscopy at a detection wavelength of 238 nm. The results are shown in Table 8. No obvious difference between the respective sections for both filaments was observed. A homogenous TA distribution along the filaments was assumed, indicated by the low standard deviations (1.03 % for F11 and 1.06 % for F12). This was already expected based on the confocal Raman microscopic images in section 3.1.5.3.1 and herewith confirmed.

Table 8. TA content [%] determination of filaments F11 and F12 at the beginning, middle and end of sampled length.

Filament	Sample	Beginning	Middle	End	mean ± s, (n = 6)
F11 (15 % HPMC)	1.	95.06	94.51	95.89	95.66 ± 1.03
	2.	94.91	97.30	96.25	
F12 (25 % HPMC)	1.	91.10	90.58	92.61	91.62 ± 1.06
	2.	91.62	90.65	93.16	

In both cases, a TA content below the label claim was found. The highest underdosed amount was 5.49 % for F11 and 9.42 % for F12. Thermal degradation is excluded as potential reason, since the API is stable until 294 °C, also confirmed via performed DSC analysis (section 3.1.4.2.1). This was further supported by subsequent performed high performance liquid chromatography (HPLC) analysis (refer to section 3.2.6.4), where no additional peak was found.

Several aspects appeared reasonable to cause the underdose. First, the micronized API tends to adhere to the glass mixing vessel wall due to electrostatic forces. Therefore, the TA content of three different powder mixtures right after blending was determined (n = 3, Figure 46). The assumptions were verified as high standard deviations were obtained. However, representative sampling was not possible, potentially due to agglomeration of micronized TA during mixing, indicated by the varying standard deviations. Therefore, tendencies are hard to interpret. Pre-blending of TA with fumed silica was not successful to avoid this. An additional segregation was considered likely due

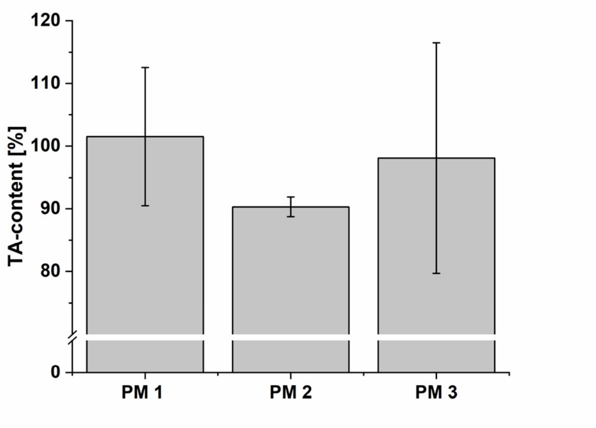

Figure 46. Exemplary content determination of different F12-powder mixtures (PM; n = 3; mean ± s).

to large differences in determined particle size of the different powder constituents as depicted in Table 9 (n = 3). This is described particularly as cause for this phenomenon [193, 194] and was already systematically investigated by Korte [109]. The author assumed a drug deposition in dead zones at the bottom of the feeder in combination with wall adherence to the mixing vessel and feeder, as drug homogeneity along the filament was also not affected. Potentially formed TA agglomerates showed also no impact on drug distribution as previously shown, as result of the intensive mixing capacity of the twin-screw HME counterbalancing observed inhomogeneities [195].

Table 9. Determined particle size [µm] of powder raw materials used for F11 and F12 (n = 3, mean ± s).

Substance	x_{10}	x_{50}	x_{90}
TA	**1.6 ± 0.3**	**8.2 ± 0.9**	**82.4 ± 4.4**
EC	**71.6 ± 13.8**	**279.8 ± 65.2**	**579.6 ± 74.6**
HPMC	**26.0 ± 0.3**	**86.9 ± 0.39**	**170.0 ± 1.8**

Secondly, the liquid plasticizer was fed at low LFR via a peristaltic pump. The feed rate was externally, gravimetrically calibrated. Discrepancies during extrusion could not be monitored via the flow sensors (the available Coriolis force sensor) due to the low feed rate and could potentially influence the filament content as well. In industrial environment, prevention of underdosing is necessary to ensure the target content, which could be enabled via split feeding, granulation, or impregnation of carrier material, depending on material characteristics (flowability, particle shape, etc.) or equipment adaptions for adherence reduction. The application of more precise pump systems and flow sensors supposed to be resolve assumed inaccuracies of plasticizer feed.

For the following studies, the TA content was considered acceptable since the reduced amount can be remedied via adaption of the printed geometries and reflected during dissolution studies. Directly after production the TA content of each filament batch was determined and considered for further studies.

3.2.5.2 Content Uniformity of 3D-printed Test Objects

To investigate the influence of obtained drug distribution along the filament on content uniformity and printing homogeneity, 3D-printed dosage forms were analysed according to Ph. Eur. 2.9.6 “Uniformity of content of single-dose preparations” Test A [196] and 2.9.40 “Uniformity of dosage units” [197]. Test objects as depicted in Figure 42 (section 3.2.3.4) were printed using filaments F11 (HPMC 15 %) and F12 (HPMC 25 %). The simplified geometry was selected as surrogate for drug-loaded implant inlays. In total 10 rectangular test objects were produced via FDM^{TM} for the respective formulation and the content was determined via HPLC (section 5.5.12.3). Printed objects were investigated as described in the experimental part 5.5.13.

According to Ph.Eur. 2.9.6 Test A the dosage form complies if the individual content of samples are between of 85 and 115 % of the mean content [196]. Test objects printed with F11 and F12 complied as individual contents were 95.57-104.92% and 89.50 -105.78 % of the respective mean content.

To meet the requirements for content uniformity according to Ph. Eur. 2.9.40 the calculated acceptance value (AV) must be below 15. The target content for the evaluation was based on the prior determined TA concentrations of filaments to investigate the impact on content deviation along the filament and printing homogeneity.

In Figure 47, the results for the TA content of printed test objects and AV are shown. Considering the requirements of Ph. Eur. 2.9.40 content uniformity could be assumed for both formulations. 3D-printed test dosage forms F11 showed an AV of 8.04 and F12 of 7.29, far beneath the specified threshold limit of 15 (dashed light-grey line). The AV indicates low variation of investigated samples and consequently sufficient printing accuracy. The high TA-recovery after printing confirmed additionally that the second heating step does not affect TA stability within the formulation. Both filaments showed therefore next to diameter homogeneity and mechanical properties, also a homogenous TA distribution along filaments to produce reliably uniform 3D-printed implants.

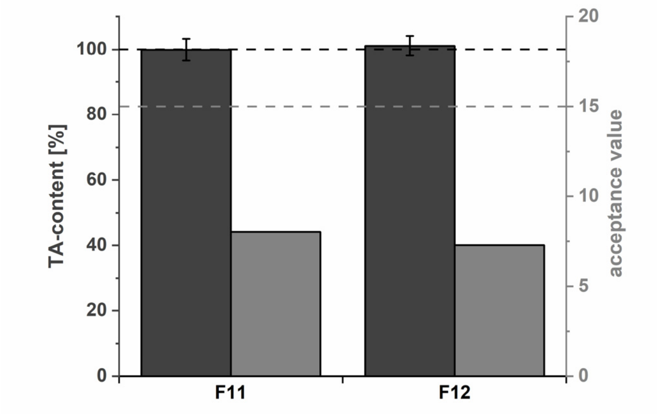

Figure 47. Content uniformity according to Ph. Eur. 2.9.40 of 3D-printed test objects using TA-loaded F11 and F12 as starting material. TA content of test objects (n =°10, mean ± s, dashed dark grey line indicates target content) and calculated acceptance value (dashed light grey line marks the upper threshold limit) are depicted.

3.2.6 Stability Analysis of Filaments according to ICH Guideline Q1A (R2)

3.2.6.1 Pretext

The establishment of on-demand manufacturing of personalized medicines via FDM^{TM} -printing in community pharmacies or hospitals presupposes the availability of drug-loaded filaments. The potential of this approach relies on the mass-production of stable, reproducible and dose-consistent filaments by the pharmaceutical industry. The physicochemical stability in appropriate primary packaging must be maintained during storage. Potentially identified instabilities are mainly physical ageing of the polymers and API-degradation. Further absorption of water or evaporation of the liquid plasticizers over storage could lead to a change of properties affecting both CQAs, content uniformity and mechanical resilience.

This part of the work focused on the stability analysis of developed filament formulations over six months according to the ICH guideline Q1A (R2) [198]. The exact experimental procedure can be found in the experimental part (refer to section 5.6). The overview of the stability testing regime is shown in Table 10. The drug-free formulation (F6), which will serve as impermeable, shape-customizable part and the two TA-loaded EC-based formulations, with 15 % or 25 % HPMC (F11 and F12) were investigated. All formulations were stored either controlled at RT without humidity control or under controlled accelerated conditions (40 °C, 75 % rH).

Table 10. Stability testing regime of filaments (T0 = start point, T0.5 = 2 weeks, T1 = 1 month, T3 = 3 months, T6 = 6 months).

	Formulation	Measurement points	F6	F11	F12
Test parameter	Solid-state properties	T0, T1, T3, T6	✓	✓	✓
	Mechanical properties	T0, T0.25 T0.5, T1, T3, T6	✓	✓	✓
	API content	T0, T1, T3, T6	-	✓	✓

To investigate the influence of the primary packaging, each filament formulation was stored open (unpacked) in water-permeable, unsealed polyethylene bags or “packed” in sealed moisture-impermeable aluminium sachets. The results of unpacked samples stored at RT also provide information about the in-use stability of filaments as they might be used for on-demand printing of multiple dosage forms [199]. Potential changes in mechanical and solid-state properties, as well as TA content of the different formulations were therefore elaborated.

3.2.6.2 Solid-State Properties

DSC measurements of produced filaments were conducted within the stability study according to Table 10. Thereby, a potential change of solid-state properties during storage under different conditions was analysed. The DSC settings can be found in section 5.5.9.

Physical ageing of amorphous polymers over storage is well known in literature [163, 200]. This phenomenon can be described by the free-volume theory [201]. During extrusion amorphous polymers are heated up above their T_g and soften. While cooling the finished product, it undergoes a change from a rubbery to a glassy state at its T_g. Here the molecular mobility (rotation and translation) reaches a steady-state [202]. This is caused by a decreased free volume, defined as “free space” between the molecules. However, below the T_g the polymer is in a metastable state at a certain temperature and exhibits an increased free volume, enthalpy and entropy compared to the thermodynamic equilibrium. In this state, they undergo a slow transformation towards equilibrium by polymer contraction [202]. This process is called physical ageing in which the free volume reduction is accompanied by a further decrease of molecular mobility responsible for structural near order changes until the lowest enthalpy is achieved. Consequently, this affects potentially mechanical properties (stiffness and brittleness). Temperature, humidity and additional excipients have a distinct impact on the ageing process and other CQAs of filaments [200].

The physical ageing process and accompanied structural changes can be analysed in DSC thermograms as enthalpy relaxation, visible as endothermic event around the T_g. During heating of aged polymers, the relaxed enthalpy changes to the equilibrium value of the rubbery-elastic state during the glass transition [203]. This exhibits a maximum in the glass transition region and its magnitude depends on annealing time and temperature. The enthalpic relaxation corresponds to the area of the overshoot, which increases with increasing time for isothermal ageing until the equilibrium is achieved [204].

Figure 48 shows exemplarily the results for F12 for the different time points (T0, T1, T3 and T6). The data of the other formulations showed comparable behaviour and can be found in the appendix (Figure A1 and Figure A2).

For the unpacked samples (Figure 48, left), especially stored at higher relative humidity, an absorption of water was observed, visible as broad endothermic event due to evaporation above 80 °C. Due to the lower humidity, this was not as pronounced in the RT samples but still visible. Packaging in sealed impermeable aluminium foils could prevent strong water incorporation, protecting from moisture.

For all samples, an enthalpy recovery peak was observed, triggered by physical ageing and embrittlement in dependency of annealing temperature below the T_g and time [163, 167, 202]. Samples stored packed at 40 °C under accelerated conditions (Figure 48, DSC thermogram top right) showed a shifted position of the glass transition event and the enthalpy recovery peak after T1, caused by the different annealing temperature compared to the RT samples [205]. The enthalpy relaxation in samples stored unpacked under accelerated conditions is likely covered by the water evaporation event. The key factor for observed differences in enthalpy relaxation is the annealing/ storage temperature independent from packaging and consequently humidity. How it will affect the ductility of developed formulations will be evaluated in section 3.2.6.3.

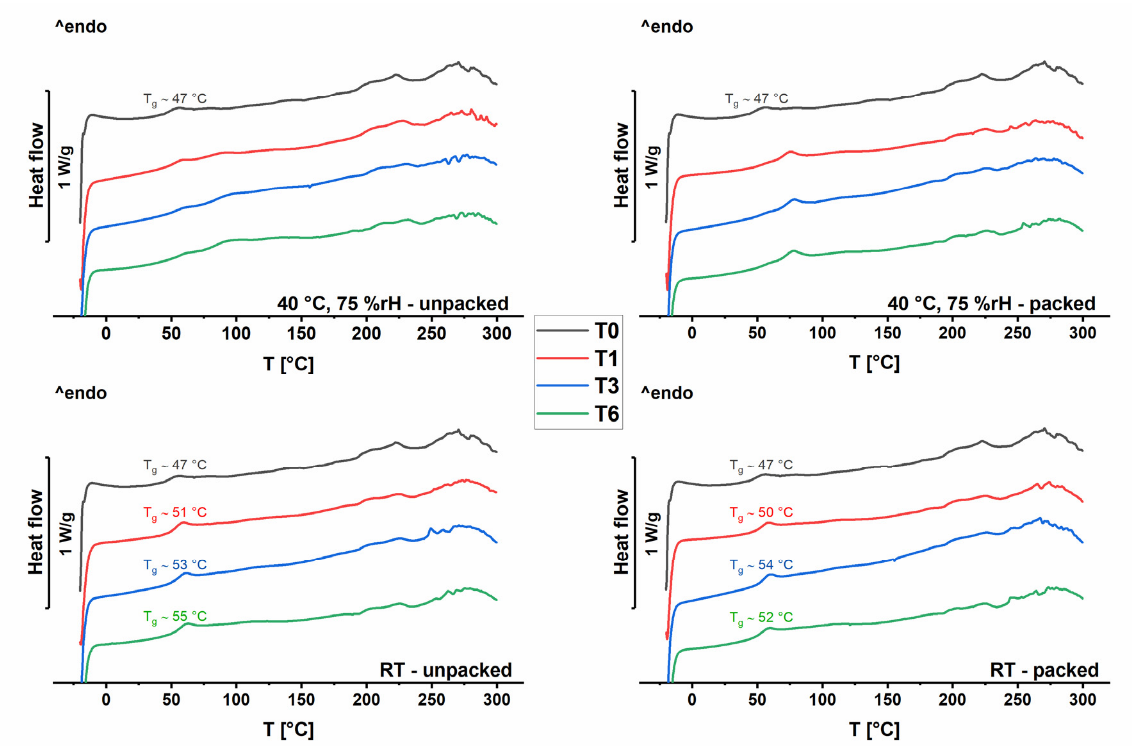

Figure 48. Recorded DSC thermograms of F12 samples unpacked (left) and right (packed) during stability-testing T0-T6. Top: stored under accelerated conditions; bottom: stored at 21 °C (RT). The T_g for T1-T6 were only indicated for samples stored at RT, as reliable determination of samples stored under accelerated conditions was not possible.

As the relaxation peak seemed not to increase further, physical ageing appeared to be nearly accomplished within T1. Further changes in mechanical properties or filament content can be most likely assigned to plasticizer evaporation or absorption of water depending on the storage conditions. A shift in glass transition was hard to interpret due to a superimposition of the T_g and events like water absorption, baseline shift, as well as shift in enthalpy relaxation especially for samples stored under accelerated conditions. However, it was exemplarily conducted for RT samples, where it seemed most reasonable. The T_g shifted slightly towards higher temperatures (T_g T0 ~ 47 °C, unpacked (RT): T6 ~ 55 °C and packed (RT): T6 ~ 52 °C). The increase was potentially induced by the physical ageing process in combination with potential plasticizer evaporation resulting likely in reduced elasticity over storage time. The concurrent water absorption and resulting plasticizing effect limits potentially a further increase of the T_g [206].

To investigate if the made assumptions related to plasticizer evaporation are correct, a dynamic vapor sorption system was used as described in section 5.5.11. Therefore, the mass change of raw materials (EC, HPMC and TEC) and filaments F6, F11 and F12 under static conditions at 40 °C was investigated over 21 days. A low relative humidity of 40 % was chosen to reduce the impact of simultaneous water absorption.

Figure 49, reflects what was previously assumed related to plasticizer evaporation. The liquid plasticizer TEC clearly showed a decrease by more than 1.5 % over three weeks, revealing evaporation at 40 °C, although the stated boiling point by the manufacturer is around 290 °C. A steady weight gain of EC and HMPC over time was observed due to their hygroscopicity and subsequent water absorption. This explains the mass loss of filaments formulation induced by plasticizer evaporation, superimposed by additional water absorption.

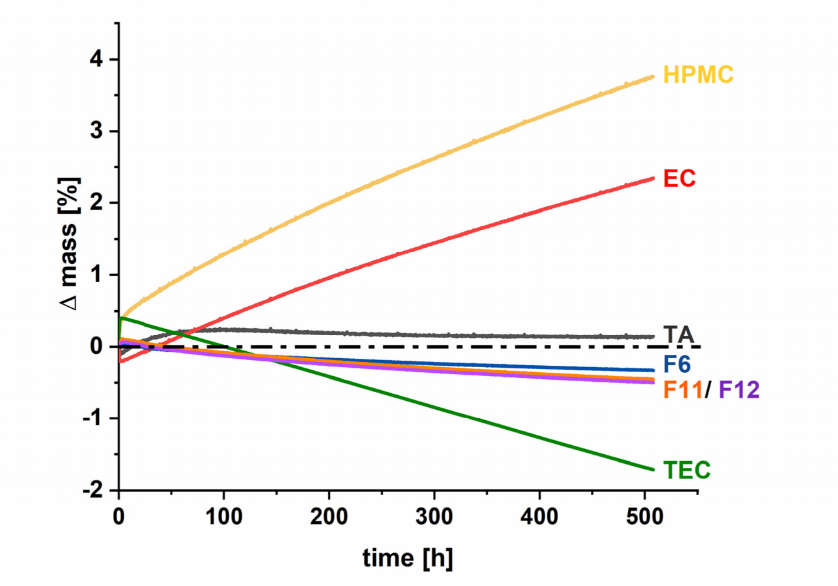

Figure 49. Change of mass of raw materials and filament formulations F6, F11 and F12 as function of time at 40 °C and 40 % rH.

3.2.6.3 Mechanical Properties

Based on the previous results, it was expected that extruded filaments are potentially affected related to their brittleness and stiffness in dependency of storage conditions. This is specifically of technical importance regarding printability and practical handling during the long-term usage of filaments. Therefore, the YM and the DaB were determined over six months (Table 10) according to section 5.5.7.

An influence on the mechanical properties depending on the storage conditions was noticed (Figure 50). Over time temperature and humidity had a distinct effect on filaments stored unpacked, while packed samples showed reduced, or no changes in dependency to the respective exposure.

Related to the YM as surrogate for the filament's stiffness, formulation F6, F11 and F12 showed a comparable behaviour/trend over storage time (Figure 51, left). The extent was dependent on the composition.

All filament formulations stored packed showed no major change in stiffness of practical relevance over the investigation period regardless of the storage conditions. All investigated filaments got slightly stiffer within six months (e.g., F11 T0; T6, $p < 0.01$; both storage conditions), potentially induced by the demonstrated plasticizer evaporation, superimposed by physical ageing effects.

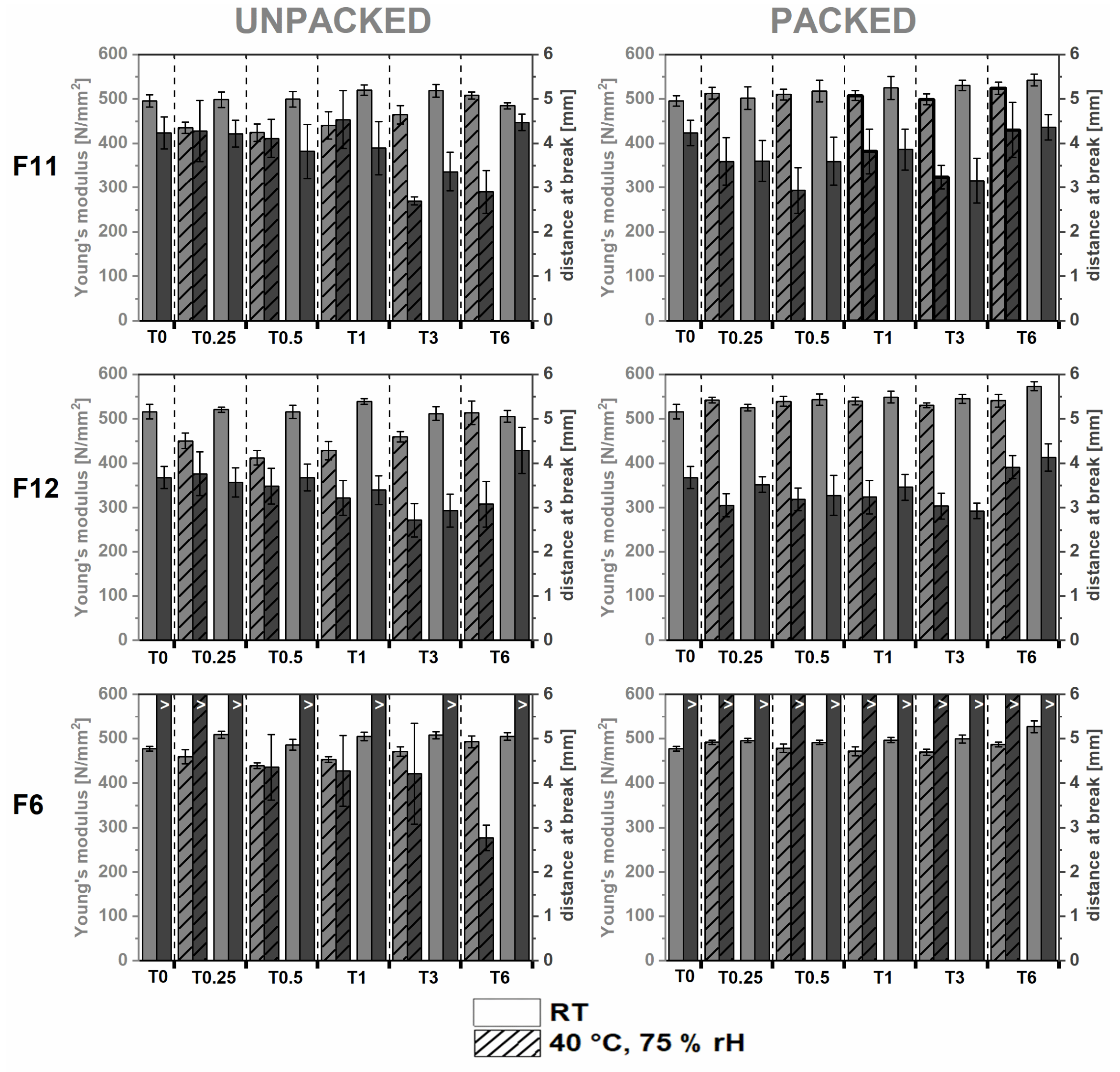

Figure 50. Influence of storage conditions on the mechanical properties (YM and DaB) of filaments over six months (n = 6, mean ± CI (α = 0.05)). Filaments that did not break under a travel depth of 19 mm during the 3PBT are marked with ”>”.

Under accelerated conditions the YM of F11 and F12 stored packed reached interestingly already a plateau after one week and in total a lower increase in stiffness compared to the RT samples (Figure 51, left). The storage only little below the T_g (~ 47 °C) might have led to a curing effect, reaching faster the thermodynamic equilibrium and freezing thereby the current status [163]. The YM of F6 stayed nearly constant under accelerated conditions.

Stiffer filaments show no disadvantage with respect to printability, consequently although significant changes (> 5 % from the initial value) according to the ICH-Guideline Q1A (R2) were found, this property was not negatively affected [198]. With a standardised post-processing curing step the differences might be circumvented.

The unpacked samples of F6, F11 and F12 stored at RT showed a comparable trend for the YM as packed samples. But in contrast after T3 the YM of F11 and F12 started to decrease towards the T0

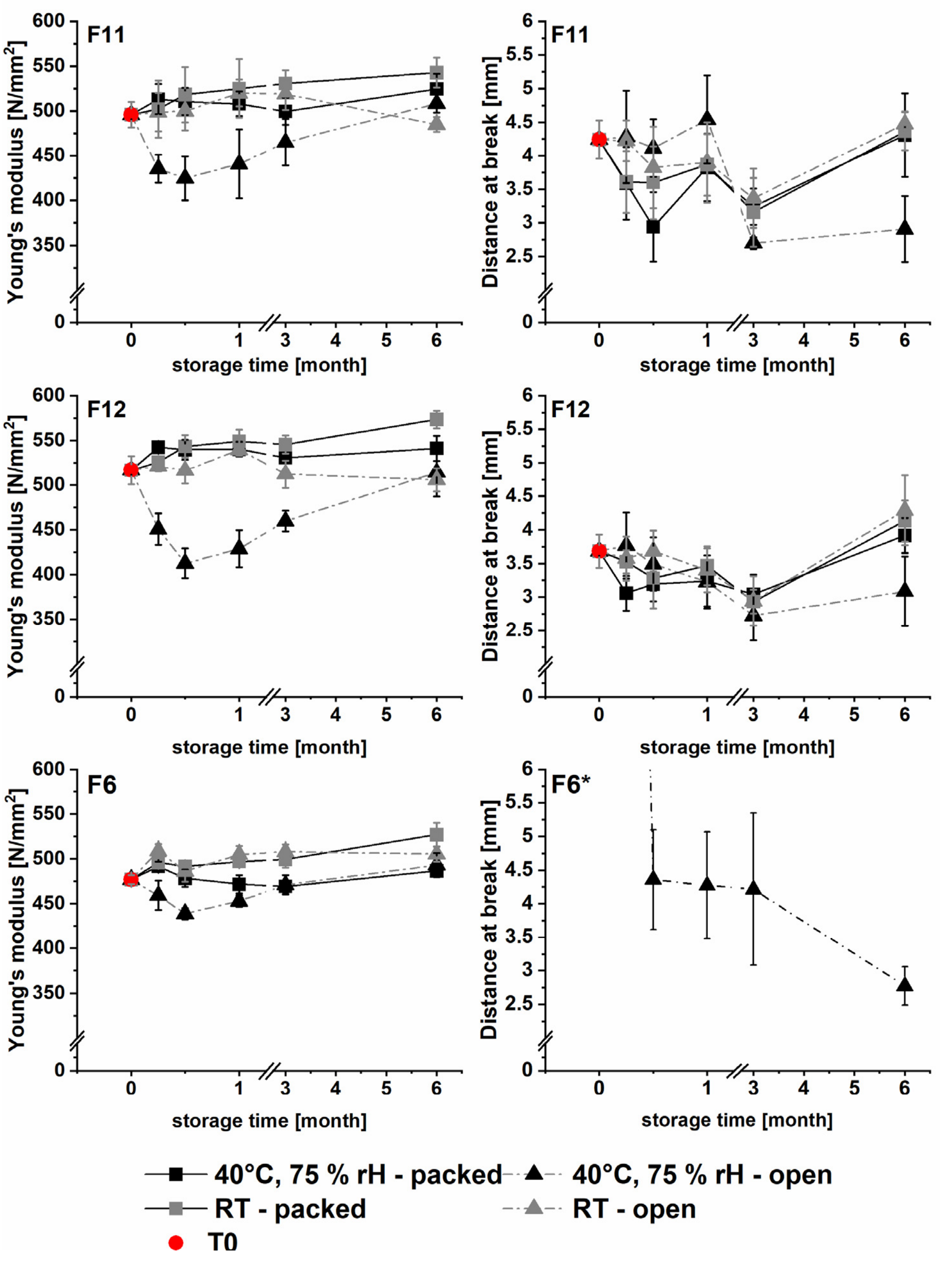

Figure 51. Determined YM (left) and DaB (right) of formulations as function of storage time (n = 6, mean ± CI (α = 0.05)). * Storage conditions, which did not lead to breakage (DaB) for F6 are not shown.

value (e.g., F12 T0 = 516.7 ± 19.9 N/mm^2; T6 = 505.9 ± 16.3 N/mm^2). The flexibility likely increased due to observed water absorption (Figure 48 and Figure 49) and its plasticizing effect during storage [206]. Filaments were stored in a climatic room without humidity control. Hence, throughout the summer months (T4-T6) an increase of the relative humidity likely led to this result. Also, for the open storage at RT the observations were not of practical relevance, as the YM after six months was still close to the start value of 500 N/mm^2, where printability was proven. This is additionally beneficial in terms of in-use shelf-life after de-packaging over six months.

Filaments stored unpacked under accelerated conditions showed the highest changes, as expected. Until T0.5 a sharp drop of the YM was observed for F6, F11 and F12, likely as result of water absorption at high relative humidity. After one month, the YM started to increase again towards the

T0 value. One reason could be the evaporation of the liquid plasticizer at higher temperature, dominating physical ageing effects assumed for packed samples [134, 147]. More plasticizer was evaporated compared to packed samples, where a closed system limited the evaporation due to saturation. A simultaneous water absorption due to the higher relative humidity is again likely.

Overall, the extent of the YM change during storage was less pronounced for the drug- and HPMC-free formulation F6 and strongest for F12. Higher amounts of HPMC, as present in F12, might lead to a higher absorption of water, due to higher hygroscopicity compared to the HPMC-free formulation F6 as visible in static vapor sorption measurements (Figure 49).

Related to the DaB as surrogate for filament brittleness, a conclusive trend depending on storage conditions was noticed (Figure 50, Figure 51, right), although in general high data variability was observed. For the drug-free formulation (F6) over storage time no break occurred under the applied testing regime, except for the filament stored unpacked under accelerated conditions (Figure 50). A breakage of filaments appeared after two weeks with high deviations and stayed constant until T3 ($p = 0.842$). After six months a decrease to 2.775 ± 0.357 mm was determined, due to the mentioned physical ageing and plasticizer evaporation. An influence of water absorption was not noticed affecting the DaB.

For the drug-loaded formulations F11 and F12 stored unpacked under accelerated conditions, correspondingly an increased brittleness was observed within three months ($p \ll 0.01$) and did not change further ($p > 0.297$).

In comparison, for formulations stored either packed or open at RT again a similar behaviour was observed. Until T3 a marginal decrease of the DaB was visible. Interestingly afterwards the DaB started to increase again regardless of the packaging towards the T0 value. The observed plasticizer evaporation affecting the stiffness did not influence the brittleness in transversal direction.

Although changes were observed, a loss of printability during further studies was not expected during storage at 21 °C. The overall stability of developed formulations was sufficient for a shelf-life period of at least six months. The packaging of filaments in heat-sealed aluminium sachets seemed to be beneficial for the preservation of the mechanical stability. Additionally, the use of a different plasticizer might be an option to avoid mechanical changes due to plasticizer evaporation.

3.2.6.4 Content of Filaments Over Storage

The content specifications are an important quality attribute to consider during shelf life. To ensure the therapeutic effectivity of the intermediate product and subsequent printed dosage forms, the content and its uniformity were investigated for the drug-loaded formulations F11 and F12 according to section 5.6 over six months (Figure 52). T0 and T1 samples were measured via UV-spectroscopy. The method was changed to HPLC, enabling the detection of potential degradation products. For verification purposes, contents of T1 samples were measured with both methods. For the HPLC samples, a constant content reduction of about 2 % was observed. Thus, the comparison of the T0 values is slightly distorted by the method change and a conclusive statistical interpretation is not possible.

The general lower TA content of F11 (95.66 ± 1.03 %) and F12 (91.62 ± 1.06 %) was already discussed in section 3.2.5.1. After three months no distinct changes related to the content and its uniformity in dependency to storage conditions and packaging were observed. As cause of water absorption next to ongoing plasticizer evaporation a slight apparent change in content was observed. In all cases, differences were below < 5 %. HPLC analysis detected no decomposition products.

After six months, a major influence of storage conditions depending on the packaging was observed. For both filament formulations stored unpacked at 40 °C and 75 % rH an apparent higher TA content was found compared to T3 (F11 = 102.6 ± 2.30 %; F12 = 102.4 ± 0.99 %; $p << 0.001$) as cause of the TEC evaporation. This was also slightly visible for the F12 sample stored packed at elevated temperatures due to minor plasticizer evaporation (92.64 ± 1.96 %) in line with the results for the mechanical properties ($p <<0.01$). For the residual F11 samples no significant change between T3 and T6 was observed ($p > 0.093$), although a tendency towards lower contents was visible.

For F12, RT samples stored open a significant apparent decrease was observed ($p << 0.01$), likely as cause of the reported water absorption throughout the summer months. Interestingly, for the packed sample stored at RT also a slight decrease was visible.

Based on the results an instability related to API content was assumed unlikely as no degradation product was detected. The true content did likely not change under the tested conditions. But in

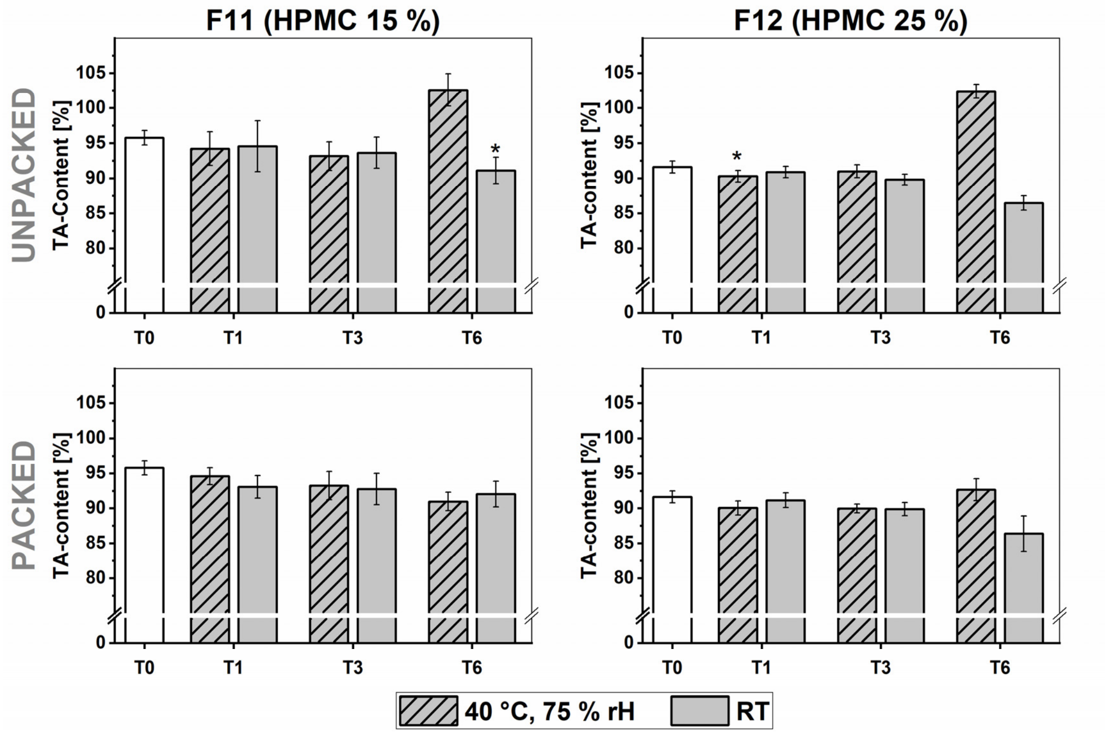

Figure 52. API content within stability testing of F11 and F12 over six months, stored under different conditions (n = 6 (*n = 5), mean ± CI (α = 0.05)).

case of unpacked samples during long-term storage a false higher content might be detected for filaments or 3D-printed dosage forms during quality control. The proper packaging of the starting material and FDM^{TM} is therefore mandatory to prevent misinterpretation and ensure safety and quality of individualized therapy.

3.2.7 Summary

In this part of the work, the systematic process development for developed filament formulations for 3D-printing of customizable implants and subsequent characterization inclusive stability analysis was covered.

The extrusion set-up was successfully optimized to obtain reliable and reproducible filament diameter via general adaptions and implementation of a winder. Thereby, the continuous manufacturing of a developed drug-free filament formulation was demonstrated.

The results of the systematic HME analysis discovered a significant impact of the SFL as surrogate for the barrel filling degree on the filament diameter homogeneity and subsequently the CQAs of filaments (mechanical properties) and 3D-printed test-geometries (uniformity of mass). Only SFLs > 0.04 resulted in a homogenous melt transport and consequently low diameter variations (IQR ≤ 0.041 mm) independent from the set PFR/ screw speed combination. The thereby achieved optimized filament diameter quality resulted in a low variation of the DaB and acceptable mass uniformity of 3D-printed test geometries according to the Ph. Eur.. Diameter variations > 0.041 mm (IQR) are not acceptable. The gained knowledge is of great importance related to throughput up-scale and simplified process development based on a QbD approach to ensure consistent quality of filaments and 3D-printed dosage forms.

The transferability of the optimized production conditions (SFL 0.057 - 0.059) for the drug-free formulation F6, as well as TA-loaded filaments F11 and F12, was demonstrated and used for their production with subsequent characterization.

Determined TA content of produced filaments F11 and F12 were below the target content (95.66 ± 1.03 % and 91.62 ± 1.06 %, respectively). Segregation as result of differences in particle sizes and agglomeration of the micronized TA, as well as adhesion to the used equipment were considered likely, whereas thermal instability was excluded. However, a homogenous drug distribution along the filament due to the extensive mixing capacity of the twin-screw HME was achieved. The target dose of 3D-printed dosage forms can be still obtained via size adaption considering the actual API content. 3D-printed test-geometries fulfilled the requirements according to Ph. Eur. 2.9.6 and showed a high printing precision according to Ph.Eur. 2.9.40 based on the filament content for both extrudates.

A stability analysis of filaments over six months stored at 21 °C and under accelerated conditions according to the ICH guidelines Q1A (R2) was performed to assess changes during shelf-life. Water absorption and plasticizer evaporation combined with physical ageing of amorphous polymers affected the mechanical properties and TA content depending on the storage conditions. The extent was dependent on the HPMC content. After six months, mechanical properties remained sufficient even under accelerated conditions to ensure printability of formulations.

Changes in TA content were induced by stated processes and likely reflect not true variations. A degradation of TA during shelf-life was suspected unlikely. Packaging of filaments in heat-sealed impermeable aluminium sachets was found to be beneficial to keep the initial quality of filaments.

3.3 Development of an Appropriate Dissolution Method for Long-term Dissolution Studies of 3D-printed Implants

3.3.1 Introduction and Objectives

The final goal of the thesis is the development of customizable implants based on the concept presented in section 3.1.2. The assessment of drug release of implants with different printed inlay networks over several months is therefore essential. A suitable analytical method is obligatory, enabling a precise TA quantification during extended-release studies, even after frequent medium change due to the low solubility of TA.

As glucocorticoids tend to degrade in aqueous dissolution media [207, 208], TA stability in the medium and dosage form must be guaranteed to ensure reliable and reproducible results during long-term studies. Hence, optimized conditions by testing different dissolution media and a protocol for the analytical conduction of drug release supposed to be implemented thereby.

In the Ph. Eur. and USP, no specified and standardized compendial dissolution method for the analysis of long-acting implants is described. Due to the high variability of parenteral depot DDS the establishment of standard methods remains challenging [209]. The assessment of *in vitro* drug release performance is crucial for quality control and discriminative analysis during product development [66, 210]. The high volume of the established apparatuses and the prevalent hydrodynamics limit an *in vivo* estimation. Commonly used techniques described in the literature are the so called “sample and separate” technique, USP apparatus IV (flow-through cell) and dialysis [211].

To assess the release kinetic of different 3D-printed implants, a suitable dissolution set-up covering a reduced volume, as present in the articular cavity, under sink conditions was aimed at. In addition, multiple different 3D-printed implants shall be investigated simultaneously, limiting the available options. Therefore, the chapter deals with the development of an appropriate “sample and separate” dissolution method meeting predefined requirements for the discriminative analysis of the different designed customizable TA-loaded 3D-printed implant network structures. A biorelevant dissolution set-up was not aimed at.

3.3.2 Analytical Development of an Appropriate Determination of Drug Concentration during Long-Term Release Studies of Implants

3.3.2.1 Preliminary Experiments

The driver of the TA stability studies in different dissolution media were the results of preliminary solubility experiments to maintain sink conditions throughout planned long-term dissolution studies. Therefore, solubility studies in the frequently used PBS at a tissue pH of 7.4 were performed at three different temperatures (37, 47 and 57 °C; refer to section 5.5.18). The TA concentration

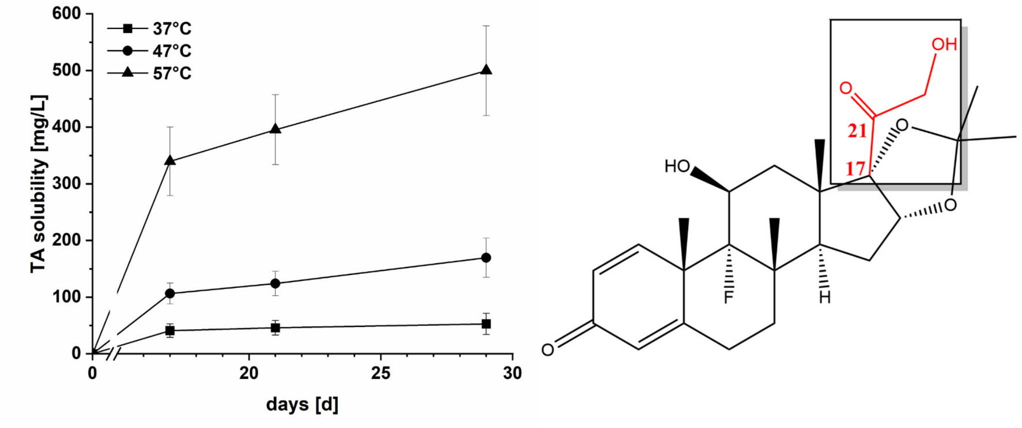

Figure 53. Left: TA solubility in PBS pH 7.4 at different temperatures as function of time (mean ± s, n = 3). Right: Chemical structure of TA with highlighted 17- side-chain sensitive for degradation.

was determined UV-spectroscopically and stopped after 29 days as no equilibrium at higher temperatures was reached (Figure 53, left). Although at 37 °C a steady state was achieved with 34.23 ± 1.08 mg/L, the result was higher compared to values specified in literature for TA (distilled water: 25.5 mg/L) [174]. Based on these results a degradation in the dissolution medium was hypothesized, although PBS has been commonly used [212-216]. A clarification was required to ensure reliable data collection during long-term dissolution studies.

Several oxidation-induced degradation products are described in the literature. The spontaneous transformation occurs predominantly at the C17-side chain of steroid's basic structure (Figure 53, right) [217-219]. As cause, trace metals – derived, e.g., as impurities from the manufacturing, extracts or leachable from primary packaging - in the presence of oxygen in buffers, depending on composition, pH and ionic strength, were discussed [208, 220]. However, the relevance of glucocorticoid decomposition during long-term release studies was not addressed, yet.

For verification of a potential degradation product formed during storage in PBS, HPLC-analyses were conducted (refer to section 5.5.12.3). Therefore, TA was dissolved in PBS and treated for 4 h in an ultrasonic bath and subsequently analysed. In the obtained HPLC chromatogram (Figure 54) compared to a TA reference sample (t = 0; prepared of ethanolic stock solution diluted in water)

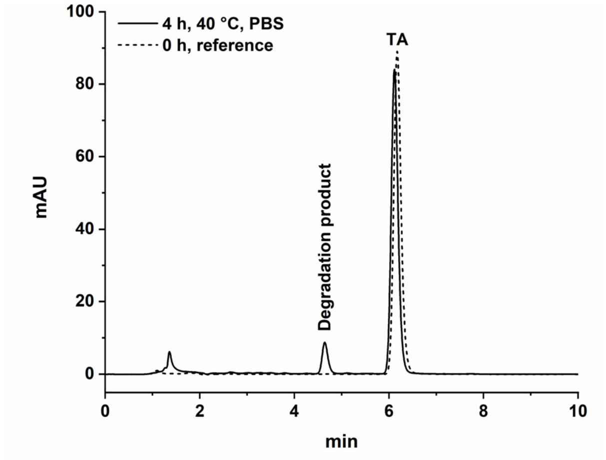

Figure 54. HPLC chromatograms of TA solutions (6 µg/mL) after t = 0 (reference, prepared of ethanolic stock-solution diluted in water) and t = 4 h (dissolved in PBS pH 7.4 and treated in an ultrasonic bath). UV detection at 241 nm (peak at ~ 1.3 min = solvent injection).

next to the TA peak (retention time (t_R) = 6.2 min) an additional peak at 4.6 min was detected. Hence, a degradation was confirmed.

TA-17-carboxylic acid and TA 21-aldehyde hydrate are the most described decomposition products in aqueous solution following an oxidative pathway [208, 219-221] (Figure 55). Latter is also described in the Ph. Eur. monograph of TA as impurity C [222]. During the planned studies of TA release of different 3D-printed implants, the quantification is prone to error if degradation occurs simultaneously. Simple UV-spectroscopy is not suitable for this matter. Consequently, systematic studies were mandatory to identify and quantify the degradation product to enable complete TA recovery during release studies. Further, the assessment of the extent and favouring conditions of decomposition was aimed at identifying potentially an improved analytical protocol.

For peak identification, an aqueous TA sample forced to degradation (treated 4h in an ultrasonic bath at 40 °C) was subjected liquid chromatography-mass spectroscopy (LC-MS) analysis (refer to section 5.5.17). The degradation product found at t_R of 4.6 min was clearly assigned to TA 21-aldehyde hydrate (impurity C) based on mass (*m/z* = 451.2). The corresponding chromatograms and spectra can be found in the appendix (Figure A3 and Figure A4). To further verify this, impurity C was synthesized as described in section 5.7 according to [223], since no pure European Directorate for the Quality of Medicines (EDQM) chemical reference standard (*CRS*) was available for additional analysis.

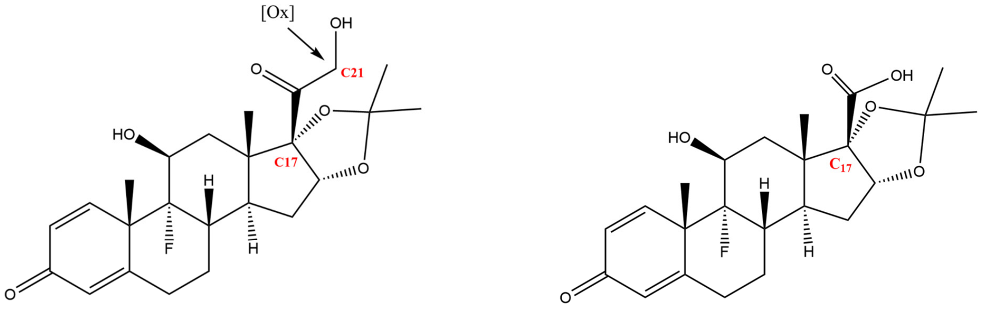

TA **TA 17-carboxylic acid**

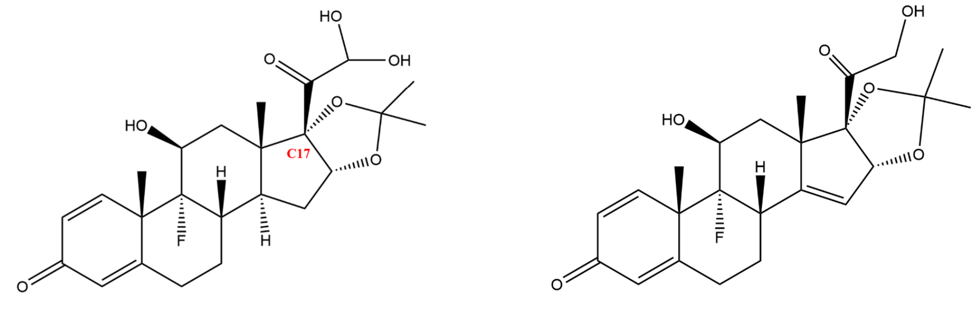

TA 21-aldehyde hydrate (impurity C) **Δ14-TA (impurity B)**

Figure 55. Chemical structures of TA and potential degradation products.

Figure 56, shows obtained HPLC chromatograms of a TA (I) and impurity C sample (II), compared to TA *CRS for system suitability* (III; containing TA, impurity C and impurity B (Δ-14-TA, Figure 55) in unspecified concentration). Based on this, the elution order was determined and impurity C eluted at t_R = 4.6 min, ultimately verifying previous results from LC-MS. The used HPLC method was able to detect TA and its main degradation product with sufficient resolution.

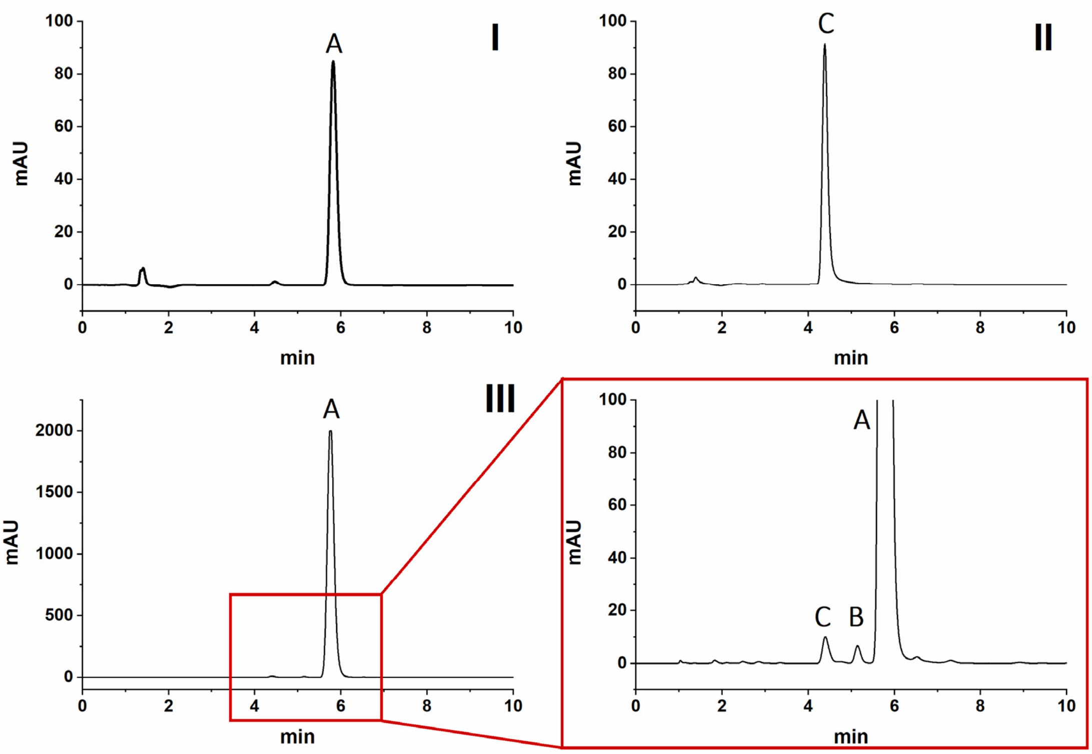

Figure 56. HPLC chromatograms of TA (I), synthesized impurity C (II) dissolved in PBS pH 7.4 (c = 6 µg/mL; injection volume 80 µL, UV detection λ = 241 nm) and TA *CRS for system suitability* in acetonitrile (ACN)/ water 60/40 V/V (c = 1 mg/mL, injection volume: 20 µL UV detection λ = 254 nm). Peak A = TA, peak B = impurity B (Δ-14-TA) and peak C = impurity C (TA 21-aldehyde hydrate).

3.3.2.2 Degradation Analysis of Triamcinolone Acetonide in Different Dissolution Media

A partial oxidative degradation of TA to impurity C in PBS and water was confirmed via the previously performed analyses. A medium-induced decomposition was therefore suspected. Different authors found for several glucocorticoids, including TA, a dependency of the used buffer system related to ionic strength, pH and salt concentration [207, 218, 224]. Oesterling et al. [208] and Bundgaard and Hansen [221, 225] hypothesized as already mentioned, trace metal contaminants as potential cause for prednisolone and hydrocortisone degradation. Buffer systems relevant for realistic pharmaceutical application at 37 °C were not examined.

Therefore, the degradation-extent in PBS compared to other pharmaceutical relevant media at pH 7.4 was systematically investigated. It should be examined if improved conditions for dissolution studies of the newly developed TA-loaded implants can be found to avoid or reduce decomposition while enabling a precise TA quantification during release studies of DDS over several months.

Results might provide additional value related to analytical set-up development for assessment of glucocorticoid-containing parenteral DDS in general.

For the study, TA was stirred in four different media at 37 ± 0.5 °C over 14 days and subsequently analysed via HPLC as described in section 5.5.19. The first selected media was the previously used PBS. As the degradation to impurity C follows an oxidative pathway, PBS was additionally enriched with 0.1 % sodium pyrosulfite (SPS) as antioxidant. This was already a successful approach to prevent oxidation in TA-containing ointments [226]. Further, the alkali-based trometamol (TRIS) and acidic-based HEPES were included as monographed Ph. Eur. buffers at pH 7.4. Although the addition of sodium edetate has been proven to reduce the decomposition of glucocorticoids [208, 218], it was not investigated as it is a potent complexing agent. This might be problematic with further excipients of implants. Figure 57 shows the measured HPLC chromatograms at predefined time points, showing TA degradation took place in all investigated media. The TA peak area decreased with progressing storage time while the one of impurity C increased. The extent and rate of TA degradation was clearly dependent on the used buffer system (Figure 58). In all cases, a first-order decomposition kinetic was determined (Figure 58; $R^2 > 0.9237$). The respective first-order constants were calculated (Table 11).

Table 11. Determined first-order degradation constants of TA in the different investigated dissolution media at 37 ± 0.5 °C over 14 days.

Buffer (pH 7.4)	**k_{obs} (d^{-1})**
PBS	5.3×10^{-2}
PBS + 0.1 % SPS	2.8×10^{-2}
TRIS	1.1×10^{-2}
HEPES	0.44×10^{-2}

The highest degradation was found for the commonly used PBS. In total 83 % of TA degraded during the investigation period. After 14 days an additional unidentified degradation product was detected ($t_R = 5.4$ min). The degradation progressed fast ($k_{ob} = 5.3 \times 10^{-2}$ d^{-1}) and after 4 h already only 93 % were recovered, leading to results prone to error, if conventional UV-spectroscopy is used. PBS was considered as inappropriate dissolution medium for the investigation of TA-loaded implants. The addition of the antioxidant SPS did not lead to satisfying results. Interestingly within the first three days, a higher TA-loss was noticed compared to pure PBS samples, although the impurity C peak-area was smaller (Figure 57). Potentially, this was caused by incomplete solubilization within the first 4 h. Consequently, undissolved TA particles might have been partially withdrawn during sampling. However, although the first-order rate of TA degradation decreased by the addition of SPS (Table 11), it was not sufficient to maintain TA stability.

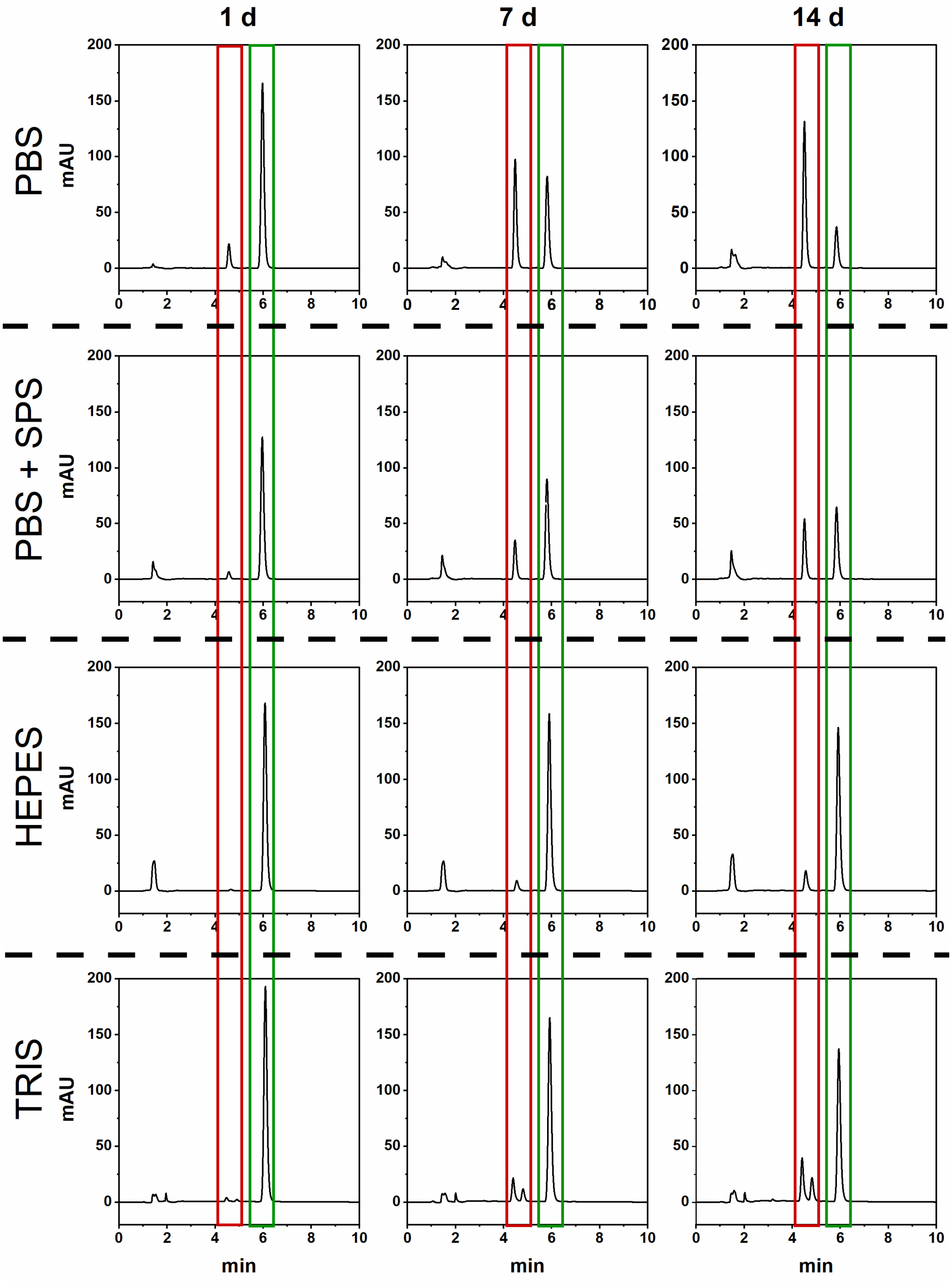

Figure 57. Exemplary HPLC chromatograms of TA dissolved in different pharmaceutical relevant media of pH 7.4 at 37 °C after 1, 7 and 14 days (UV detection at 241 nm). The red box marks the peak of degradation products and the green box marks TA.

In TRIS buffer, although the degradation rate was 5-fold reduced ($k_{obs} = 1.1 \times 10^{-2}$ d^{-1}), the formation of a second degradation product is unfavourable for a reliable TA quantification. The occurred second degradation (t_R = 4.8 min) product is likely Δ14-TA (impurity B t_R = 5.1 min; Figure 55) as the elution order is corresponding to TA *CRS for system suitability* (Figure 56, III). As TRIS represents a base, a deprotonation at position 14 is probable, although t_R is slightly shifted. The TA degradation was most prevented in HEPES buffer, reflected in a more than 10-times reduced k_{obs}-value of 0.44×10^{-2} d^{-1} and a TA recovery of 94.99 ± 0.96 % within the first three days

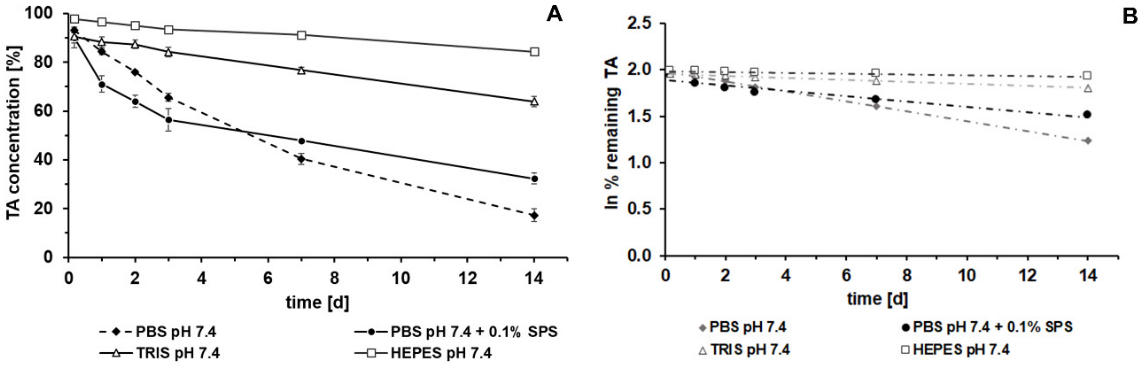

Figure 58. A = TA degradation as function of time in different investigated pharmaceutical relevant buffer systems (n = 3, mean ± s); B = corresponding first-order plots.

(Figure 58A). After seven days still 91.2 % remained. Considering that during dissolution studies of 3D-printed implants TA will be constantly dissolved, the results in HEPES were positive.

The root cause analysis for the increased stability in HEPES compared to the other investigated buffer was not performed and is not completely understood. However, it seems conceivable that the acid-based buffer shows a stabilizing effect, while PBS provokes degradation. Another assumption is that less trace metals are present in HEPES, which are known to catalyse oxidative degradation of glucocorticoids [208, 218, 224]. A verification of this hypothesis was not in the scope of this work, nevertheless studies of trace metal contents in pharmaceutical relevant buffers are desirable. Based on these results, HEPES buffer was successfully identified as preferred medium for dissolution studies of TA-loaded DDS. The results might be also valuable for the analysis of glucocorticoids in general. A medium change of at least once a week is not only important to ensure sink conditions, but also to prevent accumulation of formed impurity C and potential further degradation products.

3.3.2.3 Identification of a Drug Release Study Protocol

Although the stability of TA was successfully improved in HEPES, a precise quantification next to simultaneous proceeding degradation to impurity C was inevitable and must be monitored. Based on the first results of the preliminary solubility experiment and the structural similarity, a quantification based on the extinction coefficient appeared reasonable to avoid elaborated analysis. Therefore, the extinction coefficient ($A_{1cm}^{1\%}$) of TA and the synthesized impurity C was determined via UV-spectroscopy as described in section 5.5.21 at 241nm. Coefficients of 341 ± 4 and 316 ± 1 were found, respectively. Values deviated by 8 %, but summation of both peak areas determined via HPLC for precise recovery of released API during dissolution studies of 3D-printed implants appeared reasonable.

To test if this method allows a complete recovery, the calculation of dissolved TA based on peak summation of TA and impurity C was performed for PBS and HEPES (Figure 59A and B). In PBS, acceptable results were only obtained within the first two days of the investigation period compared to the initially measured percentage (Figure 59A; T0.17 = 94.77 ± 1.43 %; T1 = 93.81 ± 2.5 %; T2 = 93.86 ± 2.56 %). Already after three days no trustworthy data can be collected with the applied method, as recovery was only 90.38 ± 2.95 %. The lower percentage of the first sample (T0.17; 94.77 ± 1.43 %) might be caused by the removal of undissolved drug while sampling within the first 4 h, resulting in an apparent incomplete TA recovery. Reasons for the decrease of TA concentration after two days, are likely caused by the high standard deviations of PBS samples and, additionally, a second degradation product was formed (section 3.3.2.2). Therefore, the addition of peak areas of the drug and its degradation product based on a similar extinction coefficient for PBS is not valid.

For the preferred dissolution medium HEPES, however the sum of the two peak areas without additional calibration was acceptable (Figure 59B). Measured TA concentrations varied between 95.18 ± 0.78 % and 97.85 ± 1.30 % over the investigation period (Figure 59C). Small variations occurred potentially as result of the limit of detection (LOD, see section 5.5.12.3), especially if only small amounts of impurity C were formed. For example, 100 % TA were not recovered even for the first sample. Additionally, a removal of undissolved particles while sampling within the first 4 h caused potentially the deviation. However, based on the results, a reliable TA recovery during drug release studies of 3D-printed implants for discriminative analysis of different samples with HEPES as favoured medium next to ongoing, unavoidable degradation is enabled.

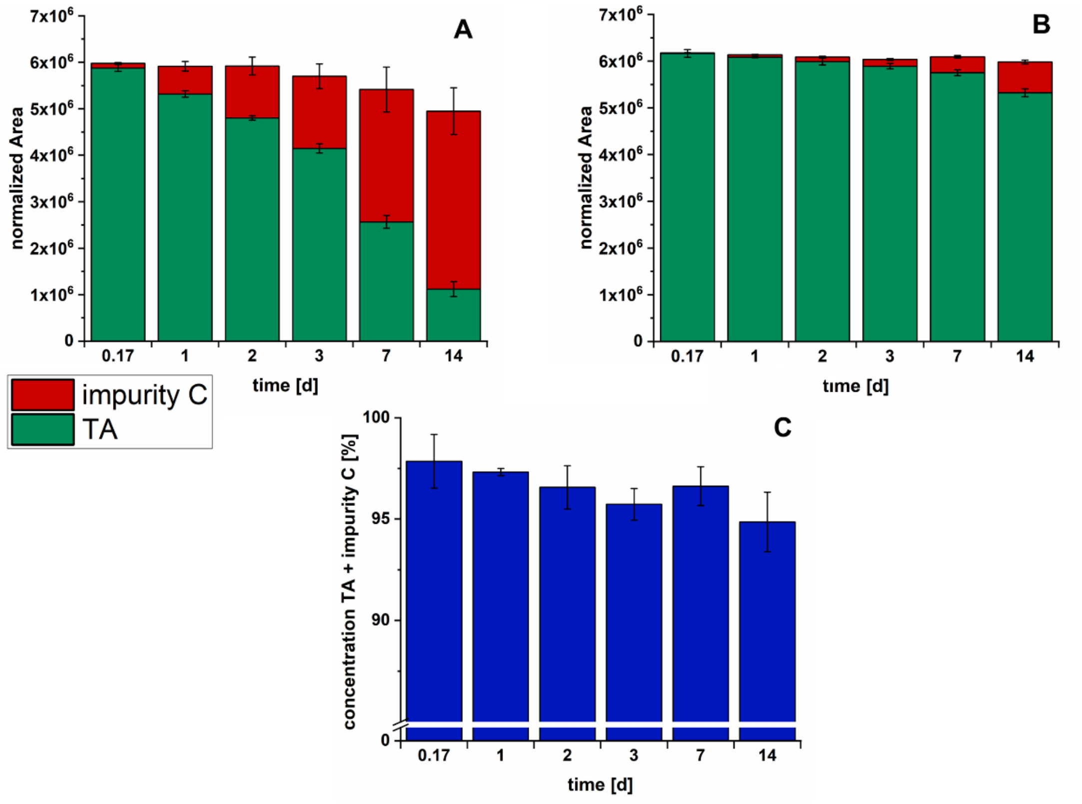

Figure 59. Sum of normalized area of impurity C and TA for each sampling time point (n = 3, mean) dissolved in A = PBS and B = HEPES, both pH = 7.4. C = Recovery of TA [%] calculated as sum of TA and impurity C in HEPES (n = 3, mean ± s).

As result of the new insights, including the identification of HEPES as favoured dissolution medium, an optimized dissolution protocol was developed. Although the degradation of TA takes place at an isosbestic point, an HPLC-based quantification of drug release compared to a simple UV-spectroscopic determination is the method of choice and was validated for this purpose (see section 5.5.12.3). The acceptance by health authorities to calculate the sum of TA and its degradation product is potentially not given without sufficient monitoring and specification of the amount of formed degradation product. Also, during long-term studies, the API might tend to other degradation reactions, e.g., to TA 17- carboxylic acid (Figure 55), especially at higher temperatures take place. This was potentially the reason why in the preliminary experiments at 47 °C and 57 °C no equilibrium was achieved (Figure 53). As consequence of the identified degradation, an acceleration of drug release studies based on the Arrhenius equation at higher temperatures was not possible as commonly performed [209].

To maintain sink

conditions, the TA solubility experiments in HEPES at 37 °C were repeated using the sum of TA and impurity C as described previously. The equilibrium was achieved faster and values of 20.27 ± 0.41 mg/L were measured, which are in accordance with the literature [159, 174] (Figure 60). Based on these results a concentration of 6 mg/L must be not exceeded to maintain sink conditions and to ensure that data reflects drug release performance of the dosage form [227].

For both, reliable TA quantification and the maintenance of sink conditions a regular medium change at least every three days (depending on the proceeding) was selected.

As TA is not dissolved but mainly suspended within the polymer matrix, a degradation within the 3D-printed TA-loaded implant is unlikely. A superimposition of in-matrix degradation and drug release kinetic was therefore considered as improbable and does not affect collected data.

The presented analytical protocol was used for the hereafter described discriminative analysis of TA release of different designed implant structures.

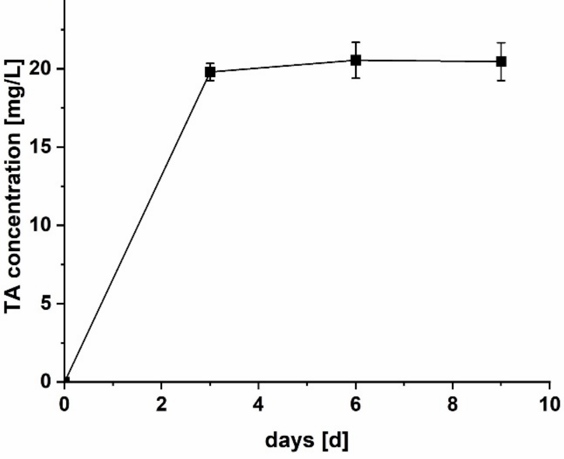

Figure 60. TA solubility in HEPES buffer at 37 °C as function of time (n = 3, mean ± s).

3.3.3 Set-up Development of a Dissolution Method for Implants

After the analytical method development was accomplished, the next step of the work package contained the development of an appropriate dissolution set-up for long-term drug release of 3D-printed implants. Different requirements for this purpose were identified and are described in the following. One goal was to consider a reduced volume of dissolution medium during release studies for two different reasons. First, a low volume was decisive to achieve a measurable TA concentration of the poorly soluble API released from a highly release-retarding matrix as present in the developed formulation [113]. Secondly, an approximation to more biorelevant volume shall be provided, as the potential application of the customizable TA-loaded implant supposed to be osteo and rheumatoid arthritis. The targeted location is amongst others the knee joint.

The present synovial fluid in healthy adults is typically below 10 mL, while in inflammatory state 25 up to 70 mL were measured [228]. The poor solubility of the API limits the possible volume reduction during *in vitro* dissolution studies for analytical reasons. A volume reduction below 10 mL was considered as not suitable. However, a volume of 50 mL means still an improved adaption and is representative for chronically affected, inflammatory knee joints and was therefore selected.

The main goal of long-term release studies was the discriminative investigation of the opportunities of 3D-printing to modify and model the drug release from parenteral dosage forms, rather than establish a biorelevant dissolution method. Therefore, the maintenance of sink conditions recommended by the Pharmacopoeia was aimed at for the analysis of the dissolution behaviour of developed dosage forms [227]. Although the flow-through apparatus has been recommended in the guidelines on dissolution/ *in vitro* release testing of novel/special dosage forms by the American Association of Pharmaceutical Scientists [229, 230], it was decided to develop a set-up facilitating multiple simultaneous analyses based on the “sample and separate” approach. As an automatic sampling was not possible, a manual procedure was mandatory, followed by TA quantification as previously described (section 3.3.2.3).

Based on the requirements, a set-up as schematically illustrated in Figure 61 was developed. The dissolution chamber is equipped with a self-developed sample holder to ensure a constant distance to the bottom of the flask and a stirrer (Figure 61A). The implant is fixed on the sample holder in vertical upright position to ensure uniform perfusion and avoid floating during studies. Thereby, little hydrodynamics, while simultaneously enabling air escape should be allowed. Hence, the investigation of the implants over several weeks in a reduced volume under standardized, reproducible conditions is possible.

For comparison purposes, filaments shall be subjected to analogue analysis. Therefore, self-designed baskets were produced via 3D-printing as depicted in Figure 61A (black). The flasks are then inserted in a water bath, which is placed on a multi-position stirrer plate (Figure 61B).

The temperature will be set via a thermostat. Using this set-up, a simple, reproducible analysis of several different 3D-printed implant networks at reduced volume was enabled and used for the investigations described in section 3.4.4.

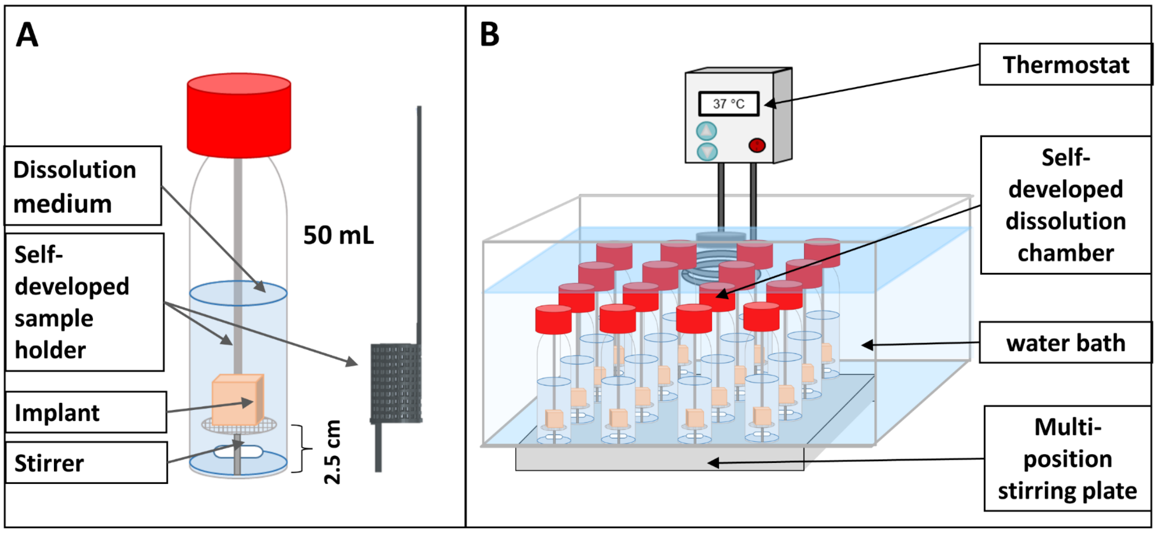

Figure 61. Schematic depiction of developed dissolution set-up for long-term dissolutions studies for parenteral DDS. A = Dissolution chamber set-up equipped with in-house built sample holder for parenteral DDS and 3D-printed filament basket (black). B = Dissolution set-up for multi-sample drug release analysis.

3.3.4 Suitability of Developed Dissolution Method

To evaluate if the developed dissolution method is suitable for a discriminative and reproducible analysis, the drug release profiles of two different two-compartment TA-loaded implant prototypes according to the concept described in section 3.1.2 and the TA-loaded filament F12 (HPMC 25 %) have been compared. The chosen implants for this purpose varied just in the strand width of the TA-loaded network with either 0.4 mm or 0.8 mm (Figure 62). The distance between the printed strands (quadratic pore size) was 0.4 mm in both cases. The drug-loaded network inlay (printed with filament F12) was surrounded by a drug-free shell (printed with filament F6). The exact implant dimensions can be found in (Table 12, section 3.4.2).

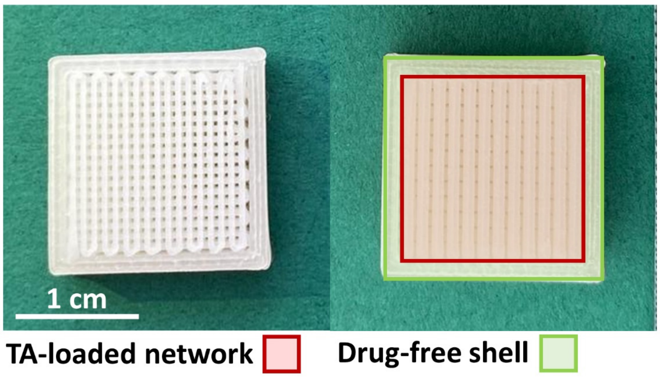

Figure 62. Picture of tested implant prototypes. Left: TA-loaded network with a strand width of 0.4 mm and a pore size of 0.4 mm; right: TA-loaded network with a strand width of 0.8 mm and a pore size of 0.4 mm.

The procedure of printing of implants and the concept to modify systematically the drug release are described in detail in the following section 3.4. Implants and filaments (three sections á 2.5 cm per sample) were subjected to an exemplary drug release study using the developed dissolution set-up, analytical method and protocol as described before (in sections 3.3.2.3 and 3.3.3). Studies were performed in 50-75 mL HEPES buffer at pH 7.4 at 37 ± 0.5 °C (n = 3) over three months. The lowest settable stirring speed of 200 rpm was applied. The released TA amount was quantified using HPLC (UV detection at 241 nm). The exact experimental conditions are described in section 5.5.22.3.

In Figure 63, the absolute cumulative TA release profiles are displayed as single curves (left) and averaged curves (right). The data demonstrated that a discriminative analysis between implant prototypes with different network strand widths and filaments are possible. The low variation of individual measurements indicates a reproducible determination of drug release. The standard deviation for later time points (> 5 d) is below the acceptance criteria of 10 % during method development set by the USP 35 “General information/ (1092) The dissolution procedure: development and validation”. It must be emphasized that stated requirements are not standardized for implants but solid oral dosage forms. Specifications for long-term studies are desirable in the future.

The slightly higher variations for the implant prototype with a strand width of 0.4 mm are most likely caused by the dosage form itself as the standard deviation of the other prototype and filament are considerably lower. The developed dissolution method and protocol is therefore considered suitable to analyse reliably the long-term TA release of different implant designs as described hereafter (section 3.4.4).

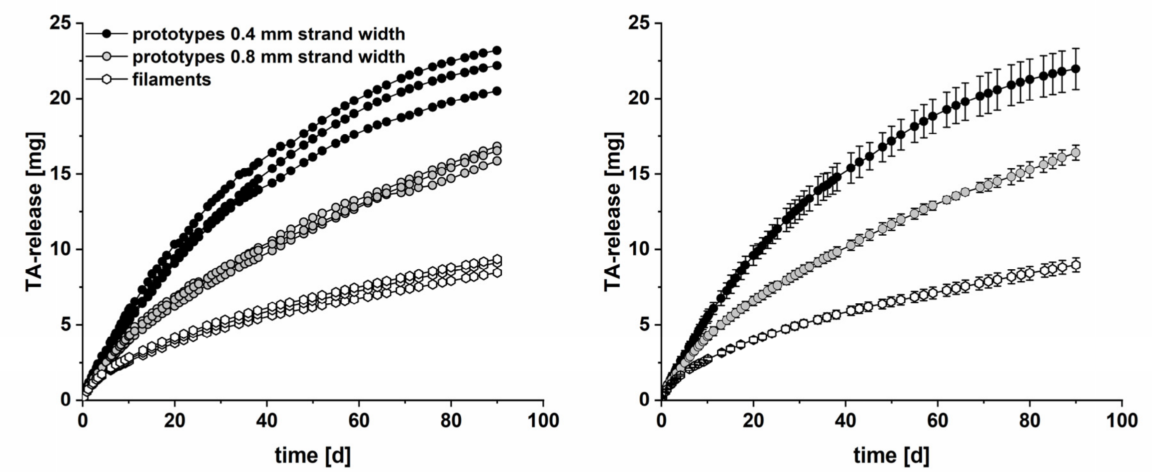

Figure 63. ***In vitro*** **dissolution profiles of implant prototypes with a network strand width of either 0.4 mm or 0.8 mm and TA-loaded filaments F12 (n = 3) using the developed dissolution method. Left: single curves; right: mean ± s.**

3.3.5 Summary

In this chapter, the development of an appropriate dissolution method, including analytical and set-up development for the analysis of different 3D-printed customizable implant networks was presented.

In a first step, a degradation product of the glucocorticoid was observed, which was successfully identified as impurity C (TA 21-aldehyde hydrate) in the commonly used PBS. In a systematic analysis of different dissolution media (PBS, PBS + 0.1 % SPS, TRIS and HEPES pH 7.4), a dependency on the used buffer system was found. PBS was classified as inappropriate for the model drug showing the highest degradation rate. HEPES however, showed a 10-fold reduced degradation rate and was therefore identified as favoured medium for the long-term dissolution studies described in section 3.4.4. The results revealed a high analytical and practical relevance, as a disregard of the findings lead to release data prone to error. Selecting the right medium, preforming frequent medium changes and a stability-indicating method is mandatory for a precise and discriminative TA release analysis. An HPLC assay is essential to monitor and quantify TA for this purpose.

Based on the extinction coefficient, a simplified TA recovery to simultaneously proceeding oxidative degradation to impurity C was established. Optimized dissolution conditions could be provided for TA-loaded parenteral dosage forms. The gained knowledge is potentially relevant and transferable to other glucocorticoid-containing DDS, simplifying analytical development.

After the successful establishment of an analytical procedure, a “sample and separate” set-up was developed including predefined requirements. An approach for long-term drug release studies under controlled conditions at reduced volume was provided. The set-up enabled a simultaneous analysis of multiple implants over several months as presented in section 3.4.4.

It has been demonstrated that the developed dissolution set-up, the analytical method and established protocol enables a discriminative and reproducible drug release analysis of different 3D-printed implant designs.

3.4 Modification and Modelling of Triamcinolone Acetonide Release from 3D-Printed Implants

3.4.1 Introduction and Objectives

The final goal of the thesis was the development of a rational approach to modify and model the sustained drug release from 3D-printed implants.

A target TA release of approximately three months was aimed at justifying minimal numbers of surgeries while optimizing therapy efficiency. An innovative modular implant concept should be provided to show the ability of the individualization degree related to drug release and shape as presented in section 3.1.2. By changing the drug-loaded inlay systematically, the opportunities to modify the drug release via 3D-printing should be examined. Ultimately, a prediction of the drug release shall be enabled based on the gained knowledge, to lower the expenditure of analytics and time, while simplifying individualization.

Hospitals and community pharmacies do not have the options to conduct such analyses. They have neither the equipment nor the time to print and analyze the required sample size in a long-term analysis of individualized printed parenteral DDS. Consequently, the gained knowledge makes the approach potentially suitable for daily use. This would be an enormous benefit to safe time during development and quality assurance of newly printed implants or comparable dosage forms.

Several authors have already studied the influence of the infill density for either dose adjustment or drug release analysis mainly for 3D-printed oral DDS [26, 58, 145, 231, 232]. The infill density specified as fill percentage is easily controlled via the slicer software. However, this approach has certain limitations. First, the degree of freedom is reduced, as the printed strand width is determined by the nozzle-diameter and printing speed within one object. Only the distance between the strands can be changed by changing the infill percentage as exemplarily depicted in Figure 64.

Secondly, a discontinuous printing of the strands to enable a real network is not possible (Figure 64). Double strands at the edges can therefore not be avoided. Depending on the object size and selected infill percentage edge effects occur, meaning the distance to the shell is not always the same, influencing medium flow-through and complicating drug release estimation [35]. Korte and Quodbach used this approach for prediction purposes [35]. Due to the mentioned limitations, drug

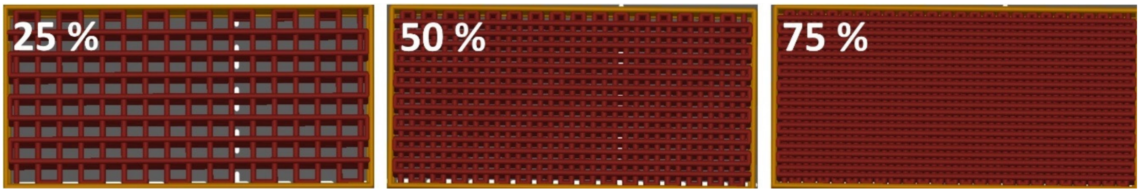

Figure 64. Variation of infill density [%] via the slicing software. Orange strands represent the required shell and the red strands the different networks.

release prediction was only possible based on linear inter- and extrapolation. This approach is therefore not applicable to printed structures not based on varying infill densities.

To overcome the stated constraints, a CAD software was used to design different drug-loaded 3D-printed objects generating a high degree of freedom for the modification of the drug release. In literature already different structures like mesh geometries and different channel diameter/ pore sizes were investigated to accelerate and modify the drug release [36, 233-237]. However, a unidirectional drug release in combination with prediction of drug release enabling shape, dose and drug release simultaneously was not reported.

In this study the different published approaches were combined to enable a predictable and controllable unidirectional, sustained release of TA-loaded implants. Using dual-printing, a simultaneous printing of the drug-free shell for the unidirectional drug release and the drug-loaded network shall be enabled. Different network structures of the drug-loaded inlay were created using two degrees of freedom - the strand width and pore size - to investigate systematically the drug release modification range/ design space of the concept.

3.4.2 A Modular Implant Concept Via CAD for Modifying the Drug Release

In this section the design development of the modular implant presented in section 3.1.2. in terms of the drug-loaded inlay is evaluated in detail.

As reminder, the implant consists of a drug-free shape-adjustable part and a drug-loaded inlay to model the dose and/ or the drug release. Consequently, the degree of individualization is highly increased. The drug-free part enables an adaption to the individual anatomy. Additionally, a unidirectional drug release is aspired to reduce potential side effects of the glucocorticoid.

To model the TA release, the idea for the drug-loaded part was to create an adaptable network structure via CAD with a 90-degree arrangement of each strand layer. Two degrees of freedom were identified to investigate the opportunities of drug release modification via 3D-printing: the strand width and pore size. These were varied systematically. Thereby either the diffusion path of TA along the matrix or the introduction of dissolution media between the network strands were influenced. Latter is important to investigate the impact of drug diffusion into the medium, which should not be the rate-limiting step. Ultimately, the optimal strand-width-pore-size combination supposed to be examined to modify the drug release using the benefits of 3D-printing for customizable drug-loaded implants.

As result of the preliminary dissolution studies, filament formulations and the estimation based on Higuchi (section 3.1.5.3.6), the TA release must be distinctly accelerated to achieve the targeted delivery over three months. An increase of the drug-releasing surface area was therefore aimed at by the reduction of the network strand diameter compared to the filament diameter of ~ 1.7 mm.

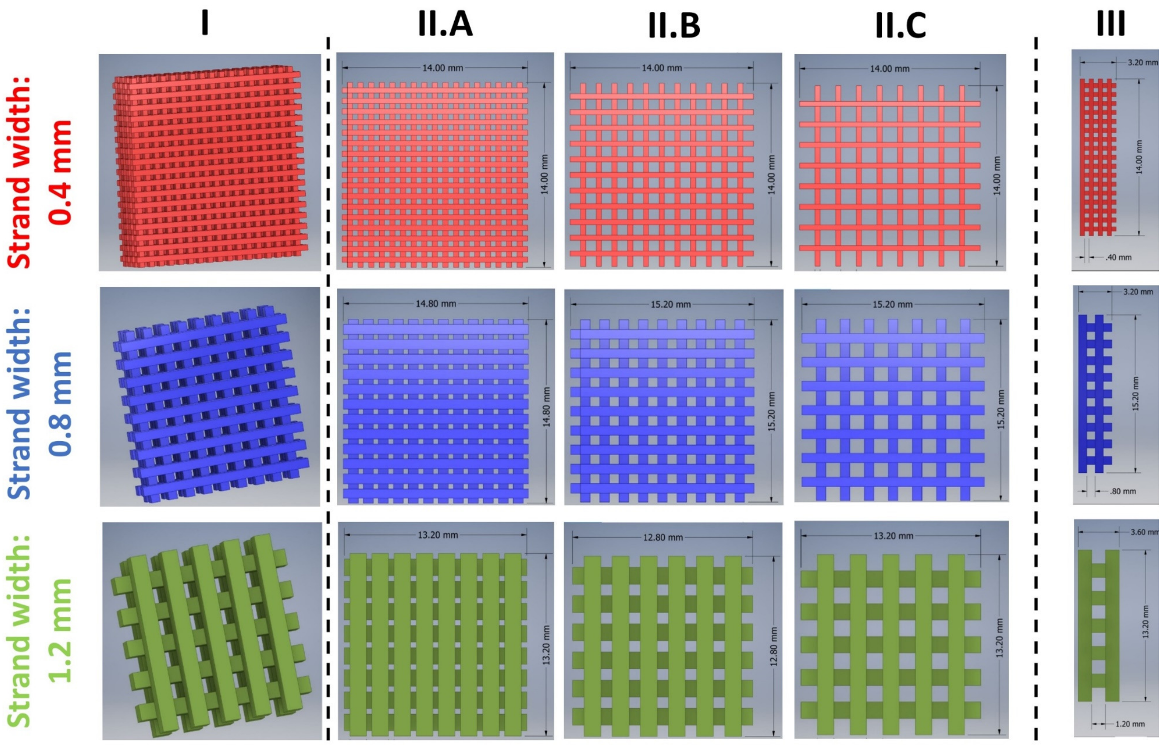

Figure 65. Drug-loaded network inlays designed via CAD software to modify the TA-drug release. I = 3D-CAD model; II = top-view; III = side view (z-direction). Strand width: 0.4 mm (red), 0.8 mm (blue) and 1.2 mm (green) were combined with a pore size of 0.4 mm (A), 0.8 mm (B) and 1.2 mm (C), respectively.

Figure 65 shows the 3D-CAD models designed with the software Inventor® Professional 2019. A colour code was used for the respective strand width to improve the presentation and overview of the results. During the design development, preliminary printing experiments revealed that the smallest printable strand width for the developed formulations is 0.4 mm. To design the network structure of the implant-inlay 0.4 mm (red) and multiples of it with 0.8 (blue) and 1.2 mm (green) as strand widths were considered. Each strand width was combined with three pore sizes in x, y-direction: 0.4, 0.8 and 1.2 mm, resulting in nine different TA-loaded networks. The pore size in z-direction (Figure 65, III) was fixed by the strand width. A quadratic form of the implant was chosen for simplification. The object size of the network (*x, y*) was planned for each strand width according to the following equations (7):

$$\begin{aligned} &\textit{Pore size 0.4 mm:} && b = xc + a(c+1) \\ &\textit{Pore size 0.8 mm:} && b = xd + 2a(d+1) \qquad (7) \\ &\textit{Pore size 1.2 mm:} && b = xf + 3a(f+1) \end{aligned}$$

Where b represents the size of the total drug-loaded part in x and y direction, x the strand width, c, d and f the number of respective strands and a the lowest pore size. The term $(c/d/f + 1)$ characterizes the number of pores. The size of the drug-loaded part with a strand width of 0.8 and 1.2 mm varied slightly since comparable dimensions for the nine inlays were targeted.

Additionally, the size was limited by the opening of the dissolution vessel. The exact network dimensions can be taken from Table 12. The height of the objects was chosen to enable a minimum dose of 13 mg TA for the lightest inlay (0.4 x 1.2 mm).

Table 12. Terminology and dimensions of the 9 designed drug-loaded network inlays.

Implant No.	Implant terminology (strand width x pore size)	Strand width [mm]	Pore size x,y [mm]	Pore size z [mm]	Network size l x w x h [mm]
1	0.4 x 0.4	0.4	0.4	0.4	14.0 x 14.0 x 3.2
2	0.4 x 0.8	0.4	0.8	0.4	14.0 x 14.0 x 3.2
3	0.4 x 1.2	0.4	1.2	0.4	14.0 x 14.0 x 3.2
4	0.8 x 0.4	0.8	0.4	0.8	14.8 x 14.8 x 3.2
5	0.8 x 0.8	0.8	0.8	0.8	15.2 x 15.2 x 3.2
6	0.8 x 1.2	0.8	1.2	0.8	15.2 x 15.2 x 3.2
7	1.2 x 0.4	1.2	0.4	1.2	13.2 x 13.2 x 3.6
8	1.2 x 0.8	1.2	0.8	1.2	12.8 x 12.8 x 3.6
9	1.2 x 1.2	1.2	1.2	1.2	13.2 x 13.2 x 3.6

To enable a unidirectional drug release the inlay was embedded into an impermeable EC shell covering five sites as depicted in Figure 66. The shell thickness was 1.2 mm for all objects. The distance between shell and printed strands was the same as the pore size to reduce additional boundary effects and enable uniform circulation of medium. As further degree of freedom the dose can be optionally adapted by changing the size and the height of the implant but was not considered in this work. The influence on drug release, especially due to the unidirectional TA release must be investigated in future studies.

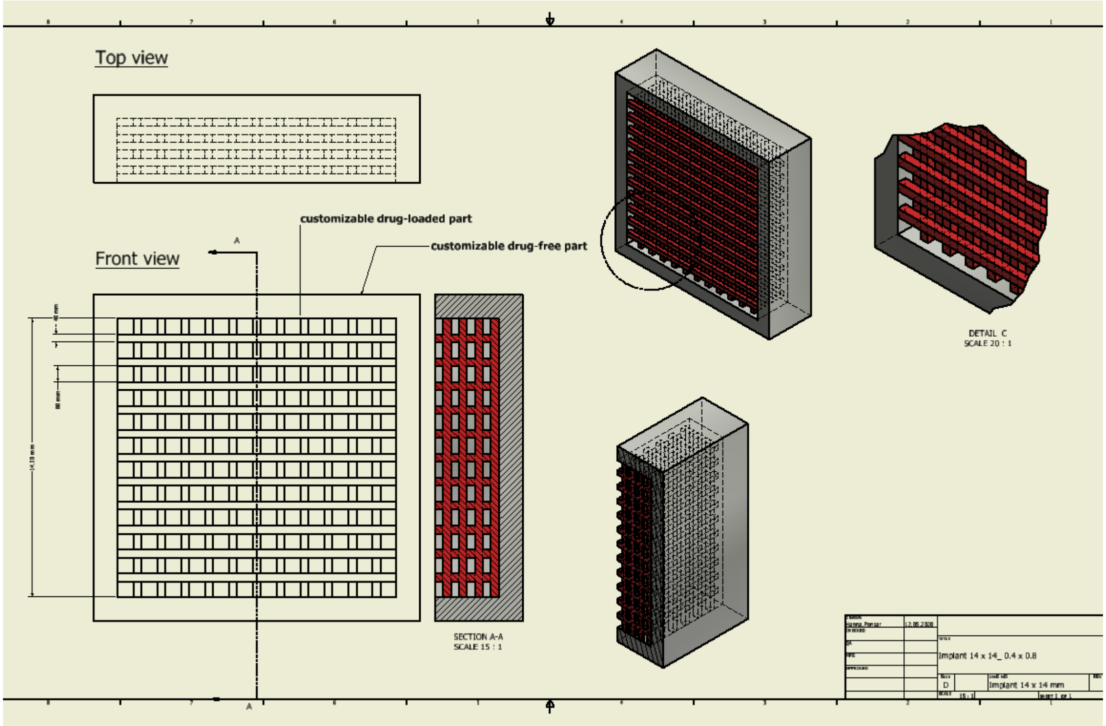

Figure 66. Technical drawing of the modular implant concept, consisting of the drug-free shell (grey) and the drug-loaded network (red).

3.4.3 3D-Printing of Different Implant Designs

3.4.3.1 Production of Two-Component Implants via 3D-Printing

In the next step, a 3D-printing process for the designed two-compartment implants was established using the developed EC-based formulations (refer to section 3.1). For the drug-loaded network part, filament formulation F12 (TA 10 %, HPMC 25 %) was selected (section 3.1.5.3.5), showing the most promising drug release properties. For the shape adaptable part, the drug-free formulation F6 was used. It was examined if dual printing of shell and inlay with the developed filament formulations is possible with sufficient quality. In preliminary experiments, slicing and print settings were determined and can be found in section 5.3.3.

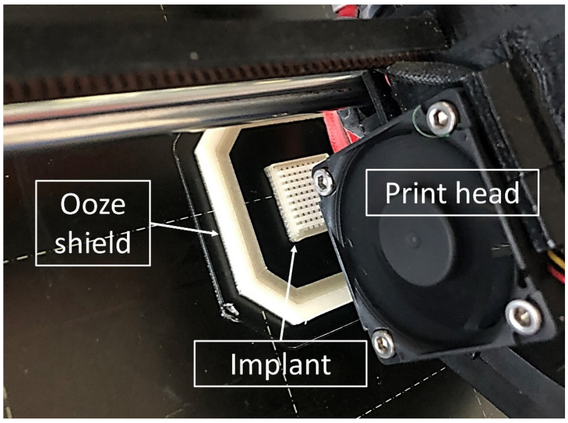

Figure 67. Picture of the 3D-printing process of a two-component implant with ooze shield.

3D-printing of the implants was done with a multiple material unit (MMU, automatic filament changer), enabling dual-printing and, consequently, a simultaneous layer-wise printing of shell and network. Although the 3D-printer used consisted only of one print-head, it is possible to print with up to five different filaments.

The MMU can swap the filament automatically using a simple mechanical system, localized on the top of the printer. It is connected via a filament guide tube to the print-head. Via a horizontally moving selector, filaments can be easily changed using motor drivers and a sensor. However, to prevent cross-contamination after the filament changes in each layer, a so-called ooze shield was printed around each implant (Figure 67).

As depicted in Figure 68, all nine designed implants were printable with a satisfactory resolution and dual printing worked properly. Filaments produced with the optimized HME extrusion settings (refer to section 3.2.4) showed acceptable diameter variations to enable homogenous prints (F6 = 1.713 ± 0.026 mm and F12 = 1.719 mm ± 0.019 mm). The creation of such sophisticated structures is hardly possible with conservative pharmaceutical manufacturing processes for implants, e.g., HME or injection moulding [10].The printing time of the implants varied between 50 to 70 min. The rate-limiting step was the printing of the ooze-shield and the duration of the filament change at each layer. This requires additional printing time and material. To circumvent this aspect, a 3D-printer consisting of two print-heads could be used, which has a comparable printing precision as the one used in the presented work. By that, a time-consuming filament change and the hazard of cross-contamination can be avoided.

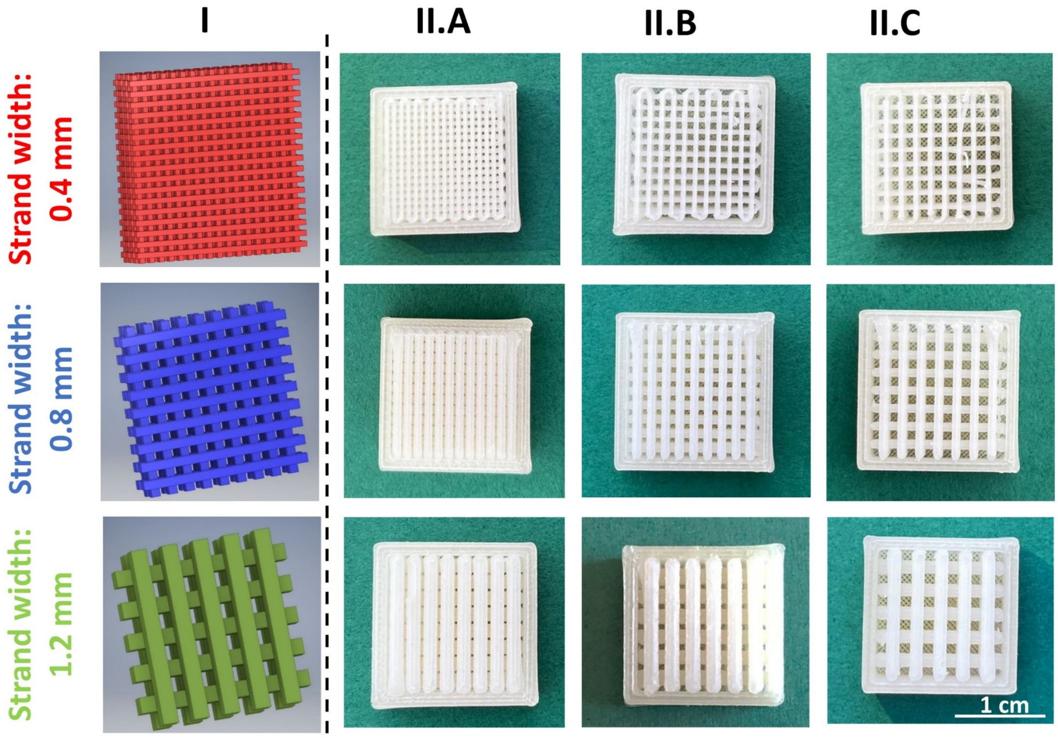

Figure 68. Overview of 3D-printed implants, consisting of the drug-free impermeable shell and the TA-loaded network inlay with varying strand width and pore size. I = 3D-CAD model of the network; II = pictures of printed implants with strand widths of 0.4 (red), 0.8 (blue) and 1.2 (green) mm combined with a pore size of 0.4 mm (A), 0.8 mm (B) and 1.2 mm (C), respectively.

3.4.3.2 Physical Properties of 3D-Printed Implants

After successful 3D-printing of implants the physical properties were determined. Implants with a mass variation below 2.5 % (n = 3) were obtained, indicating a good mass uniformity. For all implants the same filaments (F6 and F12) were used. Consequently, the mass increased with increasing strand width and decreasing pore size. To determine the actual mass of the respective drug-loaded part, the corresponding shells were printed individually (n = 10) and the average weight was subtracted from the total implant mass as described in section 5.5.14. All variations are therefore assumed to stem from the drug-loaded network structure. Masses of the TA-loaded part between 146 and 517 mg were realized, resulting in clinically relevant TA dosages between 13 and 46 mg (Figure 69). As the dimensions were slightly different for the implants with 0.8 and 1.2 mm strand width depending on the strand-width-pore-size combinations (Table 12), only for implants 0.4 x 0.4 a linear correlation of the mass was found ($R^2 = 0.998$, Figure 69). Results showed the feasibility of simplified dose adjustment via 3D-printing without changing formulation compositions.

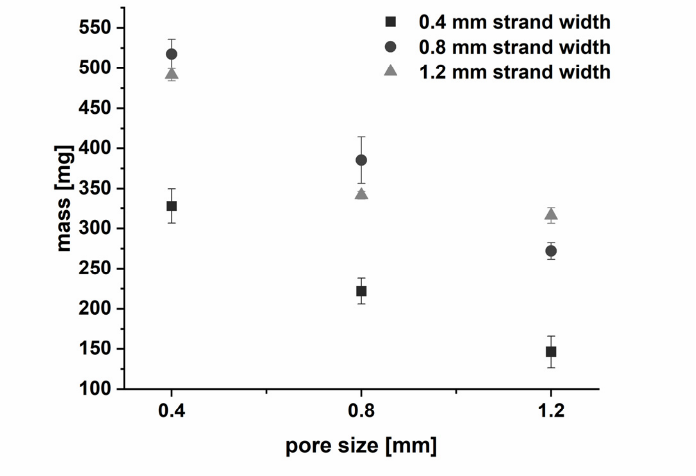

Figure 69. Mass against pore size of the 3D-printed drug-loaded implant inlays for the respective strand width of the network (n = 3; mean ± s).

In addition, 3D-printed dosage forms were subjected to X-ray microcomputed tomography to visualize the true structure of the implants. Exemplary obtained images are depicted for each strand width in Figure 70. The selected layer height during printing was 0.2 mm for all implants to obtain in each case an approximate quadratic macrostructure of the network strands. As the printed single strand is limited by the nozzle diameter (0.4 mm), one network strand of 0.4 mm consisted of two printed layers (á 0.2 mm) and one extruded branch (Figure 70b), while the strand of 0.8 mm consisted of four layers (á 0.2 mm) and two printed branches (Figure 70c) and 1.2 mm analogously of six printed layers (á 0.2 mm) and three printed branches (Figure 70d). Thus, the real strand shape deviated from an ideal quadratic one. The strands not in contact with the shell (outer edges and implant bottom) were fully surrounded by air beside the contact points with the next network layer (Figure 70d).

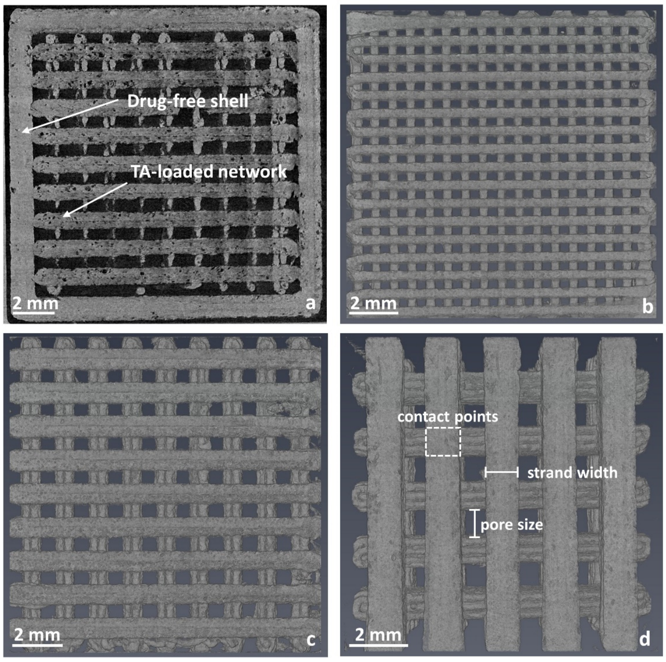

Figure 70. Reconstructed X-ray images of 3D-printed implants. (a) total implant (shell + network; 0.8 x 0.8 mm). (b) drug-loaded network 0.4 x 0.4 mm. (c) drug-loaded network 0.8 x 0.8 mm. (d) drug-loaded network 1.2 x 1.2 mm.

X-ray computed tomography was additionally used to determine the true surface area available for drug release of the TA-loaded network by subtracting areas in contact with the shell as described in detail in section 5.5.16. Results for the surface area can be found in Table 13. Due to the surface roughness as cause of the printing process and contact points at the edges close to the shell, the true surface area deviated from the calculated one. In addition, the strand width deviated slightly from the set one. For a pore size of 0.4 mm, the surface area was in all cases lower. It was hypothesized that weight from the upper layers resulted in flattening of the subjacent layer. Due the low pore size, which was distinctly influenced by this circumstance, the area was lower than expected. For the other pore sizes this effect at the contact points was negligible and due to the surface roughness, the surface area was increased compared to the calculated one. However, as expected, the surface area decreased with increasing strand width or decreasing pore size. The implant 0.4 x 0.4 showed the highest surface area while the implant 1.2 x 1.2 showed the lowest one.

The implants with 0.8-mm strand width were an exception. The true surface area of the implant 0.8 x 0.8 was larger than for 08 x 0.4, although in theory, it should be the other way around, caused by the mentioned reasons (Table 13). For the implants 0.4 x 1.2 and 0.8 x 1.2 interestingly the same true surface area was found.

For comparison purposes three filaments with a length of 2.5 cm and a diameter of 1.75 mm (~ 20 mg TA) have a theoretical surface area of 3.75 cm^2. Consequently, a 2- to 5-fold surface enlargement was achieved. As the contact areas with the impermeable shell increased with increasing strand width and the objects had a slight varying dimension (Table 12) linear fitting was not applicable.

Table 13. Calculated and true drug-releasing surface area (A) and specific surface area (SSA) of TA-loaded network of implants (n = 1).

	Implant								
Strand width [mm]	**0.4**	**0.4**	**0.4**	**0.8**	**0.8**	**0.8**	**1.2**	**1.2**	**1.2**
Pore size [mm]	**0.4**	**0.8**	**1.2**	**0.4**	**0.8**	**1.2**	**0.4**	**0.8**	**1.2**
A_{cal} [cm^2]	23.02	16.93	12.45	15.78	13.31	10.89	10.25	8.06	7.27
A_{true} [cm^2]	20.54	18.54	13.08	12.95	15.30	13.08	9.80	8.69	7.91
A_{true}/ A_{cal} [-]	0.89	1.10	1.05	0.82	1.15	1.20	0.96	1.08	1.09
SSA [cm^2/g]	62.6	83.5	89.3	25.0	39.7	48.1	19.9	25.4	25.0

3.4.4 Long-term Dissolution Studies of 3D-Printed Drug-Loaded Implants

3D-printed implants were subjected to *in vitro* long-term dissolution studies (n = 3). Thereby the influence of the different created networks on the TA release behaviour was investigated.

The self-developed set-up, study protocol and analytical method presented in section 3.3.2 and 3.3.3 were used. Tests were performed in 50-75 mL HEPES buffer at pH 7.4 at 37 ± 0.5 °C and the lowest settable stirring speed of 200 rpm was applied (section 5.5.22.3). Quantification was done using HPLC (UV detection at 241 nm).

In Figure 71, the drug release profiles of the nine different network structures compared to filaments (Ø 1.72 mm) are illustrated. In the following, the dissolution behaviour is discussed and the analyses of the dissolution kinetic will be performed afterwards (section 3.4.5). The non-erodible EC-matrix stayed intact over the whole investigation period, as expected. Initially for all DDS a prolonged burst effect was observed, due to TA present on the matrix surface. After approximately five days the drug release rate decreased distinctly. A fast release at the beginning of therapy might be beneficial to relieve inflammatory associated pain promptly to improve patient conditions.

Depending on the strand width and pore size, a different release performance was observed, showing a big degree of individualization and adaptability. The TA release could be varied from 20 to 80 % within three months, using the same starting material (Figure 71). This was only true considering the relative drug release as the absolute TA dose varied depending on the strand-width-pore-size combination.

Implants with higher strand width tended to release TA slower compared to DDS with a smaller strand width as expected (Figure 71a, Figure 74) as diffusion path lengths were increased. The relative drug release from the implants was in the order according to their specific surface area (Table 13). Interestingly, the drug release of the filament (Ø 1.72 mm) showed a drug release behaviour comparable to implants with a strand width of 0.8 mm, although the specific surface area

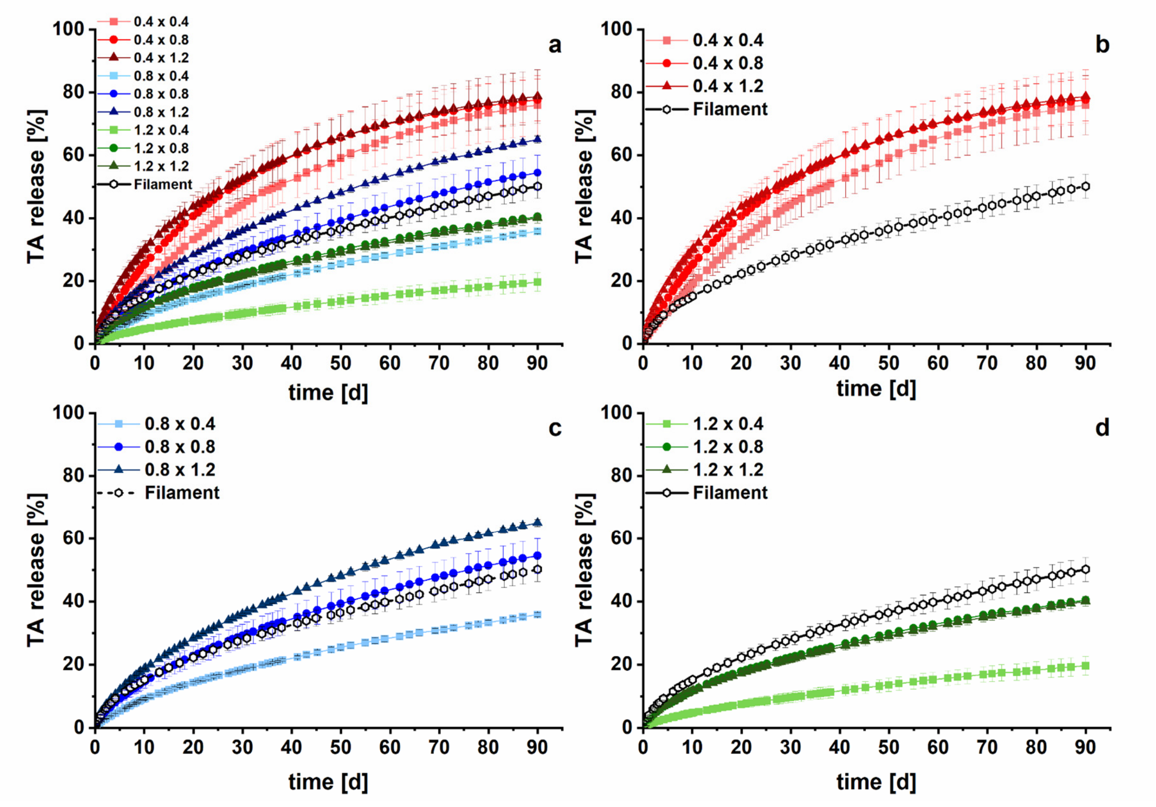

Figure 71. ***In vitro*** **drug release of TA-loaded implants with different strand widths (first number) and varying pore size (second number) over three months (n = 3, mean ± s). (a) depicts the overview of the nine different implants, (b) implants with a strand width of 0.4 mm, (c) 0.8 mm and (d) 1.2 mm in comparison to the filament.**

was considerably lower (~ 18 cm^2/g). This indicates the strong influence of the shell and the resulting unidirectional drug release. Additionally, the pore size might affect drug diffusion due to a local saturation within the pores.

The absolute released TA amount was increased compared to the filaments as intended, except for the implant 1.2 x 0.4 within three months (Figure 72). The extent of acceleration was limited due to the unidirectional drug release. Nevertheless, a successful TA release variation between 8.58 ± 1.38 mg (1.2 x 0.4) and 21.93 mg ± 1.31 mg (0.4 x 0.4) was achieved, covering the clinically relevant dosages, depending on the severity of systems and joint sizes [114].

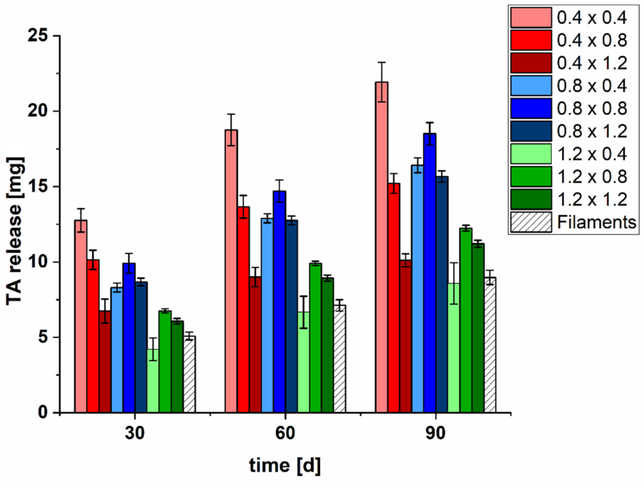

Figure 72. Released absolute TA amount [mg] for each implant after 30, 60 and 90 days compared to the filament formulation ((n = 3, mean ± s).

Different factors like surface area, diffusion path length, pore size and resulting ability of medium perfusion, as well as unidirectional liberation, have influenced the drug release simultaneously. The drug release was primarily driven by the drug-releasing surface area as expected. A pore size of 0.4 mm showed a strong influence of the drug release as depicted for the implants 0.8 x 0.4 and 1.2 x 0.4. The drug release was reduced although the surface area was higher (Table 13). Up to 0.8 mm pore size the influence of the drug diffusion into the medium seemed to be negligible and is not rate-controlling. This was not the case for implants with a 0.4-mm strand width, potentially caused by a higher influence of the incorporated pore former HPMC. At a low strand width, the pore formation and reduced diffusion paths accelerated the TA release in combination with a higher specific surface area compared to larger strand widths. Surprisingly the released absolute drug amount of the implants 0.4 x 0.8 and 0.4 x 1.2 were lower compared to the 0.8-mm-implants with the same pore size although the surface areas were always higher (Table 13), except for 0.4 x 1.2 (A = 12.08 cm^2). Apparently, the pore size of 0.4 mm in z-direction reduced the release rate. With the presented approach, it was possible to modify and successfully accelerate the absolute drug release of different doses within three months compared to the filament.

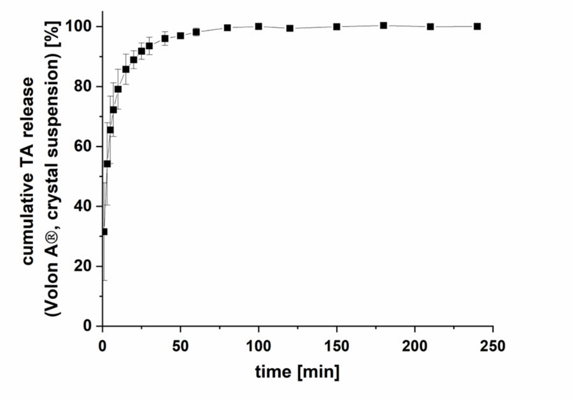

Figure 73. Dissolution profile of a marketed TA crystal suspension Volon® A (n = 3, mean ± s).

To enable a comparison to the currently marketed therapy options, a dissolution profile of a TA crystal suspension (Volon® A 10-5 mL, n = 3) was measured. The analysis was performed in USP apparatus II in 1000 mL HEPES pH 7.4 at 37 ± 0.5 °C with a stirring speed of 100 rpm. Experimental settings had to be adapted and a maximum dose of 6 mg was selected to maintain sink conditions as a medium change with a suspension was not possible (refer to section 5.5.22.2). This enabled a discriminative comparison. The result is depicted in Figure 73. TA crystals of the suspension were completely dissolved within 100 min, which was also reported in the literature [116, 238]. In the same period, a maximum of 2 % were released from implants. 6 mg TA were released between 13 and 40 days depending on the network arrangement. It must be emphasized that the *in vitro* results do not reflect the *in vivo* conditions in humans, as the residence time in an articular cavity is around three days for TA crystal suspensions [117].

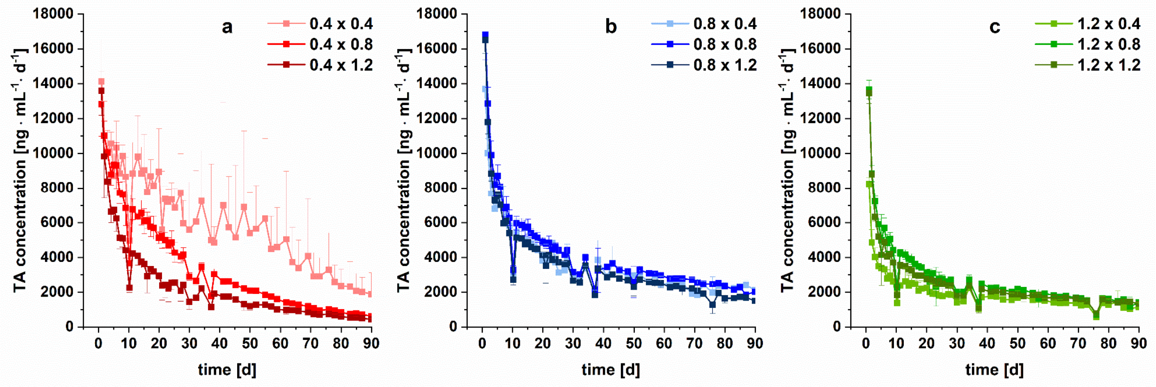

Figure 74. Daily TA release of 3D-printed implants with (a) 0.4 mm, (b) 0.8 mm, (c) 1.2 mm strand width and varying pore size (n = 3, mean ± s). Values are normalised to a volume of 50 mL.

Considering the daily TA concentration, a distinct decrease within the first 30 days for all implants was observed, assuming a synovial fluid volume of 50 mL (Figure 74). Implants with lower strand widths led to higher initial concentrations. As consequence, the TA concentration within the joint cavity might be adapted to the individual patient status. Afterwards the daily concentration-decrease slowed down, leading to approximately constant levels between 444 and 2030 ng · mL^{-1} · d^{-1} after 90 days for maintenance treatment. As mentioned in the introduction, next to the TA crystal suspension, extended-release microsphere-based formulations were investigated and recently marketed (Zilretta®) to improve therapy efficiency, as articular residence time is prolonged and TA concentrations increased [116, 124, 125].

Comparing the data of the 0.8 x 0.8 implants with results of *in vivo* studies of Kraus et al. [116] of TA-loaded PLGA microspheres (FX600), the achieved TA concentrations were considerably higher after three months (implant 0.8 x 0.8 = 2158 ng/mL vs. FX 600 = 0.3 ng/mL). 3D-printed implants might therefore result in even longer residence times and local concentrations adapted to the patient conditions. However, as the synovial clearance was not considered during *in vitro* studies, a bridging to the *in vivo* data is hardly possible. The systemic absorption, synovial fluid volume, composition and other pharmacokinetic relevant conditions influence distinctly the *in vivo* performance [212]. *In-vivo-in-vitro* correlation are desirable in the future to estimate the performance of newly developed DDS in human patients correlated with clinical endpoints.

With the data collected, it was demonstrated that 3D-printing represents an efficient method for the manufacturing of complex, customizable implants, enabling a modification of the drug release. A sustained controlled-release was enabled to likely result in a longer residence time within the articular cavity applying developed 3D-printed DDS compared to other approaches on the market. Thereby the therapy efficiency might be further increased.

3.4.5 Kinetic Analysis of Dissolution Data

Based on the preliminary dissolution results of filaments during formulation development (refer to section 3.1.5.3.5), a square-root-of-time kinetic was expected also for the implants. To verify the assumption obtained dissolution curves were subjected a kinetic analysis according to Korsmeyer's and Peppas' approach to determine the present release mechanisms based on the diffusional release exponent n using Equation (1) described in section 3.1.5.3.5 [179].

Table 14 shows the diffusional release exponents n of implants by fitting the drug release data to the double logarithmic depiction of Equation (1) (Equation (2), section 3.1.5.3.5). Values > 5 % drug release were included to cover the linear range as the drug release of the first days was comparatively fast and not representative for the residual drug release behaviour (max. up to 60 % drug release). According to Ritger and Peppas a release exponent of n = 0.45 indicates a square-root-of-time kinetic, while n = 1 proves a zero-order kinetic for cylindrical shaped matrix geometries [178, 179].

Table 14. Data of kinetic analysis of implants fitted to Korsmeyer-Peppas model.

	Implant								
Strand width [mm]	**0.4**	**0.4**	**0.4**	**0.8**	**0.8**	**0.8**	**1.2**	**1.2**	**1.2**
Pore size [mm]	**0.4**	**0.8**	**1.2**	**0.4**	**0.8**	**1.2**	**0.4**	**0.8**	**1.2**
n [mean ± s]	0.76 ± 0.02	0.69 ± 0.05	0.54 ± 0.01	0.66 ± 0.02	0.68 ± 0.03	0.60 ± 0.01	0.65 ± 0.01	0.59 ± 0.02	0.58 ± 0.00
R^2	> 0.9933	> 0.9924	> 0.9887	> 0.9952	> 0.9991	> 0.9992	> 0.9986	> 0.9964	> 0.9988

For all implants, diffusional coefficients > 0.45 were obtained and varied depending on the pore size between 0.58 and 0.70. This indicated an anomalous (non-Fickian) transport [178]. The applicability of the stated thresholds was limited due to the contact points between the strands and deviation from a cylindric geometry of printed structures (Figure 70). Although the API was entirely suspended in a non-erodible matrix, the assumption of a square-root-of-t-kinetic (diffusion-controlled) seemed not to be valid for 3D-printed implants. Kinetic deviations to filaments might occur by impacts of different appearing factors. First, a uniform perfusion of the medium was likely not given at lower pore sizes. This resulted in a slower release and changes in the drug release kinetic as already reported by Korte and Quodbach [35]. In addition, the influence of HPMC concentration as swellable polymer might have interfered [151]. Likewise, the unidirectional drug release showed an impact depending on the strand width. For release modelling and description of the obtained release curves different mathematical models are supposed to be fitted.

3.4.6 Modelling and Prediction of Drug Release

Drug release studies of long-term parenteral dosage forms are time-consuming, especially in the context of quality control and individualized therapy. Often accelerated *in vitro* release methods based on, e.g., temperature, solvent or surfactant addition are used [66]. However, such variables might influence and potentially change the drug release mechanism [66, 209]. Mathematical modelling is therefore advantageous and was tested for modular implants. Different models in the literature are available to describe dissolution curves accordingly [239].

Based on the matrix properties of the filaments and 3D-printed implants a square-root-of-t-kinetic was expected, while the kinetic analysis via Korsmeyer-Peppas (refer to section 3.4.5) indicated an anomalous transport. The following mathematical models were selected to fit the obtained dissolution data for the implants with varying strand width and pore size (refer to 5.5.24).

For planar polymer matrix systems with suspended API, as is the case for the novel implants, the drug release mechanism can be described with the Higuchi equation, also known as square-root-of- t kinetic (Equation (3)) [180, 240].

To describe anomalous drug release the Peppas-Sahlin equation (Equation (8)) is valid, coupling diffusion and relaxation mechanisms [241].

$$\frac{M_t}{M_\infty} = k_1\, t^n + k_2\, t^{2n} \tag{8}$$

The first part of the equation describes the Fickian diffusion, while the second term depicts the Case-II-transport. n is the diffusional release exponent, obtained via the Korsmeyers-Peppas model (Equation (1) and (2)). k_1 and k_2 represent kinetic constants.

The Weibull equation (Equation (9)) was chosen, as it can be applied to any kind of dissolution profile, independent from the underlying physical drug release mechanism [239]. It depicts only an empirical model simply describing the curve, not containing further information about the underlying mechanisms.

$$c_t = 1 - e^{\frac{-(t-T_i)^b}{a}} \tag{9}$$

The variable c_t describes the cumulative drug release at timepoint t. T_i is a location parameter in case of a lag time (no lag time; $T_i = 0$) and a represents a scale parameter defining the time scale of the drug release. The shape parameter b characterizes the curve (exponential: $b = 1$; sigmoid: $b > 1$; parabolic $b < 1$).

In Table 15, the coefficients of determination (R^2) for the respective curve fit are depicted. Values until 60 % drug release were considered, as the Higuchi equation is only valid until this limit [242]. The Weibull curve fits showed the best results for all implants, followed by the Peppas-Sahlin-function compared to the Higuchi-model (Figure 75).

Table 15. Obtained R^2 -values for the curve fitting of mathematical models.

Implant No.	Implant (strand width x pore size)	Higuchi	Peppas-Sahlin	Weibull
		R^2	R^2	R^2
1	0.4 x 0.4	0.9355	0.9944	0.9994
2	0.4 x 0.8	0.9567	0.9961	0.9997
3	0.4 x 1.2	0.9929	0.9977	0.9994
4	0.8 x 0.4	0.9733	0.9995	0.9998
5	0.8 x 0.8	0.9818	0.9999	0.9997
6	0.8 x 1.2	0.9859	0.9994	0.9990
7	1.2 x 0.4	0.9660	0.9998	0.9998
8	1.2 x 0.8	0.9900	0.9993	0.9997
9	1.2 x 1.2	0.9906	0.9998	0.9997

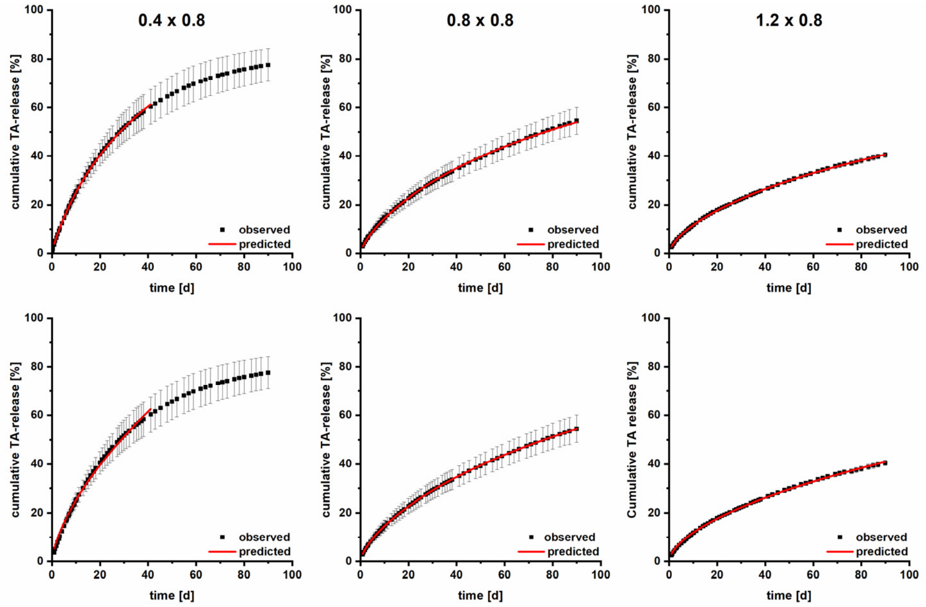

Figure 75. Exemplary fitted dissolution curves for TA-loaded implants (n = 3, mean ± s) using the Weibull (top) and Peppas-Sahlin (bottom) function.

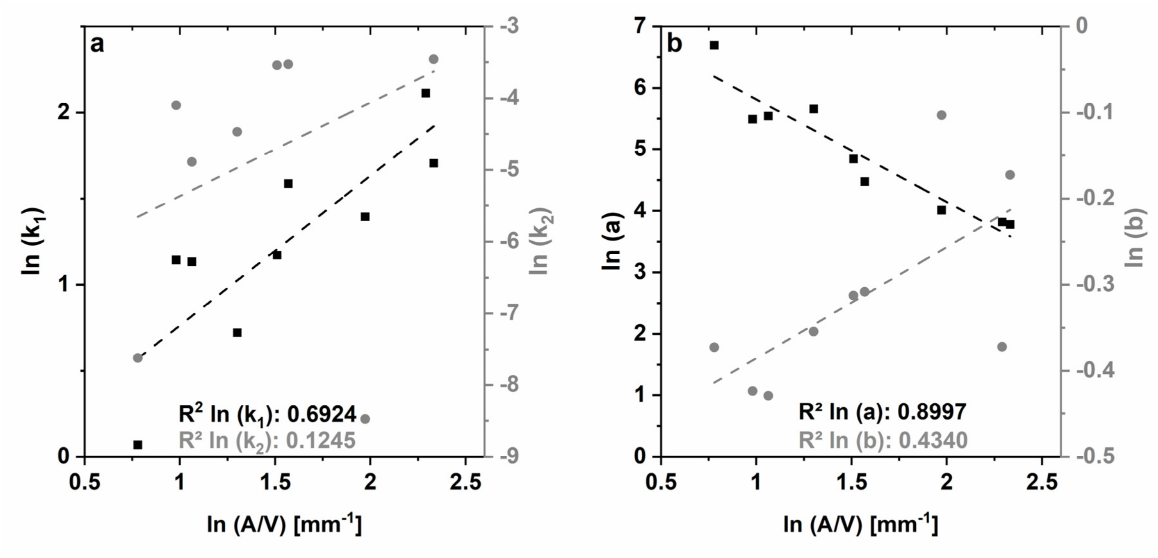

Figure 76. Logarithmic correlation of the constants k_1 and k_2 of the Peppas-Sahlin function (a) and constants a and b of the Weibull function (b) with the A/V ratio of implants according to [243].

Windolf et al. [243] used the obtained parameter (Peppas-Sahlin: k_1 and k_2; Weibull a and b) from fits with both equations to predict successfully dissolution profiles of 3D-printed dosage forms with different surface area to volume (A/V) ratio. In the study, DDS with different A/V ratios were printed and dissolution profiles were analysed. The dissolution data was used to determine the respective unknown variables in dependency of the A/V ratio. For both, the Peppas-Sahlin and the Weibull variables, a linear relationship in a common logarithmic depiction was found. Thereby the dissolution profiles of oral dosage forms with different A/V were predicted.

This approach was evaluated for the nine different printed implants to potentially predict the drug release. In Figure 76, the logarithmic correlation of the respective constants and the A/V ratio of implants are displayed. Neither for the Peppas-Sahlin nor for Weibull function a linear fit was obtained. The contact areas within the network and with the shell, as well as unidirectional drug release and the associated low hydrodynamics limit most likely the applicability. The correlation with the specific surface area or the surface area did not lead to satisfactory results. A drawback of this approach is that at least three data sets are required for proper linearization. In addition, the prediction based on Peppas-Sahlin presupposes the identical diffusional exponent n for each dosage form, which is not the case for the printed implants (Table 14), limiting the applicability. Although the presented approach by Windolf et al. is attractive, a drug release prediction of 3D-printed drug-loaded implants with unidirectional drug release does not appear to be suitable.

Although the quality of fits was comparably lower (Table 15), the Higuchi model (Equation (3)) represents a simple approach to describe the drug releases from non-erodible matrix systems with suspended API [180]. The equation was tested to predict the API release from printed implants as already evaluated by Korte and Quodbach for printed dosage forms with varying infill density [35]. Accordingly, Equation (3) can be simplified as follows:

$$M_t = D_k A\sqrt{t}, \text{ with } D_k = \frac{Q}{\sqrt{t}} \quad \textbf{(10)}$$

D_k combines the diffusivity (D) of the API in the polymer, the porosity ε and the tortuosity τ of the porous matrix, as well as the initial (C_0) and saturation (C_s) concentration. D_k was determined as slope of the Higuchi-plot (Q against $\sqrt{t}$) as exemplary depicted in Figure 77 (until 60 % of TA release). Q was calculated as quotient of the cumulative absolute TA release M_t and the surface area of implants determined via X-ray computed tomography ($Q = \frac{M_t}{A}$).

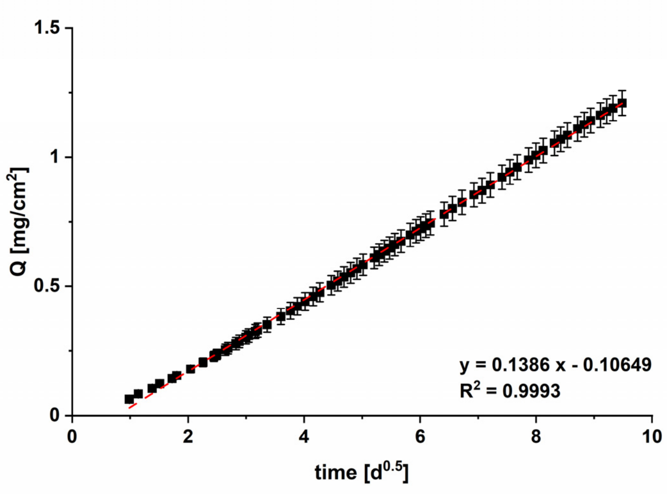

Figure 77. Exemplary Higuchi-plot of TA release from printed implant 0.8 x 0.8 (n = 3; mean ± s).

For printing of all implants, filament formulation F12 was used. Hence, it was originally expected that D_k will be identical if the pore former HPMC does not considerably swell during dissolution studies. If HPMC tends to swell, it was expected that with pore sizes of 0.4 mm D_k is smaller, since pores are potentially closed, presenting a diffusion barrier and limiting medium perfusion [35].

In Table 16, the D_k for the 3D-printed implants and R^2 of linear fits are displayed. The obtained results based on the measured surface area via X-ray computed tomography deviated slightly from the previously made assumptions. The D_k of implants was only comparable for implants with the same strand width and pore sizes ≥ 0.8 mm, indicating an impact of HPMC depending on the strand width. The diffusion coefficient (D) is consequently not constant and time-dependent [244]. For implants with 0.4 mm pore size and a strand width of 0.4 and 0.8 mm, D_k-values were unexpectedly larger (0.4 x 0.4, 0.8 x 0.4). It must be considered that the determination of the surface area was only done n = 1 for each implant, leading potentially to deviations from the true D_k.

In addition, contact areas with the surrounding shell were subtracted manually to determine the TA-releasing surface area (refer to 5.5.16). The resulted inaccuracy in surface area is larger in case of implants with many small surfaces, as the case for strand width with 0.4 and 0.8 mm, compared to 1.2 mm. This is further supported by the fact that the deviation between the D_ks increased for pore sizes > 0.4 mm with increasing strand width.

Table 16. D_k of 3D-printed implants obtained from Higuchi-Plots and R^2 of linear fits.

Implant (strand width x pore size)	$D_k = \frac{Q}{\sqrt{t}}$ [$mg \cdot cm^{-2} \cdot d^{-0.5}$] based on measured A	$D_k = \frac{Q}{\sqrt{t}}$ [$mg \cdot cm^{-2} \cdot d^{-0.5}$] based on theoretical A	R^2
0.4 x 0.4	0.1401	0.1250	0.9935
0.4 x 0.8	0,1182	0.1295	0.9977
0.4 x 1.2	0.1031	0.1083	0.9981
0.8 x 0.4	0.1460	0.1199	0.9988
0.8 x 0.8	0.1386	0.1594	0.9993
0.8 x 1.2	0.1371	0.1647	0.9994
1.2 x 0.4	0.1005	0.0960	0.9952
1.2 x 0.8	0.1592	0.1716	0.9997
1.2 x 1.2	0.1575	0.1713	0.9994

If the theoretically calculated ideal surface area (without considering the surface structure and printing unevenness) is taken for the D_k determination, results tend to correspond to previous expectations (Table 16), but for pore sizes > 0.4 mm higher D_k-values were obtained. In general, the quality of linear fits for 0.4 mm pores were worst, likely due to the low and inhomogeneous medium perfusion.

In the following, it was evaluated whether a prediction of TA release is feasible. Due to the limitation of the implants with a pore size of 0.4 mm, this data was excluded for prediction. For each strand width, the drug release of implants were predicted using D_k of the respective different pore size (Table 17).The released API amount was calculated for each time point using the respective D_k and the measured or calculated surface area of the drug-loaded network according to Equation (10). Obtained values were divided by the total TA content. Values until 60 % drug release were used.

In Figure 78, the results of the observed and predicted dissolution curves of implants are depicted using the measured surface area. Although the order of D_k was as previously expected using the theoretical surface area, the coefficients derived from measured surface area fitted better to the observed drug release data. This is also visible from the root mean squared error of prediction (RMSEP) values (Table 17). With decreasing strand width of implants, the deviation between observed and predicted values increased. In the study fits with an RMSEP ≤ 5 % were considered suitable.

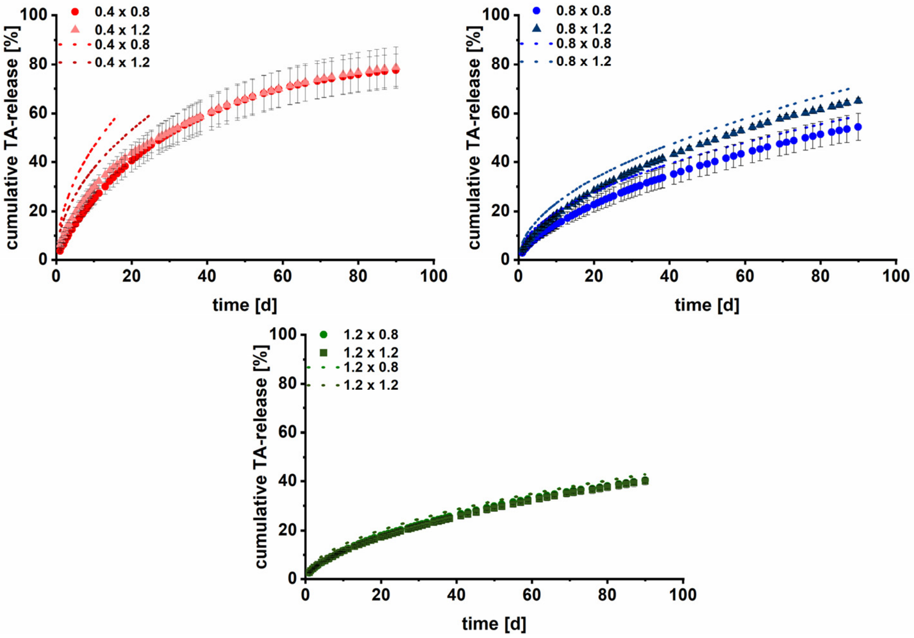

Figure 78. 8. Observed (n = 3, mean ± s; 37 ± 0.5 °C, 200 rpm, 50-75 mL HEPES pH = 7.4) and predicted dissolution curves (dotted line) for printed implants with different strand widths (first number; 0.4 mm = red; 0.8 mm = blue and 1.2 mm = green) with varying pore size (second number). Predictions are based on the surface area measured via X-ray computed tomography.

The prediction for implants with 0.4 mm strand width is not sufficient in all cases (RMSEP > 5 %). The impact of HPMC is relatively higher and the surface area determination is most prone to error. Additionally, for these implants the pore size is always 0.4 mm in z-direction (Figure 65III), resulting in non-uniform mediums perfusion and consequently a deviating dissolution kinetic. The prediction for the implants with a strand width of 0.8 mm and 1.2 mm worked for both pore sizes.

Table 17. Calculated RMSEP-values of prediction of drug release curves via the Higuchi model.

Implant (strand width x pore size)	Data set used for prediction	RMSEP [%], based on measured A	RMSEP [%], based on theoretical A
0.4 x 0.8	0.4 x 1.2	19.44	18.17
0.4 x 1.2	0.4 x 0.8	8.24	9.63
0.8 x 0.8	0.8 x 1.2	4.29	6.31
0.8 x 1.2	0.8 x 0.8	4.67	3.03
1.2 x 0.8	1.2 x 1.2	2.32	2.54
1.2 x 1.2	1.2 x 0.8	2.65	2.44

The lowest RMSEP-values were obtained for drug-loaded networks with a strand width of 1.2 mm (2.32 and 2.65 %). Surface changes induced by swelling of HPMC is - relatively seen - less pronounced with broader strand widths. Generally, the model is very sensitive. Small changes in the fit have a high impact on the predictive performance.

Based on the results the Higuchi model is a promising and simple approach to predict the drug release behaviour of parenteral matrix dosage forms with pores as only one data set per is required.

Thereby individualized product development of 3D-printed DDS is potentially facilitated. It is possible to predict the drug release with sufficient performance for one strand width. The applicability is restricted to implants with strand widths and pore sizes > 0.4 mm, as consequence of the non-uniform medium perfusion [35]. Due to the impact of the HPMC in dependency on the strand width, it might be beneficial to incorporate non-swelling pore former, e.g., salts or polyethylene glycol to predict potentially implants with deviating strand width.

To reduce the analytical and time effort of future studies, the Higuchi model was again applied. It was evaluated if based on the initial dissolution data of 15 and 30 days the drug release for the remaining time can be predicted. Therefore, the cumulative relative TA release was plotted against $\sqrt{t}$. The obtained linear regression was used to calculate the drug release for the remaining 60 or 75 days but maximum until 60 % drug release. The results of observed and predicted dissolution curves are exemplarily depicted for implants with varying strand width and a pore size of 0.8 mm in Figure 79. The R^2-values for linear fits and the respective RMSEP-values to evaluate the predictive performance for all implants are shown in Table 18. As expected, linear fits based on data points for 30 days were better compared to those based on 15 days, reflected in RMSEP-values. For all implants the goodness of predictive performance based on the data of the initial 15 days up to 60 % drug release was sufficient (RMSEP ≤ 3.15 %). Thereby the time for analysis of implants can be drastically reduced to two weeks, which is promising for future studies and quality control.

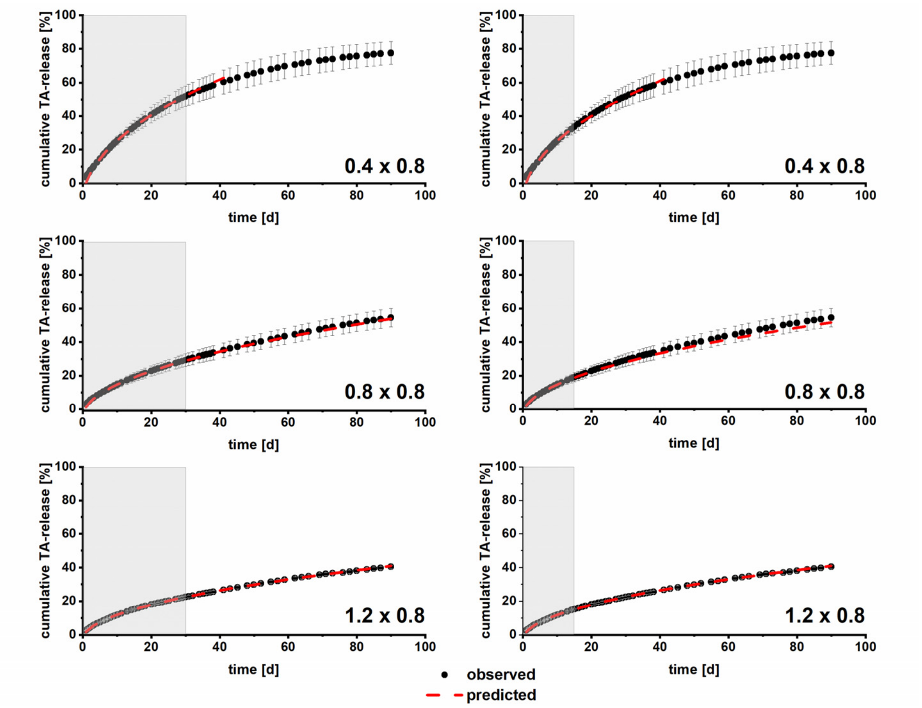

Figure 79. Exemplary observed (n = 3, mean ± s; 37 ± 0.5 °C, 200 rpm, 50-75 mL HEPES pH = 7.4) and predicted dissolution curves for F12 printed implants with varying strand width and a pore size of 0.8 mm based on drug release data of initial 30 days (left) and 15 days (right).

Table 18. R^2 values for linear fits (cumulative TA release against $\sqrt{t}$) and calculated RMSEP-values of prediction of drug release curves via the Higuchi model based on initial 30 and 15 days.

Implant (strand width x pore size)	Prediction based on initial 30 days		Prediction based on initial 15 days	
	R^2	RMSEP [%]	R^2	RMSEP [%]
0.4 x 0.4	0.9996	1.63	0.9974	2.19
0.4 x 0.8	0.9997	1.23	0.9989	0.62
0.4 x 1.2	0.9976	1.55	0.9999	3.15
0.8 x 0.4	0.9996	0.81	0.9982	0.86
0.8 x 0.8	0.9997	0.66	0.9989	1.85
0.8 x 1.2	0.9998	0.52	0.9998	1.21
1.2 x 0.4	0.9993	1.16	0.9988	1.41
1.2 x 0.8	0.9995	0.21	0.9979	0.21
1.2 x 1.2	0.9994	0.57	0.9962	0.57

3.4.7 Summary

In this chapter, a novel modular two-compartment implant design was presented, enabling an independent customization of the shape or drug release/ dose realized by CAD and applied FDM^{TM}-printing. This shows the opportunities of 3D-printing of sophisticated unique structures, which cannot be realized with conventional manufacturing methods.

The implant consists of a drug-free shell to adapt the shape and allow simultaneously a unidirectional drug release. Within the shell a drug-loaded network inlay is embedded, which can be varied in strand width and pore size to modify the dose and drug release.

In the first part of the study, nine different inlay networks were designed via CAD with varying strand width (0.4, 0.8 and 1.2 mm) and pore size (0.4, 0.8 and 1.2 mm). Thereby, the flexibility of 3D-printing to modify the TA release was examined. It was demonstrated that dual printing of different network structures was feasible to enable manufacturing of two-component implant composited of the drug-free shell and the TA-loaded inlay with sufficient resolution. Implants with mass variations below 2.5 % were obtained. The dose could be varied between 13 mg and 46 mg depending on the network structure. Another approach to adapt the dose might be the object size, while keeping the strand width and pore size constant.

In long-term drug release studies over three months using a newly developed set-up, it has been successfully shown that the TA release could be varied using the same starting material. It can be concluded that using the developed modular implant concept - realized via FDM^{TM}-printing - is promising to optimize and individualize the parenteral therapy of TA.

Clinically relevant doses between 8.6 and 22 mg TA were liberated. With decreasing strand widths, the relative TA release was considerably increased. Further, the dissolution kinetics was influenced by the pore size and resulting medium perfusion. Above 0.8 mm the pore size seemed to be not rate-limiting anymore. The TA release acceleration compared to filaments was slower than expected due to the unidirectional drug release. However, it was shown that the drug release can be easily adapted by changing the network structure using CAD.

Compared to a marketed crystal suspension (Volon® A) TA release was successfully prolonged and consequently the residence time within the joint cavity might be drastically increased. Using the novel 3D-printed implants, the TA therapy efficiency is potentially improved, while decreasing systemic adverse drug effects. *In vivo* studies are however to be conducted in order to verify obtained results.

A prediction based on mathematical modelling is promising for individualized therapy and accelerated quality control of extended-release parenteral DDS. Different factors, such as unidirectional drug release, non-uniform medium perfusion at lower pore sizes and the impact of HPMC depending on the strand width limited the predictive performance of mathematical models based on Peppas-Sahlin, Weibull and Higuchi. However, predictions based on Higuchi for one strand width and different pore sizes (> 0.4 mm) based on one data set of implants was feasible to a limited extent. The use of different non-swellable pore former might expand the applicability of the model.

A prediction based on the dissolution data of the initial 15 days was feasible until 60 % drug release for all implants, considerably facilitating the development and reducing the analytical effort.

4. Summary

The aim of the presented work has been the development of customizable drug-loaded implants via fused deposition modelling (FDM^{TM}), addressing all phases of classical drug dosage form development. Triamcinolone acetonide (TA) was chosen as model active pharmaceutical ingredient (API) as it shows a need for individualized treatment and improvements related to therapy efficiency and systemic side effects for parenteral intraarticular (i.art.) applications.

First, an implant concept was designed to define the formulation requirements. For the first time, a modular two-compartment implant concept was established, consisting of a drug-free shell for shape adaption to individual anatomical structures and a drug-loaded inlay to personalize dose and drug release behaviour independently.

As for the 3D-printing technology FDM^{TM} a filament as starting material is required, the initial part of the work focused on a systematic formulation development of a drug-free and a TA-loaded printable filament via twin-screw hot-melt extrusion (HME). Therefore, the mechanical properties and targeted drug release behaviour over several months were taken as critical selection attributes based on an adjusted concept of Korte [109]. Ethyl cellulose (EC) was selected as sustained-release polymer to allow a strong retardation effect. Plasticizers were necessary to improve processability related to melt viscosity during HME. They needed to be incorporated to achieve sufficient mechanical resilience of filaments to be processed inside the print-head as key attribute for printability. Further, the handling during continuous filament production was taken into consideration to allow a winding on spools for proper storage and continuous feeding during 3D-printing. Two different plasticizers, the solid stearic acid and liquid triethyl citrate (TEC) were investigated in different concentrations. Drug-free and TA-loaded filament formulations with 10 % TEC as plasticizer resulted in the best overall performance. They showed appropriate mechanical properties with sufficient stiffness in longitudinal direction, expressed in an increased Young's modulus and a reduced brittleness in transversal direction expressed in a high distance at break.

Once a suitable base filament was found, hypromellose (HPMC) was successfully incorporated as pore former in different concentrations to accelerate the TA release from the strong sustaining EC-matrix. The mechanical properties remained sufficient to ensure printability. Concentrations of 15 and 25 % HPMC appeared most promising based on the estimated time for drug release via the Higuchi model.

Afterwards, a rational HME process analysis for optimization of the filament production was performed related to critical quality attributes of filaments and printed dosage forms using a drug-free formulation consisting of EC, 10 % TEC and 15 % HPMC. This was done to obtain high-quality filaments and subsequently printed, sophisticated implant geometries, meeting the requirements of the European Pharmacopoeia (Ph.Eur.). The diameter homogeneity was identified as key attribute. A winder was successfully implemented in advance into the extrusion line to establish a reproducible continuous pharma-grade filament production towards manufacturing within the pharmaceutical industry.

In the systematic analysis, the specific feed load (> 0.04) as dimensionless surrogate for the barrel filling degree was identified as key parameter for homogenous melt transport and consistent filaments with low diameter variations. A threshold of diameter variations (interquartile range (IQR) ≤ 0.041 mm) was empirically determined. IQR-values > 0.041 mm negatively affected the critical quality attributes of filaments (distance at break) printed test-geometries (mass uniformity according to Ph. Eur. 2.9.5). The gained knowledge is an important step forward in terms of throughput upscale and simplified process development for filament production.

Drug-free and TA-loaded filaments were successfully manufactured using the optimized extrusion settings. Filaments with low diameter variations and homogenous drug distribution were obtained. The stability analysis according to the International Council for Harmonisation of Technical Requirements for Pharmaceuticals for Human Use (ICH) Guidelines Q1A (R2) revealed an impact of water absorption and plasticizer evaporation during storage on filament quality. Packaging in sealed aluminium sachets was found to keep the initial quality over at least six months.

To assess the TA release from novel parenteral dosage forms, analytical development of a dissolution set-up for long-term studies over several months was performed. During studies it was found that TA degrades rapidly in the commonly used phosphate-buffered saline at pH 7.4.

After degradation studies in different dissolution media, 4-(2-hydroxyethyl)-1-piperazineethanesulfonic acid (HEPES) buffer was identified as suitable medium to reduce distinctly the decomposition rate. A method protocol with frequent medium change and simplified quantification next to simultaneously proceeding degradation based on the extinction coefficient was established. A so-called “sample and separate set-up” was developed to allow an investigation of multiple implants at reduced volume over an extended period.

Finally, innovative two-compartment modular implants were designed via computer-aided design and successfully manufactured via FDM^{TM}-printing to enable a customizable therapy over several months. The drug-free filament consisting of EC, 10 % TEC for the impermeable shell and the drug-loaded formulation containing additionally 10 % TA and 25 % HPMC for the drug-loaded inlay were used. By changing the strand width and pore size of the TA-loaded network inlay the TA release could be modified and varied between 20 and 80 % over three months.

Compared to current TA therapy options for i.art. application the release was drastically extended. Novel 3D-printed implants are therefore promising to improve therapy efficiency of the model API.

A prediction of drug release from the implants based on the Higuchi model was partially feasible. Limitations are caused by kinetic changes due to inhomogeneous medium perfusion, impact of HPMC and the unidirectional drug release. Using the dissolution data of the initial 15 days, the drug release of all implants for the remaining 75 days (maximum up to 60 % drug release) could be described accurately with root mean squared error of prediction values ≤ 3.15 %. Hence, time-consuming drug release studies also in the context of quality control can be avoided.

It can be stated that the development of customizable implants related to shape, dose and drug release was performed successfully. The generated knowledge in the present work is an important step towards continuous filament production and simplified drug product development while establishing 3D-printing as novel technology for individualized and optimized parenteral therapy.

5. Experimental Part

5.1 Pretext

Parts of the methods were already published in a peer-reviewed journal. Sections, tables and figures were partially extended and linguistically adapted.

I. Ponsar H., Wiedey R., Quodbach J., 2020. *Hot-Melt Extrusion Process Fluctuations and their Impact on Critical Quality Attributes of Filaments and 3D-printed Dosage Forms*. Pharmaceutics. 12(6): p. 511.
DOI: 10.3390/pharmaceutics12060511

5.2 Materials

Table 19. Model drug

Substance	Abbreviation	Source of supply
Triamcinolone acetonide, micronized	TA	Caelo, Hilden, Germany

Table 20. Substances used for HME manufacturing of filaments.

Substance	Trade Name/Grade	Abbreviation	Source of supply
Ethyl cellulose	Aqualon® N10	EC	Ashland, KY; USA
Hydroxypropyl methylcellulose	Metolose 60SH 50	HPMC	Shin Etsu, Tokyo, Japan
Triethyl citrate	Citrofol AI Extra	TEC	Jungbunzlauer, Basel, Switzerland
Stearic acid	Baerocid SP-1 A	SA	Bärlocher, Ludwigshafen, Germany
Fumed silica	Aerosil 200 VV Pharma	-	Evonik, Darmstadt, Germany

Table 21. Materials for drug-free 3D-Printing

Substance	Trade Name/Grade	Source of supply
PLA Filament	Prusament PLA, galaxy silver	Prusa Research, Prague, Czech Republic

Table 22. Substances used for analytical methods.

Substance	Grade	Abbreviation	Source of supply
Acetonitrile	HPLC Grade	ACN	Fisher Chemicals, Hampton UK
Ethanol, absolute	p.a.	EtOH	Fisher Chemicals, Hampton, UK
Distilled (ultrapure) water	-	-	freshly prepared via Barnstead MicroPure System (Thermo Fisher Scientific, Massachusetts, USA)
Potassium dihydrogen orthophosphate	p.a.	-	Fisher Chemicals, Hampton, UK
Trometamol	p.a.	TRIS	VWR, Pennsylvania, USA
4-(2-hydroxyethyl)-1-piperazineethanesulfonic acid	bioreagent	HEPES	Fisher Chemicals, Hampton, UK
Sodium pyrosulfite	p.a.	SPS	AppliChem Panreac, Darmstadt, Germany
Sodium hydroxide 1M	p.a.	-	Fisher Chemicals, Hampton, UK
Orthophosphoric acid	p.a.	-	Fisher Chemicals, Hampton, UK

Table 23. Used buffer and media according to the Ph.Eur. 9.0.

Buffer	Substance	Abbreviation
Phosphate-buffered saline pH 7.4 (0.05 M)	Potassium dihydrogen orthophosphate	PBS
Phosphate-buffered saline pH 7.4 (0.05 M) + SPS*	Potassium dihydrogen orthophosphate, sodium pyrosulfite	PBS + 0.1 % SPS
Trometamol buffer pH 7.4 (0.5 M)	Trometamol	TRIS
HEPES buffer pH 7.4 (0.1 M) **	4-(2-hydroxyethyl)-1-piperazineethanesulfonic acid	HEPES

* SPS was added as antioxidant (not described in the Ph.Eur.)

** according to the Ph. Eur. 9.0 HEPES pH 7.5 labelled, pH adjustment was changed to pH 7.4

Table 24. Substances for synthesis of TA 21-aldehyde hydrate (impurity C)

Substance	Grade	Source of supply
Copper (II) acetate	p.a.	Merck, Darmstadt, Germany
Disodium edetate	p.a.	Merck, Darmstadt, Germany
Sodium sulphate anhydrous	p.a.	Merck, Darmstadt, Germany
Dichloromethane	p.a.	Fisher Chemicals, Hampton, UK
Methanol	p.a.	Fisher Chemicals, Hampton, UK

Table 25. Chemical reference standards

Substance	Composition	Source of supply
Triamcinolone acetonide	-	EDQM, Strasbourg, France
Triamcinolone acetonide for system suitability	TA, TA 21-aldehyde hydrate (impurity C), Δ14-TA (impurity B)	EDQM, Strasbourg, France

5.3 Manufacturing Methods

5.3.1 Preparation of Powder Blends

To produce powder blends, fumed silica was sieved through a 355-µm-sieve prior weighing to remove powder agglomerates. Powder components, usually the API, polymers, fumed silica and solid plasticizer (if used) were blended in a Turbula® mixer (T2C, W.A. Bachofen, Switzerland) for 30 min. The exact formulation compositions can be found in Table 1. Formulations and batch sizes varied for different studies (Table 26).

Table 26. Formulations used in different sections, including study names and batch sizes.

Study		Formulation	Batch size [g]	Section
Formulation development		F1-F12	300-600	3.1.4.1/ 3.1.5.2
Winder implementation		F13	300-1000 (2 x 500)	3.2.3.2
Process analysis and optimization	Influence of PFR	F13	400	3.2.3.3/ 3.2.3.4
	Influence of screw speed		500/ 400	
	Influence of SFL		500	
Long-term stability		F11	400	3.2.6
		F12	400	
Filaments for printing of implants for drug release studies		F12	500	3.4.3
		F6	500	

5.3.2 Filament Production via Hot-Melt Extrusion

5.3.2.1 Twin-Screw Hot-Melt Extrusion for Formulation Development

For the manufacturing of printable filaments powder blends were fed gravimetrically (KT 20, K-Tron Soder, Switzerland) into the tempered extruder barrel. The dosing device was internally calibrated prior each extrusion. HME was performed using a 16 mm 40D co-rotating twin-screw extruder (Pharmalab HME 16, Thermo Fisher Scientific, Germany) equipped with a 1.75 mm die (thickness 4.4 mm). For the formulation development (section 3.1) filaments were stretched and cooled behind the extruder outlet on a conveyor belt (model 846102.001, Brabender, Germany) to achieve the targeted diameter, which was monitored inline (section 5.5.6). For the determination of the CBS the time for one-meter conveyance was measured on predefined levels in triplicates. In Figure 80A, the obtained calibration is depicted.

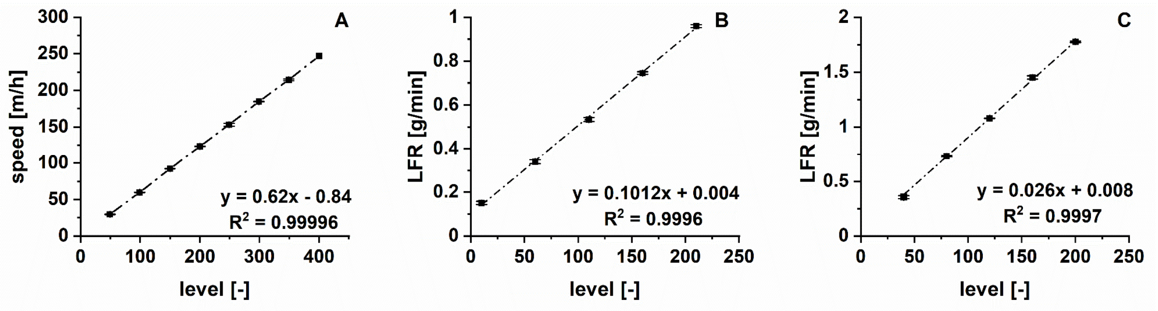

Figure 80. Calibration of CBS (A), LFR of TEC with a peristaltic (B) and a micro annular gear pump (C) as function of level (n = 3, mean ± s).

For F5-F13 the liquid plasticizer TEC was used. During the formulation development studies (section 3.1) TEC was fed via a peristaltic pump (Minipuls 2, Gilson, USA) into the barrel. For the subsequent studies this was replaced by a micro annular gear pump (MZR 7205, HNP Mikrosysteme, Germany) equipped with a nozzle of 0.12 mm inner diameter to ensure a constant liquid flow. The LFR (g/min) of TEC was gravimetrically determined prior each extrusion using an analytical balance (CP 224S, Sartorius, Germany). The corresponding calibration functions for the respective pump are exemplarily depicted in Figure 80B and C. The PFR was 5 g/min and the screw speed 30 or 35 rpm. Screw configuration I, applied during formulation development, is displayed in Figure 81. The extrusion set-up used for formulation development is schematically depicted in Figure 13.

The applied barrel temperatures and the conveyor belt speed were adjusted individually for the respective formulation (Table 2 and Table 3). Sampling of filaments was started once process equilibrium was reached, indicated by a constant material pressure and power consumption. The material pressure and -temperature were measured at the die (2075J-D8-100B, Terwin, UK). Process parameters and PFR were recorded with a sampling rate of 1 Hz using an in-house written LabVIEW 2015 application (National Instruments, Texas, USA).

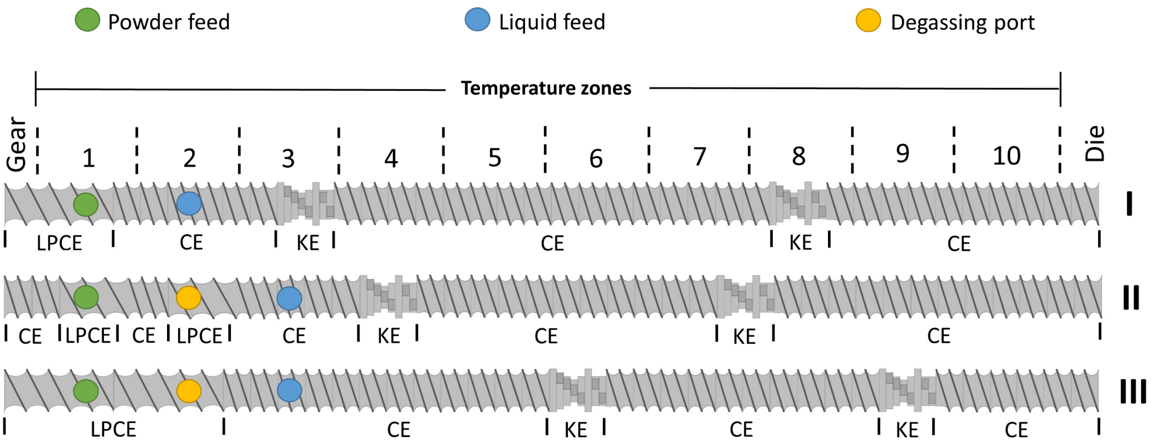

No.	Screw configuration: gear → die
I	4D LPCE – 6D CE – 1D KE 4 x 30° – 1D KE 4 x 60° – 16D CE – 1D KE 4 x 30° – 1D KE 4 x 60° – 10D CE
II	2D CE – 2D LPCE – 2D CE – 2D LPCE – 5D CE – 1D KE 4 x 30° – 1D KE 4 x 60° – 11D CE – 1D KE 4 x 30° – 1D KE 4 x 60° – 12D CE
III	8D LPCE – 12D CE – 1D KE 4 x 30° – 1D KE 4 x 60° – 10D CE – 1D KE 4 x 30° – 1D KE 4 x 60° – 6D CE

Figure 81. Screw configurations (I, II and III) applied during HME with indicated barrel and temperature zones (1-10). LPCE = long pitch conveying elements (helix of 3/2 L/D), CE = conveying elements (helix of 1 L/D); KE = kneading elements.

5.3.2.2 Twin-Screw Hot-Melt Extrusion Coupled with a Winder

For process analysis/ -optimization and subsequent filament production for stability analysis and printing of implants (section 3.2, 3.2.6 and 3.4.3) the described HME set-up was expanded by a winder (Model 846700, Brabender, Germany). This enabled a more precise and reproducible diameter adaption. The winder consists of a traverse, a haul-off and a winder unit (rotatable spool) as schematically depicted in Figure 82.

The adapted extrusion set-up is visualized in Figure 31B. Extrusion set-up was described in section 5.3.2.1 and only changes are described in this section. The extruder was equipped with a 1.85 mm die (thickness: 4.4 mm). Behind the die, obtained filaments were cooled on a static conveyor belt between extruder and winder.

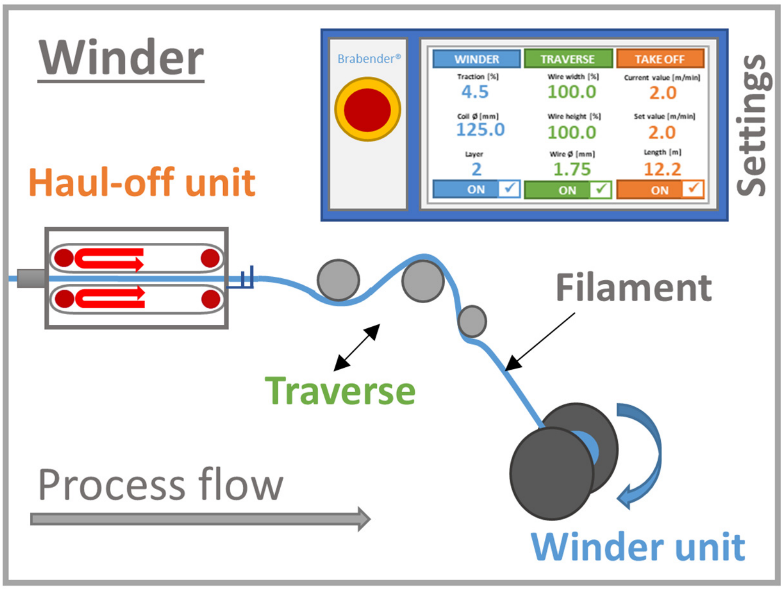

WINDER	TRAVERSE	TAKE OFF
Traction [%] 4.5	Wire width [%] 100.0	Current value [m/min] 2.0
Coil Ø [mm] 125.0	Wire height [%] 100.0	Set value [m/min] 2.0
Layer 2	Wire Ø [mm] 1.75	Length [m] 12.2
ON ✓	ON ✓	ON ✓

Figure 82. Schematic extrusion line extension to the Brabender® winder.

Via the haul-off unit of the winder, filaments were stretched to obtain the target diameter of approx. 1.75 mm. The haul-off speed was adjusted to the PFR as indicated in the respective section. For the implementation studies of the winder (section 3.2.3.2), filaments were wound up on a 125 mm spool with a traction of 4.5 % (percentage of the maximum engine power).

For the rational HME analysis process parameters varied as presented in Table 4 and Table 6. Filament formulations F6, F11 and F12 were produced with a PFR of 5 g/min and a screw speed of 20 rpm. For the process analysis and optimization screw configuration II was used and a degas port was implemented to enable evaporation of TEC-vapor (Figure 81). Afterwards, this was further optimized for filament production for subsequent implant printing (F6, F11 and F12). Further TEC evaporation was reduced by the adaption of the barrel temperature as depicted in Table 27. Therefore, the screw configuration was adapted (screw configuration III, Figure 81).

Table 27. HME barrel temperatures and haul-off speeds applied for the different filaments during and after process analysis.

Formulation	Barrel temperature from zone T1 (gear) to T10 (die) [°C]										Haul-off speed [m/min]
	T1	T2	T3	T4	T5	T6	T7	T8	T9	T10	
F6, F12	-	30	80	120	170	180	180	190	190	190	2.1
F11	-	30	80	120	170	180	180	190	190	190	2.0
F13	-	30	100	170	170	180	180	190	190	190	2.0-4.1*

* haul-off speed was systematically varied for process analysis (section 3.2)

5.3.3 Fused Deposition Modeling (FDM^{TM})

5.3.3.1 3D-Model Processing

For 3D-printing of test geometries and implants, 3D-models were designed using the CAD software Inventor® Professional 2019 (Autodesk®, San Rafael, USA). The CAD-models were converted into *.stl*-files and further processed for 3D-printing using a slicing software. For the simple test geometries (Figure 42, section 3.2.3.4 and 3.2.5.2) the open-source software Slic3r Prusa Edition (Prusa, Prague Czech Republic) was used. Processing the more complex two-component implants, the Simplify3D® software (Ohio, USA) was required, since additional settings for print realization were needed. The G-codes were generated based on the *.stl*-files, dividing the objects into layers and containing the instructions for the 3D-printer operations (print, printer and filament settings). The applied slicing and printing settings were adapted for the respective aim of the study and the used filament formulation. In Table 28, an overview of the most important print parameters is depicted. In the appendix, the detailed slicing parameter can be found for each slicing software and dosage form (Table 31 and Table 32). The filament diameter was adapted for each batch prior printing.

Table 28. Overview of the printing processes, including printer and applied slicing parameters.

Settings	Rectangular test objects (sections 3.2.3.4 and 3.2.5.2)		Two-component implants (section 3.4.3)			
	Commercial Filament	EC/HPMC based Filament	Drug-free shell	Drug-loaded network inlays		
				0.4 mm	0.8 mm	1.2 mm
Software	Slic3r Prusa Edition		Simplify3D			
Filament	PLA	F11, F12, F13	F6	F12	F12	F12
Printer	Prusa i3 MK3	Prusa i3 MK3	Prusa i3 MK3S + MMU2S			
Print temperature [°C]	210	180	185	185	185	185
Build plate temperature [°C]	60	90	90	90	90	90
Nozzle diameter [mm]	0.4		0.4			

Settings	Rectangular test objects (sections 3.2.3.4 and 3.2.5.2)		Two-component implants (section 3.4.3)			
	Commercial Filament	EC/HPMC based Filament	Drug-free shell	Drug-loaded network inlays		
				0.4 mm	0.8 mm	1.2 mm
Layers and perimeters						
Layer height (first layer height) [mm]	0.1 (0.1)	0.1 (0.1)	0.2 (0.2)	0.2 (0.2)	0.2 (0.2)	0.2 (0.2)
Perimeters	1	1	1	0	1	1
Solid layers (top and bottom)	0	0	0	0	0	0
Seam position	nearest	nearest	nearest	nearest	nearest	nearest
Infill						
Infill density [%]	85	85	100	100	100	100
Fill pattern	rectilinear	rectilinear	rectilinear			
Fill angle [°]	90	90	45	90	90	90
Speed [mm/s]						
Perimeters	15	15	25	10	20	15
Infill	15	15	20	8	16	12
Travel	180	180	80	120	80	120
First layer	15	15	12.5	10	10	15
Others						
Extrusion width [mm]	0.45	0.45	0.39	0.39	0.4	0.4
Infill/perimeter overlap [%]	25	25	5	N/A	5	5
Ooze shield	no	no	yes	yes	yes	yes

5.3.3.2 3D-Printing

3D-printing of test geometries and implants were performed using the FDM™ printing technology. Depending on the printed dosage form, two different Prusa-3D-printer were utilized (Prusa Research, Prague, Czech Republic, Table 28). Both were equipped with a polyetherimide print bed. For the printing of one-component test objects the printer model Prusa i3 MK3 was used.

The printing of the two-component implants (F6, F12) was performed using the Prusa i3 MK3S. This FDM™ printer was equipped with a MMU 2S, which consists of an automatic filament changer, enabling a dual component print. An ooze shield was printed around the implant to prevent cross-contamination between F6 and F12 after filament change during printing as depicted in Figure 67 (section 3.4.3).

5.4 Data Handling, Graphing and Statistical Analysis Methods[1]

Data evaluation related to arithmetic operations and conventional statistical analysis were performed using Microsoft Excel 2016 (Microsoft Cooperation, Redmond, USA). Two-sample t-tests were performed with Origin Pro 2019/2020 (OriginLab Corporation, Northampton, USA) on a significance level of $\alpha = 0.05$.

The bootstrap analysis used in section 3.2.3.3 was conducted to test the statistical differences of IQRs using the software tool R (Version 3.6, R Core Team, Vienna, Austria). As the distribution function of the dataset was not known, conventional statistical tests were not applicable. Therefore, data sets to be analysed were combined and bootstrap samples were taken with replacement. The combined set was split into two parts and the respective IQR was calculated. Subsequently, the differences in IQR were determined. The described process was repeated 100,000 times to generate the distribution of all possible differences in IQR (based on the assumption the two datasets belong to the same population). By calculating in how many of the 100,000 cases the observed difference in IQR was as high or higher than the observed value, the p-value was determined.

Data depiction was performed with Origin Pro 2019/2020 (OriginLab Corporation, Northampton, USA). Depicted chemical structures were drawn using ChemDraw® Professional 19.1 (PerkinElmer Informatics, Waltham, USA).

5.5 Analytical Methods

5.5.1 Particle Size Distribution

The particle size distribution of the TA and excipients was determined (n = 3) using laser diffraction with the dry dispersion unit Aero S (Mastersizer 3000, Malvern Panalytical, Malvern, UK). The Fraunhofer approximation was used for the data evaluation. The dispersion pressure of 3.0 bar was selected to deagglomerate potential powder agglomerates.

5.5.2 Helium Density

The true density of formulations was determined (n = 3) via helium pycnometer (AccuPyc 1330, Micromeritics, Norcross, GA, USA) equipped with a water bath (Paratherm, King of Prussia, USA) for temperature control (25 ± 0.1 °C). A sample chamber of 3.5 cm^3 volume filled with ~1 g of formulation was selected for measurements. The sample weight was determined using an analytical balance (MC210 P, Sartorius, Goettingen, Germany). Measurement accuracy was calibrated with a cube of defined volume on each measurement day.

---

[1] The bootstrap analysis was performed together with Dr. Raphael Wiedey at the Institute of Pharmaceutics and Biopharmaceutics at the Heinrich Heine University Duesseldorf.

5.5.3 Scanning Electron Microscopy (SEM)

Scanning electron microscopy (SEM) was carried out using a Phenom G2 pro (Phenom World, Eindhoven, The Netherlands) to visualise surface morphology of extrudates with different HPMC contents (F9-F12, Table 1). A voltage of 5 to 10 kV was applied. Filament samples were attached to aluminium stubs with double-sided carbon tape. Gold-sputter-coating before measurements was not required, as no charging effects were observed.

5.5.4 Offline Analysis of Powder Feed

5.5.5 Offline Analysis of Powder Feed Accuracy

Within the scope of the HME process analysis (section 3.2.3), the dosing accuracy of the loss-in-weight powder feeder (KT 20, K-Tron Soder, Switzerland) at a PFR 5 g/min was examined. An offline dosing experiment was performed. For this purpose, the powder mixture F13 was fed on a pan placed on an external analytical balance (Sartorius CP 1224, Goettingen, Germany) connected to a computer. The software SartoConnect 3.5.2 (Sartorius, Goettingen, Germany) was used to record the fed mass as function of time in Microsoft Excel 2016 (Microsoft, Corporation, Redmond, USA). A sampling rate of 0.5 Hz was chosen for the determination of the PFR over 60 min. For the evaluation of the data, the absolute mass error and the normalized absolute mass error were determined according to Meier et al. [187]. As the true fed mass scattered around the set value, the integrals between actual and set feed rate could be calculated. Therefore, sections of underdosed (-) and overdosed (+) fed powder mass were determined. Sectionalized negative and positive mass errors were plotted as function of time intervals. Subsequently, the normalized absolute mass error was determined, by dividing the individual absolute mass errors by the set fed mass in the respective time interval.

5.5.6 Diameter and Ovality Determination of Filaments

The filament diameter was monitored and recorded inline using a laser-based measurement module (Laser 2025 T, Sikora, Bremen, Germany), consisting of three lasers as depicted in Figure 16. Thereby, the diameter cross-sections were recorded in three different directions with a sampling rate of 1 Hz, also captioning shape information. For data evaluation and the calculation of the cross-sectional area for the YM determination, the smallest measured diameter was used. For the feasibility study of the winder (section 3.2.3.2) the filament diameter was measured offline after the winding process again. The filament was conveyed with the same haul-off speed as during extrusion. The ovality of the filament cross-sections was calculated as difference between the minimum and maximum recorded diameter per second.

For the initial extrusion line set-up during formulation development the laser was placed behind the conveyor belt. After the winder implementation and process set-up optimization it was located between the cooling section and the haul-off unit of the winder. For comparison purposes, the diameter of commercial PLA-filament was measured over 300 s with a winder haul-off speed of 2.0 m/min.

5.5.7 Mechanical Characterization

5.5.7.1 General

The mechanical properties of self-produced filament were investigated using a Texture analyser (TA.XT plus, Stable Micro Systems, Godalming, UK). The applied testing regime was adopted from Korte and Quodbach [27]. The YM in combination with the DaB were determined for the characterization of filaments for 3D-printing. The applied test set-up, settings and data evaluation were used according to [27, 28]. For representative sampling, filament sections from the beginning, the middle and the end of the extrusion process were selected. Samples were tested one day after manufacturing to avoid changes during storage except for stability analysis (section 3.2.6).

5.5.7.2 Young's Modulus

The Young`s Modulus (YM) is a measure for the stiffness of filaments in longitudinal direction [27]. A tensile test was performed for the determination of the YM (n = 6). Therefore, filament sections of 20 mm length were fixed between two holders (90° offset orientation) containing a groove for test specimen. A torque of 1 Nm was chosen to ensure consistent test conditions and sufficient fixation without breakage or shifting. The experimental set-up is depicted in Figure 83. Using a test speed of 0.01 mm/s, the elongation and corresponding forces were measured and recorded with the Exponent software 6.1.5.0 (Stable Micro Systems, Godalming, UK). Corresponding tensions were calculated by dividing the measured forces by the respective cross-

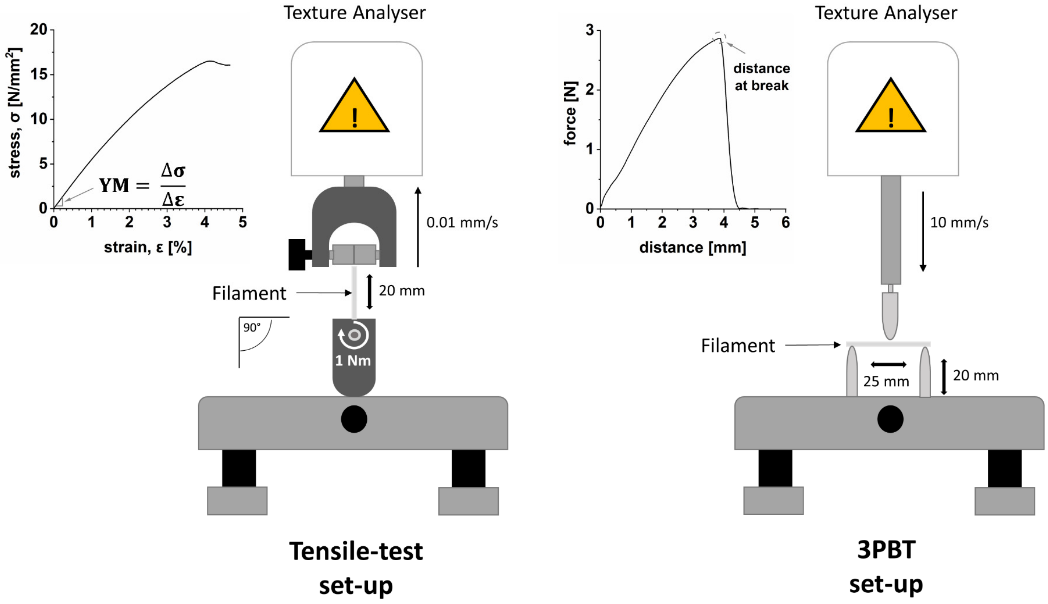

Figure 83. Texture analyser set-up for the determination of mechanical properties (tensile test and 3PBT) and corresponding recorded curves.

sectional area of filaments. The YM was calculated as slope between 0.05 and 0.25 % elongation in obtained stress-strain curves according to DIN EN ISO 527-1 (Figure 83) [173]. All samples showed linear elastic behaviour $\leq$ 0.25 % strain.

5.5.7.3 Distance at Break

The distance at break (DaB) as measure for brittleness of extrudates was determined in a three-point bend test (3PBT, n = 6) according to [28]. Therefore, filament sections of approx. 30 mm were placed on two holders 25 mm (= test length) apart. The U-shaped test-probe of the texture analyser moved down with a speed of 10 mm/s to load filaments centrically. The experimental set-up is depicted in Figure 83. The applied force upon initial resistance due to first filament contact was measured as function of distance. The DaB was defined as distance triggering filament breakage (Figure 83). Filaments without breakage under selected test conditions were classified as "not breakable". During initial formulation development as described in section 3.1.4.2.3 a test-probe immersion depth of 5 mm was chosen according to Korte et al. [27], which was afterwards extended to 19 mm to be able to see differences with less brittle filaments.

5.5.8 Printability of Filaments

Printability of filaments is restricted to the feeding performance as described in section 3.1.4.2.3. For the assessment, the filaments were fed through the print-head at the temperatures displayed in Table 28. Printability was given if constant conveying without breakage or deformation was possible.

5.5.9 Confocal Raman Microscopy[2]

For surface and composition analyses of filaments, topographic Raman images and spectra of filaments were recorded using a WITec alpha 300 R confocal Raman microscope (WITec, Ulm, Germany), equipped with a 532 nm excitation laser, a UHTS 300 spectrometer and an iDus Deep Depletion CCD detector (Andor, Belfast, UK). Using a 600 g/mm grating, a spectral range from 68 to 3742 cm^{-1} was recorded with an average spectral resolution of 3.8 cm^{-1}/pixel. For each sample, an area of 200 x 200 µm with a spatial resolution of 1 µm was measured. Using an exposure time of 0.2 s, 40000 Raman spectra could be measured in 40 min. During the measurement, the laser power at 532 nm was set to 20 mW. A 100x/0.9 NA objective was applied for formulations F9 and F10, whereas a 50x/0.8 NA objective was used for formulations F11 and F12. The reason for the change of the microscope objective was the higher surface roughness with increasing HPMC content. The lower magnification of the microscope objective allows a larger depth of field for topographic measurement of rough sample surfaces.

---

[2] Measurements and parts of the data evaluation were performed by Dr. Björn Fischer at the Institute of Pharmaceutics and Biopharmaceutics at the Heinrich-Heine University in Düsseldorf.

5.5.10 Differential Scanning Calorimetry (DSC)[3]

For thermal analysis samples of powders (API, polymers, solid plasticizer) and filaments were measured via DSC (DSC 1, Mettler-Toledo, Columbus, OH, USA). Samples of approx. 5 mg were weighed on an analytical balance (XP56, Mettler Toledo, Columbus, OH, USA) and analysed (n = 2) in a sealed aluminium pen with a punctured lid. The raw materials were subjected to two heating cycles, whereas for filaments only one heating step was applied. The temperature profiles for the formulations and applications are depicted in Table 29. The data evaluation and determination of thermal events (glass transition and melting temperature (T_g and T_m) were conducted using the STAR® software (Version 9.20, Mettler-Toledo, Columbus, OH, USA).

Table 29. Applied temperature profiles for DSC in the respective section. *Pre-heating to remove residual water.

Material classification	Sample	Heating and cooling profile	Section
Raw materials	TA	60 °C, 30 min* 0-310 °C, 20 K/min 310-0 °C, 20 K/min 0-310°C, 20 K/min	3.1.4.2.1
	EC	0-200 °C, 10 K/min 200-0 °C, 20 K/min 0-200 °C, 20 K/min	3.1.4.2.1
		60 °C, 30 min* 0-310 °C, 20 K/min 310-0 °C, 20 K/min 0-310°C, 20 K/min	3.1.5.3.2
	HPMC	60 °C, 30 min* 0-310 °C, 20 K/min 310-0 °C, 20 K/min 0-310°C, 20 K/min	3.1.5.3.2
	SA	0-120 °C, 20 K/min 120-0 °C, 20 K/min 0-120 °C, 20 K/min	3.1.4.2.1
Filaments	F4, F6	-20-220 °C, 10 K/min	3.1.4.2.1
	F9, F11, F12	-20-220 °C, 20 K/min	3.1.5.3.2
	F6	-20-220 °C, 20 K/min	3.2.6
	F11, F12	-20-300 °C, 20 K/min	3.2.6

5.5.11 Static Vapor Sorption Measurement

A dynamic vapor sorption system (SPS11, ProUmid, Ulm, Germany) was used to determine the evaporation of the plasticizer TEC during filament storage. Therefore, pure excipients (n = 1; TEC n = 2) of the formulation as reference and filament formulations F6, F11, F12 (n = 2, 10 x ~3 cm filament length) were subjected to the analysis. Until the measurement, filaments were stored at RT in sealed aluminium sachets in a climatic room. Samples were measured at constant settings with 40 °C and 40 % rH to investigate the plasticizer evaporation under defined conditions over 21 days.

---

[3] Measurements and parts of the data evaluation were performed by Karin Matthée and Andrea Michel at the Institute of Pharmaceutics and Biopharmaceutics at the Heinrich-Heine University in Düsseldorf.

40 % rH was selected to minimize the impact of the relative humidity and subsequent water absorption. Each sample was measured every ten min. The potential plasticizer evaporation was evaluated as weight loss (%) as function of time and potential simultaneous water absorption as weight gain [%].

5.5.12 Triamcinolone Acetonide Assay

5.5.12.1 Pretext

For the determination of triamcinolone acetonide (TA) concentration in different studies, two assay methods were applied. In Table 30, the used methods for the respective studies, purposes and associated sections are depicted. During initial formulation development and the first month of filament stability analysis UV-spectroscopy was used. In the further course and during dissolution studies this was replaced by HPLC.

Table 30. Overview of the applied TA assay methods for different studies, purposes and corresponding sections.

Study	Purpose		Method	Section	
				Sample preparation	Results and Discussion part
Formulation development	Preliminary TA release from filaments, incl. residual content determination		UV	5.5.22.1	3.1.4.2.4 3.1.5.3.5
Triamcinolone acetonide assay	Drug distribution along the filament		UV	5.5.12.2	3.2.5.1
	Content uniformity of printed test objects		HPLC	5.5.12.3 5.5.13	3.2.5.2
Stability analysis of filament formulations	Content analysis	0-1 month	UV	5.6	3.2.6.4
		3, 6 months	HPLC		
Development of an appropriate dissolution method	Determination of TA solubility		UV HPLC	5.5.18	3.3.2.1 3.3.2.3
	Degradation analysis		HPLC	5.5.19	3.3.2.2 3.3.2.3
Modelling and modification of drug release	Dissolution tests		HPLC	5.5.22.2 5.5.22.3	3.4.4

5.5.12.2 UV-Spectroscopy

The application of UV/Vis-spectroscopy for different purposes can be found in Table 30.

For content analysis, sections were taken over the whole filament length (~ 200 mg, n = 6) ensuring representative sampling. Extrudates were dissolved in 100 mL ethanol 90 % [w/w] at ~40 °C using sonification until a colloidal solution was obtained. Samples were filtered through a 0.45 µm pore sized polypropylene (PP) membrane filter (VWR, Leuven, Belgium) prior further dilution to remove undissolved polymer. Dilution (1:10) was performed to fit the range of the calibration function (5-30 µg/mL) (Figure 84). For the determination of residual TA content in intact EC-matrices after preliminary drug release studies (n = 3), samples were treated similarly. Measurements were either performed using the UV-spectrometer Lambda 25, (PerkinElmer, Waltham, USA) or UV-1800 (Shimadzu, Kyōto, Japan) at a wavelength of 238 nm. Each solution was measured in triplicates. Calibration was performed on each measurement day, showing a coefficient of determination > 0.999 to quantify TA amount in samples. A blank solution of drug-free extruded EC-matrix showed a minimal absorption at 238 nm, since it is colloidally dissolved, indicated via laser scattering. For this reason, an ethanolic blank solution with corresponding EC concentration was used for content analysis to consider potential interferences. The UV quantification method was tested with respect to TA recovery mimicking different EC sample concentrations (60, 85 and 90 %, n = 3). Therefore, corresponding EC amounts were dissolved and a defined TA amount was added via stock solution. Samples were filtered and diluted to obtain the target concentration simulating sample preparation as described above. TA recoveries between 99.29 ± 0.45 % and 100.61 ± 0.73 % were achieved.

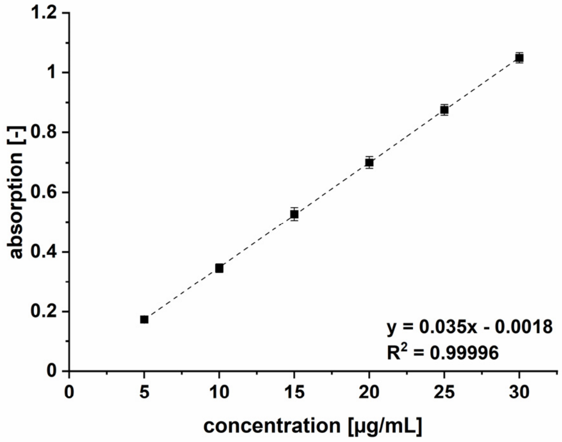

Figure 84. Linear fit of TA calibration in ethanol 90 % [w/w] (n = 3, mean ± s); λ = 238 nm.

5.5.12.3 High Performance Liquid Chromatography (HPLC)

HPLC was used for different purposes as depicted in Table 30. A method with isocratic elution modified from literature [222, 245] was selected and validated. An Elite LaChrome System (Hitachi, VWR, Darmstadt, Germany) was used for analyses. It was equipped with an autosampler L-2000, an oven L-2300 and an UV-detector L-2400. As stationary phase served a column Eurospher II 100-5 C18A with integrated precolumn (150 mm x 4.6 mm). The mobile phase consisted of acetonitrile (ACN) and purified water (40/60 V/V). A flow rate of 1.0 mL/min and an oven temperature of 40 °C was set. Usually, detection was done at a wavelength of 241 nm.

TA *CRS* for system suitability was measured additionally at a detection wavelength of 254 nm according to TA monograph in the Ph. Eur. 9.0 [222]. The injection volume for content determination was 20 µL. Due to the low TA concentrations in degradation and drug release samples, limited by the solubility in aqueous medium, the injection volume was increased to 80 µL for detection.

The sample preparation for TA content determination of filaments and 3D-printed test objects was the same as described for UV-spectroscopy (section 5.5.12.2). Sample preparation for other purposes can be found in the respective method section (Table 30).

All samples were filtered prior analyses through an 0.45 µm pore sized PP or nylon membrane filter (VWR, Leuven, Belgium). In preliminary experiments the TA filter absorption was tested by determining recovery rates after filtering. A sample rejection of the first filtered 2 mL for PP filters and 5 mL for nylon filters was necessary.

The developed HPLC method was validated for all TA assays according to the Reviewer Guidance (1994) in alignment to ICH guideline Q2 [246, 247]. In Figure 85, a typical chromatogram of a TA-loaded filament (F12) dissolved in ethanol for content determination is depicted. The t_R was 5.7 min. The small peak at 3 min originated from the solvent ethanol. Figure 86 shows an exemplary chromatogram of a TA peak of a drug release sample in HEPES pH 7.4 with a t_R of 6.1 min. The additional peak at ~ 4.5 min is TA 21-aldehyde hydrate (impurity C), which is the oxidative degradation product of the API, as described in section 3.3.2. Variances in t_R occurred between 5.6 and 6.2 min, due to a column replacement. The method was validated in terms of linearity, accuracy/recovery, specificity, repeatability, intermediate precision and specificity. In addition, the selectivity and the limit of quantitation (LOQ) was determined for drug release studies.

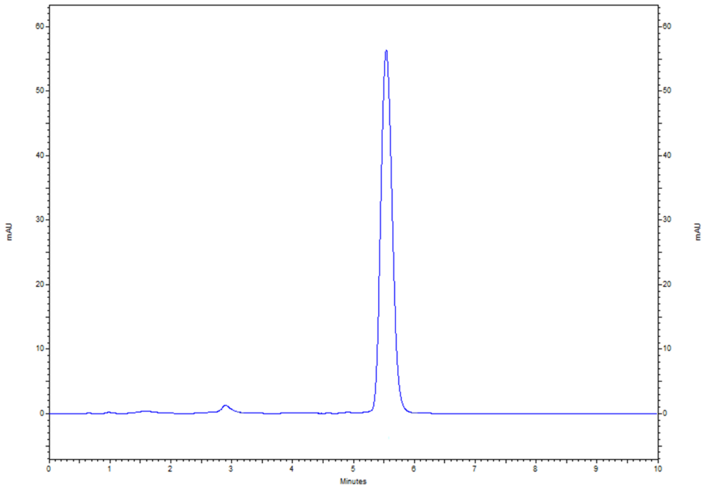

Figure 85. Typical chromatogram of an ethanolic solution of a drug-loaded filament sample (F12) for TA content analysis; injection volume: 20 µL; UV detection at 241 nm.

The linearity was demonstrated by calibration curves measured on six consecutive days in the respective medium including five TA concentrations evenly spread over three different concentration ranges. To ensure complete dissolution of TA in HEPES a stock solution in ACN/water (60/40 V/V) was prepared and diluted with HEPES to obtain the target concentrations. Residual concentrations of ACN in final samples was ≤ 0.3 %. For content analysis a range of 10 to

30 mg/L was tested. The coefficient of determination varied between 0.99969 and 0.99993. For drug release determination, a low concentration range of 0.2 to 0.8 mg/mL and a higher range of 2 to 12 mg/mL was evaluated, resulting in coefficients of determination between 0.99991and 0.99998.

The repeatability was determined by measuring a sample prepared once 10-times (content determination: 20 mg/L; drug release: 0.6 mg/L and 6 mg/L), resulting in a CoV between 0.2 and 0.43 %. In addition, six separately prepared solutions with the same concentrations for each work range were measured. Obtained CoVs were 1.25 %, 1.73 % and 1.35 %.

For intermediate precision between different days each solution (content determination: 20 mg/L; drug release: 0.6 mg/L and 6 mg/L) was prepared on six consecutive days and measured in triplicates. The CoVs over the measurement period were 1.3 %, 1.75 % and 0.52 %.

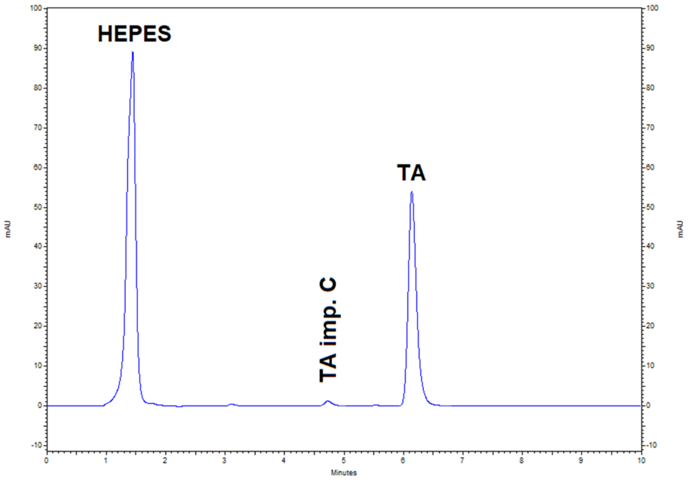

Figure 86. Typical chromatogram of long-term TA release from two-component implants in HEPES buffer pH 7.4; injection volume: 80 µL; UV detection at 241 nm.

To exclude influences of the matrix of the DDS, the specificity was determined by measuring pure solvents (ethanol 90 % [w/w] and HEPES pH 7.4) and a solution of a corresponding drug-free filament amount in EtOH and the corresponding HPMC concentration in HEPES. At a wavelength of 241 nm, no influence of the matrix or ethanol was found. HEPES showed no interaction with the stationary phase and was separated with sufficient resolution as depicted in Figure 86.

To determine the recovery of the respective method, defined TA concentrations were added to the media (EtOH and HEPES), covering 80-120 % of the working range. For content analysis concentrations of 16, 20 and 24 mg/L were measured inclusive the corresponding drug-free filament amount and recoveries of 100.03 %, 98.49 % and 99.40 % were obtained. In terms of drug release, concentrations of 0.48, 0.6 and 0.72 mg/L, as well as 4.8, 6 and 0.72 mg/L in HEPES were tested. Recoveries between 98.46 and 101.81 % were determined. Obtained values were all in the range of 97.5 and 102 %.

To ensure sample stability during overnight runs, the ethanolic recovery samples (20 mg/L, n = 3) were exposed to light for 72 h. The difference was 0.6 %, which is within the analytical error range of the system. The stability of the drug release samples in HEPES is described elsewhere (3.3.2.2).

During drug release studies, a reliable quantitation of low API concentrations must be ensured. TA degraded to impurity C at a certain quantity during drug release testing as described in section 3.3.2.2. For this reason, the LOQ and LOD were determined according to the ICH guideline Q2 based on the standard deviation of the response (σ) und the slope (m) using Equation (11) and (12) [246]. Therefore, the low calibration range consisting of five evenly distributed concentrations (0.2-1.0 mg/L) were measured on five consecutive days. The residual standard deviation of each regression line and the slope were determined. The LOD varied between 1.6 x 10^{-2} and 2.5 x 10^{-2} mg/L and the LOQ between 0.041 and 0.127 mg/L. Since impurity C was self-synthesized and a purity grade could not be determined, the LOQ could not be measured. However, it showed a similar specific extinction coefficient (section 3.3.2.3), Therefore, it was assumed that even low amounts were reliably detectable and quantifiable.

$$LOQ = 10 \cdot \frac{\sigma}{m} \tag{11}$$

$$LOD = 3.3 \cdot \frac{\sigma}{m} \tag{12}$$

To show specificity and selectivity between TA and impurity C, the degradation of TA was forced in PBS pH 7.4 at 37 °C. As depicted in Figure 87, the method was able to distinguish between both substances. The resolution was > 1.5 in all cases.

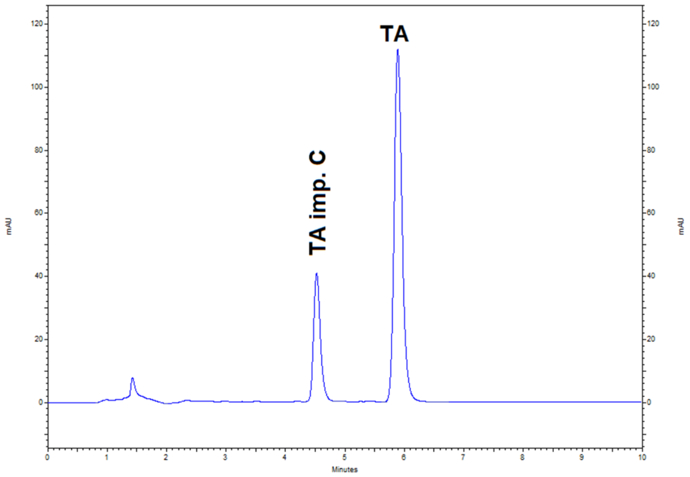

Figure 87. Exemplary chromatogram of TA and impurity C in PBS pH 7.4 after 72 h (1 µg/mL). UV detection at 241 nm. Peak at ~ 1.5 min =solvent peak.

5.5.13 Content Uniformity of 3D-printed Test Objects

Test objects of drug-loaded filament formulations F11 and F12 were tested according to the Ph. Eur. 2.9.6 “Uniformity of content of single-dose preparations” [196] and the Ph. Eur. 2.9.40 “Uniformity of dosage units” [197]. Therefore, 10 rectangular shapes (3.5 x 15 7.5 mm, Figure 42) were printed with the settings displayed in Table 28, respectively and weighed precisely using an analytical balance (Sartorius CP 1224, Goettingen, Germany). The content of samples was determined with the HPLC method described in section 5.5.12.3.

For the test of the Ph.Eur. 2.9.6 the individual contents of dosage units were calculated as percentage of the mean content. The dosage forms comply with Test A if all individual contents are between 85 and 115 % of the mean content.

For the analysis according to the Ph.Eur. 2.9.40 the target content of printed dosage forms based on mass and predetermined filament content was considered. Subsequently, the acceptance value (AV) was calculated according to Equation (13), where M is the reference value dependent from $\bar{X}$, which is the mean of the 10 tested dosage units, here expressed as the percentage of the mean measured filament content. k represents the acceptability constant (k = 2.4 for n = 10) and s the standard deviation of the 10 individual contents. The Ph. Eur. specifies an AV < 15 for given uniformity of dosage units at the first testing level (Q1).

$$AV = |M - \bar{X}| + k \cdot s \tag{13}$$

5.5.14 Determination of the Drug-load of Two-component Implants

The label claim of 3D-printed two-component implants was determined based on mass for the evaluation of the long-term drug release. Drug-loaded network inlays were connected to the respective drug-free shell and could therefore not be separated. To determine non-destructively the mass of the drug-loaded implant part, 10 drug-free shells (F6) were printed individually for the respective implant size (Table 12) using the same print settings as during dual-printing (Table 28). Obtained shells were weighed precisely on an analytical balance (Sartorius CP 1224, Goettingen, Germany). The mean mass of implant shell (Figure 88) was subtracted from the total implant mass of the respective two-component implant. The label claim was determined based on the calculated masses and the determined filament content. The determined API content of implants was used for the quantification of the released TA amount from implants.

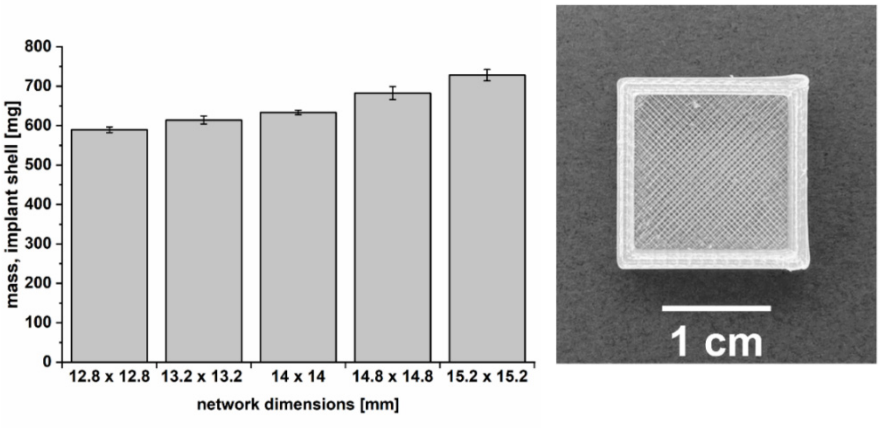

Figure 88. Left: Determined mass of pure shells per implant size (n = 10, mean ± s) for the calculation of the mass of the drug-loaded network inlay of two-component implants. Right: Exemplary image of the individually 3D-printed drug-free shell.

5.5.15 Mass Uniformity of Printed Test Objects

For the evaluation of the impact of different diameter fluctuations on the quality of 3D-printed test objects, the mass uniformity was determined according to Ph. Eur. 2.9.5 “Uniformity of mass for single-dose preparations” (section 3.2.3.4) [192]. Therefore, twenty rectangular shapes (3 x 15 x 7.5 mm, Figure 42) were printed from filaments (F13) manufactured at different screw speeds (Table 5; B1, B4-B7) using printing settings depicted in Table 28. Obtained geometries were weighed precisely on an analytical balance (Sartorius CP 1224, Goettingen, Germany). The procedure was repeated with commercial PLA filaments for comparison purposes. According to the requirements of the Ph. Eur. for tablets for oral use with mass ≥ 250 mg, only one mass may deviate by more than 5 % and none by more than 10 % from the mean value [192]. The specification of tablets was chosen for implants, as no definition for solid parenteral dosage forms is given.

5.5.16 X-ray Microcomputed Tomography[4]

The surface area and dimensions of the drug-loaded networks of the two-component implants were determined via X-ray microcomputed tomography (CT-COMPACT 130, ProCon X-ray, Sarstedt, Germany, n = 1). The following scanning settings were applied: 1300 projections, 20 µm voxel size, 80 kV acceleration voltage and 187 µA current. The reconstruction of projections was done using VG Studio software 3.0.1 (Volume Graphics, Heidelberg, Germany). Image processing for visualization, surface area and dimension determination were performed with Avizo Fire 9.0.1

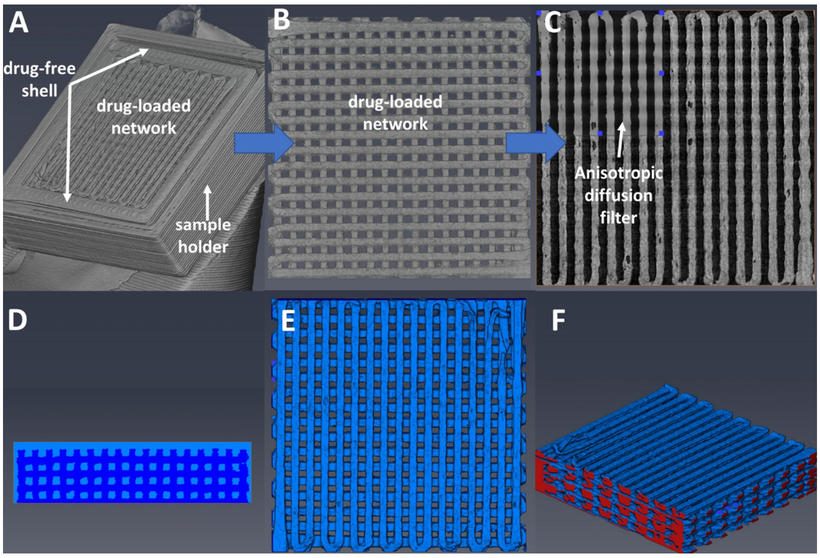

Figure 89. Intermediate steps of µCT-image processing for surface area determination with Avizo Fire 9.0.1 software.
A = 3D-image of reconstruction; B = 3D-depiction of drug-loaded network structure after subtracting sample holder and shell; C = Applied anisotropic filter on 2D-images to denoise scalar volume data; D = Image after segmentation step (light blue = air; dark blue = polymer); E = Top view of segmented 3D-image; F = Site view of segmented 3D-image with excluded edges (red) for surface area calculation

---

[4] Measurements were conducted by ProCon X-Ray GmbH (Sarstedt, Germany). Parts of the data evaluation were performed by Dr. Raphael Wiedey at the Institute of Pharmaceutics and Biopharmaceutics at the Heinrich Heine University Duesseldorf.

software (Thermo Fisher Scientific, Waltham, USA). The holder and drug-free shell volume of two-component implants were subtracted manually to obtain the individual drug-loaded networks, relevant for further analyses (Figure 89A, B). For denoising scalar volume data and contrast increase, Avizo's anisotropic diffusion filter was applied (Figure 89C). Image segmentation via grey value thresholding was performed to set start points (air: 0-10,000 and polymer: 25,000-65,535; subsequently shrunk by one voxel in all spatial directions). Based on these starting points, a watershed algorithm was applied to achieve full separation of air and polymer. The described methods ascribed closed pores to the "air"-material, though pore surface is not available for drug release. Therefore, the coherent air volume was isolated from the closed pores using Avizo's labelling and arithmetic functions and subsequently inverted to generate the final polymer construct (Figure 6E).

Finally, the inlays' surface area was calculated using Avizo's label-analysis function. The contact area of the inlay and the drug-free shell – which is also not available for drug release – was assigned as a separate material ("edges") and its surface area subtracted from the previous result (Figure 89F).

5.5.17 Liquid Chromatography-Mass Spectrometry (LC-MS) Analysis[5]

LC-MS analysis was performed using a maXis system equipped with an electrospray ionization source (UHR-QTOF maXis 4G, Bruker Daltonics, Billerica, USA). The UHPLC-plant Ultimate 300 RS (Dionex, Sunnyvale, USA) was coupled with the MS. Molecular masses were scanned from m/z 50-1500 with a gas flow of 9.0 L/min, a gas temperature of 225 °C and a voltage of 4 kV. The mobile phase consisted of ACN and purified water. The TA sample was prepared in water ($c_{TA} = 6$ µg/mL) and impurity C was tested in ACN ($c_{ImpC} = 25$ µg/mL). Obtained data were evaluated using the software Bruker Compass Data Analysis 4.2, (Bruker Daltonics, Billerica, USA). Mass spectra were used for the identification of the found degradation product impurity C and the analyses of the self-synthesized product.

5.5.18 Determination of Solubility

The solubility of TA was determined to maintain sink conditions during the long-term dissolution studies of filaments and 3D-printed implants. Therefore, an excess of TA was placed in glass bottles with watertight closure containing 50.0 mL of the test medium. Samples were stirred (200 rpm) over several days at predefined temperatures in a water bath placed on a multi-position magnetic stirrer. At defined time points, samples were extracted using a 5 mL syringe, filtered through an 0.45 µm pore sized PP membrane filter. A defined sample volume was withdrawn using a one-

---

[5] Measurements and parts of the data evaluation were performed by Dr. Peter Tommes at the Institute of organic chemistry at the Heinrich Heine University Düsseldorf.

channel pipette (Research® Plus, Eppendorf, Hamburg, Germany) and diluted with the respective medium to prevent recrystallisation and to fit in the calibration range.

The solubility determination in PBS during formulation development was determined at three different temperatures (37 °C, 47 °C and 57 °C with maximum variation of ± 0.5 °C each, n = 3). Flasks were pre-treated in an ultrasonic bath for 1.5 h at 70 °C to ensure a supersaturation and recrystallization at lower temperatures and thus a faster achievement of a saturated equilibrium. Afterwards, samples were stirred at the predefined temperatures over 20 days. The concentration was measured UV-spectroscopically at 241 nm (UV 1800, Shimadzu, Kyōto, Japan).

After the degradation analysis of TA (section 3.3.2.2) and the determination of suitable dissolution media, experiments were repeated with HEPES buffer pH 7.4 at 37 ± 0.5 °C to ensure sink conditions. Therefore, untreated TA samples (n = 6) were stirred over nine days until saturation equilibrium was reached. Sample preparation was kept the same. TA concentrations were measured with the HPLC method described in section 5.5.12.3. The total dissolved TA concentration was calculated as sum of TA and impurity C (refer to section 3.3.2.3).

5.5.19 Examination of TA Degradation in Different Dissolution Media

For stability analysis of TA during long-term drug release studies, the degradation in different dissolution media was investigated as described in section 3.3.2.2. Studies were conducted in PBS, PBS enriched with SPS (0.1 %), TRIS and HEPES buffer at pH 7.4 over 14 days. TA was added to the respective medium in flasks with watertight closures yielding a final concentration of 10 µg/mL. Samples (n = 3) were stirred in a water bath at 37 ± 0.5 °C placed on a multi-position magnetic stirrer (200 rpm), mimicking conditions during long-term release studies. Sampling of precise volume at predefined time-points (0.17, 1, 2, 3, 4 7 and 14 days) was conducted using a one-channel pipette (Research® Plus, Eppendorf, Hamburg, Germany). Analysis was performed via HPLC as described in section 5.5.12.3. First-order rate constants were calculated for assessment (5.5.20).

5.5.20 Determination of First-Order Rate Constants (k_{obs})

For the evaluation of TA degradation kinetics in different media at pH 7.4, the observed first-order rate constants (k_{obs}) were calculated as slope of the linear functions of the semi-logarithmic plot of remained TA-percentage as function of time.

5.5.21 Determination of the Specific Extinction Coefficient

The specific extinction coefficient $A_{1\,cm}^{1\%}$ at 241 nm was determined for TA and impurity C (n = 3). Substances were dissolved in ACN-water mixtures (60/40 V/V) yielding a concentration of 25 µg/mL, respectively. The absorbance was measured UV-spectroscopically (Lambda 25, PerkinElmer, Waltham, USA, n = 1). According to the Lambert-Beer law the molar extinction coefficient ε was determined using Equation (14), where A is the dimensionless absorbance, c the molar concentration and l the path length.

$$\varepsilon = \frac{A}{c * l} \tag{14}$$

The specific extinction coefficient $A_{1\,cm}^{1\%}$ was determined with the following equation according to the Ph. Eur. monograph 2.2.25 “UV/VIS Spectroscopy” (Equation (15):

$$A_{1\,cm}^{1\%} = \frac{10\,\varepsilon}{M_r} \tag{15}$$

where ε is the molar extinction coefficient and M_r the molar mass of the respective substance.

5.5.22 Dissolution Testing

5.5.22.1 USP Apparatus I (Rotating Basket)

For preliminary dissolution experiments during formulation development (refer to section 3.1.4.2.4 and 3.1.5.3.6) the drug release of different filament formulations (F9-F12) was examined in an USP-Apparatus I, the rotating basket (DT 756, Erweka, Langen, Germany). The dissolution device was equipped with a reciprocating pump (PCP 820, Erweka, Langen, Germany) and an UV/Vis-photometer (UV-1800, Shimadzu, Kyōto, Japan). TA release of filaments (n = 3) was performed in 1000 mL PBS pH 7.4 at 37 ± 0.5 °C. One sample consisted of six filament sections á 2.5 cm corresponding to approximately 40 mg TA. This was done to keep the surface available for drug release comparable. Filaments were placed in the basket to avoid floating and a rotational speed of 100 rpm was used. Studies were performed over seven days and for F11 and F12 additionally over 31 days. Sampling was conducted automatically and measured UV-spectrophotometrically at λ = 241 nm in a 10 mm flow-through cuvette. As presented in section 3.3.2.2 in later experiments it was proven, that the stability of TA in PBS was not given over a longer period. For initial assessment results were still considered conclusive. For the investigation over seven days, measurements were performed every 10 min for the first 24 h, every 30 min for the subsequent 24 h, every 120 min on the 3rd day and for the residual four days every 240 min. During sampling over 31 days additionally every 240 min until day ten and for the remaining 21 days every 480 min were measured. Measurements were performed under sink conditions [227]. A medium change was not necessary, as a maximum of 25 % TA were released over the investigation period. The EC matrices were still intact after dissolution studies as it is a non-erodible polymer. Consequently, the remaining TA content of each sample was determined after completion according to section 5.5.12.2. The sum of the released API amount and the residual API in EC-matrix was considered as total TA content.

5.5.22.2 USP Apparatus II (Paddle Apparatus)

The dissolution of the medicinal product Volon® A 10-5 mL (TA crystal suspension, Dermapharm, Gruenwald, Germany) was investigated over 4 h using the USP apparatus II (Paddle, DT 700, Erweka, Langen, Germany). Studies were performed in 1000 mL HEPES buffer pH 7.4 at 37 ± 0.5 °C. The applied stirring speed was 100 rpm. The TA suspension samples of 0.6 mL (= 6 mg TA, n = 3) were taken using a tuberculin syringe equipped with a Luer-Lock connection cannula 0.90 x 40 mm and transferred to a vessel. Thereby sink conditions were maintained with a maximum concentration of 6 mg/L TA [227]. Drug release samples of 8.0 mL were withdrawn after predetermined time points using an automatic syringe pump (Legato 111, KD Scientific, Holliston, USA) with a rate of 30 mL/min, enabling reproducible and precise sampling. Syringes were equipped with a 10 µm pore sized glass frit to reduce to the greatest possible extent the removal of undissolved drug crystals. The withdrawn volume was replaced by fresh medium using a one-channel pipette (Research® Plus, Eppendorf, Hamburg, Germany). Sampling was conducted after 1, 3, 5, 7, 10, 15, 20, 25, 30, 40, 50, 60, 80, 100, 120, 150, 180, 210 and 240 min. Afterwards samples were directly filtered through an 0.45-µm pore sized nylon membrane filter (VWR, Leuven, Belgium). Released TA amount was determined via HPLC as described in section 5.5.12.3. The API amount after reaching the plateau was considered as total API content, since a complete avoidance of drug crystal removal was not possible.

A determination of the TA release of Volon® A suspension with the newly developed dissolution set-up described in section 5.5.22.3 was not possible due to the limitations of TA solubility (20.27 ± 0.41 mg/L at 37 °C, n = 6) and precise dosing of the suspension.

5.5.22.3 Long-Term Dissolution Testing in Self-Developed Set-up

For the investigation of the long-term drug release behaviour from different printed two-component implants (Figure 68, n = 3), a “sample and separate” dissolution set-up was developed in a reduced volume (50-75 mL) to enable precise TA quantification as described in section 3.3.3. In addition, a simultaneous investigation of 30 samples over three months was enabled. For comparison purposes,

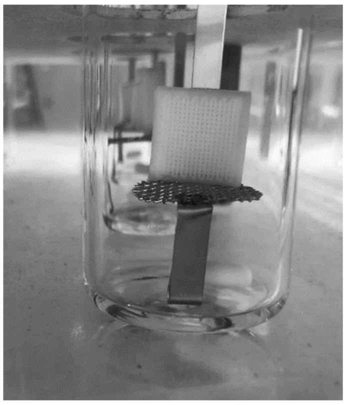

Figure 90. Picture of implant fixed in upright position using the inhouse built sample holder for long-term dissolution studies.

filaments (F12) were also analysed (n = 3). The set-up is exemplary depicted in Figure 61 (section 3.3.3). Glass flasks with watertight closure equipped with a magnetic stirrer were used as dissolution vessels (volumetric capacity approx. 85 mL). As implant holder an in-house built inlay was used (Figure 61), consisting of a grid. The implant was fixed upright on the grid with a cyanoacrylate based, solvent-free glue (UHU® Alleskleber super, UHU GmbH & Co. KG, Bühl, Germany) over the drug-free shell (Figure 90). For the analysis of filaments, three sections per sample with a length of 2.5 cm were placed in an in-house designed 3D-printed basket to avoid floating (Figure 61). Thereby, the surface area available for drug release was kept comparable.

Both sample holders were equipped with a spacer, providing a 2.5-cm distance between the implant/filament and the flask bottom. Flasks were placed in a water bath located on a multi position magnetic stirrer (Labomag (4 x 4), SHP Steriltechnik, Haldensleben, Germany). Dissolution studies were performed in 50 mL HEPES pH 7.4 at 37 ± 0.5 °C, ensured via thermostats, under sink conditions. Over the weekends, the volume was increased to 70 or 75 mL to maintain sink conditions during sampling breaks of two days. The minimum available stirring speed of 200 rpm was applied.

For manual sampling at early time points (implants until 10 days and filaments until eight days) a volume of 5-30.0 mL depending on the time intervals per day was withdrawn using a one channel pipette (Research® Plus, Eppendorf, Langen, Germany). A complete media change was conducted either over night or sampling intervals of one day at later time points to maintain sink conditions. The withdrawn volume was replaced with fresh dissolution medium. A medium change was usually performed after two days, at the latest after three days to reduce TA-degradation in the medium.

Within the initial 8 h of studies, extraction of implant samples was conducted every 2 h and for the subsequent nine days twice a day (minimum 6 h in between). Afterwards it varied between once a day, every two or maximum three days. The sampling of filaments was carried out similarly. A detailed sampling plan, inclusive withdrawn volume can be found in the appendix (Table 33). Samples were filtered promptly through an 0.45 µm pore sized PP or nylon membrane filter (VWR, Leuven, Belgium) and analysed latest three days after sampling via HPLC (section 5.5.12.3). The released TA concentration was calculated based on the area sum of impurity C and TA as proved in section 3.3.2.3. Prepared HPLC vials, which could not be analysed directly due to instrument occupancy or instrument defect, were frozen (-18 °C) until measurement to avoid further TA degradation. Prior analyses, samples were thawed in an ultrasonic bath at 40 °C and vortexed.

Non-erodible EC-based implants remained predominantly intact after three months drug release. The drug load of implants was determined as described in section 5.5.14, considered as total TA content and used for the calculation of the percentage amount drug released. Intact filament matrices were analysed regarding their remaining TA content according to section 5.5.12.2. The sum of the released API amount from filaments (TA + impurity C) and the residual API in filaments was considered as total TA content to calculate the released percentage.

5.5.23 Dissolution Kinetics

For the analyses of drug release behaviour of different implant inlay networks in comparison to filaments, the dissolution kinetics of differential curves were determined according to Equation (2). Therefore, the released API [%] was plotted against the time [d] in a double logarithmic plot. Values above 5 % were evaluated to cover the linear range as the initial drug release of the first days was comparatively fast and thus not representative for the actual drug release behaviour (max. up to 60 % drug release). For the determination of the present release kinetic, the diffusional release exponent n was determined as slope of the linear function obtained in the bilogarithmic depiction.

5.5.24 Fitting of Drug Release Curves

For the modelling of release profiles, dissolution curves were fitted to the respective mathematical equation (Peppas-Sahlin, Weibull and Higuchi; Equations (8), (9) and (10)) using the NLFit application of the software Origin Pro 2019/2020 (OriginLab Corporation, Northampton, USA). The Levenberg-Marquard algorithm was applied for iteration. Thereby non-defined constants of the respective models were determined. Fits were performed up to 60 % of drug release.

5.5.25 Prediction of Drug Release Based on the Higuchi-Model

The prediction of TA release from printed implants was done based on D_K (refer to Equations (3) and (10)) according to Korte and Quodbach [35]. The surface area was either calculated based on CAD (theoretical) or measured via X-ray computed tomography (refer to 5.5.16). D_K was determined as slope of Higuchi-plots (Q against $\sqrt{t}$). Q (mg/cm^2) represents the quotient of the absolute released API and the surface area of the dosage form (in this case drug-loaded network). Based on D_k of an implant with the same strand width and the surface area of the implant to be predicted the release curve was determined.

For the prediction based on the initial 15 and 30 days of drug release of the respective implant the relative released API amount was plotted against $\sqrt{t}$ as Higuchi plot. The equation of the obtained linear regression was used to predict the dissolution curve of the remaining time (60 or 75 days).

5.5.26 Root-Mean Square Error of Prediction (RMSEP)

The goodness of a prediction model was evaluated by calculating the RMSEP according to Equation (16), where n is the number of samples i, y_i the observed and $\hat{y}_i$the predicted value for each time point of dissolution studies [248].

$$RMSEP = \sqrt{\frac{\sum_{i=1}^{n}(y_i - \hat{y}_i)^2}{n}} \qquad \textbf{(16)}$$

5.6 Stability Testing of Filaments according to ICH Q1A (R2)

Filaments F6, F11 and F12 were subjected a stability analysis according to ICH guideline Q1A (R2) [198] over a period of six months. For this purpose, all filament formulations were stored open (unsealed, permeable polyethylene bags) or packed (sealed impermeable aluminium sachets). Sampling within one batch was done using filament sections from the beginning, middle and end of the manufacturing process. Packed and unpacked samples were stored at RT (21 °C) and at uncontrolled relative humidity and under accelerated conditions at 40 °C and 75 % rH in a climate chamber (KBF 720, Binder, Tuttlingen, Germany). As quality attributes the mechanical properties, thermal stability (DSC) and additionally the API stability (content) for drug-loaded filaments (F11, F12) were chosen. Tests were conducted according to the overview listed in Table 10. As starting point (T0), the mechanical properties and DSC analysis were performed one day and the API stability two days after extrusion according to the methods described in section 5.5.7 and 5.5.12. Content analyses for T0 and T1 (1 month) was done via UV/Vis-spectroscopy (section 5.5.12.2), whereas residual measurements were performed using the HPLC method for content determination described in section 5.5.12.3 to detect potential degradation products.

5.7 Synthesis of Impurity C[6]

For proper identification and analyses of the degradation product of TA via HPLC, impurity C was synthesised. The synthesis was performed based on literature [217, 223]. 600 mg of TA (1.38 mmol and 31.5 mg of copper (II) acetate (0.17 mmol) were dissolved in 150 mL methanol absolute. Air was bubbled through the solution for 60 min using a tube equipped with a cannula. The addition of 20 mL aqueous disodium edetate solution (2.5 mg/mL) quenched the induced chemical reaction. Under vacuum the solution volume was reduced to 30 mL. The aqueous solution was extracted twice with 200 mL dichloromethane.

Afterwards the obtained two organic phases were combined and extracted twice with aqueous disodium edetate solution (2.5 mg/mL). The residual water was removed with sodium sulphate anhydrous. The filtered organic solution was evaporated at RT to yield impurity C. The obtained white solid was analysed via HPLC (section 5.5.12.3) and LC-MS as described in section 5.5.17 (HPLC RT: 4.6 min.; m/z calculated for $[C_{24}H_{31}FO_7]^+$: 451.2, found: 451.2 (Figure 91), Yield > 95 %).

---

[6] The synthesis was performed together with Dr. Tanja Knaab at the Institute of Pharmaceutics and Biopharmaceutics at the Heinrich Heine University Duesseldorf.

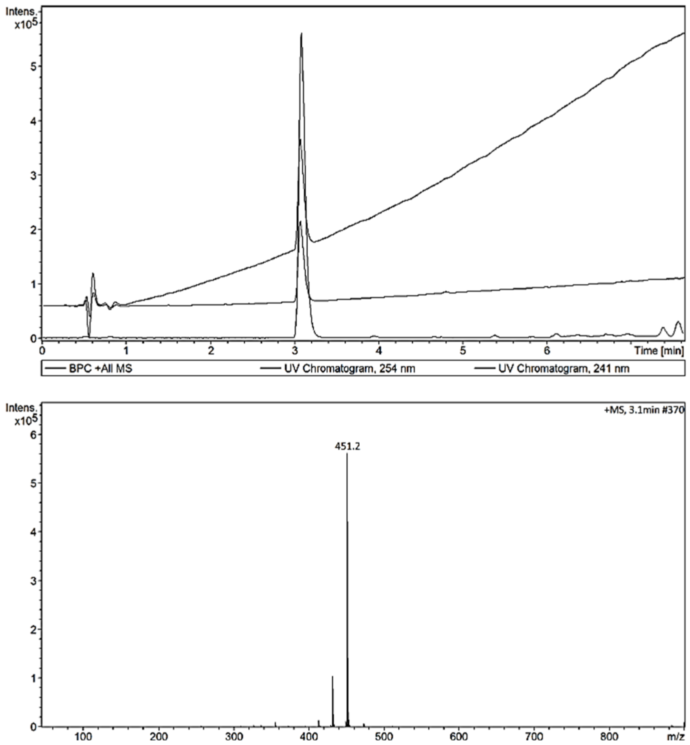

Figure 91. LC (top) and MS (bottom) spectra of synthesized impurity C (m/z 451.2).

6. Appendix

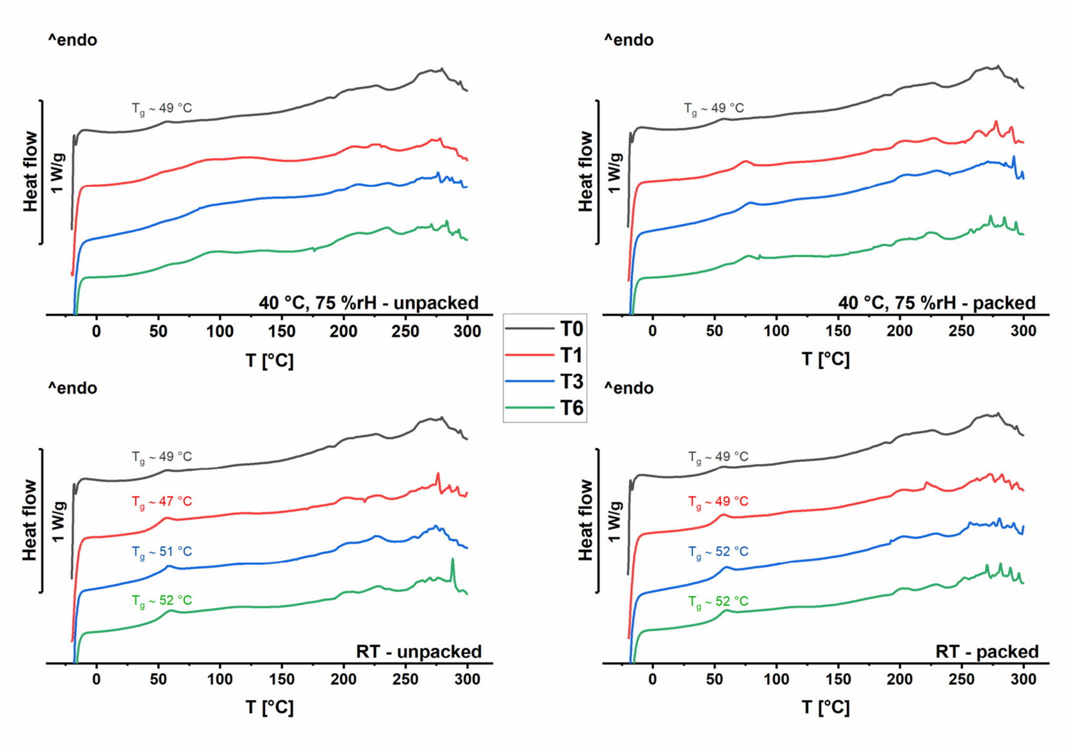

Figure A1. Recorded DSC thermograms of F11 samples unpacked (left) and right (packed) during stability testing T0-T6. Top: stored under accelerated conditions; bottom: stored at 21 °C (RT).

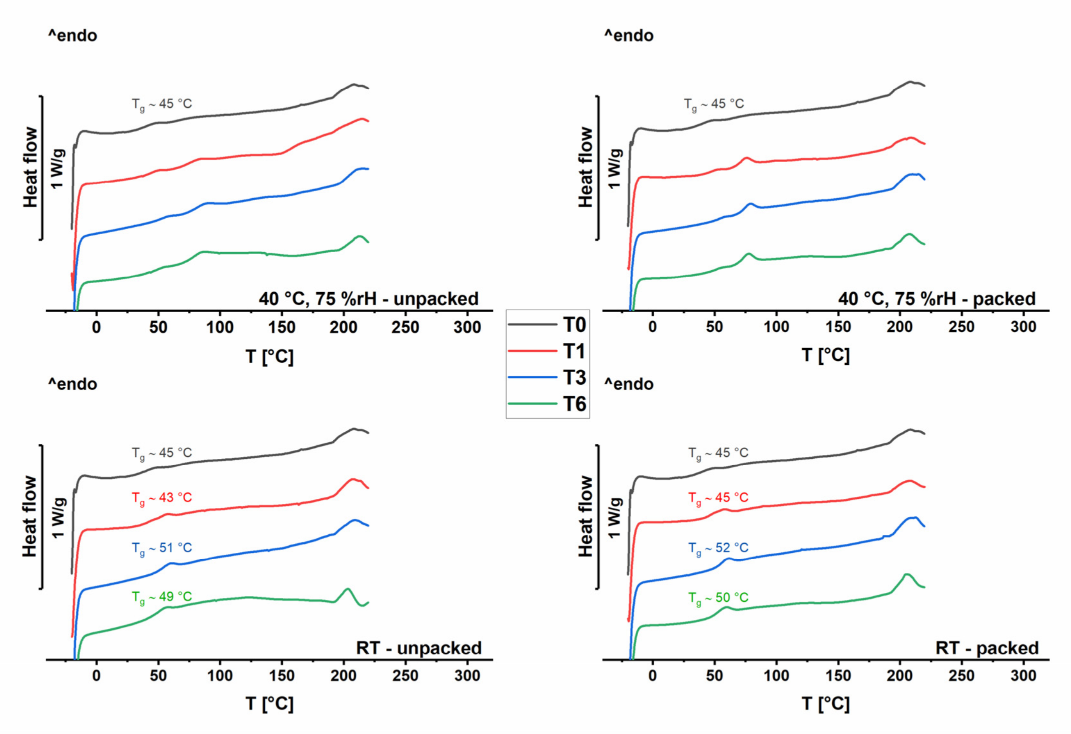

Figure A2. Recorded DSC thermograms of F6 samples unpacked (left) and right (packed) during stability testing T0-T6. Top: stored under accelerated conditions; bottom: stored at 21 °C (RT).

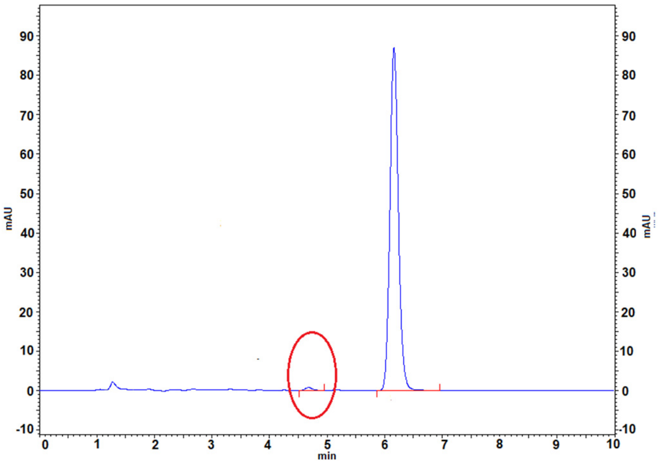

Figure A3. HPLC chromatogram of TA sample in water (6 µg/mL) via LC-MS (Figure A4) treated for 4 h in an ultrasonic bath at 40 °C to force degradation. Measured with developed HPLC method to ensure the presence of the degradation product. Red marker indicates the found degradation product (see section 3.3.2.1).

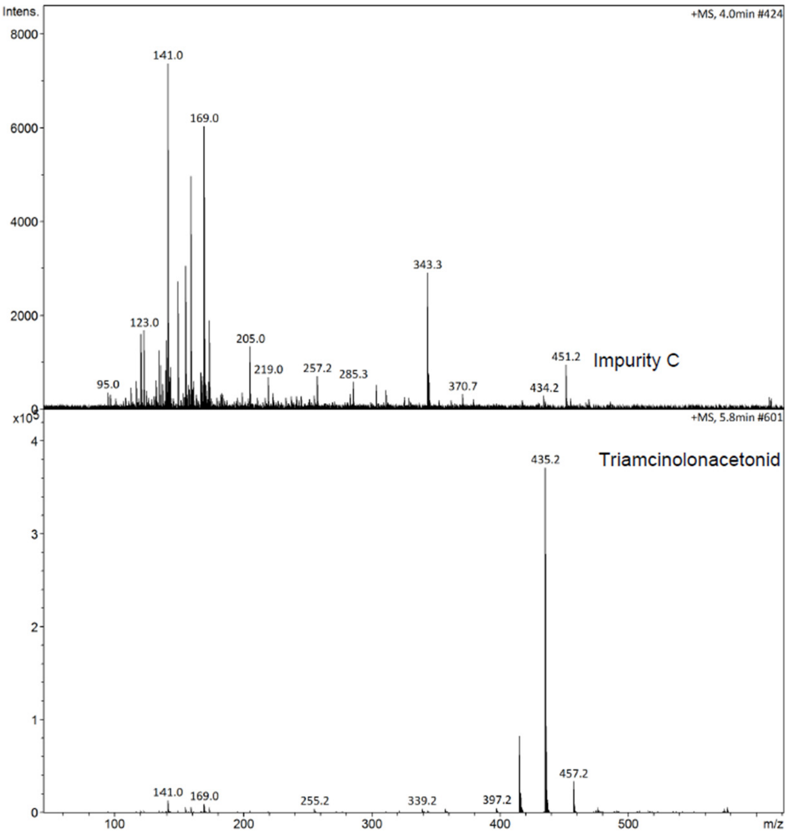

Figure A4. LC-MS chromatogram of aqueously treated TA sample (4 h, 40 °C ultrasonic bath), impurity C was detected at min 4 with the applied method (*m/z* 451.2) and TA at min 5.8 (*m/z* 435.2).

Table 31. Detailed slicing settings using Slic3r Prusa Edition. Categorization was adapted from software.

Settings	Rectangular test objects (sections 3.2.3.4 and 3.2.5.2)	
	Commercial Filament	EC/HPMC based Filament
Software	Slic3r Prusa Edition	
Filament	PLA	F11, F12, F13
Print temperature [°C]	210	185 for F11 and F12, 180 for F13
Heat bed temperature [°C]	60	90
Nozzle diameter [mm]	0.4	0.4
Layer settings		
Layer height (first layer height) [mm]	0.1	0.1
Perimeters	1	1
Solid layers (top and bottom)	0	0
Seam position	nearest	nearest
Infill settings		
Infill density [%]	85	85
Fill pattern	rectilinear	rectilinear
Fill angle [°]	90	90
Combine infill every	1	1
Skirt and Brim		
Skirt loops minimum	1	1
Distance from object [mm]	2	2
minimum extrusion length [mm]	4	4
Brim width	0	0
Support		
Generate support structures	No	No
Speed		
Perimeters	15	15
Small perimeters (r < 6.5 mm)	25	25
External perimeter	25	25
Infill	15	15
Travel	180	180
First layer speed	15	15
Advanced: Extrusion width [mm]		
Default extrusion width	0.45	0.45
First layer	0.42	0.42
Perimeters	0.45	0.45
External perimeters	0.45	0.45
Infill	0.45	0.45
Advanced: Overlap		
Infill/perimeter	25	25
Cooling		
Fan speed [%]	100	100
Disable fan for the first _ layers	1	1

Table 32. Detailed slicing settings using Simplify3D. Categorization was adapted from the software.

Settings	Two-component implants (section 3.4.3)			
	Drug-free shell	Drug-loaded network inlays		
		0.4 mm	0.8 mm	1.2 mm
Software	Simplify3D			
Filament	F6	F12	F12	F12
Print temperature [°C]	185	185	185	185
Build plate temperature [°C]	90	90	90	90
EXTRUDER				
Overview				
Nozzle diameter [mm]	**0.4**	**0.4**	**0.4**	**0.4**
Extrusion multiplier	**1**	**1**	**1**	**1**
Extrusion width (manual) [mm]	**0.39**	**0.39**	**0.4**	**0.4**
Ooze Control				
Retraction distance [mm]	**1**	**5**	**5**	**5**
Extra restart distance [mm]	**-0.01**	**0**	**-0.01**	**-0.01**
Retraction vertical lift	**0.1**	**0.1**	**0.1**	**0.3**
Retraction speed [mm/s]	**80**	**80**	**80**	**80**
LAYER				
Layer settings				
Primary extruder	**2**	**1**	**1**	**1**
Primary layer height [mm]	**0.2**	**0.2**	**0.2**	**0.2**
Top solid layers	**all**	**0**	**all**	**0**
Bottom solid layers	**all**	**0**	**all**	**0**
Perimeters	**1**	**0**	**1**	**1** **(1.2 x 0.8 mm = 2)**
First layer settings [% from set values for all layers]				
First layer height	**100**	**100**	**100**	**100**
First layer width	**100**	**100**	**100**	**100**
First layer speed	**50**	**50**	**50**	**100**
Start points				
Optimize start points for fastest printing speed	**yes**	**yes**	**yes**	**yes**
ADDITIONS				
Use Skirt and Brim				
Skirt extruder	**2**	**2**	**2**	**2**
Skirt layers	**1**	**1**	**1**	**1**
Skirt offset from part [mm]	4	4	4	4
Skirt outlines	2	2	2	2
Use Ooze Shield				
Ooze shield extruder	all	all	all	all
Offset from part [mm]	10	10	10	10
Ooze shield outlines	8	8	8	8
Sidewall shape	waterfall	waterfall	waterfall	waterfall
Sidewall angle change [°]	30	30	30	30
Speed multiplier	200	200	200	200
INFILL				
General				
Infill extruder	2	1	1	1
Internal fill pattern	rectilinear	rectilinear	rectilinear	rectilinear

Settings	**Two-component implants (section 3.4.3)**			
	Drug-free shell	**Drug-loaded network inlays**		
		0.4 mm	**0.8 mm**	**1.2 mm**
External fill pattern	rectilinear	rectilinear	rectilinear	rectilinear
Infill percentage	100	100	100	100
Outline overlap [%]	5	not relevant	5	5
Infill extrusion width	100	100	100	100
Min. infill length [mm]	5	0.8	5	5
Combine infill every_layer	1	1	1	1
Internal/external angle offset [°] **n x angle***	45 -45	2 x 0 2 x 90 2 x 0 2 x 90 2 x 0 2 x 90 2 x 0 2 x 90	not relevant; only perimeters printed	6 x 0 6 x 90 6 x 0 6 x 90
SUPPORT				
Generate support material	**No**	**No**	**No**	**No**
COOLING				
Pre layer fan controls				
Fan speed [%]	layer 1: 0 other: 100	layer 1: 0 other: 100	layer 1: 0 other: 100	layer 1: 0 other: 100
SPEED				
Speeds				
Default printing speed [mm/s]	25	10	20	15
Outline underspeed [%]	50	50	50	50
Solid Infill underspeed [%]	80	80	80	80
X/Y axis movement speed [mm/s]	80	120	80	120
Z-axis movement speed [mm/s]	16.7	16.7	16.7	16.7
OTHERS				
Tool change retraction				
Change retraction distance [mm]	**85**	**85**	**85**	**85**
Extra restart distance [mm]	**-25**	**-3**	**-25**	**-30**
Retraction speed [mm/s]	**20**	**40**	**20**	**40**
ADVANCED				
Thin wall behaviour				
External thin wall type	**Perimeters only**	**Single extrusion walls**	**Perimeters only**	**Perimeters only**
Internal thin wall type	**Allow gap fill**	**Allow single extrusion infill**	**Allow gap fill**	**Allow single extrusion infill**
Allowed perimeter overlap [%]	**10**	**10**	**10**	**10**
Single extrusions				
Minimum extrusion length [mm]	**Not relevant**	**1**	**Not relevant**	**1**
Minimum printing width [%]	**Not relevant**	**50**	**Not relevant**	**50**
Maximum printing width [%]	**Not relevant**	**200**	**Not relevant**	**200**
Endpoint extension distance [mm]	**Not relevant**	**0.7**	**Not relevant**	**0.2**
Ooze control behaviour				
Only retract when crossing open spaces	**yes**	**no**	**no**	**yes**
Force retraction between layers	**yes**	**yes**	**yes**	**yes**
Minimum travel for retraction	**-**	**-**	**-**	**-**

Settings	**Two-component implants (section 3.4.3)**			
	Drug-free shell	**Drug-loaded network inlays**		
		0.4 mm	**0.8 mm**	**1.2 mm**
Perform retraction during wipe movement	**no**	**yes**	**no**	**no**
Only wipe extruder for outer most perimeters	**yes**	**yes**	**yes**	**yes**

* as network braces of inlays are arranged in 90° to each other, the infill angle per brace (consisting of n layers) needs to be changed between 0 and 90° to adapt the printing direction to brace orientation. Therefore, the angle 0° was entered n-times (one brace) and then this was repeated for 90° until all braces are covered (n = layer number for one network brace (e.g., 1.2 mm brace consists of six 0.2-mm-layers).

Table 33. Sampling overview of long-term drug release from two-component implants (9, n = 3) and filaments (F12). Grey-shading indicates medium change.

Sampling no.	**Implants**			**Filaments**		
	Sampling time [d]	**Sampling volume [mL]**	**Total volume [mL])**	**Sampling time [d]**	**Sampling volume [mL]**	**Total volume [mL])**
1	0.08	5	50	0.08	20	50
2	0.17	5	50	0.17	20	50
3	0.25	5	50	0.25	20	50
4	0.33	5	50	0.88	50	50
5	0.97	50	50	1.17	50	50
6	1.30	10	50	1.96	50	50
7	1.90	50	50	2.27	50	50
8	2.28	10	50	2.90	50	50
9	2.96	50	50	3.26	50	50
10	3.25	20	50	4.12	50	50
11	4.17	50	50	6.07	70	70
12	5.09	50	50	7.15	20	50
13	5.97	50	50	8.08	20	50
14	6.22	20	50	9.16	50	50
15	6.97	50	50	10.07	50	50
16	7.21	10	50	13.08	75	75
17	7.97	50	50	14.98	50	50
18	8.30	20	50	17.20	50	50
19	8.97	50	50	19.98	50	75
20	9.24	20	50	21.92	50	50
21	9.97	30	50	23.98	50	50
22	10.22	50	50	26.95	75	75
23	11.29	50	50	28.94	50	50
24	12.94	70	70	30.88	50	50
25	14.15	50	50	33.92	75	75
26	15.07	50	50	35.92	50	50
27	16.13	50	50	37.95	50	50
28	17.27	50	50	41.13	75	75
29	18.23	50	50	42.95	50	50
30	19.94	75	75	44.90	50	50
31	20.95	50	50	47.95	50	50
32	21.95	50	50	49.83	50	50
33	23.06	50	50	51.94	50	50
34	24.11	50	50	54.94	50	50
35	25.18	50	50	56.92	50	50
36	27.11	70	70	58.92	50	50
37	27.99	50	50	61.91	50	50

Sampling no.	**Implants**			**Filaments**		
	Sampling time [d]	**Sampling volume [mL]**	**Total volume [mL])**	**Sampling time [d]**	**Sampling volume [mL]**	**Total volume [mL])**
38	28.98	20	50	63.96	50	50
39	29.94	50	50	65.96	50	50
40	30.92	20	50	68.96	50	50
41	32.13	50	50	70.96	50	50
42	33.98	70	70	72.96	50	50
43	35.15	20	50	75.97	50	50
44	36.06	20	50	78.08	50	50
45	37.17	50	50	79.94	50	50
46	38.13	50	50	83.18	50	50
47	41.13	75	75	84.91	50	50
48	42.98	50	50	87.02	50	50
49	45.19	50	50	90.00	50	50
50	47.98	75	75			
51	49.93	50	50			
52	51.98	50	50			
53	54.94	75	75			
54	56.94	50	50			
55	58.89	50	50			
56	61.93	75	75			
57	63.93	50	50			
58	65.94	50	50			
59	69.14	75	75			
60	70.94	50	50			
61	72.90	50	50			
62	75.94	50	50			
63	77.92	50	50			
64	79.95	50	50			
65	82.95	50	50			
66	84.94	50	50			
67	86.95	50	50			
68	89.94	50	50			

7. Bibliography

1. M. A. Alhnan, T. C. Okwuosa, M. Sadia, K. W. Wan, W. Ahmed, and B. Arafat, *Emergence of 3D printed dosage forms: opportunities and challenges.* Pharm Res, 2016. 33: 1817-1832.
2. J. Gardan, *Additive manufacturing technologies: state of the art and trends.* Int J Prod Res, 2016. 54: 3118-3132.
3. CAD file for lattice cube. Available from: www.thingiverse.com/thing:1856832. Last access: 30.12.2020.
4. F. P. Melchels, J. Feijen, and D. W. Grijpma, *A review on stereolithography and its applications in biomedical engineering.* Biomaterials, 2010. 31: 6121-6130.
5. K. Low, K. Leong, C. Chua, Z. Du, and C. Cheah, *Characterization of SLS parts for drug delivery devices.* Rapid Prototyp J, 2001. 7: 262-268.
6. F. Fina, A. Goyanes, C. M. Madla, A. Awad, S. J. Trenfield, J. M. Kuek, P. Patel, S. Gaisford, and A. W. Basit, *3D printing of drug-loaded gyroid lattices using selective laser sintering.* Int J Pharm, 2018. 547: 44-52.
7. A. Awad, F. Fina, A. Goyanes, S. Gaisford, and A. W. Basit, *3D printing: principles and pharmaceutical applications of selective laser sintering.* Int J Pharm, 2020. 586: 119594.
8. M. N. Cooke, J. P. Fisher, D. Dean, C. Rimnac, and A. G. Mikos, *Use of stereolithography to manufacture critical-sized 3D biodegradable scaffolds for bone ingrowth.* J Biomed Mater Res B Appl Biomater, 2003. 64: 65-69.
9. C. W. Hull (1986). Apparatus for production of three-dimensional objects by stereolithography. United States Patent No. US4575330A.
10. J. Norman, R. D. Madurawe, C. M. V. Moore, M. A. Khan, and A. Khairuzzaman, *A new chapter in pharmaceutical manufacturing: 3D-printed drug products.* Adv Drug Deliv Rev, 2017. 108: 39-50.
11. Spritam® - Zipdose® Technology - Making Medicine Using 3D Printing. 2021. Available from: www.spritam.com/#/patient/zipdose-technology/making-medicine-using-3d-printing. Last access: 10.10.2021.
12. M. E. Aulton and K. Taylor, *Aulton's Pharmaceutics: the design and manufacture of medicines*. 2013. Elsevier Health Sciences, Edinburgh, UK.
13. I. El Aita, H. Ponsar, and J. Quodbach, *A critical review on 3D-printed dosage forms.* Curr Pharm Des, 2018. 24: 4957-4978.
14. D. G. Yu, C. Branford-White, Y. C. Yang, L. M. Zhu, E. W. Welbeck, and X. L. Yang, *A novel fast disintegrating tablet fabricated by three-dimensional printing.* Drug Dev Ind Pharm, 2009. 35: 1530-6.
15. I. Gibson, D. W. Rosen, B. Stucker, and M. Khorasani, *Additive manufacturing technologies*. Vol. 17. 2021. Springer, Cham, Switzerland.
16. J. J. Adams, E. B. Duoss, T. F. Malkowski, M. J. Motala, B. Y. Ahn, R. G. Nuzzo, J. T. Bernhard, and J. A. Lewis, *Conformal printing of electrically small antennas on three-dimensional surfaces.* Adv Mater, 2011. 23: 1335-1340.
17. J. Rahman and J. Quodbach, *Versatility on demand - The case for semi-solid micro-extrusion in pharmaceutics.* Adv Drug Deliv Rev, 2021. 172: 104-126.
18. S. A. Khaled, J. C. Burley, M. R. Alexander, and C. J. Roberts, *Desktop 3D printing of controlled release pharmaceutical bilayer tablets.* Int J Pharm, 2014. 461: 105-111.
19. S. A. Khaled, J. C. Burley, M. R. Alexander, J. Yang, and C. J. Roberts, *3D printing of tablets containing multiple drugs with defined release profiles.* Int J Pharm, 2015. 494: 643-650.
20. S. A. Khaled, M. R. Alexander, R. D. Wildman, M. J. Wallace, S. Sharpe, J. Yoo, and C. J. Roberts, *3D extrusion printing of high drug loading immediate release paracetamol tablets.* Int J Pharm, 2018. 538: 223-230.
21. S. A. Khaled, *3D printing of five-in-one dose combination polypill with defined immediate and sustained release profiles.* J Control Release, 2015. 217: 308-314.

22. M. Siyawamwaya, L. C. du Toit, P. Kumar, Y. E. Choonara, P. P. P. D. Kondiah, and V. Pillay, *3D printed, controlled release, tritherapeutic tablet matrix for advanced anti-HIV-1 drug delivery.* Eur J Pharm Biopharm, 2018. 138: 99-110.
23. International Conference on Harmonisation of Technical Requirements for Registration of Pharmaceuticals for Human Use, *Impurities: Guideline for residual solvents Q3C(R6)*, 2016.
24. E. Fuenmayor, M. Forde, A. V. Healy, D. M. Devine, J. G. Lyons, C. McConville, and I. Major, *Material considerations for fused-filament fabrication of solid dosage forms.* Pharmaceutics, 2018. 10: 44.
25. J. Skowyra, K. Pietrzak, and M. A. Alhnan, *Fabrication of extended-release patient-tailored prednisolone tablets via fused deposition modelling (FDM) 3D printing.* Eur J Pharm Sci, 2015. 68: 11-17.
26. A. Goyanes, A. B. M. Buanz, A. W. Basit, and S. Gaisford, *Fused-filament 3D printing (3DP) for fabrication of tablets.* Int J Pharm, 2014. 476: 88-92.
27. C. Korte and J. Quodbach, *Formulation development and process analysis of drug-loaded filaments manufactured via hot-melt extrusion for 3D-printing of medicines.* Pharm Dev Technol, 2018. 23: 1117-1127.
28. J. Zhang, X. Feng, H. Patil, R. Tiwari, and M. Repka, *Coupling 3D printing with hot-melt extrusion to produce controlled-release tablets.* Int J Pharm, 2017. 519: 186-197.
29. A. Goyanes, P. Robles Martinez, A. Buanz, A. Basit, and S. Gaisford, *Effect of geometry on drug release from 3D printed tablets.* Int J Pharm, 2015. 494: 657-663.
30. K. Pietrzak, A. Isreb, and M. A. Alhnan, *A flexible-dose dispenser for immediate and extended release 3D printed tablets.* Eur J Pharm Biopharm, 2015. 96: 380-7.
31. A. Goyanes, J. Wang, A. Buanz, R. Martïnez-Pacheco, R. Telford, S. Gaisford, and A. W. Basit, *3D printing of medicines: engineering novel oral devices with unique design and drug release characteristics.* Mol Pharm, 2015. 12: 4077-4084.
32. A. Maroni, A. Melocchi, F. Parietti, A. Foppoli, L. Zema, and A. Gazzaniga, *3D printed multi-compartment capsular devices for two-pulse oral drug delivery.* J Control Release, 2017. 268: 10-18.
33. Q. Li, H. Wen, D. Jia, X. Guan, H. Pan, Y. Yang, S. Yu, Z. Zhu, R. Xiang, and W. Pan, *Preparation and investigation of controlled-release glipizide novel oral device with three-dimensional printing.* Int J Pharm, 2017. 525: 5-11.
34. C. I. Gioumouxouzis, A. Baklavaridis, O. L. Katsamenis, C. K. Markopoulou, N. Bouropoulos, D. Tzetzis, and D. G. Fatouros, *A 3D printed bilayer oral solid dosage form combining metformin for prolonged and glimepiride for immediate drug delivery.* Eur J Pharm Sci, 2018. 120: 40-52.
35. C. Korte and J. Quodbach, *3D-printed network structures as controlled-release drug delivery systems: Dose adjustment, API release analysis and prediction.* AAPS PharmSciTech, 2018. 19: 3333-3342.
36. M. Sadia, B. Arafat, W. Ahmed, R. T. Forbes, and M. A. Alhnan, *Channelled tablets: An innovative approach to accelerating drug release from 3D printed tablets.* J Control Release, 2018. 269: 355-363.
37. G. G. Pereira, S. Figueiredo, A. I. Fernandes, and J. F. Pinto, *Polymer selection for hot-melt extrusion coupled to fused deposition modelling in pharmaceutics.* Pharmaceutics, 2020. 12: 1-63.
38. D. K. Tan, M. Maniruzzaman, and A. Nokhodchi, *Advanced pharmaceutical applications of hot-melt extrusion coupled with fused deposition modelling (FDM) 3D printing for personalised drug delivery.* Pharmaceutics, 2018. 10: 203.
39. W. Kempin, C. Franz, L. C. Koster, F. Schneider, M. Bogdahn, W. Weitschies, and A. Seidlitz, *Assessment of different polymers and drug loads for fused deposition modeling of drug loaded implants.* Eur J Pharm Biopharm, 2017. 115: 84-93.
40. A. Melocchi, F. Parietti, A. Maroni, A. Foppoli, A. Gazzaniga, and L. Zema, *Hot-melt extruded filaments based on pharmaceutical grade polymers for 3D printing by fused deposition modeling.* Int J Pharm, 2016. 509: 255-263.

41. J. M. Nasereddin, N. Wellner, M. Alhijjaj, P. Belton, and S. Qi, *Development of a simple mechanical screening method for predicting the feedability of a pharmaceutical FDM 3D printing filament.* Pharm Res, 2018. 35: 1-13.
42. E. Prasad, M. T. Islam, D. J. Goodwin, A. J. Megarry, G. W. Halbert, A. J. Florence, and J. Robertson, *Development of a hot-melt extrusion (HME) process to produce drug loaded Affinisol™ 15LV filaments for fused filament fabrication (FFF) 3D printing.* Additiv Manuf, 2019. 29: 100776.
43. M. Sadia, A. Sosnicka, B. Arafat, A. Isreb, W. Ahmed, A. Kelarakis, and M. A. Alhnan, *Adaptation of pharmaceutical excipients to FDM 3D printing for the fabrication of patient-tailored immediate release tablets.* Int J Pharm, 2016. 513: 659-668.
44. N. Gottschalk, M. Bogdahn, M. Harms, and J. Quodbach, *Brittle polymers in fused deposition modeling: an improved feeding approach to enable the printing of highly drug loaded filament.* Int J Pharm, 2021. 597: 120216.
45. A. Goyanes, A. B. M. Buanz, G. B. Hatton, S. Gaisford, and A. W. Basit, *3D printing of modified-release aminosalicylate (4-ASA and 5-ASA) tablets.* Eur J Pharm Biopharm, 2015. 89: 157-162.
46. W. Jamróz, M. Kurek, E. Łyszczarz, J. Szafraniec, J. Knapik-Kowalczuk, K. Syrek, M. Paluch, and R. Jachowicz, *3D printed orodispersible films with aripiprazole.* Int J Pharm, 2017. 533: 413-420.
47. A. Awad, S. J. Trenfield, A. Goyanes, S. Gaisford, and A. W. Basit, *Reshaping drug development using 3D printing.* Drug Discov, 2018. 23: 1547-1555.
48. G. Verstraete, A. Samaro, W. Grymonpre, V. Vanhoorne, B. Van Snick, M. N. Boone, T. Hellemans, L. Van Hoorebeke, J. P. Remon, and C. Vervaet, *3D printing of high drug loaded dosage forms using thermoplastic polyurethanes.* Int J Pharm, 2018. 536: 318-325.
49. A. Goyanes, H. Chang, D. Sedough, G. B. Hatton, J. Wang, A. Buanz, S. Gaisford, and A. W. Basit, *Fabrication of controlled-release budesonide tablets via desktop (FDM) 3D printing.* Int J Pharm, 2015. 496: 414-20.
50. G. Kollamaram, D. M. Croker, G. M. Walker, A. Goyanes, A. W. Basit, and S. Gaisford, *Low temperature fused deposition modeling (FDM) 3D printing of thermolabile drugs.* Int J Pharm, 2018. 545: 144-152.
51. C. I. Gioumouxouzis, O. L. Katsamenis, N. Bouropoulos, and D. G. Fatouros, *3D printed oral solid dosage forms containing hydrochlorothiazide for controlled drug delivery.* J Drug Deliv Sci Technol, 2017. 40: 164-171.
52. T. Ehtezazi, M. Algellay, Y. Islam, M. Roberts, N. M. Dempster, and S. D. Sarker, *The application of 3D printing in the formulation of multilayered fast dissolving oral films.* J Pharm Sci, 2018. 107: 1076-1085.
53. M. Alhijjaj, P. Belton, and S. Qi, *An Investigation into the use of polymer blends to improve the printability of and regulate drug release from pharmaceutical solid dispersions prepared via fused deposition modeling (FDM) 3D printing.* Eur J Pharm Biopharm, 2016. 108: 111-125.
54. M. Alhijjaj, J. Nasereddin, P. Belton, and S. Qi, *Impact of processing parameters on the quality of pharmaceutical solid dosage forms produced by fused deposition modeling (FDM).* Pharmaceutics, 2019. 11: 633.
55. W. Kempin, V. Domsta, I. Brecht, B. Semmling, S. Tillmann, W. Weitschies, and A. Seidlitz, *Development of a dual extrusion printing technique for an acid- and thermo-labile drug.* Eur J Pharm Sci, 2018. 123: 191-198.
56. W. Kempin, V. Domsta, G. Grathoff, I. Brecht, B. Semmling, S. Tillmann, W. Weitschies, and A. Seidlitz, *Immediate release 3D-printed tablets produced via fused deposition modeling of a thermo-sensitive drug.* Pharm Res, 2018. 35: 124.
57. M. A. Repka, N. Langley, and J. DiNunzio, *Melt extrusion - Material, technology and drug product design*. 2013. Springer, New York, USA.
58. J. Zhang, W. Yang, A. Q. Vo, X. Feng, X. Ye, D. W. Kim, and M. A. Repka, *Hydroxypropyl methylcellulose-based controlled release dosage by melt extrusion and 3D printing: structure and drug release correlation.* Carbohydr Polym, 2017. 177: 49-57.

59. N. G. Solanki, M. Tahsin, A. V. Shah, and A. T. M. Serajuddin, *Formulation of 3D printed tablet for rapid drug release by fused deposition modeling: screening polymers for drug release, drug-polymer miscibility and printability.* J Pharm Sci, 2018. 107: 390-401.
60. N. R. Dumpa, S. Bandari, and M. A. Repka, *Novel gastroretentive floating pulsatile drug delivery system produced via hot-melt extrusion and fused deposition modeling 3D printing.* Pharmaceutics, 2020. 12: 52.
61. J. Zhang, R. Thakkar, Y. Zhang, and M. Maniruzzaman, *Structure-function correlation and personalized 3D printed tablets using a quality by design (QbD) approach.* Int J Pharm, 2020. 590: 119945.
62. A. Samaro, P. Janssens, V. Vanhoorne, J. Van Renterghem, M. Eeckhout, L. Cardon, T. De Beer, and C. Vervaet, *Screening of pharmaceutical polymers for extrusion-based additive manufacturing of patient-tailored tablets.* Int J Pharm, 2020. 586: 119591.
63. European Directorate for the Quality of Medicines & Healthcare, *Parenteral preparations*, in *European Pharmacopoeia 10.0*. 2020. Deutscher Apotheker Verlag, Stuttgart, Germany.
64. K. Chaudhary, M. M. Patel, and P. J. Mehta, *Long-acting injectables: current perspectives and future promise.* Crit Rev Ther Drug Carrier Syst, 2019. 36: 137-181.
65. C. I. Nkanga, A. Fisch, M. Rad-Malekshahi, M. D. Romic, B. Kittel, T. Ullrich, J. Wang, R. W. M. Krause, S. Adler, and T. Lammers, *Clinically established biodegradable long acting injectables: an industry perspective.* Adv Drug Deliv Rev, 2020. 167: 19-46.
66. D. J. Burgess, D. J. Crommelin, A. S. Hussain, and M.-L. Chen, *Assuring quality and performance of sustained and controlled release parenterals: EUFEPS workshop report.* AAPS PharmSci, 2004. 6: 100-111.
67. S. L. Fialho and A. d. Silva Cunha, *Manufacturing techniques of biodegradable implants intended for intraocular application.* Drug Deliv, 2005. 12: 109-116.
68. K. Hirano, T. Ichihashi, and H. Yamada, *Studies on the absorption of practically water-insoluble drugs following injection. I. intramuscular absorption from water-immiscible oil solutions in rats.* Chem Pharm Bull, 1981. 29: 519-531.
69. E. Merisko-Liversidge and G. G. Liversidge, *Nanosizing for oral and parenteral drug delivery: A perspective on formulating poorly-water soluble compounds using wet media milling technology.* Adv Drug Deliv Rev, 2011. 63: 427-440.
70. S. S. H. Abadi, A. Moin, and G. H. Veerabhadrappa, *Fabricated microparticles: an innovative method to minimize the side effects of NSAIDs in arthritis.* Crit Rev Ther Drug Carrier Syst, 2016. 33: 433-488.
71. N. V. N. Jyothi, P. M. Prasanna, S. N. Sakarkar, K. S. Prabha, P. S. Ramaiah, and G. Srawan, *Microencapsulation techniques, factors influencing encapsulation efficiency.* J Microencapsul, 2010. 27: 187-197.
72. N. K. Varde and D. W. Pack, *Microspheres for controlled release drug delivery.* Expert Opin Biol Ther, 2004. 4: 35-51.
73. R. Vaishya, V. Khurana, S. Patel, and A. K. Mitra, *Long-term delivery of protein therapeutics.* Expert Opin Drug Deliv, 2015. 12: 415-440.
74. R. R. S. Thakur, H. L. McMillan, and D. S. Jones, *Solvent induced phase inversion-based in situ forming controlled release drug delivery implants.* J Control Release, 2014. 176: 8-23.
75. C. Rabin, Y. Liang, R. S. Ehrlichman, A. Budhian, K. L. Metzger, C. Majewski-Tiedeken, K. I. Winey, and S. J. Siegel, *In vitro and in vivo demonstration of risperidone implants in mice.* Schizophr Res, 2008. 98: 66-78.
76. A. Santos, M. S. Aw, M. Bariana, T. Kumeria, Y. Wang, and D. Losic, *Drug-releasing implants: current progress, challenges and perspectives.* J Mater Chem B, 2014. 2: 6157-6182.
77. S. A. Stewart, J. Domínguez-Robles, R. F. Donnelly, and E. Larrañeta, *Implantable polymeric drug delivery devices: Classification, manufacture, materials, and clinical applications.* Polymers, 2018. 10: 1379.
78. F. Corduas, E. Mancuso, and D. A. Lamprou, *Long-acting implantable devices for the prevention and personalised treatment of infectious, inflammatory and chronic diseases.* J Drug Deliv Sci Technol, 2020. 60: 101952.

79. J. C. Quarterman, S. M. Geary, and A. K. Salem, *Evolution of drug-eluting biomedical implants for sustained drug delivery.* Eur J Pharm Biopharm, 2020. 159: 21-35.

80. A. C. Freire, A. W. Basit, R. Choudhary, C. W. Piong, and H. A. Merchant, *Does sex matter? The influence of gender on gastrointestinal physiology and drug delivery.* Int J Pharm, 2011. 415: 15-28.

81. L. Elens, B. Vandercam, J.-C. Yombi, D. Lison, P. Wallemacq, and V. Haufroid, *Influence of host genetic factors on efavirenz plasma and intracellular pharmacokinetics in HIV-1-infected patients.* Pharmacogenomics, 2010. 11: 1223-1234.

82. J. Breitkreutz and J. Boos, *Paediatric and geriatric drug delivery.* Expert Opin Drug Deliv, 2007. 4: 37-45.

83. U. Klotz, *The elderly - a challenge for appropriate drug treatment.* Eur J Clin Pharmacol, 2008. 64: 225-226.

84. J.-F. Schlender, M. Meyer, K. Thelen, M. Krauss, S. Willmann, T. Eissing, and U. Jaehde, *Development of a whole-body physiologically based pharmacokinetic approach to assess the pharmacokinetics of drugs in elderly individuals.* Clin Pharmacokinet, 2016. 55: 1573-1589.

85. M. A. Hamburg and F. S. Collins, *The path to personalized medicine.* N Engl J Med, 2010. 363: 301-304.

86. J. S. Cohen, *Ways to minimize adverse drug reactions: individualized doses and common sense are key.* Postgrad Med, 1999. 106: 163-172.

87. A. A. Exner, *Drug-eluting polymer implants in cancer therapy.* Expert Opin Drug Deliv, 2008. 5: 775.

88. M. Fazil, A. Ali, S. Baboota, J. K. Sahni, and J. Ali, *Exploring drug delivery systems for treating osteoporosis.* Expert Opin Drug Deliv, 2013. 10: 1123-1136.

89. M. Varkey, *Growth factor delivery for bone tissue repair: an update.* Expert Opin Drug Deliv, 2004. 1: 19.

90. M. Arruebo, N. Vilaboa, and J. Santamaria, *Drug delivery from internally implanted biomedical devices used in traumatology and in orthopedic surgery.* Expert Opin Drug Deliv, 2010. 7: 589-603.

91. J. Dong, S. Zhang, H. Liu, X. Li, Y. Liu, and Y. Du, *Novel alternative therapy for spinal tuberculosis during surgery: reconstructing with anti-tuberculosis bioactivity implants.* Expert Opin Drug Deliv, 2014. 11: 299-305.

92. D. Mansour, *Nexplanon®: what Implanon® did next.* J Fam Plann Reprod Health Care, 2010. 36: 187-189.

93. V. Brache, *Abstracts of WHO Symposium (WHO1): Background and study methodology of a multicentre randomized clinical trial of two implantable contraceptives for women: Jadelle® and Implanon®.* Eur J Contracept Reprod Health Care, 2014. 19: 44.

94. B. M. Wu, S. W. Borland, R. A. Giordano, L. G. Cima, E. M. Sachs, and M. J. Cima, *Solid free-form fabrication of drug delivery devices.* J Control Release, 1996. 40: 77-87.

95. A. Sutradhar, J. Park, D. Carrau, and M. J. Miller, *Experimental validation of 3D printed patient-specific implants using digital image correlation and finite element analysis.* Comput Biol Med, 2014. 52: 8-17.

96. A. Marro, T. Bandukwala, and W. Mak, *Three-dimensional printing and medical imaging: a review of the methods and applications.* Curr Probl Diagn Radiol, 2016. 45: 2-9.

97. P. M. Gronet, G. A. Waskewicz, and C. Richardson, *Preformed acrylic cranial implants using fused deposition modeling: A clinical report.* J Prosthet Dent, 2003. 90: 429-433.

98. E. L. Nyberg, A. L. Farris, B. P. Hung, M. Dias, J. R. Garcia, A. H. Dorafshar, and W. L. Grayson, *3D-printing technologies for craniofacial rehabilitation, reconstruction, and regeneration.* Ann Biomed Eng, 2017. 45: 45-57.

99. V. Domsta and A. Seidlitz, *3D-Printing of drug-eluting implants: An overview of the current developments described in the literature.* Molecules, 2021. 26: 4066.

100. S. A. Stewart, J. Domínguez-Robles, V. J. McIlorum, E. Mancuso, D. A. Lamprou, R. F. Donnelly, and E. Larrañeta, *Development of a biodegradable subcutaneous implant for prolonged drug delivery using 3D printing.* Pharmaceutics, 2020. 12: 105.

101. B. Allen, C. Moore, T. Seyler, and K. Gall, *Modulating antibiotic release from reservoirs in 3D-Printed orthopedic devices to treat periprosthetic joint infection.* J Orthop Res, 2020. 38: 2239-2249.
102. N. Sandler, I. Salmela, A. Fallarero, A. Rosling, M. Khajeheian, R. Kolakovic, N. Genina, J. Nyman, and P. Vuorela, *Towards fabrication of 3D printed medical devices to prevent biofilm formation.* Int J Pharm, 2014. 459: 62-4.
103. J. J. Water, A. Bohr, J. Boetker, J. Aho, N. Sandler, H. M. Nielsen, and J. Rantanen, *Three-dimensional printing of drug-eluting implants: preparation of an antimicrobial polylactide feedstock material.* J Pharm Sci, 2015. 104: 1099-107.
104. J. A. Weisman, D. H. Ballard, U. Jammalamadaka, K. Tappa, J. Sumerel, H. B. D'Agostino, D. K. Mills, and P. K. Woodard, *3D printed antibiotic and chemotherapeutic eluting catheters for potential use in interventional radiology: in vitro proof of concept study.* Acad Radiol, 2019. 26: 270-274.
105. W. Huang, Q. Zheng, W. Sun, H. Xu, and X. Yang, *Levofloxacin implants with predefined microstructure fabricated by three-dimensional printing technique.* Int J Pharm, 2007. 339: 33-8.
106. Z. Rahman, S. F. B. Ali, T. Ozkan, N. A. Charoo, I. K. Reddy, and M. A. Khan, *Additive manufacturing with 3D printing: progress from bench to bedside.* AAPS J, 2018. 20: 1-14.
107. M. Di Prima, J. Coburn, D. Hwang, J. Kelly, A. Khairuzzaman, and L. Ricles, *Additively manufactured medical products – the FDA perspective. 3D Printing in Medicine.* Vol. 2. p. 1-6. 2016.
108. German Federal Ministry of Health (BMG), *Ordinance on the operation of pharmacies (Verordnung über den Betrieb von Apotheken), Section 7*, 1987.
109. C. Korte, *3D-drug-printing: extrusion of printable drug-loaded filaments and development of novel solid dosage forms,* PhD thesis. Heinrich Heine University, Institute of Pharmaceutics and Biopharmaceutics, 2018.
110. M. Nixon, R. Andrew, and K. E. Chapman, *It takes two to tango: dimerisation of glucocorticoid receptor and its anti-inflammatory functions.* Steroids, 2013. 78: 59-68.
111. M. Schäfer-Korting, B. Kleuser, M. Ahmed, H. D. Höltje, and H. C. Korting, *Glucocorticoids for human skin: new aspects of the mechanism of action.* Skin Pharmacol Physiol, 2005. 18: 103-114.
112. L. S. Fernández, M. F. Castro, and J. L. A. Sánchez, *Use of glucocorticosteroids in rheumatoid arthritis. How and when should steroids be used in rheumatoid arthritis?* Reumatol Clin 2007. 3: 262-269.
113. H. Derendorf, G. Hochhaus, S. Rohatagi, H. Möllmann, J. Barth, H. Sourgens, and M. Erdmann, *Pharmacokinetics of triamcinolone acetonide after intravenous, oral, and inhaled administration.* J Clin Pharmacol 1995. 35: 302-305.
114. *Volon A 40/A 40-5 ml Summary of product characteristics (Fachinformation), Dermapharm*, 2021.
115. M. Østergaard and P. Halberg, *Intra-articular corticosteroids in arthritic disease.* Biodrugs, 1998. 9: 95-103.
116. V. B. Kraus, P. G. Conaghan, H. A. Aazami, P. Mehra, A. J. Kivitz, J. Lufkin, J. Hauben, J. R. Johnson, and N. Bodick, *Synovial and systemic pharmacokinetics (PK) of triamcinolone acetonide (TA) following intra-articular (IA) injection of an extended-release microsphere-based formulation (FX006) or standard crystalline suspension in patients with knee osteoarthritis (OA).* Osteoarthr Cartil, 2018. 26: 34-42.
117. H. Derendorf, H. Möllmann, A. Grüner, D. Haack, and G. Gyselby, *Pharmacokinetics and pharmacodynamics of glucocorticoid suspensions after intra-articular administration.* Clin Pharmacol Ther, 1986. 39: 313-317.
118. N. Gerwin, C. Hops, and A. Lucke, *Intraarticular drug delivery in osteoarthritis.* Adv Drug Deliv Rev, 2006. 58: 226-242.
119. P. Jüni, R. Hari, A. W. S. Rutjes, R. Fischer, M. G. Silletta, S. Reichenbach, and B. R. da Costa, *Intra-articular corticosteroid for knee osteoarthritis.* Cochrane Database Syst Rev, 2015. Art. No.: CD005328.

120. M. Godwin and M. Dawes, *Intra-articular steroid injections for painful knees. Systematic review with meta-analysis.* Can Fam Physician, 2004. 50: 241-248.

121. W. Zhang, R. W. Moskowitz, G. Nuki, S. Abramson, R. D. Altman, N. Arden, S. Bierma-Zeinstra, K. D. Brandt, P. Croft, M. Doherty, M. Dougados, M. Hochberg, D. J. Hunter, K. Kwoh, L. S. Lohmander, and P. Tugwell, *OARSI recommendations for the management of hip and knee osteoarthritis, Part II: OARSI evidence-based, expert consensus guidelines.* Osteoarthritis Cartilage, 2008. 16: 137-162.

122. Flexion Therapeutics Inc. Zilretta® (triamcinolone acetonide extended-release injectable suspension), Approval Letter. 2017. Available from: www.accessdata.fda.gov/drugsatfda_docs/nda/2017/208845Orig1s000Approv.pdf. Last access: 27.02.2021.

123. J. Paik, S. T. Duggan, and S. J. Keam, *Triamcinolone acetonide extended-release: a review in osteoarthritis pain of the knee.* Drugs, 2019. 79: 455-462.

124. P. G. Conaghan, D. J. Hunter, S. B. Cohen, V. B. Kraus, F. Berenbaum, J. R. Lieberman, D. G. Jones, A. I. Spitzer, D. S. Jevsevar, N. P. Katz, D. J. Burgess, J. Lufkin, J. R. Johnson, N. Bodick, and F. X. P. Investigators, *Effects of a single intra-articular injection of a microsphere formulation of triamcinolone acetonide on knee osteoarthritis pain: A double-blinded, randomized, placebo-controlled, multinational study.* J Bone Joint Surg, 2018. 100: 666-677.

125. N. Bodick, J. Lufkin, C. Willwerth, A. Kumar, J. Bolognese, C. Schoonmaker, R. Ballal, D. Hunter, and M. Clayman, *An intra-articular, extended-release formulation of triamcinolone acetonide prolongs and amplifies analgesic effect in patients with osteoarthritis of the knee: a randomized clinical trial.* J Bone Joint Surg, 2015. 97: 877-888.

126. M. J. Ho, S. R. Kim, Y. W. Choi, and M. J. Kang, *Recent advances in intra-articular drug delivery systems to extend drug retention in joint.* J Pharm Investig, 2019. 49: 9-15.

127. M. Verjans, M. Asseln, and K. Radermacher, *Rapid prototyping of replica knee implants for in vitro testing.* Curr Dir Biomed Eng, 2016. 2: 553-556.

128. Y. Wang, L. Sun, Z. Mei, F. Zhang, M. He, C. Fletcher, F. Wang, J. Yang, D. Bi, Y. Jiang, and P. Liu, *3D printed biodegradable implants as an individualized drug delivery system for local chemotherapy of osteosarcoma.* Mater Des, 2020. 186: 108336.

129. Deutsches Institut für Normung, *DIN EN ISO 66001: Informationsverarbeitung - Sinnbilder und ihre Anwendung*, 2003. Beuth Verlag, Berlin, Germany.

130. E. J. Laukamp, *Melt extruded drug formulations for individual dosing by the solid dosage pen,* PhD thesis. Heinrich Heine University, Institute of Pharmaceutics and Biopharmaceutics, 2014.

131. P. Tack, J. Victor, P. Gemmel, and L. Annemans, *3D-printing techniques in a medical setting: a systematic literature review.* Biomed Eng Online, 2016. 15: 115.

132. D. P. Elder, M. Kuentz, and R. Holm, *Pharmaceutical excipients — quality, regulatory and biopharmaceutical considerations.* Eur J Pharm Sci, 2016. 87: 88-99.

133. T. Feuerbach, S. Callau-Mendoza, and M. Thommes, *Development of filaments for fused deposition modeling 3D printing with medical grade poly(lactic-co-glycolic acid) copolymers.* Pharm Dev Technol, 2018. 24: 487-493.

134. M. A. Frohoff-Hülsmann, A. Schmitz, and B. C. Lippold, *Aqueous ethyl cellulose dispersions containing plasticizers of different water solubility and hydroxypropyl methylcellulose as coating material for diffusion pellets: I. Drug release rates from coated pellets.* Int J Pharm, 1999. 177: 69-82.

135. G. Shlieout and G. Zessin, *Investigation of ethylcellulose as a matrix former and a new method to regard and evaluate the compaction data.* Drug Dev Ind Pharm, 2008. 22: 313-319.

136. European Directorate for the Quality of Medicines & Healthcare, *Ethyl cellulose* in *European Pharmacopoeia 10.0*. 2020. Deutscher Apotheker Verlag, Stuttgart, Germany.

137. O. Pillai and R. Panchagnula, *Polymers in drug delivery.* Curr Opin Chem Biol, 2001. 5: 447-451.

138. F. Casati, F. Briatico-Vangosa, F. Baldi, A. Melocchi, A. Maroni, A. Gazzaniga, and L. Zema, *Assessment of hot-processability and performance of ethylcellulose-based materials for injection-molded prolonged-release systems: an investigational approach.* Int J Pharm, 2018. 548: 400-407.
139. E. Verhoeven, *Influence of formulation and process parameters on the release characteristics of ethylcellulose sustained-release mini-matrices produced by hot-melt extrusion.* Eur J Pharm Biopharm, 2008. 69: 312-319.
140. A. Meena, T. Parikh, S. S. Gupta, and A. T. M. Serajuddin, *Investigation of thermal and viscoelastic properties of polymers relevant to hot melt extrusion-II: cellulosic polymers.* J Excip Food Chem, 2016. 5: 1002.
141. E. Pinto and T. Dürig, *Cellulose ethers for extrusion applications*, in *Melt extrusion: materials, technology and drug product design*. p. 123-144. 2013. Springer, New York, USA.
142. M. R. Sanoufi, A. Aljaberi, I. Hamdan, and N. Al-Zoubi, *The use of design of experiments to develop hot melt extrudates for extended release of diclofenac sodium.* Pharm Dev Technol, 2020. 25: 187-196.
143. C. De Brabander, C. Vervaet, and J. P. Remon, *Development and evaluation of sustained release mini-matrices prepared via hot melt extrusion.* J Control Release, 2003. 89: 235-247.
144. A. Goyanes, A. Fernandez-Ferreiro, A. Majeed, N. Gomez-Lado, A. Awad, A. Luaces-Rodriguez, S. Gaisford, P. Aguiar, and A. W. Basit, *PET/CT imaging of 3D printed devices in the gastrointestinal tract of rodents.* Int J Pharm, 2018. 536: 158-164.
145. Y. Yang, *3D printed tablets with internal scaffold structure using ethyl cellulose to achieve sustained ibuprofen release.* Eur J Pharm Sci, 2018. 115: 11-18.
146. S. M. Maru, M. de Matas, A. Kelly, and A. Paradkar, *Characterization of thermal and rheological properties of zidovidine, lamivudine and plasticizer blends with ethyl cellulose to assess their suitability for hot melt extrusion.* Eur J Pharm Sci, 2011. 44: 471-478.
147. D. Desai, H. Sandhu, N. Shah, W. Malick, H. Zia, W. Phuapradit, and S. R. K. Vaka, *Selection of solid-state plasticizers as processing aids for hot-melt extrusion.* J Pharm Sci, 2018. 107: 372-379.
148. European Directorate for the Quality of Medicines & Healthcare, *Triethyl citrate*, in *Commentary of the European Pharmacopoeia 5.0*. 2006. Deutscher Apotheker Verlag, Stuttgart, Germany.
149. R. V. Nellore, G. S. Rekhi, A. S. Hussain, L. G. Tillman, and L. L. Augsburger, *Development of metoprolol tartrate extended-release matrix tablet formulations for regulatory policy consideration.* J Control Release, 1998. 50: 247-256.
150. P. Colombo, *Swelling-controlled release in hydrogel matrices for oral route.* Adv Drug Deliv Rev, 1993. 11: 37-57.
151. J. Siepmann and N. A. Peppas, *Modeling of drug release from delivery systems based on hydroxypropyl methylcellulose (HPMC).* Adv Drug Deliv Rev, 2012. 64: 163-174.
152. A. T. Pham and P. I. Lee, *Probing the mechanisms of drug release from hydroxypropylmethyl cellulose matrices.* Pharm Res, 1994. 11: 1379-1384.
153. J. Aho, A. Halme, J. Boetker, J. J. Water, A. Bohr, N. Sandler, J. Rantanen, and S. Baldursdottir, *The effect of HPMC and MC as pore formers on the rheology of the implant microenvironment and the drug release in vitro.* Carbohydr Polym, 2017. 177: 433-442.
154. J. Boetker, J. Water, J. Aho, L. Arnfast, A. Bohr, and J. Rantanen, *Modifying release characteristics from 3D printed drug-eluting products.* Eur J Pharm Sci, 2016. 90: 47-52.
155. United States Pharmacopeia 38th Edition, *Hypromellose*, 2015. United States Pharmacopeial Convention, Rockville, USA.
156. W. Gunder, B. Lippold, and B. Lippold, *Release of drugs from ethyl cellulose microcapsules (diffusion pellets) with pore formers and pore fusion.* Eur J Pharm Sci, 1995. 3: 203-214.
157. P. Mura, M. T. Faucci, A. Manderioli, S. Furlanetto, and S. Pinzauti, *Thermal analysis as a screening technique in preformulation studies of picotamide solid dosage forms.* Drug Dev Ind Pharm, 1998. 24: 747-756.

158. J. L. Ford and P. Timmins, *Pharmaceutical thermal analysis: techniques and applications*. 1989. Ellis Horwood Ltd, Chichester, UK.
159. F. Bracher, P. Heisig, P. Langguth, E. Mutschler, G. Rücker, G. Scriba, E. Stahl-Biskup, and R. Troschütz, *Triamcinolone acetonide*. Commentary of the European Pharmacopoeia 7.5. 2013. Wissenschaftliche Verlagsgesellschaft, Stuttgart, Germany.
160. C. Näther and I. Jeß, *New news about an old drug: Investigations on the polymorphism of triamcinolone acetonide.* Angew Chem Int Ed, 2006. 45: 6381-6383.
161. H. L. Lai, K. Pitt, and D. Q. M. Craig, *Characterisation of the thermal properties of ethylcellulose using differential scanning and quasi-isothermal calorimetric approaches.* Int J Pharm, 2010. 386: 178-184.
162. M. V. Velaco, J. L. Ford, and A. R. Rajabi-Siaboomi, *Use of Dynamic Differential Scanning Calorimetry in Identifying Glass Transition Temperatures of Ethylcellulose and Surelease Films.* Pharmacy and Pharmacology Communications, 1999. 5: 259-263.
163. R. Greiner and F. R. Schwarzl, *Volume relaxation and physical aging of amorphous polymers I. Theory of volume relaxation after single temperature jumps.* Colloid Polym Sci, 1989. 267: 39-47.
164. H. A. Barnes, *A handbook of elementary rheology*. Vol. 1. 2000. Aberystwyth: University of Wales, Institute of Non-Newtonian Fluid Mechanics
165. N. Genina, J. Holländer, H. Jukarainen, E. Mäkilä, J. Salonen, and N. Sandler, *Ethylene vinyl acetate (EVA) as a new drug carrier for 3D printed medical drug delivery devices.* Eur J Pharm Sci, 2016. 90: 53-63.
166. Z. Muwaffak, A. Goyanes, V. Clark, A. W. Basit, S. T. Hilton, and S. Gaisford, *Patient-specific 3D scanned and 3D printed antimicrobial polycaprolactone wound dressings.* Int J Pharm, 2017. 527: 161-170.
167. J. Aho, J. P. Boetker, S. Baldursdottir, and J. Rantanen, *Rheology as a tool for evaluation of melt processability of innovative dosage forms.* Int J Pharm, 2015. 494: 623-642.
168. R. Lenk, *The Effect of melt elasticity on extrusion and other melt processing operations*, in *Polymer Rheology*. p. 101-112. 1978. Springer, Dordrecht, The Netherlands.
169. C. Hopmann and W. Michaeli, *Monoextrusion dies for thermoplastics* in *Extrusion dies for plastics and rubber: design and engineering computations*. 2016. Carl Hanser Verlag GmbH Co KG, München, Germany.
170. H. Palza, S. Filipe, I. F. C. Naue, and M. Wilhelm, *Correlation between polyethylene topology and melt flow instabilities by determining in-situ pressure fluctuations and applying advanced data analysis.* Polymer, 2010. 51: 522-534.
171. J. Aho, J. P. Bøtker, N. Genina, M. Edinger, L. Arnfast, and J. Rantanen, *Roadmap to 3D-printed oral pharmaceutical dosage forms: feedstock filament properties and characterization for fused deposition modeling.* J Pharm Sci, 2019. 108: 26-35.
172. A. Goyanes, U. Det-Amornrat, J. Wang, A. W. Basit, and S. Gaisford, *3D scanning and 3D printing as innovative technologies for fabricating personalized topical drug delivery systems.* J Control Release, 2016. 234: 41-48.
173. Deutsches Institut für Normung, *DIN EN ISO 527-1 Kunststoffe - Bestimmung der Zugeigenschaften - Teil 1: Allgemeine Grundsätze*, 2003. Beuth Verlag GmbH, Berlin, Germany.
174. L. H. Block and R. N. Patel, *Solubility and dissolution of triamcinolone acetonide.* J Pharm Sci, 1973. 62: 617-621.
175. P. Sakellariou and R. Rowe, *The morphology of blends of ethylcellulose with hydroxypropyl methylcellulose as used in film coating.* Int J Pharm, 1995. 125: 289-296.
176. Y.-Y. Lua, X. Cao, B. R. Rohrs, and D. S. Aldrich, *Surface characterizations of spin-coated films of ethylcellulose and hydroxypropyl methylcellulose blends.* Langmuir, 2007. 23: 4286-4292.
177. P. Sakellariou, R. C. Rowe, and E. F. T. White, *Polymer/polymer interaction in blends of ethyl cellulose with both cellulose derivatives and polyethylene glycol 6000.* Int J Pharm, 1986. 34: 93-103.

178. P. L. Ritger and N. A. Peppas, *A simple equation for description of solute release I. Fickian and non-fickian release from non-swellable devices in the form of slabs, spheres, cylinders or discs.* J Control Release, 1987. 5: 23-36.
179. R. W. Korsmeyer, R. Gurny, E. Doelker, P. Buri, and N. A. Peppas, *Mechanisms of solute release from porous hydrophilic polymers.* Int J Pharm, 1983. 15: 25-35.
180. T. Higuchi, *Mechanism of sustained-action medication. Theoretical analysis of rate of release of solid drugs dispersed in solid matrices.* J Pharm Sci, 1963. 52: 1145-1149.
181. P. L. Ritger and N. A. Peppas, *A simple equation for description of solute release II. Fickian and anomalous release from swellable devices.* J Control Release, 1987. 5: 37-42.
182. J. Holländer, N. Genina, H. Jukarainen, M. Khajeheian, A. Rosling, E. Mäkilä, and N. Sandler, *Three-dimensional printed PCL-based implantable prototypes of medical devices for controlled drug delivery.* J Pharm Sci, 2016. 105: 2665-2676.
183. H. Ponsar, R. Wiedey, and J. Quodbach, *Hot-melt extrusion process fluctuations and their impact on critical quality attributes of filaments and 3D-printed dosage forms.* Pharmaceutics, 2020. 12: 511.
184. A. Melocchi, F. Parietti, G. Loreti, A. Maroni, A. Gazzaniga, and L. Zema, *3D printing by fused deposition modeling (FDM) of a swellable/erodible capsular device for oral pulsatile release of drugs.* J Drug Deliv Sci Technol, 2015. 30: 360-367.
185. R. C. R. Beck, P. S. Chaves, A. Goyanes, B. Vukosavljevic, A. Buanz, M. Windbergs, A. W. Basit, and S. Gaisford, *3D printed tablets loaded with polymeric nanocapsules: an innovative approach to produce customized drug delivery systems.* Int J Pharm, 2017. 528: 268-279.
186. R. Meier, K.-P. Moll, M. Krumme, and P. Kleinebudde, *Impact of fill-level in twin-screw granulation on critical quality attributes of granules and tablets.* Eur J Pharm Biopharm, 2017. 115: 102-112.
187. R. Meier, M. Thommes, N. Rasenack, K. P. Moll, M. Krumme, and P. Kleinebudde, *Granule size distributions after twin-screw granulation – do not forget the feeding systems.* Eur J Pharm Biopharm, 2016. 106: 59-69.
188. F. M. Dekking, C. Kraaikamp, H. P. Lopuhaä, and L. E. Meester, *A Modern Introduction to Probability and Statistics: Understanding why and how*. Vol. 488. p. 236. 2005. Springer, London.
189. K. Kohlgrüber and W. Wiedmann, *Co-rotating twin-screw extruders - fundamentals, technology, and applications*. 2008. Carl Hanser Publisher Munich, Germany.
190. A. R. Forrest, *Antialiasing in practice*, in *Fundamental algorithms for computer graphics*. p. 113-134. 1985. Springer, Berlin.
191. G. D'Antona and A. Ferrero, *Digital signal processing for measurement systems: theory and applications*. p. 115-126. 2006. Springer, New York, USA.
192. European Directorate for the Quality of Medicines & Healthcare, *2.9.5 Mass uniformity of single-dose preparation*, in *European Pharmacopoeia 9.0*. 2017. Deutscher Apotheker Verlag, Stuttgart, Germany.
193. K. Kunnath, Z. Huang, L. Chen, K. Zheng, and R. Davé, *Improved properties of fine active pharmaceutical ingredient powder blends and tablets at high drug loading via dry particle coating.* Int J Pharm, 2018. 543: 288-299.
194. P. Lacey, *Developments in the theory of particle mixing.* J Appl Chem, 1954. 4: 257-268.
195. J. Harting, *Entwicklung einer Raman spektroskopischen Methode zur kontinuierlichen inline Gehaltsbestimmung und Charakterisierung eines Feuchtgranulierprozesses,* PhD thesis. Heinrich Heine University, Institute of Pharmaceutics and Biopharmaceutics, 2019.
196. European Directorate for the Quality of Medicines & Healthcare, *2.9.6 Uniformity of content of single-dose preparations*, in *European Pharmacopoeia 10.0*. 2020. Deutscher Apotheker Verlag, Stuttgart, Germany.
197. European Directorate for the Quality of Medicines & Healthcare, *2.9.40 Uniformity of dosage units* in *European Pharmacopoeia 9.1*. 2017. Deutscher Apotheker Verlag, Stuttgart, Germany.
198. International Council for Harmonisation of Technical Requirements for Pharmaceuticals for Human Use, *Stability testing of new drug substances and products Q1A(R2)*, 2003.

199. Commitee for Properietary Medicinal Products (CPMP) - European Agency for the Evaluation of Medicinal Products (EMEA), *Note for guidance in in-use stability testing of human medicinal products*, 2001.
200. S. A. Kucera, L. A. Felton, and J. W. McGinity, *Physical aging in pharmaceutical polymers and the effect on solid oral dosage form stability.* Int J Pharm, 2013. 457: 428-436.
201. L. C. E. Struik, *Physical aging in plastics and other glassy materials.* Polym Eng Sci, 1977. 17: 165-173.
202. J.-H. Guo, *Aging processes in pharmaceutical polymers.* Pharm Sci Technolo Today, 1999. 2: 478-483.
203. H. J. Ott, *Einfluß der thermischen Vorgeschichte auf die Enthalpie von PMMA.* Angew Makromol Chem, 1978. 74: 317-322.
204. Z. Černošek, J. Holubová, E. Černošková, and M. Liška, *Enthalpic relaxation and the glass transition.* J Optoelectron Adv Mater, 2002. 4: 489-503.
205. R. Androsch, K. Jariyavidyanont, and C. Schick, *Enthalpy relaxation of polyamide 11 of different morphology far below the glass transition temperature.* Entropy, 2019. 21: 984.
206. J. S. Boateng, H. N. E. Stevens, G. M. Eccleston, A. D. Auffret, M. J. Humphrey, and K. H. Matthews, *Development and mechanical characterization of solvent-cast polymeric films as potential drug delivery systems to mucosal surfaces.* Drug Dev Ind Pharm, 2009. 35: 986-996.
207. C. Monder, *Stability of corticosteroids in aqueous solutions.* Endocrinology, 1968. 82: 318-326.
208. T. O. Oesterling and D. E. Guttman, *Factors influencing stability of prednisolone in aqueous solution.* J Pharm Sci, 1964. 53: 1189-1192.
209. J. Shen and D. J. Burgess, *Accelerated in-vitro release testing methods for extended-release parenteral dosage forms.* J Pharm Pharmacol, 2012. 64: 986-996.
210. C. Larsen, S. W. Larsen, H. Jensen, A. Yaghmur, and J. Østergaard, *Role of in vitro release models in formulation development and quality control of parenteral depots.* Expert Opin Drug Deliv, 2009. 6: 1283-1295.
211. M. Kastellorizios and D. J. Burgess, *In vitro drug release testing and in vivo/in vitro correlation for long acting implants and injections*, in *Long acting injections and implants*. p. 475-503. 2012. Springer, New York, USA.
212. F. C. H. Pinto, A. D. S.-C. Junior, R. L. Oréfice, E. Ayres, S. P. Andrade, L. D. C. Lima, S. A. L. Moura, and G. R. Da Silva, *Controlled release of triamcinolone acetonide from polyurethane implantable devices: application for inhibition of inflammatory-angiogenesis.* J Mater Sci Mater Med, 2012. 23: 1431-1445.
213. J.-S. Ahn, H.-K. Choi, M.-K. Chun, J.-M. Ryu, J.-H. Jung, Y.-U. Kim, and C.-S. Cho, *Release of triamcinolone acetonide from mucoadhesive polymer composed of chitosan and poly(acrylic acid) in vitro.* Biomaterials, 2002. 23: 1411-1416.
214. Y.-M. Kim, J.-O. Lim, H.-K. Kim, S.-Y. Kim, and J.-P. Shin, *A novel design of one-side coated biodegradable intrascleral implant for the sustained release of triamcinolone acetonide.* Eur J Pharm Biopharm, 2008. 70: 179-186.
215. S.-C. Shin and J.-Y. Kim, *Enhanced permeation of triamcinolone acetonide through the buccal mucosa.* Eur J Pharm Biopharm, 2000. 50: 217-220.
216. R. Sheshala, G. C. Hong, W. P. Yee, V. S. Meka, and R. R. S. Thakur, *In situ forming phase-inversion implants for sustained ocular delivery of triamcinolone acetonide.* Drug Deliv Transl Res, 2019. 9: 534-542.
217. R. Pearlman, B. S. Rutherford, K. M. Pozsgai, and C. A. Hirsch, *The isolation and identification of some degradation products of flurandrenolide in Cordran cream.* Int J Pharm, 1984. 18: 53-65.
218. J. Hansen and H. Bundgaard, *Studies on the stability of corticosteroids V. The degradation pattern of hydrocortisone in aqueous solution.* Int J Pharm, 1980. 6: 307-319.
219. Z. Wu, M. L. Thatcher, J. K. Lundberg, M. K. Ogawa, C. B. Jacoby, J. L. Battiste, and K. A. Ledoux, *Forced degradation studies of corticosteroids with an alumina-steroid-ethanol model for predicting chemical stability and degradation products of pressurized metered-dose inhaler formulations.* J Pharm Sci, 2012. 101: 2109-2122.

220. M. L. Lewbart and V. R. Mattox, *Destruction of cortisone and related steroids by traces of copper during purification procedures.* Nature, 1959. 183: 820-821.
221. H. Bundgaard and J. Hansen, *Studies on the stability of corticosteroids. IV. Formation and degradation kinetics of 21-dehydrocorticosteroids, key intermediates in the oxidative decomposition of 21-hydroxy corticosteroids.* Arch Pharm Chem, Sci Edn, 1980. 8: 187-206.
222. European Directorate for the Quality of Medicines & Healthcare, *Triamcinolone acetonide*, in *European Pharmacopoeia 9.0*. 2017. Deutscher Apotheker Verlag, Stuttgart, Germany.
223. A. J. P. van Heugten, W. de Boer, W. S. de Vries, C. M. A. Markesteijn, and H. Vromans, *Development and validation of a stability-indicating HPLC-UV method for the determination of triamcinolone acetonide and its degradation products in an ointment formulation.* J Pharm Biomed Anal, 2018. 149: 265-270.
224. V. Das Gupta, *Stability of triamcinolone acetonide solutions as determined by high-performance liquid chromatography.* J Pharm Sci, 1983. 72: 1453-1456.
225. J. Hansen and H. Bundgaard, *Studies on the stability of corticosteroids I. Kinetics of degradation of hydrocortisone in aqueous solution.* Arch Pharm Chem, Sci Edn, 1979. 7: 135-146.
226. A. J. P. van Heugten, W. S. de Vries, M. M. A. Markesteijn, R. J. Pieters, and H. Vromans, *The role of excipients in the stability of triamcinolone acetonide in ointments.* AAPS PharmSciTech, 2018. 19: 1448-1453.
227. European Directorate for the Quality of Medicines & Healthcare, *5.17.1 Recommendations on dissolution testing* in *European Pharmacopoeia 10.0*. 2020. Deutscher Apotheker Verlag, Stuttgart, Germany.
228. V. B. Kraus, T. V. Stabler, S. Y. Kong, G. Varju, and G. McDaniel, *Measurement of synovial fluid volume using urea.* Osteoarthr Cartil, 2007. 15: 1217-1220.
229. S. Iyer, W. Barr, and H. T. Karnes, *Profiling in vitro drug release from subcutaneous implants: a review of current status and potential implications on drug product development.* Biopharm Drug Dispos, 2006. 27: 157-170.
230. M. Siewert, J. Dressman, C. Brown, and V. Shah, *FIP/AAPS guidelines for dissolution/in vitro release testing of novel/special dosage forms.* AAPS PharmSciTech, 2003. 4: 6-15.
231. Q. Li, X. Guan, M. Cui, Z. Zhu, K. Chen, H. Wen, D. Jia, J. Hou, W. Xu, X. Yang, and W. Pan, *Preparation and investigation of novel gastro-floating tablets with 3D extrusion-based printing.* Int J Pharm, 2018. 535: 325-332.
232. P. Arany, I. Papp, M. Zichar, M. Csontos, J. Elek, G. Regdon, Jr., I. Budai, M. Béres, R. Gesztelyi, P. Fehér, Z. Ujhelyi, G. Vasvári, Á. Haimhoffer, F. Fenyvesi, J. Váradi, V. Miklós, and I. Bácskay, *In vitro tests of FDM 3D-printed diclofenac sodium-containing implants.* Molecules 2020. 25: 5889.
233. P. F. Costa, A. M. Puga, L. Diaz-Gomez, A. Concheiro, D. H. Busch, and C. Alvarez-Lorenzo, *Additive manufacturing of scaffolds with dexamethasone controlled release for enhanced bone regeneration.* Int J Pharm, 2015. 496: 541-50.
234. Z.-L. Farmer, E. Utomo, J. Domínguez-Robles, C. Mancinelli, E. Mathew, E. Larrañeta, and D. A. Lamprou, *3D printed estradiol-eluting urogynecological mesh implants: influence of material and mesh geometry on their mechanical properties.* Int J Pharm, 2021. 593: 120145.
235. J. Holländer, R. Hakala, J. Suominen, N. Moritz, J. Yliruusi, and N. Sandler, *3D printed UV light cured polydimethylsiloxane devices for drug delivery.* Int J Pharm, 2018. 544: 433-442.
236. C. Wu, Y. Luo, G. Cuniberti, Y. Xiao, and M. Gelinsky, *Three-dimensional printing of hierarchical and tough mesoporous bioactive glass scaffolds with a controllable pore architecture, excellent mechanical strength and mineralization ability.* Acta Biomater, 2011. 7: 2644-2650.
237. Y. Yang, X. Qiao, R. Huang, H. Chen, X. Shi, J. Wang, W. Tan, and Z. Tan, *E-jet 3D printed drug delivery implants to inhibit growth and metastasis of orthotopic breast cancer.* Biomaterials, 2020. 230: 119618.

238. M. J. Ho, S. R. Kim, Y. W. Choi, and M. J. Kang, *A novel stable crystalline triamcinolone acetonide-loaded PLGA microsphere for prolonged release after intra-articular injection.* Bull Korean Chem Soc, 2016. 37: 1496-1500.
239. P. Costa and J. M. S. Lobo, *Modeling and comparison of dissolution profiles.* Eur J Pharm Sci, 2001. 13: 123-133.
240. T. Higuchi, *Rate of release of medicaments from ointment bases containing drugs in suspension.* J Pharm Sci, 1961. 50: 874-875.
241. N. A. Peppas and J. J. Sahlin, *A simple equation for the description of solute release. III. Coupling of diffusion and relaxation.* Int J Pharm, 1989. 57: 169-172.
242. J. Siepmann and N. A. Peppas, *Higuchi equation: Derivation, applications, use and misuse.* Int J Pharm, 2011. 418: 6-12.
243. H. Windolf, R. Chamberlain, and J. Quodbach, *Predicting drug release from 3D printed oral medicines based on the surface area to volume ratio of tablet geometry.* Pharmaceutics, 2021. 13: 1453.
244. J. Siepmann and F. Siepmann, *Modeling of diffusion controlled drug delivery.* J Control Release, 2012. 161: 351-362.
245. L. Matysova, R. Hajkova, J. Šícha, and P. Solich, *Determination of methylparaben, propylparaben, triamcinolone acetonide and its degradation product in a topical cream by RP-HPLC.* Anal Bioanal Chem, 2003. 376: 440-443.
246. International Council for Harmonisation of Technical Requirements for Pharmaceuticals for Human Use, *Validation of analytical procedures: text and methodology Q2 (R1)*, 2005.
247. Center for Drug Evaluation and Research (CDER), *Validation of chromatographic methods* in *Reviewer guidance*. 1994. US Food and Drug Adminstration, Rockville, MD, USA.
248. S. Barimani and P. Kleinebudde, *Monitoring of tablet coating processes with colored coatings.* Talanta, 2018. 178: 686-697.

8. Danksagung

Die vorliegende Arbeit entstand unter der Leitung von Herrn Prof. Dr. Jörg Breitkreutz und der Betreuung von Herrn Dr. Julian Quodbach, Herrn Prof. Dr. Dr. h.c. Peter Kleinebudde, und Herrn Dr. Werner Hoheisel im Rahmen meiner Tätigkeit als Doktorandin im Drug Delivery Innovation Center (DDIC) der INVITE GmbH, sowie als wissenschaftliche Mitarbeiterin am Institut für Pharmazeutische Technologie und Biopharmazie der Heinrich-Heine-Universität, Düsseldorf.

Mein besonderer Dank gilt Dr. Julian Quodbach, der durch seine Betreuung und Unterstützung einen wesentlichen Anteil am Entstehen und Erfolg dieser Arbeit beigetragen hat. Ich danke ihm insbesondere für sein Vertrauen, die Motivation, Diskussionsbereitschaft und aufbauenden Worte während allen „Aufs und Abs“ dieser Arbeit. Seine ständige Ansprechbarkeit und sein Glaube an mich haben mir vor allem während herausfordernden Phasen das nötige Durchhaltevermögen gegeben. Danke Dir für Alles.

Meinem Doktorvater, Herrn Prof. Dr. Jörg Breitkreutz möchte ich besonders danken für die Aufnahme in seinen Arbeitskreis und das Ermöglichen an einem sehr facettenreichen und innovativen Forschungsthema frei zu arbeiten. Ich danke ihm für seine kreativen Denkanstöße, die Hilfestellungen, fachlichen Diskussionen und Motivation während der letzten Jahre. Die Rivalität zwischen Köln und Mönchengladbach konnte das Verhältnis nur selten trüben.

Bei Herrn Prof. Dr. Dr. h.c. Peter Kleinebudde möchte ich mich herzlich für die Übernahme des Koreferats bedanken. Seine Ansprechbarkeit, guten Ratschläge und konstruktive Kritik während Fokus-Gruppen und Vorträgen haben dazu beigetragen die Arbeit stetig zu verbessern.

Bei beiden Professoren möchte ich mich für die großartige, kollegiale Arbeitsatmosphäre am Institut und die Ermutigung für die Teilnahme an Konferenzen und Fortbildungen bedanken. Das hat die Promotion zu etwas ganz Besonderem gemacht.

Mein Dank gilt zudem Dr. Armin Schweiger und Dr. Werner Hoheisel für die Aufnahme bei INVITE und dem DDIC, wodurch die Anfertigung der Promotionsarbeit realisiert werden konnte. Vielen Dank für sämtliche Mittel, die mir für die Durchführung der Arbeit zur Verfügung gestellt wurden. Insbesondere möchte ich mich für die Ermöglichung der Teilnahme an diversen Konferenzen und Seminaren bedanken. Ich danke dem gesamten INVITE-Team für die gute Zusammenarbeit.

Außerdem danke ich allen Mitgliedern des DDICs für die konstruktiven und hilfreichen Ratschläge.

Meine Arbeit im Rahmen dieses interdisziplinären Konsortiums durchführen zu dürfen, haben maßgeblich zu meiner fachlichen und persönlichen Entwicklung beigetragen.

Den Studierenden Sharon von Harrach und Shadfar Mehrabani danke ich für Ihre Arbeitsbereitschaft, Unterstützung und tollen Einsatz während Ihres Wahlpflichtpraktikums.

Herrn Dr. Klaus Knop danke ich für die guten Ratschläge während Fokus-Gruppen und immerwährende Hilfestellungen, wann immer notwendig.

Dorothee Eikeler möchte ich von Herzen danken für Ihre Unterstützung über die gesamte Promotionszeit, vor allem bei unzähligen Extrusionen, Verdünnungsreihen und manuellen Probenzügen. Danke für die vielen Gespräche (fachlicher und weniger fachlicher Natur), gemeinsamen Pausen und die daraus entstandene Freundschaft. Danke für deine aufmunternden Worte in Zeiten von Verzweiflung meinerseits und die vielen lustigen Momente.
Andrea Michel danke ich für unzählige DSC-Messungen, praktische Hilfestellung und die gemeinsame Zeit.
Karin Matthée danke ich ebenfalls für viele DSC-Messungen. Es war mir eine Ehre dein letztes AFL-Praktikum mit dir zu betreuen.
Lisa Man danke ich für die Bestellung von Materialien und die Bereitstellung von Eis und Kaffee während den Instituts-Mittagspausen.
Für die zuverlässige und kreative Anfertigung von Halterungen für meine Freisetzungsapparatur, Reparaturen, und die Organisation von Aufträgen an die Glasbläserei danke ich Herrn Stefan Stich.
Frau Simone Mönninghoff-Pützer danke ich für die Bestellung von Materialien, sowie den schnellen Hilfestellungen rund um das Thema HPLC-Troubleshooting.

Dr. Björn Fischer danke ich für die Durchführung der konfokalen Raman-Messungen.
Bei Dr. Raphael Wiedey möchte ich mich für die Unterstützung in allen statistischen und µCT-betreffenden Fragestellungen bedanken. Zudem danke ich Ihm für sein offenes Ohr und die vielen ausgetauschten „Freundlichkeiten“, die mir den Promotionsalltag erheitert haben.
Dr. Tanja Knaab stand mir vor allem bei chemischen Fragestellungen der Promotionsarbeit mit Rat und Tat zur Seite. Ich danke ihr für die Unterstützung während der Degradationsanalyse und Synthese, aber auch für die entstandene Freundschaft und gemeinsamen Gespräche über fachliche und weniger fachlichen Themen.

Meinen Bürokollegen Sebastian Pohl (aka Ronny) und Sebastian Bollmann (aka Bolle) danke ich von Herzen für die gemeinsame Zeit, die vielen witzigen Situationen, das gemeinsame Fluchen und die vielen fachlichen und persönlichen Gespräche. Ihr habt die Promotionszeit für mich

unvergesslich gemacht.
Vielen Dank Ronny für die vielen schönen und vor allem von Lachen geprägten gemeinsamen Momente auch außerhalb des Instituts. Es war mir ein Fest mit Dir von Beginn gemeinsame durch die schönen und unschönen Zeiten der Promotion zu gehen. Danke für deine großartige Freundschaft. Ohne Dich, deine unvergleichliche Art und den Kaffee (manchmal auch Wein), hätte ich das nicht durchgestanden.

Den Mädels Dr. Carolin Korte, Dr. Svenja Niese, Dr. Isabell Keser, Dr. Kira Tromp, Dr. Julia Harting und Svenja Schneider vom Stammtisch Pottwal danke ich von Herzen für die großartige Zeit im und außerhalb des Instituts. Danke für die entstandene Freundschaft, die schönen Abende und die vielen aufmunternden Momente, auch über die Promotionszeit hinaus. Mein besonderer Dank gilt Dr. Carolin Korte, für das Einarbeiten in die Geheimnisse der Schmelzextrusion von Filamenten, die gemeinsamen Reisen, Ihr stets offenes Ohr und aufmunternden Worte, vor allem wenn es mal nicht so gut lief.

Allen Doktorandinnen und Doktoranden des Instituts danke ich für eine unvergessliche Zeit, die besondere, großartige Arbeitsatmosphäre und ausgiebigen Kaffeepausen mit vielen fachlichen und persönlichen Diskussionen. Die vielen fröhlichen Momenten und Erlebnisse auf gemeinsamen Konferenzreisen und privaten Aktivitäten werden mir in besonderer Erinnerung bleiben. Mein besonderer Dank gilt Dr. Vincent Lenhart für die vielen ausgetauschten erheiternden „Freundlichkeiten“, Christopher Nüboldt für die unzähligen gemeinsamen Autofahrten von dem wunderschönen Köln in die verbotene Stadt, sowie Dr. Annika Wilms, Jhinuk Rahman und Sebastian Pohl für das gemeinsame Durchstehen unzähliger Berichte und Vorträge im Rahmen des DDICs.

Meinen Freunden bin ich unendlich dankbar für Ihre Unterstützung außerhalb des Promotionslebens und Ihr Verständnis in den vergangenen Jahren, wenn die Freizeit mal wieder begrenzt war. Das hat mir gezeigt, dass ich mich immer auf Euch verlassen kann.

Carstens und meiner Familie danke ich für die grenzenlose Unterstützung, die Ermutigungen und die Motivation vor allem in Zeiten des Studiums und der Promotion. Meinen Eltern, meiner Schwester und meinem Großvater danke ich besonders für den bindungslosen Rückhalt und der immerwährende Glaube an mich. Ohne Euch wäre all das nicht möglich gewesen.

Mein absolut größter Dank gilt meinem Ehemann Carsten, der mich, während all der turbulenten Zeit begleitet hat, sich mit mir gefreut und viele Tränen getrocknet hat. Danke von ganzem Herzen für deine liebevolle und humorvolle Art, die mich stets aufgebaut und motiviert hat. Danke für deine bedingungslose, unermüdliche Unterstützung, deine Geduld, das Ablenken nach langen Arbeitstagen an der Uni und die viele geopferte Freizeit. Du hättest Dir damit definitiv einen eigenen Titel verdient.

9. Eidestattliche Erklärung

Hiermit erkläre ich gemäß §5 Absatz 1 der Promotionsordnung der Mathematisch-Naturwissenschaftlichen Fakultät der Heinrich-Heine-Universität Düsseldorf an Eides Statt, dass die Dissertation von mir selbstständig und ohne unzulässige fremde Hilfe unter Beachtung der „Grundsätze zur Sicherung guter wissenschaftlicher Praxis an der Heinrich-Heine-Universität Düsseldorf“ erstellt worden ist und dass ich diese in der vorgelegten oder in ähnlicher Form noch bei keiner anderen Fakultät eingereicht habe.

Hanna Ponsar